NASA Technical Memorandum 87698

Wind-Tunnel Acoustic Results of Two Rotor Models With Several Tip Designs

R. M. Martin and Andrew B. Connor

JULY 1986

NASA

NASA Technical Memorandum 87698

Wind-Tunnel Acoustic Results of Two Rotor Models With Several Tip Designs

R. M. Martin and Andrew B. Connor
Langley Research Center
Hampton, Virginia

National Aeronautics
and Space Administration
Scientific and Technical Information Branch
1986

This Page Intentionally Left Blank

CONTENTS

SUMMARY

A three-phase research program has been undertaken to study the acoustic signals due to the aerodynamic interaction of rotorcraft main rotors and tail rotors. During the first phase, two different rotor models (a high-twist system and a low-twist system) with several interchangeable tips were tested in the Langley 4- by 7-Meter Tunnel on the U.S. Army rotor model system. An extensive acoustic data base was acquired, with special emphasis on blade-vortex interaction (BVI) noise. The details of the experimental procedure, acoustic data acquisition, and reduction are documented. The relative importance and trends of the noise characteristics for the nine rotor systems are also discussed.

It is shown that the overall sound pressure levels (0 to 12 700 Hz) of the high-twist rotor systems are relatively insensitive to flight speed but generally increase with rotor tip-path-plane angle. The overall sound pressure levels of the high-twist rotors are dominated by acoustic energy in the low-frequency harmonics, rather than by energy at a higher frequency. The overall sound levels of the low-twist rotor systems show more dependence on flight speed than the high-twist rotors, in addition to being quite sensitive to tip-path-plane angle.

A midfrequency, integrated band-limited sound pressure level, limited by 500 to 3000 Hz, is shown to be a useful metric to quantify the occurrence of BVI noise. The overall sound pressure levels of the low-twist rotors are also strongly influenced by the midfrequency band-limited sound levels (500 to 3000 Hz), indicating that the blade-vortex impulsive noise is a more dominant noise source for this rotor design than for the high-twist rotors. The midfrequency acoustic levels for both rotor systems show a very strong dependence on rotor tip-path-plane angle. The tip-path-plane angle at which the maximum midfrequency sound level occurs consistently decreases with increasing flight speed. The maximum midfrequency sound level measured at a given location is constant regardless of the flight speed.

INTRODUCTION

The Langley Research Center, the U.S. Army Aerostructures Directorate, and Sikorsky Aircraft have jointly undertaken a rotor acoustics research program. The primary objective of the effort is to study the acoustic signals due to the aerodynamic interaction of helicopter main rotors and tail rotors. Additional objectives are (1) to characterize the impulsive noise due to blade-vortex interaction (BVI) created by various blade tip geometries as a function of rotor operating parameters, (2) to characterize the noise of tail rotors and tail rotor installation effects, (3) to acquire an acoustic data base for use in the development and validation of a BVI noise prediction method, and (4) to make comparisons with other scaled acoustic data.

The program is being conducted in three phases. The first of these, the scope of this paper, treats the main rotor alone. This test was conducted in 1983 in the Langley 4- by 7-Meter Tunnel with two rotor systems. The two systems were similar in planform, solidity, and blade number. They differed in airfoil section details, twist distribution, chord, and geometry of their several interchangeable blade tips. The second phase of the program was conducted in 1984 by Sikorsky at the United

Technologies Research Center (UTRC) anechoic wind tunnel with two tail rotor models and various pylon-stabilator configurations. The third phase was conducted in 1985 in the Langley 4- by 7-Meter Tunnel where selected configurations from phases I and II were tested in a full experiment of the noise interaction between the main rotor and tail rotor.

One of the least understood and most troublesome of the many helicopter noise mechanisms is the blade-vortex interaction. This phenomenon typically occurs during low-power descending flight or maneuvers or during conditions of low rotor inflow when the rotor wake is blown back into the rotor disk. The concentrated tip vortices shed from the blade tips are embedded in the rotor wake. Interaction of a blade with the shed tip vortex of a previous blade passage gives rise to the distinctive BVI impulsive noise. The local aerodynamic flow field that generates the impulsive signal is strongly dependent on the orientation and proximity of the vortex to the blade. The impulsive acoustic signal is generally in the frequency range most sensitive to human subjective response (500 to 5000 Hz) and thus has importance to both civil community acceptance and military detectability.

Some acoustic results of the phase I experiment have been previously published. The data were first applied in an acoustic-ray tracing technique (ref. 1) to determine the region on the rotor where the blade-vortex interactions occurred. The experimental results were compared with analytic predictions of blade-vortex encounters using a generalized rotor-wake prediction code (ref. 2). The acoustic data have also been compared with 1/20- and full-scale acoustic data in work reported by Shenoy (ref. 3). This paper is intended to document fully the details of the phase I experiment and to present a summary and general analysis of the results.

SYMBOLS

Values are given in SI Units but, where considered useful, they are also given in U.S. Customary Units. Measurements and calculations were made in U.S. Customary Units.

A	acoustic pressure amplitude, dynes/cm^2
A_0	peak acoustic pressure amplitude, dynes/cm^2
C	chord of rotor blade, m
c	speed of sound, m/sec
f	frequency, Hz
K	acoustic wave number, $2\pi f/c$, m^{-1}
ℓ	distance from center of rotor tip path plane to microphone, measured in rotor tip path plane, $(x^2 + y^2)^{1/2}$, m
R	rotor radius, 1.42 m (4.67 ft)
r	radial distance from center of rotor tip path plane to microphone, $(x^2 + y^2 + z^2)^{1/2}$, m

Δt elapsed time from echo, sec

V tunnel free-stream velocity, m/sec (knots)

x microphone coordinate relative to center of rotor tip path plane, positive upstream, m

y microphone coordinate relative to center of rotor tip path plane, positive to left looking upstream, m

z microphone coordinate relative to center of rotor tip path plane, positive up, m

α rotor tip-path-plane angle, also called "rotor angle of attack" (see subsection entitled "Rotor Control"), positive when vehicle nose is up, deg

θ polar angle, angle down from rotor tip path plane, positive down, $\tan^{-1}(z/\ell)$, deg

ψ azimuth angle, angle in plane of rotor, positive counterclockwise, zero over aircraft tail, $\tan^{-1}(y/x)$, deg

Abbreviations:

BLSPL band-limited sound pressure level (500 to 3000 Hz), dB (re 0.0002 dynes/cm^2)

BVI blade-vortex interaction

ITS locations inside tunnel test section

Mic. microphone location

OASPL overall sound pressure level (0 to 12 700 Hz), dB (re 0.0002 dynes/cm^2)

OTS locations outside tunnel test section

DESCRIPTION OF EXPERIMENT

Wind-Tunnel Facility

The Langley 4- by 7-Meter Tunnel is a closed-circuit atmospheric wind tunnel that can be operated either in the open-jet or closed-jet mode. The open-jet mode is accomplished by removing test section walls, raising a movable ceiling, and introducing a bell-mouth collector. The dimensions of the rectangular jet facility when operated as an open-jet test chamber are 4.42 m (14.50 ft) high and 6.63 m (21.75 ft) wide. The ceiling in the open-throat configuration is approximately 7.50 m (24.60 ft) above the test chamber floor. The floor of the test section remains in place so that three sides of the jet are open. The rotor model and test rig in the open-jet test chamber are shown in figure 1.

The acoustic characteristics of this facility as originally constructed have been documented (ref. 4). Because this facility was not originally designed for acoustic testing, acoustic treatment was applied during the experiment reported herein to reduce acoustic reflections from the walls, floor, and ceiling of the test chamber. The test section floor was lined with 12.7-cm (5.0-in.) fiberglass panels covered with perforated sheet metal. The floor, ceiling, and wall areas adjacent to the test section were covered with 15.2-cm (6.0-in.) open-cell polyurethane foam. The locations of this acoustic treatment, identified by the crosshatched areas, are shown in figure 2. The effects of this acoustic treatment and the accuracy of the resulting acoustic data are discussed in the section entitled "Data Quality."

In addition to acoustic treatment, small triangular vanes were installed around the inside perimeter of the jet exit. The purpose of these vanes was to reduce a low-frequency flow pulsation (refs. 5 and 6) that occurred at low speeds in the open-jet mode. Initially, these vanes increased the tunnel background noise levels; however, some innovative treatment was applied and the noise created was restored to that of the unmodified tunnel (refs. 7 and 8).

Rotor Model System

Two four-bladed rotor models were tested using the general rotor model system (GRMS) described in reference 9. The GRMS is employed by the U.S. Army Aerostructures Directorate for rotor systems research in the Langley 4- by 7-Meter Tunnel. Details of the two rotor models are presented in figures 3 and 4, which show their planform, twist, and tip configurations. Other pertinent data for these models are listed in table I. These particular rotor blades and tips were chosen for two reasons: they represent contemporary technology in rotor and tip design and there is a considerable amount of full- and model-scale data available for the same designs. The high-twist model was a 17-percent-scale model, and the low-twist model was a 21-percent-scale model of the full-scale rotors. The fuselage model employed was a generic fuselage shape of approximately the same scale as that of the high-twist and low-twist rotor systems.

High-twist rotor and tips.- The rotor blade for the high-twist model is shown in figure 3 and the blade tips are shown in figure 4. The four tips are standard, swept tapered with an SC1095 airfoil section, swept tapered with an SSC-A07 airfoil section, and parabolic with an SSC-A07 airfoil section.

Low-twist rotor and tips.- The low-twist rotor blade and tips are also shown in figures 3 and 4. The five tips are standard, anhedral, swept, tapered, and square. This rotor model is described in detail in reference 10.

Test Procedure

Test conditions.- The research objective was to map the noise generation as a function of forward speed and tip-path-plane angle at fixed thrust coefficient for each rotor configuration, with emphasis on the measurement of BVI impulsive noise. The rotors were tested over a speed range from 50 to 80 knots at tip-path-plane angles ranging from -6° to 10°. The rotor test matrices reported here are shown in figure 5. Other parametric variations were measured, such as tip speed ratio, thrust coefficient, and tip Mach number, but they are not reported here. Forward speed and tip-path-plane angle were the principal operating parameters. The range of tip-path-plane angle was intended to bracket the region of minimum BVI noise, the onset of BVI

noise, and the maximum BVI noise at each flight speed. The tunnel background noise levels at high speeds limited the tunnel speed to less than 90 knots. At low speeds, large open-jet aerodynamic boundary corrections, in addition to a low-frequency aerodynamic pulsation in the open-jet tunnel, limited the tunnel speed to greater than 40 knots.

Rotor control.- Conventional helicopter terminology will be employed throughout this paper in the discussions about and descriptions of these test rotors. Readers not familiar with these terms and conventions are referred to a classical text such as reference 11.

The rotor tip-path-plane angle α was set by setting the rotor shaft angle. To ensure that rotor shaft angle, or rotor angle of attack, and tip-path-plane angle were essentially equal, flapping angles were set to 0 with cyclic pitch control. The procedure was to trim the rotor to zero flapping for a given tunnel speed and to step the rotor angle of attack in 2° increments at each speed. The nominal rotor angles of attack were corrected for the actual tunnel flow conditions; thus the data will usually be given in some value approximating an integer step of 2°. The nominal value of α, rather than the corrected value, will customarily be presented here for simplicity. To change rotor angle of attack, the rotor hub was pivoted about a reference point approximately 73.7 cm (29 in.) below the rotor hub. Thus, when the rotor angle of attack was changed, the physical location of the rotor hub in the test section changed also. Collective pitch was adjusted after each angle-of-attack change to maintain a constant thrust coefficient.

Rotor performance data.- Rotor performance data (ref. 12) were acquired using a computer-controlled data acquisition system. The performance data were acquired while the acoustic signals were recorded on tape in order to relate the character of the noise to rotor operating parameters. Cyclic and collective pitch angles were measured at the swashplate, blade flapping and lag angles were measured at their hinge pins, and the entire system was mounted upon a six-component strain-gauge balance to measure rotor forces and moments. The rotor performance parameters were continuously computed and updated from these measurements during the test. Upon achieving a steady-state operating condition, all data were acquired and stored for later processing. The later processing included cross-plotting of rotor thrust coefficient, flapping angles, and rotor moments to ensure that the acoustic data were acquired at the correct operating conditions. The mean flow angle and mean free-stream velocity of the tunnel were corrected for open-jet boundary effects using the theory of reference 13.

Acoustic Data Acquisition

Nineteen 0.635-cm-diameter (0.25-in.) free-field condenser microphones were installed in and around the open-throat test section as shown in figure 2. These particular locations were chosen initially with the intention of acquiring acoustic data at several specific angles relative to the rotor disk (θ) for a range of azimuth angle in the disk plane (ψ). The exact locations in terms of Cartesian coordinates (x, y, z) and in terms of the radial distance, angle below the disk plane, and azimuth angle (r, θ, ψ) are presented in table II; the orientation of these two coordinate systems is also shown. Inspection of table II shows that several microphones were located at angles of θ near 25°, near 0° (in the disk plane), and near -25°. The azimuth angle ψ varied in multiples of 45° from 45° to 270°.

Microphone 1 was mounted to the fuselage, very close to the rotor disk, in a location known to be sensitive to BVI noise. The geometry between the rotor hub and this microphone remained constant with rotor attitude change. Since all the other microphones were fixed to the test chamber floor, their relative locations changed with changes in rotor shaft angle. This condition means that for these locations, a true assessment of directivity cannot be made. The changes in polar angle θ, radial distance r, and azimuth angle ψ with changes in rotor angle α are presented in tables III, IV, and V, respectively.

The acoustic data were recorded on two 14-channel frequency-modulated magnetic tape recorders. A once-per-revolution impulse signal was recorded on magnetic tape simultaneously with the acoustic signals to record blade azimuth angle, in addition to IRIG-A time code. The recording method was Wideband I and the tape speed was 76.2 cm/sec (30 in/sec). Daily calibrations were performed using a standard piston-phone calibrator at 250 Hz, 124 dB. The analog signals were not high-pass filtered (as is often done to remove low-frequency wind noise) because of the phase distortion of the available filters. (Since the impulsive time history was of primary interest to this study, nonlinear phase distortion could seriously alter the waveforms, particularly at low frequencies near the filter cutoff frequency.)

Each complete microphone system (including the microphone, preamplifier, and adapter) was calibrated using the electrostatic actuator method prior to the experiment for its pressure response. This response was found to be flat to approximately 7 kHz, at which the correction was approximately -0.5 dB and became as much as -1.4 dB at 10 kHz. Typical rotor acoustic spectra acquired during this experiment had the highest levels at the first few blade passage harmonics (100, 200, and 300 Hz). The rotor acoustic levels at 7 kHz were typically 30 dB lower than these low-frequency levels. In this case the pressure response corrections would not have a measurable effect on the results, and therefore the corrections were not applied.

To verify the frequency response characteristics of each acoustic data acquisition system, an in-line white noise signal was inserted simultaneously into each data channel. The relative time error between each data channel was calculated from the phase of the cross power spectral density function of the white noise for each unique pair of channels. The relative time error between channels was found to be small enough (approximately 20 percent of the time between digitized samples at a sample rate of about 26 000 samples per second) that it could be considered negligible.

Acoustic Data Reduction

The analog acoustic signals were digitized using a conditional sampling technique based on the rotor once-per-revolution signal. A synchronizer sampled the acoustic signals at 1024 equally spaced intervals in each rotor revolution such that the 1024 points defining each rotor revolution are at the same relative azimuth angle. The synchronizer constantly updated the sample rate to adjust for small changes in rotor rotational speed. The acoustic time histories of 50 rotor revolutions were sampled in this manner and then were ensemble averaged to obtain an average acoustic waveform and standard deviation for each test condition. The effect of this averaging technique is to remove random fluctuations such as background noise and to enhance the periodic content of the signal. The averaged time history, standard deviation band, and five revolutions of instantaneous time history data were stored on a computer disk.

To obtain spectra, 200 rotor revolutions were conditionally sampled, and the data of four sequential rotor revolutions were transformed to the frequency domain using a 4096-point fast Fourier transform algorithm. This approach yielded 50 spectra with a bandwidth of exactly 1/16th of the blade passage frequency. The results of each of these 50 power spectra were then averaged to get an average power spectrum for each test condition, which was stored on a computer disk. Considering each power spectrum as a Chi-squared random variable, the statistical accuracy of the spectral results is ±0.8 dB for an 80-percent confidence interval.

It should be noted that a time domain weighting or spectral window was not applied to these data. The harmonic analysis approach employed minimizes leakage of the acoustic energy at the blade passage frequency and its harmonics, and thus a Hanning or other window is not required. In addition, since the digitization rate was tied to the rotor shaft speed, which varied slightly during each recording sequence (±2 rpm at 1480 rpm), the spectral calculations are actually estimates of the acoustic energy at multiples of the shaft frequency, rather than at particular frequencies. However, since the variation in rotor rotational speed was very small, the variation in sample rate was also small, and thus the error in the nominal frequency is very small (typically 6.7 Hz ± 0.0002 Hz for the high-twist system data and 5.8 Hz ± 0.003 Hz for the low-twist system data).

To obtain integrated sound pressure levels, the squared acoustic pressures of the power-averaged spectra were summed from 0 to 12 500 kHz for an overall sound pressure level (OASPL) at each rotor test condition, and they were summed from 500 to 3000 Hz to acquire a band-limited sound pressure level (BLSPL). Since the overall levels of rotors are often dominated by the low-frequency levels, this band-limited sound level was calculated to emphasize changes in the midfrequency range. The range of 500 to 3000 Hz was chosen because changes in model scale BVI noise levels were observed to be the most significant in this region.

DATA QUALITY

The Langley 4- by 7-Meter Tunnel was not originally designed for acoustic research, and thus there are fundamental limits to taking acoustic data in the facility. At the higher tunnel speeds (above 90 knots), the major limiting factor is tunnel background noise. At lower speeds (less than 40 knots), a low-frequency flow pulsation has been a problem in the past (ref. 5). Work is currently underway (refs. 6 and 14) to provide solutions to these aerodynamic and acoustic problems. The following paragraphs describe some of these factors that may affect the quality of the acoustic data acquired. A summary is presented at the end of this section.

Background Noise

Background noise data were acquired for all microphone locations with the model installed, the rotor hub spinning (without rotor blades), and for tunnel speeds from 50 to 120 knots in 10-knot increments. For all the microphone locations, the predominant noise is the low-frequency tunnel background noise, which typically decreases by 25 to 30 dB at 1000 Hz. The background noise above 5000 Hz is generally near the noise floor of the recording system for a system with approximately 40 dB of dynamic range. An example of the background noise spectra for a typical inflow location inside the tunnel test section (ITS) at 50 to 90 knots is shown in figure 6.

Figure 7 shows the overall background noise levels for microphone locations 1, 2, 3, 4, 5, 9, 12, and 17 as a function of tunnel speed. The lowest noise levels over the range of tunnel speed are at locations 1, 3, and 4. Higher levels are exhibited by locations 2 and 17; those in the middle are locations 5, 9, and 12.

Figure 8 shows the background noise levels for the microphones located outside the tunnel test section (OTS) and split into two groups. The first group (microphone locations 7, 8, 16, and 19) exhibits the lower overall levels (fig. 8(a)), the second group (microphone locations 10, 11, 13, 14, 15, and 18) exhibits the higher levels (fig. 8(b)). The first OTS group has lower overall levels than the ITS locations, but most of the second OTS group have higher levels than the ITS. It was observed during the test that this latter group of OTS microphones experienced a great amount of wind-induced noise and that they were too close to the tunnel jet shear layer. Calculations made prior to the test (based on a shear layer expansion angle of 15°) indicated that these locations would be outside the jet shear layer and in a relatively quiet environment; however, this was not the case. It is probable that the use of the jet exit vanes, which were used to reduce pulsations in the jet shear layer, also increased its thickness significantly (refs. 5 to 7).

Several typical rotor test conditions were chosen and the rotor and background data were plotted together. For the ITS microphones, the signal-to-noise ratio is good except at the very lowest frequencies where the wind noise can be quite close to the lowest rotor harmonics. An example of this comparison is shown in figure 9.

Since the background noise levels were relatively high at the higher tunnel speeds, the integrated sound pressure levels and the averaged acoustic spectra were corrected by subtracting the background noise on an acoustic power (mean-squared pressure) basis. The time history data have not been corrected for background noise. The effect of averaging time histories serves to remove some random energy.

Reflections

To measure reflections at each microphone, small explosive charges were ignited in the test section to create an impulsive noise source at each of the following tunnel speeds: 0, 50, 80, and 120 knots. The acoustic signals were recorded on tape and analyzed to measure the reflections at each microphone location. The impulse signal had most of its energy in the spectral region from 0 to 3000 Hz; and because of the very short period of the emitted impulse, the signal was very useful in identifying reflections with very short path lengths (approximately 30 cm (1 ft)), such as those arriving from some of the microphone support stands. An example of the impulse data and reflections measured at zero tunnel speed is shown for microphones 1 and 3 in figures 10(a) and 10(b), respectively. The direct and echo signals are marked in this figure. Table VI contains the estimated reflection delay times, relative amplitudes, and possible reflecting surfaces for all the microphones for the 0- and 80-knot cases. Most of the reflections have relative amplitudes in the range from 0.1 to 0.3, or about 20.0 and 10.5 dB down from the incident wave. Since the accuracy of the spectral averaging method is ±0.8 dB, a reflection with a relative amplitude less than 0.4 (which adds 0.6 dB to the total rotor signal) has an effect on the integrated acoustic results that is less than the uncertainty of the data reduction approach.

A tone burst generator was also used in the test section to generate short bursts of pure tones at frequencies of 500, 1000, 3000, and 5000 Hz. Inspection of these data confirmed the results of the impulsive source data. Examples of the tone

burst data for microphone 1 at 1000 Hz and microphone 3 at 500 Hz are shown in figures 11(a) and 11(b), respectively. The direct and reflected signals are marked in these figures. In general, the 500-Hz tones exhibited the highest reflection amplitudes. This result indicates that the low-frequency content (less than 1000 Hz) of the rotor signal may be more contaminated by reflected signals than the higher frequency content (greater than 1000 Hz).

In an attempt to correct the measured rotor acoustic spectra for the reflection contamination, the power cepstrum technique was investigated (ref. 15). The power cepstrum is a Fourier transform technique that has been used to correct acoustic reflections from contaminated jet noise spectra (refs. 16 and 17). The success of this correction technique was limited by the unknown nonlinear effects of the reflecting surfaces and complications due to the highly periodic nature of rotor signals. However, it was concluded (ref. 15) that the echo contamination can be partially removed from the measured spectra to yield an improved estimate of the free-field spectrum. The acoustic spectra presented in this report have been corrected for the major reflections. Because this technique in its present state must be applied on a case-by-case basis and typically is only a small correction to integrated noise levels, and because of the very large amount of data presented here, the overall integrated sound metrics (OASPL and BLSPL) have not been corrected for reflections. The reader should note also that the acoustic time history data presented here are not corrected for acoustic reflections.

Geometric and Acoustic Near-Field

All the microphones employed during this test were located within 4 rotor radii of the rotor hub. (See table II.) These locations were limited by the physical size of the tunnel test chamber. Although there is no clear definition of the geometric near-field of a rotor, the measurements presented here are believed to be in the geometric near-field of the rotor. The acoustic near-field may be defined relative to the wave number of the noise source, and it is generally defined by the relation $Kr > 1$, where K is the acoustic wave number and r is the distance from source to receiver. For the first rotor harmonic (100 Hz), the closest microphone locations (locations 1 and 2) are in the acoustic near-field of the rotor. Above the first harmonic, all locations can be considered to be in the acoustic far-field.

Refraction

Refraction through the free-jet shear layer is another limiting factor for the OTS microphone locations. The utility of these locations will be more qualitative than quantitative in that differences in level for similar velocity conditions can be assessed. It is possible to predict theoretically the effect of transmission through a jet shear layer on the measured amplitude and direction of an acoustic signal (ref. 18). However, this theory assumes that the source is compact. In the case of a rotor model, the rotor is relatively large compared to the distances to the microphones, and the signal location of origin is not known, making it quite difficult (if not impossible) to include such a correction to the measured data. Fortunately, the amplitude and directivity angle corrections are not severe for flow speeds in the range considered here (Mach number range from 0.06 to 0.12). Because of the aforementioned complications, no shear layer corrections have been applied to the OTS acoustic data presented herein.

Repeatability

During the test, several conditions were repeated on different days to provide an assessment of data repeatability. The averaged time histories and spectra of three microphones for all these repeat runs were compared. In general, the repeatability was quite good. A typical example of the repeatability is given in figure 12, which shows a comparison of the averaged acoustic signal plotted against time (normalized by 1 rotor period) for two similar test conditions acquired on different days.

Summary of Data Quality

The microphone locations to be presented here are 1, 2, 3, 4, 5, 7, 8, 9, 12, and 17. All microphones, except 7 and 8, are located inside the tunnel test section (ITS). All may be considered to be in the geometric near-field of the source. Most locations are in the acoustic far-field for frequencies above 300 Hz (the third rotor harmonic). For the microphone data presented here, in the speed range of 40 to 90 knots, the tunnel background noise is not a serious contaminant. The average spectra and overall levels (OASPL and BLSPL) are corrected on a squared pressure basis for the measured background noise. The spectra are also corrected using the power cepstrum technique for acoustic reflections. The averaged and instantaneous time history data presented are not corrected in any manner. The effect of shear layer refraction is contained in the data of locations 7 and 8, although this effect is judged to be small because of the lower Mach number range tested. The repeatability of the acoustic data has been found to be acceptable.

DISCUSSION

The following discussion is a summary based on the data presented in appendixes A and B. In the following text, only data for the baseline-tip high-twist rotor and the baseline-tip low-twist rotor are presented. Appendix A presents comparisons, using two analysis methods, of sound pressure levels plotted against tip-path-plane angle as a function of forward velocity. (See figs. A1 to A10.) Each figure shows two different sound pressure level metrics (OASPL and BLSPL) plotted against rotor tip-path-plane angle for each of the unique rotor configurations (tip designs shown in fig. 4). Each curve in figure 5 is for a constant tunnel speed. The shaded symbols represent the OASPL results and the open symbols represent the BLSPL results. As will be explained subsequently, the BLSPL is believed to be a useful tool for extracting the BVI impulsive noise from the total rotor noise. Appendix B presents representative instantaneous time history and average spectral data for selected test points in appendix A. (See figs. B1 to B10.)

Near-Field Location

Microphone 1 was affixed to the model fuselage and moved with the model through all its position changes. The microphone coordinates in terms of radial distance r, polar angle θ, and azimuth angle ψ for this microphone are 0.67 m (2.2 ft), 35°, and 110°, respectively. The trends shown in figure 13 are typical of almost all the rotor configurations tested. The overall sound pressure level (OASPL) increases consistently with rotor angle, with the highest levels at high tip-path-plane angles. For the high-twist standard rotors at each rotor angle, the OASPL values are within 5 dB for the range of flight speed. This effect is illustrated by figure 13(a),

which shows the OASPL and BLSPL trends with flight speed and tip-path-plane angle for the baseline-tip high-twist rotor. The low-twist rotors exhibit a greater range of overall sound level at each rotor angle. This effect is illustrated by figure 13(b), which shows the same data for the baseline-tip low-twist rotor. Here the difference in sound level is as much as 15 dB at $\alpha = 0°$. In addition, a comparison of figures 13(a) and 13(b) shows the OASPL of the low-twist rotors to be more heavily influenced by the midfrequency acoustic energy (BLSPL) than the high-twist rotors, particularly for the tip-path-plane angles between 0° and 5°. This effect can also be observed in the other tip designs for the high-twist and low-twist rotors at microphone 1. (See fig. A1.) The band-limited sound pressure level (BLSPL) increases with tip-path-plane angle to a maximum for each speed; however, this maximum is at a different angle for each velocity. This maximum BLSPL occurs at progressively smaller tip-path-plane angles as the velocity increases. This feature is illustrated in figure 14, which shows the tip-path-plane angle for maximum BLSPL plotted against tunnel speed for both baseline rotors at microphone 1. Note that the maximum BLSPL is at about the same decibel level at each speed.

To investigate the reasons for the two sound metrics in figure 13 to exhibit differing trends, the narrowband spectra may be examined. Figure 15 shows the narrowband spectra for the 70-knot data (run 106 in fig. 13(a)) of the high-twist baseline rotor for tip-path-plane angles α from -6° to 8°. Note that the acoustic level of the fundamental frequency (about 100 Hz), typically 10 dB greater than any other higher harmonics, begins to increase at $\alpha = 0°$ and reaches a maximum at $\alpha = 10°$. Also note that the harmonic levels above 500 Hz also increase, evident at about $\alpha = -2°$, and reach a maximum at $\alpha = 4°$. Not only do the harmonic levels increase to a peak at $\alpha = 4°$, but also it appears that "sidebands" (multiples of the shaft frequency) of these harmonics are increasing. This is particularly evident at $\alpha = 0°$ and 2°. These midfrequency harmonics then decrease as α increases to 8°, as also shown in figure 13(a). These differing trends of the low-frequency blade passage harmonics and the midfrequency shaft and blade passage harmonics with tip-path-plane angle are measured directly by the integrated OASPL and BLSPL values.

To examine further the changes in the spectral content, the averaged time histories may be examined (fig. 16). The curve in the middle represents the mean signal, and the upper and lower curves for each test condition represent the standard deviation about the mean signal. At $\alpha = -6°$ and -4°, the signal is nearly sinusoidal, indicating the dominance of the fundamental frequency. At $\alpha = -2°$, some evidence of impulsive activity is seen in the waveform. This activity is seen particularly near 0.8 percent of the rotor period, in the "spikey" character of the mean and standard deviation data. At $\alpha = 0°$ strong impulses are seen in the waveform. These impulses are very repeatable in both amplitude and phase, as shown by the standard deviation bands. At $\alpha = 2°$ and 4° the impulsiveness is still seen but appears to have more variability in peak level and location of the impulse in rotor revolution. At $\alpha = 6°$ there is still some indication of impulsive content, but at $\alpha = 8°$ the signal again is dominated by the fundamental frequency with no impulsive content. These changes in the impulsive character are a direct result of the changing wake geometry, and thus the changing blade-vortex interaction process.

Inspection of figure 13(a) shows that the maximum BLSPL at a tunnel speed of 70 knots (run 106) occurs at $\alpha = 4°$. However, inspection of the time history curves of figure 16 could lead to the conclusion that the condition of maximum BVI impulsive noise occurs at $\alpha = 0°$. This apparent contradiction is due to the time averaging of the acoustic signals. Figure 17 displays an instantaneous (unaveraged) time history for each of the averaged signals of figure 16. A comparison of the averaged and instantaneous signals at $\alpha = -6°$, -4°, -2°, 0°, and 2° indicates that the averaging

process yields a reasonable smoothed estimate of the instantaneous signals while removing random variability and background noise. However, a comparison of the averaged and instantaneous signals at $\alpha = 4°$ (compare figs. 16 and 17) indicates that the BVI impulses have enough variability in phase that the averaging process "smears" them out. Although the average time history of figure 16(f) does not show impulsive behavior, the standard deviation bands do indicate a significant amplitude variation. Thus, in this case the averaged time history is not a useful representation of the actual rotor signal. (However, because of high background noise levels in the data, the instantaneous time history data are also not considered as a reasonable estimate of the actual signal.) This variability in the emission time of the BVI impulses is attributed to variability and instability of the blade-vortex encounter process at that particular operating condition. Interestingly, this specific test condition was also the maximum BLSPL condition at 70 knots. It is concluded from these observations that the best available indicator of BVI impulsive noise for this data base is the acoustic energy or spectral characteristics of the midfrequency bands. Caution must be exercised when interpreting the BVI noise variation based on the conditional averaged or instantaneous time history data alone.

Under Flight Path

Microphones 2, 3, 4, and 5 were mounted along the tunnel centerline, ahead of the rotor, essentially along the flight path. The acoustic data for all the rotor systems measured at location 2, with (r, θ, ψ) coordinates of (1.90 m (6.2 ft), 66°, 162°), show generally the same trends as microphone 1. Two examples of the sound level trends are shown in figure 18, which shows the OASPL and BLSPL trends for the baseline high- and low-twist rotor systems. For all the rotor systems, the OASPL is more dominated by the midfrequency energy (BLSPL), particularly for values of α between -2° and 6° as shown in figure 18.

The OASPL data of microphone 3, with (r, θ, ψ) coordinates of (2.53 m (8.3 ft), 44°, 184°), show essentially the same trends of increasing sound level with increasing tip-path-plane angle, but the BLSPL values are still quite close to the OASPL values, especially in the mid-α region (fig. 19). The OASPL values for microphone location 3 show almost a bucket shape for some of the rotor systems (see figs. A3(b), (d), (e), (f), and (g)), particularly at the lower speeds. The BLSPL curves still show the peaking of sound level at a progressively decreasing tip-path-plane angle with increasing flight speed. Note again that the peak BLSPL is at about the same acoustic level for all the flight speeds.

Microphone 4 (4.27 m (14.0 ft), 13°, 172°) was located quite close to microphone 5 (4.42 m (14.5 ft), 23°, 177°), but closer to the hub (a 3-percent difference in distance). Although the trends for each location are quite similar, the levels are generally a little higher at microphone location 5 than at microphone location 4, even though location 4 is closer to the source. This comparison is seen in figures 20 and 21. It is not likely that reflections are causing this discrepancy because the reflections received at each microphone were about the same amplitude. (See table VI.) Differences in background noise should not be a factor either since this effect has been corrected from the results shown here. It could be inferred from these data that the radiation pattern from the lifting rotor must be highly directional, an effect which may be causing these easily discernible level differences. Another possible explanation is the fact that the microphones are in the acoustic and geometric near-field. The OASPL values at microphones 4 and 5 are very much dependent on the BLSPL values, especially for the low-twist models.

Above Rotor Disk Plane

Microphone 7 (5.27 m (17.3 ft), -22°, 91°) and microphone 8 (5.88 m (19.3 ft), -23°, 64°) were located outside the tunnel test section (OTS) and above the rotor on the advancing side. Microphone 7 data for the baseline high-twist and low-twist rotors are shown in figure 22, and microphone 8 data are shown in figure 23. Both locations exhibit a very linear increase in both OASPL and BLSPL with tip-path-plane angle, but the BLSPL has a steeper slope than the OASPL curves. The BLSPL data for the low-twist rotors show some of the peaking that is characteristic with α as seen in the near-field microphone and flight path locations (locations 1, 2, and 3), but only at the higher speeds. (See the 70- and 80-knot curves of figs. 22(b) and 23(b).)

In Rotor Plane

Microphone 9 was located in the rotor plane at (3.54 m (11.6 ft), -2°, 132°). The OASPL curves for the high-twist rotors are fairly insensitive to changes in tip-path-plane angle (fig. 24(a)). This result is as might be expected from theory (ref. 19) and experiment (ref. 20), which have shown that the sound levels in the plane of the rotor are dominated by thickness noise. These levels are a function only of rotor geometry and tip speed and are not sensitive to loading noise; thus, they are not a function of rotor load distribution or angle of attack. The OASPL of the low-twist rotors seems to be more influenced by the midfrequency content (BLSPL) than the high-twist rotors, especially at the higher speeds (70 to 80 knots). This effect is reflected by the OASPL data that seem to display the same dependence on tip-path-plane angle as the BLSPL data (fig. 24(b)).

Advancing Side

Microphone 12 (3.96 m (13.0 ft), 25°, 133°) measured the sideline noise on the advancing side of the disk at about the same angle below the hub as at microphone 5 (4.42 m (14.5 ft), 23°, 177°). The high-twist OASPL curves appear fairly insensitive to tip-path-plane angle (fig. 25(a)), whereas the low-twist OASPL curves (fig. 25(b)) show the same steady increase in sound level with tip-path-plane angle seen in the near-field microphone (location 1). Inspection of all low-twist data for location 12 shows again that the OASPL values of the low-twist systems were more heavily influenced by the midfrequency levels (BLSPL) than the high-twist systems.

Retreating Side

Microphone 17 was located under the retreating side of the rotor at (2.71 m (8.9 ft), 36°, 270°). The trends of OASPL and BLSPL for all the rotor models are generally the same, showing an increase for moderate tip-path-plane angles and a decrease at very small and very large tip-path-plane angles (fig. 26). This dependence of OASPL on tip-path-plane angle is different from that seen at the other locations. The tip-path-plane angle seems to be the most important parameter, with velocity having a secondary effect. For all the rotors, the BLSPL curves are consistently 10 to 15 dB lower than the OASPL values, showing that the major contribution to the OASPL is from the first four harmonics.

Comparison of Rotor Systems

In general, for the moderate speed range tested, the high-twist levels are relatively insensitive to speed and are more strongly affected by tip-path-plane angle of attack. The OASPL data for the low-twist rotor at all microphones exhibit more variability with flight speed than the data for the high-twist rotor. The acoustic signals of the high-twist rotor are dominated by the first several rotor harmonic levels. The midfrequency acoustic energy (as indicated by the BLSPL metric) created by the low-twist systems also seems, in general, to be a larger contributor to the overall levels than it does for the high-twist rotors.

The primary difference between the high-twist and low-twist rotors tested during this experiment is the twist distribution and chord, aside from the tip design between 92 percent radius and the tip. The high-twist blades have -16° of twist and the low-twist blades have -10° of twist. (See fig. 3(b).) The chord of the high-twist blades was 9.1 cm (3.6 in.) and the chord of the low-twist blades was 7.9 cm (3.1 in.). Since the low-twist rotor configurations tested exhibited a higher level of midfrequency acoustic energy than the high-twist rotors at almost every microphone location considered, it is concluded that the twist distribution and/or chord of the rotor blade have a greater effect on the midfrequency impulsive noise generated by a rotor than the tip design.

This conclusion should not be surprising since the twist distribution has an important effect on the radial loading distribution on the rotor blade surface, and thus an important effect on the strength and characteristics of the vorticity shed from the blade. The strength, size, and trajectory of the shed vorticity and tip vortices are the important parameters for the amplitude levels and impulsive content of the BVI noise.

Operating Conditions for Minimum Noise Levels

It is well-known that BVI noise is primarily a problem when the rotor is flown at a moderate forward speed during descent. Inspection of the acoustic data for the advancing flight path locations (microphone locations 2, 3, 4, 5, and 12) shows that to minimize the midfrequency acoustic levels in descent, the rotor approach should be at the highest forward speed and highest descent rate feasible. To minimize the overall levels in descent, the rotor should be flown at the lowest forward speed and lowest descent rate feasible. Unfortunately, these two conditions are mutually exclusive. The data presented in this report indicate that for a rotor in descent, the overall noise levels (dominated by the low-frequency harmonic levels) will be close to their maximum levels if the minimum midfrequency noise levels are attained.

CONCLUDING REMARKS

A three-phase research program has been jointly undertaken by the Langley Research Center, the U.S. Army Aerostructures Directorate, and Sikorsky Aircraft to study the acoustic signals due to the aerodynamic interaction of rotorcraft main rotors and tail rotors. During the first phase, two different Sikorsky rotor models with several interchangeable tips were tested in the Langley 4- by 7-Meter Tunnel on the U.S. Army rotor model system. An extensive acoustic data base was acquired of the signals generated by these models. The details of the experimental procedure, acoustic data acquisition, and reduction are documented. Two sound level metrics, the overall sound pressure level and a midfrequency (500 to 3000 Hz) band-limited

sound pressure level, are presented for 10 microphone locations as a function of flight speed and rotor tip-path-plane angle. The relative importance and trends of these sound metrics for the two baseline rotor systems are discussed. A more complete set of data for all the rotor configurations tested are presented in the appendixes for the reader's use.

It is shown that the overall sound pressure levels of the high-twist rotor systems are relatively insensitive to flight speed but generally increase with rotor tip-path-plane angle. The overall sound pressure levels of the high-twist rotors are dominated by acoustic energy in the low-frequency harmonics, rather than by energy at a higher frequency. The overall sound levels of the low-twist rotor systems show more dependence on flight speed, in addition to being quite sensitive to rotor tip-path-plane angle. A midfrequency, integrated band-limited sound level, limited by 500 to 3000 Hz, is shown to be a useful metric to quantify the occurrence of blade-vortex interaction (BVI) noise. The overall sound levels of the low-twist rotors are also strongly influenced by the midfrequency noise levels, a result indicating that the blade-vortex impulsive noise is a more dominant noise source for this rotor design than for the high-twist rotors. It is proposed that this finding is due to the different twist distribution and chord of the two rotor systems and that the different tip shapes have a secondary effect on the midfrequency noise characteristics. The midfrequency acoustic levels for all rotor systems show a strong dependence on tip-path-plane angle. The tip-path-plane angle at which the maximum midfrequency sound level occurs consistently decreases with increasing flight speed. The maximum midfrequency noise level measured at a given location is constant regardless of the flight speed.

NASA Langley Research Center
Hampton, VA 23665-5225
April 23, 1986

REFERENCES

1. Martin, R. M.; Elliott, J. W.; and Hoad, D. R.: Comparison of Experimental and Analytical Predictions of Rotor Blade-Vortex Interactions Using Model Scale Acoustic Data. AIAA-84-2269, Oct. 1984.

2. Egolf, T. Alan; and Landgrebe, Anton J.: Helicopter Rotor Wake Geometry and Its Influence in Forward Flight.
   Volume I - Generalized Wake Geometry and Wake Effect on Rotor Airloads and Performance. NASA CR-3726, 1983.
   Volume II - Wake Geometry Charts. NASA CR-3727, 1983.

3. Shenoy, K. Rajarama: The Role of Scale Models in the Design of "Low BVI Noise" Rotorcraft. 41st Annual Forum Proceedings, American Helicopter Soc., 1985, pp. 239-248.

4. Hayden, R. E.; and Wilby, J. F.: Sources, Path, and Concepts for Reduction of Noise in the Test Section of the NASA Langley 4 × 7m Wind Tunnel. NASA CR-172446-1, 1984.

5. Sellers, William L., III; Applin, Zachary T.; Molloy, John K.; and Gentry, Garl L., Jr.: Effect of Jet Exit Vanes on Flow Pulsations in an Open-Jet Wind Tunnel. NASA TM-86299, 1985.

6. Applin, Zachary T.: Flow Improvements in the Circuit of the Langley 4- by 7-Meter Tunnel. NASA TM-85662, 1983.

7. Hoad, Danny R.; and Martin, Ruth M.: Background Noise Measurements From Jet Exit Vanes Designed To Reduce Flow Pulsations in an Open-Jet Wind Tunnel. NASA TM-86383, AVSCOM TM 85-B-1, 1985.

8. Martin, Ruth M.; Brooks, Thomas F.; and Hoad, Danny R.: Reduction of Background Noise Induced by Wind Tunnel Jet Exit Vanes. AIAA J., vol. 23, no. 10, Oct. 1985, pp. 1631-1632.

9. Wilson, John C.: A General Rotor Model System for Wind-Tunnel Investigations. J. Aircr., vol. 14, no. 7, July 1977, pp. 639-643.

10. Jepson, D.; Moffitt, R.; Hilzinger, K.; and Bissell, J.: Analysis and Correlation of Test Data From an Advanced Technology Rotor System. NASA CR-3714, 1983.

11. Gessow, Alfred; and Myers, Garry C., Jr.: Aerodynamics of the Helicopter. Macmillan Co., c.1952.

12. Hoad, Danny R.; Elliott, Joe W.; and Orie, Nettie M.: Rotor Performance Characteristics From an Aeroacoustic Helicopter Wind-Tunnel Test Program. NASA TM-87661, AVSCOM TM 86-B-1, 1986.

13. Heyson, Harry H.: Use of Superposition in Digital Computers To Obtain Wind-Tunnel Interference Factors for Arbitrary Configurations, With Particular Reference to V/STOL Models. NASA TR R-302, 1969.

14. Yu, James C.; and Abrahamson, A. Louis: Acoustic Treatment of the NASA Langley 4- by 7-Meter Tunnel: A Feasibility Study. NASA TP-2563, 1986.

15. Martin, R. M.; and Burley, C. L.: Power Cepstrum Technique With Application to Model Helicopter Acoustic Data. NASA TP-2586, 1986.

16. Miles, Jeffrey H.; Stevens, Grady H.; and Leininger, Gary G.: Application of Cepstral Techniques to Ground-Reflection Effects in Measured Acoustic Spectra. J. Acoust. Soc. America, vol. 61, no. 1, Jan. 1977, pp. 35-38.

17. Syed, A. A.; Brown, J. D.; Oliver, M. J.; and Hills, S. A.: The Cepstrum: A Viable Method for the Removal of Ground Reflections. J. Sound & Vib., vol. 71, no. 2, July 22, 1980, pp. 299-313.

18. Amiet, R. K.: Refraction of Sound by a Shear Layer. J. Sound & Vib., vol. 58, no. 4, June 1978, pp. 467-482.

19. Farassat, F.: Theory of Noise Generation From Moving Bodies With an Application to Helicopter Rotors. NASA TR R-451, 1975.

20. Schmitz, F. H.; and Yu, Y. H.: Helicopter Impulsive Noise: Theoretical and Experimental Status. NASA TM-84390, USAAVRADCOM TR 83-A-2, 1983.

TABLE I.- DETAILS OF ROTOR MODELS

Hub type	Fully articulated
Number of blades	Four
Airfoil section	See figure 3(a)
Hinge offset, cm (in.)	7.6 (3.0)
Root cutout, cm (in.):	
High-twist rotor	18.5 (7.3)
Low-twist rotor	25.9 (10.2)
Pitch-flap coupling angle, deg	-2
Twist	See figure 3(b)
Radius, cm (in.):	
High-twist rotor	142.8 (56.2)
Low-twist rotor	142.2 (56.0)
Chord, cm (in.):	
High-twist rotor	9.1 (3.6)
Low-twist rotor	7.9 (3.1)

TABLE II.- MICROPHONE LOCATIONS WITH RESPECT TO MODEL HUB AT ZERO PITCH

Microphone	x, m (ft)	y, m (ft)	z, m (ft)	r, m (ft)	θ, deg	ψ, deg	r/R
1	0.18 (0.6)	-0.52 (-1.7)	-0.40 (-1.3)	0.67 (2.2)	35	110	0.5
2	.73 (2.4)	-.24 (-.8)	-1.74 (-5.7)	1.90 (6.2)	66	162	1.3
3	1.83 (6.0)	.15 (.5)	-1.74 (-5.7)	2.53 (8.3)	44	184	1.8
4	4.12 (13.5)	-.61 (-2.0)	-.98 (-3.2)	4.27 (14.0)	13	172	3.0
5	4.09 (13.4)	-.24 (-.8)	-1.71 (-5.6)	4.42 (14.5)	23	177	3.1
6	2.35 (7.7)	-2.65 (-8.7)	1.19 (3.9)	3.75 (12.3)	-19	132	2.6
7	.12 (.4)	-4.88 (-16.0)	1.95 (6.4)	5.27 (17.3)	-22	91	3.7
8	-4.09 (-7.7)	-4.88 (-16.0)	2.32 (7.6)	5.88 (19.3)	-23	64	4.1
9	2.39 (7.8)	-2.62 (-8.6)	.12 (.4)	3.54 (11.6)	-2	132	2.5
10	.06 (.2)	-4.88 (-16.0)	.09 (.3)	4.88 (16.0)	-1	91	3.4
11	-2.50 (-8.2)	-4.79 (-15.7)	.09 (.3)	5.40 (17.7)	-1	62	3.8
12	2.44 (8.0)	-2.65 (-8.7)	-1.68 (-5.5)	3.96 (13.0)	25	133	2.8
13	.12 (.4)	-4.73 (-15.5)	-2.01 (-6.6)	5.15 (16.9)	23	91	3.6
14	-2.41 (-7.9)	-4.91 (-16.1)	-1.95 (-6.4)	5.82 (19.1)	20	64	4.1
15	-2.38 (-7.8)	-4.66 (-15.3)	-1.74 (-5.7)	5.52 (18.1)	18	297	3.9
16	-.88 (-2.9)	-5.34 (-17.5)	-1.04 (-3.4)	5.52 (18.1)	11	81	3.9
17	0 (0)	2.20 (7.2)	-1.62 (-5.3)	2.71 (8.9)	36	270	1.9
18	-.70 (-2.3)	4.88 (16.0)	-1.07 (-3.5)	5.06 (16.6)	12	278	3.6
19	3.75 (12.3)	-4.33 (-14.2)	.12 (.4)	5.73 (18.8)	-1	131	4.0

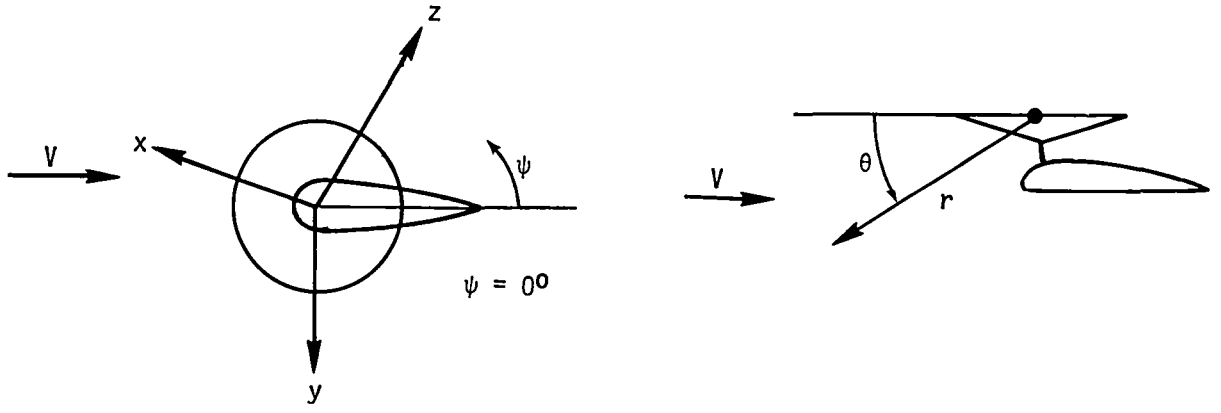

TABLE III.- VARIATION IN POLAR ANGLE OF MICROPHONE LOCATIONS DUE TO CHANGES IN TIP-PATH-PLANE ANGLE

Tip-path-plane angle, α, deg	Polar angle, θ, deg, of microphone location -								
	2	3	4	5	7	8	9	12	17
-6	58.33	36.34	7.08	16.32	-21.86	-20.63	-5.97	20.49	35.97
-5	59.62	37.51	8.09	17.37	-21.86	-21.06	-5.31	21.24	36.09
-4	60.91	38.68	9.11	18.42	-21.86	-21.49	-4.64	22.00	36.18
-3	62.20	39.86	10.12	19.47	-21.85	-21.92	-3.97	22.74	36.26
-2	63.49	41.05	11.15	20.53	-21.83	-22.34	-3.31	23.48	36.31
-1	64.78	42.24	12.17	21.58	-21.82	-22.76	-2.64	24.22	36.35
0	66.07	43.43	13.20	22.64	-21.80	-23.17	-1.97	24.95	36.36
1	67.35	44.63	14.23	23.71	-21.77	-23.58	-1.31	25.68	36.35
2	68.63	45.84	15.26	24.78	-21.74	-23.99	-.64	26.40	36.31
3	69.90	47.05	16.29	25.85	-21.71	-24.39	.03	27.12	36.26
4	71.17	48.26	17.33	26.92	-21.67	-24.78	.69	27.83	36.18
5	72.42	49.48	18.37	27.99	-21.63	-25.18	1.36	28.53	36.09
6	73.65	50.70	19.42	29.07	-21.58	-25.56	2.02	29.23	35.97
7	74.86	51.93	20.47	30.15	-21.53	-25.95	2.69	29.92	35.83
8	76.04	53.16	21.52	31.24	-21.48	-26.32	3.35	30.60	35.67
9	77.19	54.40	22.57	32.33	-21.42	-26.69	4.01	31.27	35.49
10	78.28	55.64	23.63	33.42	-21.36	-27.06	4.67	31.93	35.29

TABLE IV.- VARIATION IN RADIAL DISTANCE OF MICROPHONE LOCATIONS DUE TO CHANGES IN TIP-PATH-PLANE ANGLE

Tip-path-plane angle, α, deg	Radial distance, r, m, of microphone location -								
	2	3	4	5	7	8	9	12	17
-6	1.94	2.59	4.35	4.51	5.26	5.86	3.59	4.02	2.73
-5	1.93	2.58	4.34	4.50	5.26	5.86	3.59	4.02	2.73
-4	1.92	2.57	4.32	4.48	5.26	5.87	3.58	4.01	2.73
-3	1.92	2.56	4.31	4.47	5.26	5.87	3.57	4.00	2.73
-2	1.91	2.55	4.30	4.46	5.26	5.88	3.56	3.99	2.73
-1	1.91	2.54	4.29	4.45	5.26	5.88	3.55	3.98	2.73
0	1.90	2.53	4.27	4.43	5.26	5.89	3.54	3.97	2.73
1	1.90	2.52	4.26	4.42	5.25	5.89	3.53	3.97	2.73
2	1.89	2.51	4.25	4.41	5.25	5.90	3.52	3.96	2.73
3	1.89	2.50	4.24	4.40	5.25	5.90	3.52	3.95	2.73
4	1.88	2.49	4.22	4.39	5.25	5.91	3.51	3.94	2.73
5	1.88	2.48	4.21	4.38	5.25	5.91	3.50	3.94	2.73
6	1.88	2.48	4.20	4.36	5.25	5.92	3.49	3.93	2.73
7	1.87	2.47	4.19	4.35	5.25	5.92	3.48	3.92	2.73
8	1.87	2.46	4.18	4.34	5.25	5.93	3.47	3.92	2.73
9	1.87	2.45	4.16	4.33	5.25	5.93	3.46	3.91	2.73
10	1.87	2.44	4.15	4.32	5.25	5.94	3.46	3.90	2.74

TABLE V.- VARIATION IN AZIMUTH ANGLE OF MICROPHONE LOCATIONS DUE TO CHANGES IN TIP-PATH-PLANE ANGLE

Tip-path-plane angle, α, deg	Azimuth angle, ψ, deg, of microphone location -								
	2	3	4	5	7	8	9	12	17
-6	166.12	184.19	171.88	176.77	89.94	62.87	132.82	135.28	263.59
-5	165.53	184.28	171.83	176.74	90.19	63.09	132.74	134.87	264.65
-4	164.88	184.36	171.79	176.71	90.44	63.32	132.65	134.45	265.71
-3	164.17	184.46	171.74	176.68	90.69	63.55	132.55	134.01	266.78
-2	163.39	184.55	171.69	176.65	90.94	63.79	132.45	133.56	267.85
-1	162.53	184.65	171.63	176.62	91.18	64.04	132.33	133.09	268.92
0	161.57	184.76	171.57	176.58	91.43	64.30	132.21	132.60	269.99
1	160.49	184.88	171.51	176.55	91.68	64.57	132.07	132.10	271.07
2	159.28	185.00	171.45	176.51	91.93	64.84	131.93	131.58	272.14
3	157.91	185.13	171.38	176.47	92.17	65.12	131.78	131.04	273.21
4	156.35	185.27	171.30	176.43	92.42	65.41	131.61	130.49	274.28
5	154.57	185.42	171.23	176.38	92.66	65.71	131.44	129.92	275.34
6	152.50	185.58	171.14	176.33	92.91	66.02	131.26	129.33	276.40
7	150.10	185.75	171.06	176.29	93.15	66.33	131.07	128.72	277.45
8	147.28	185.93	170.97	176.23	93.39	66.66	130.87	128.09	278.49
9	143.94	186.13	170.88	176.18	93.63	66.99	130.66	127.44	279.53
10	139.95	186.34	170.78	176.12	93.87	67.32	130.44	126.77	280.55

TABLE VI.- ESTIMATED REFLECTION AMPLITUDES AND DELAY TIMES FROM IMPULSE DATA

Microphone	V = 0 knot			V = 80 knots		
	Δt, sec	A/A_0	Surface[a]	Δt, sec	A/A_0	Surface[a]
1	0.00136	0.25	Fuselage	0.00116	0.40	Fuselage
	.01000	.17	Floor	.01112	.16	Floor
2	.00308	.57	Floor	.00312	.56	Floor
	.00984	.22	?	.00992	.21	?
3	.00248	.49	Floor	.00224	.33	Floor
	.024	.10				
4	.00404	.20	Floor	.00376	.12	Floor
5	.0018	.18	Mic. stand	.0019	.11	Mic. stand
6	.001	.15	Mic. stand			
	.009	.15	Floor			
7	.001	.22	Mic. stand	.002	.22	Mic. stand
	.010	.10	?	.009	.13	?
	.013	.10	?			
	.016	.10	?			
8	.00075	.18	?			
	.009	.18	?	.009	.23	?
	.013	.18	?	.013	.10	
9	.0073	.22	?	.0023	.16	
10	.006	.20	?	.001	.25	?
				.006	.25	
11	.006	.35	?	.006	.55	?
	.016	.16	?	.019	.18	?
	.019	.16	?	.022	.18	?
12	.002	.49	Floor	.00204	.43	Floor
13	.002	.25	Mic. stand	.002	.20	Mic. stand
	.027	.10	?			
14	.002	.20	Mic. stand	.001	.27	Mic. stand
	.020	.14	Floor	.018	.10	Floor
15	.003	.27	?	.0015	.23	?
	.032	.18	Control room	.019	.12	?
16	.002	.10	Mic. stand	.004	.20	?
	.040	.10	South wall	.025	.18	Floor
17	.003	.38	?	.003	.23	?
	.010	.11	Floor			
18	.026	.17	Control room	.003	.18	?
				.011	.18	?
				.014	.18	
				.020	.18	?
				.025	.18	Control room
19	.006	.22	South wall	.005	.35	?

[a]The question mark (?) indicates that echo delay time could not be easily related to an existing surface in test chamber.

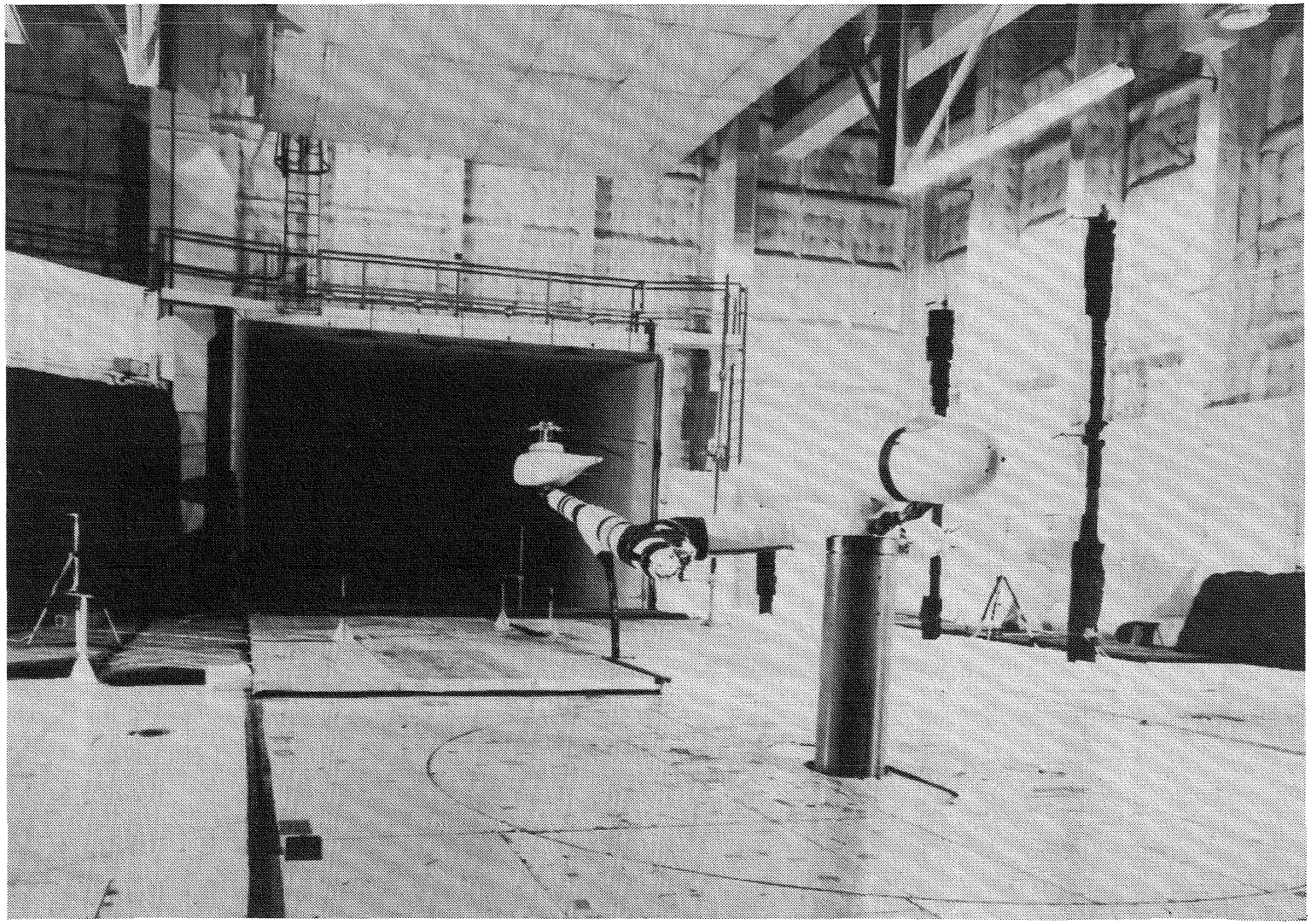

L-83-11,595

(a) View looking upstream.

Figure 1.- Photograph of main rotor model and test rig when sting mounted in the Langley 4- by 7-Meter Tunnel.

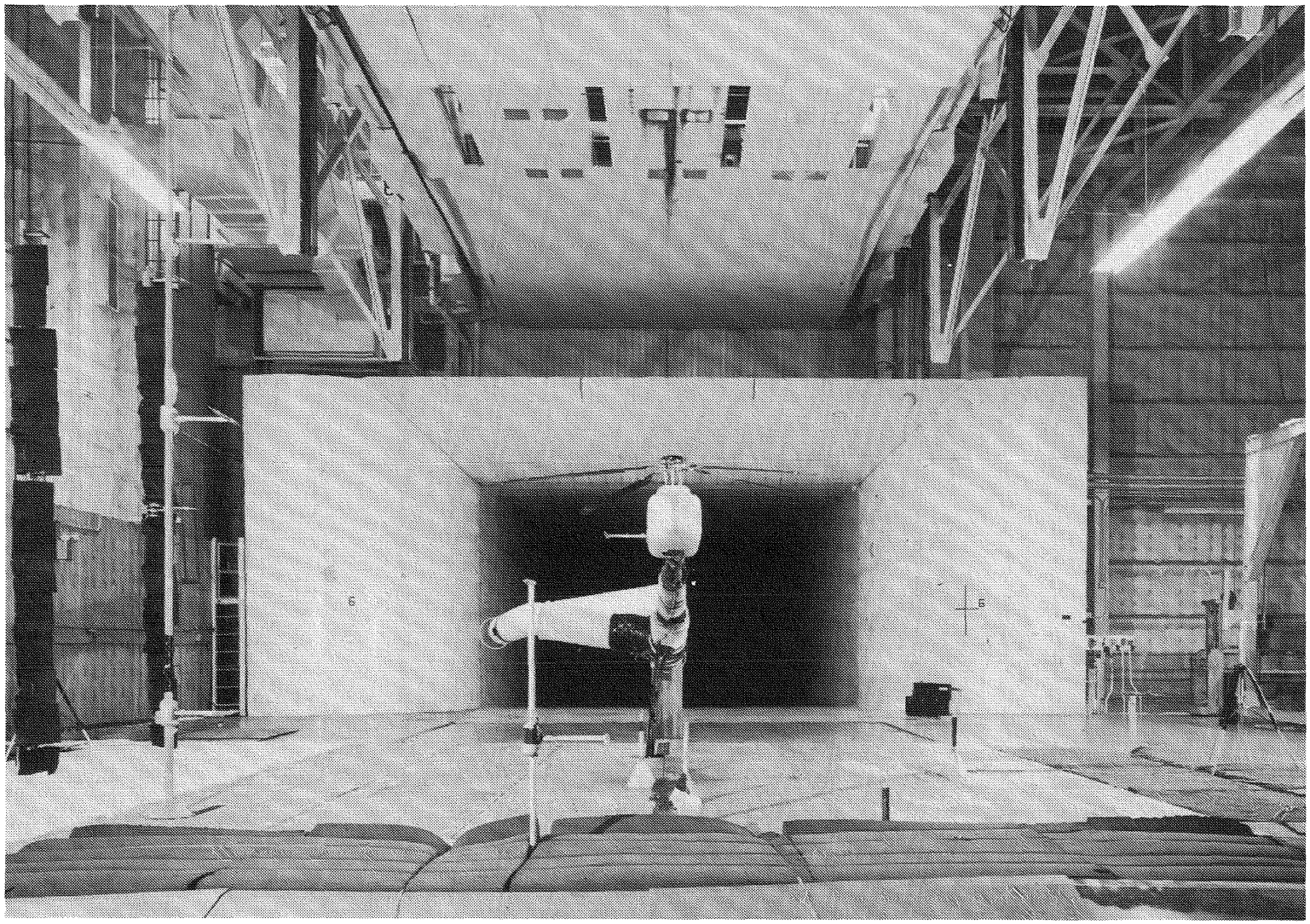

L-83-7012

(b) View looking downstream.

Figure 1.- Concluded.

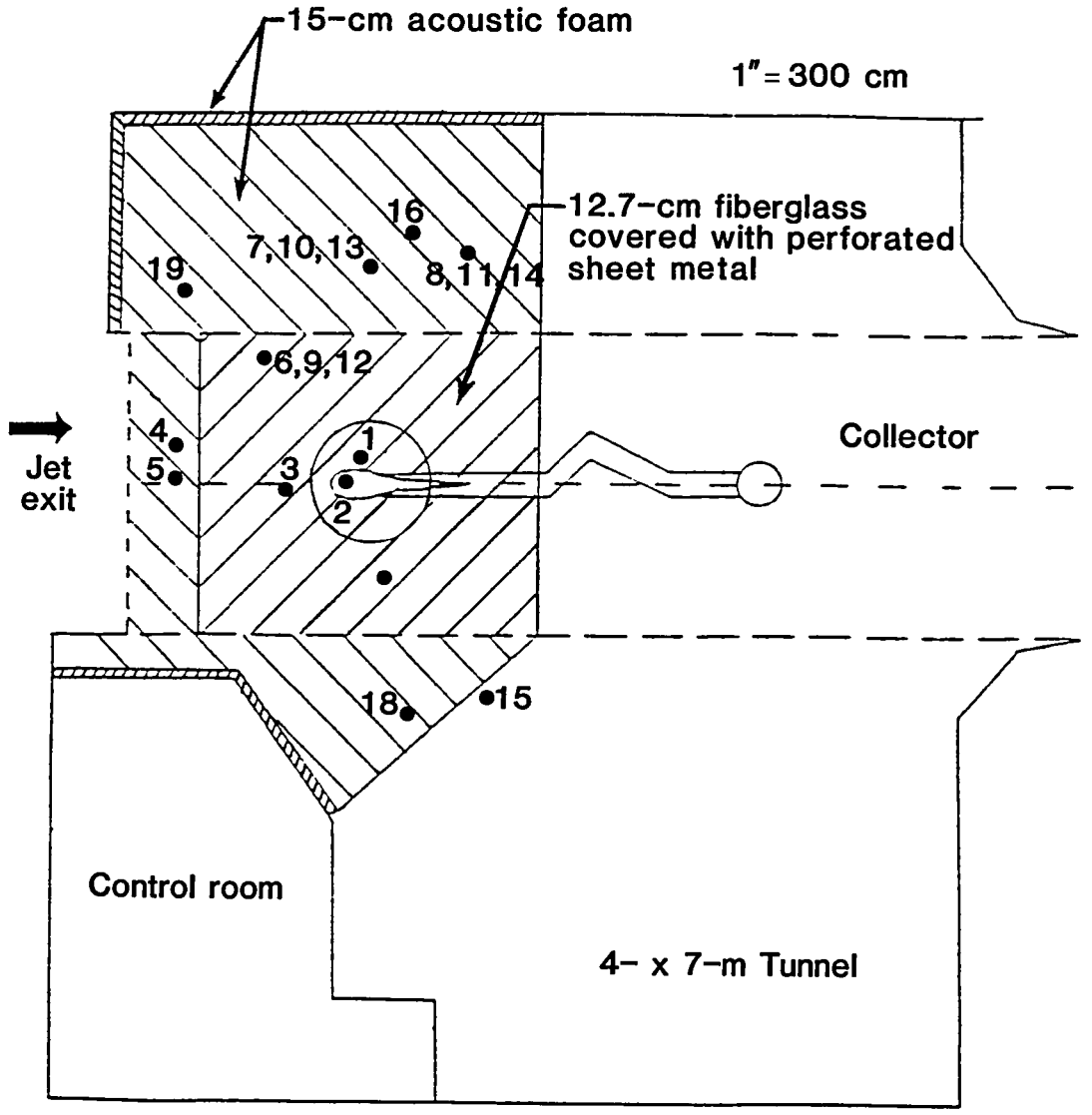

(a) Plan view.

Figure 2.- Schematic diagram of the Langley 4- by 7-Meter Tunnel showing microphone locations (numbered bullets) and acoustic treatment in test section.

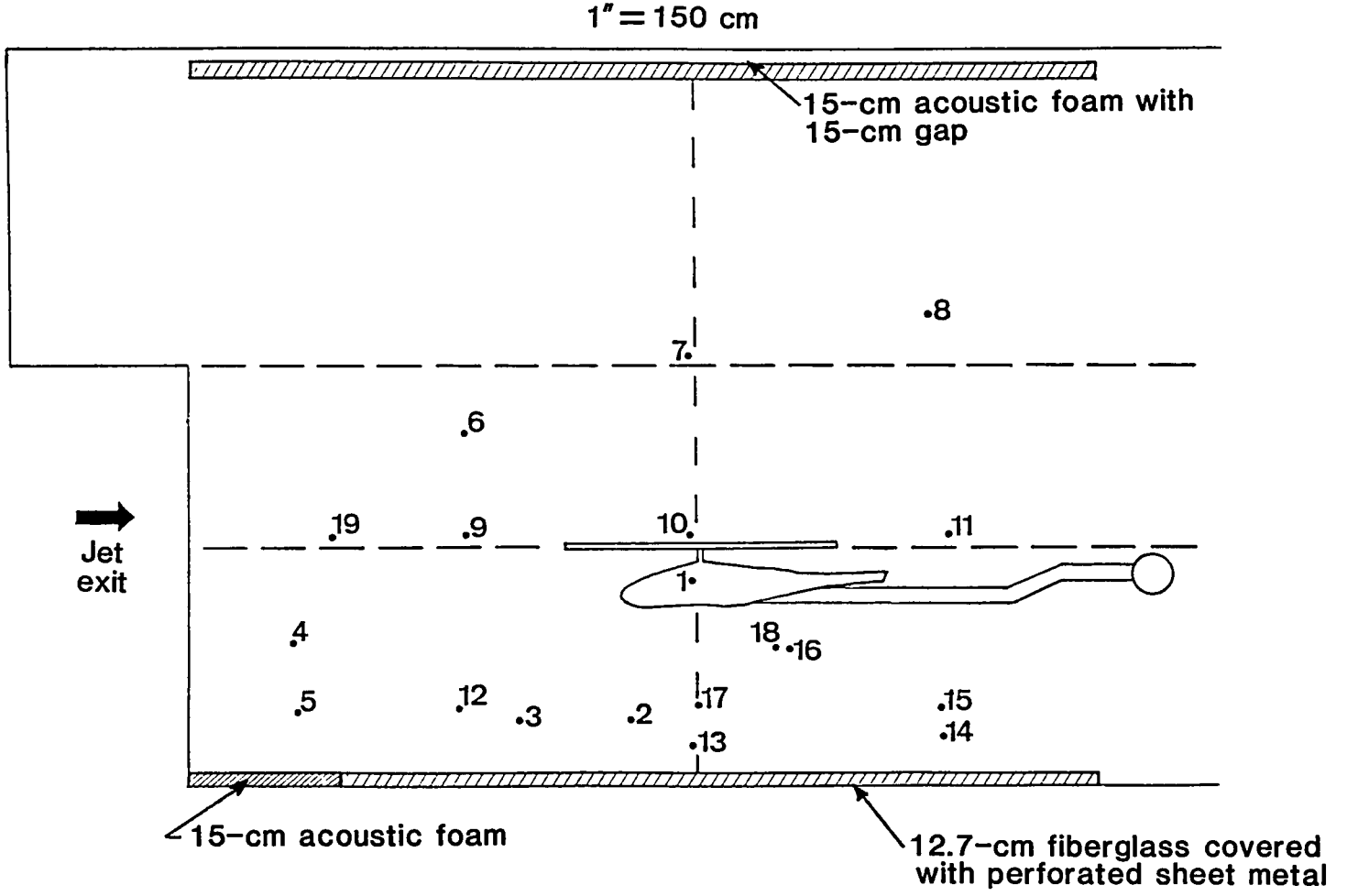

(b) Elevation.

Figure 2.- Concluded.

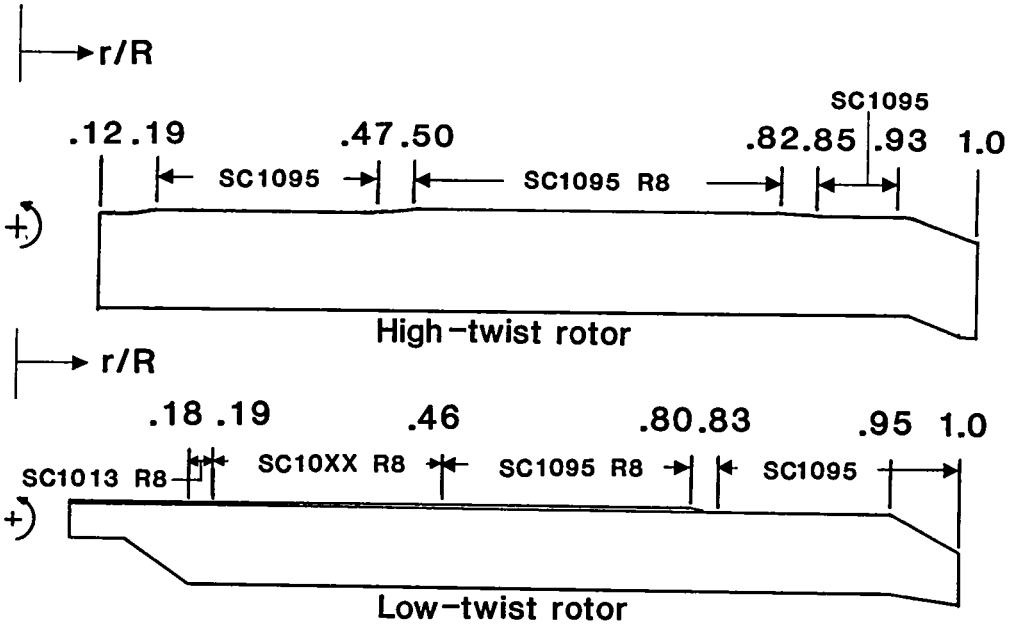

(a) Rotor blade planform.

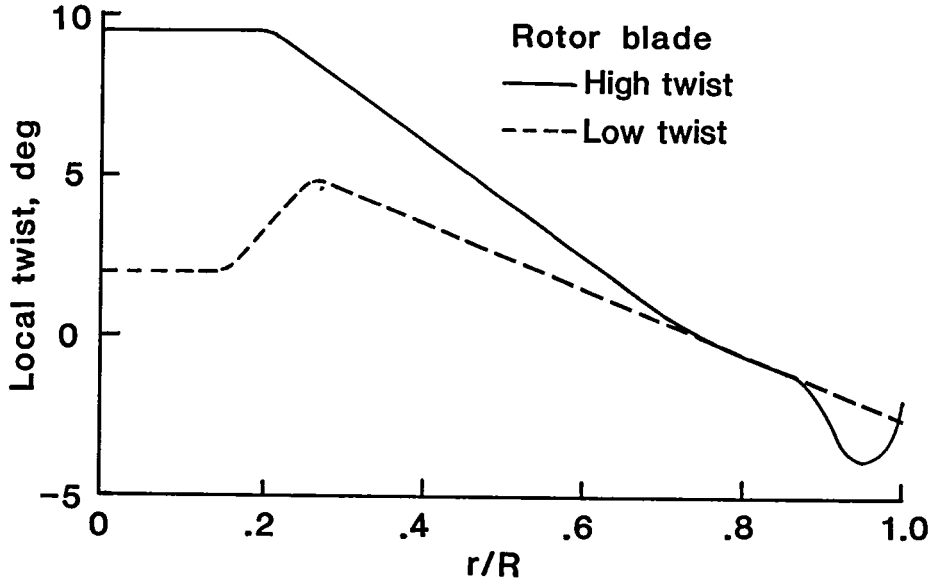

(b) Rotor blade twist distribution.

Figure 3.- General description showing blade planform, airfoil section, and twist distribution of two rotor models.

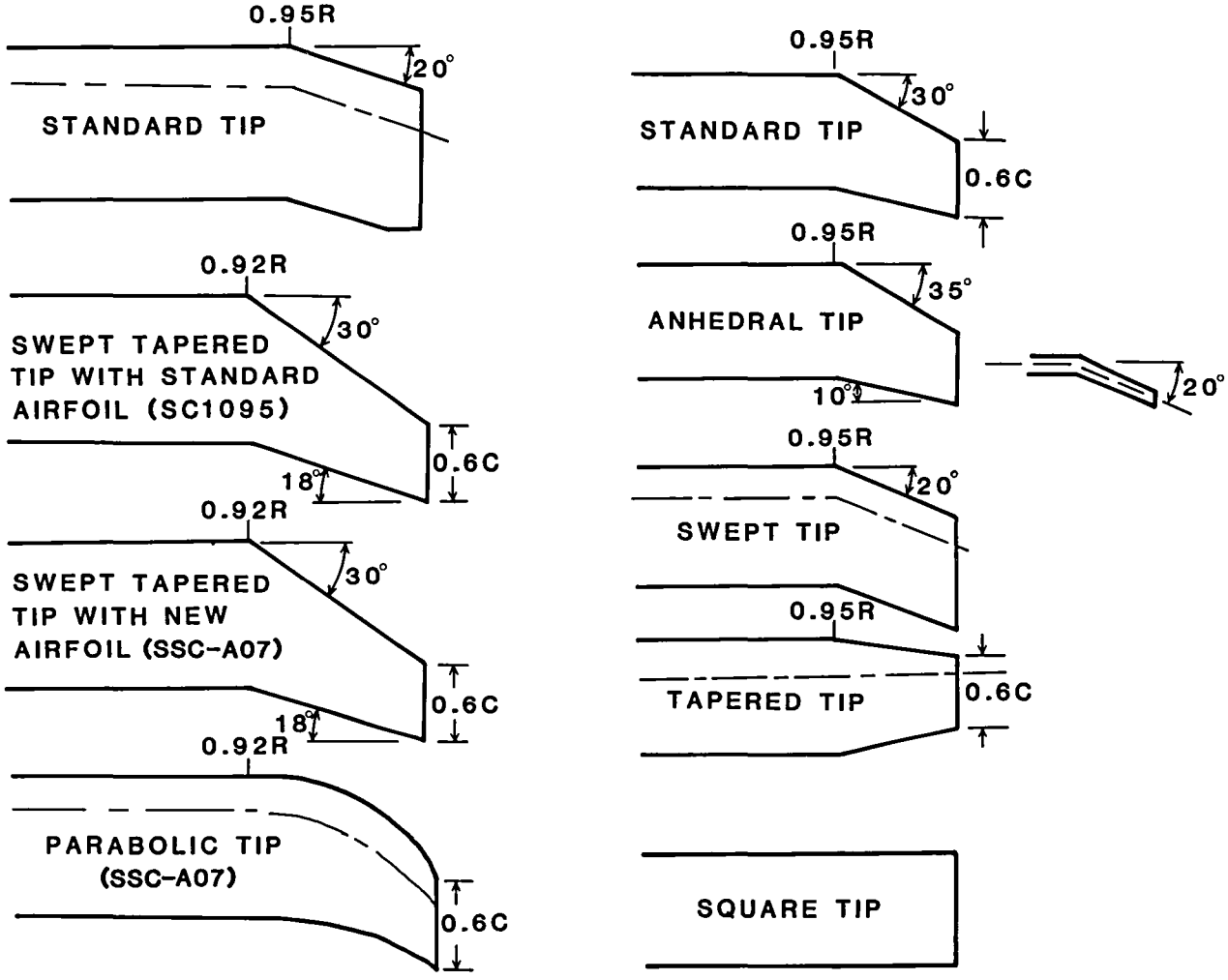

(a) High-twist tips.

(b) Low-twist tips.

Figure 4.- Geometric description of interchangeable blade tips of rotor models.

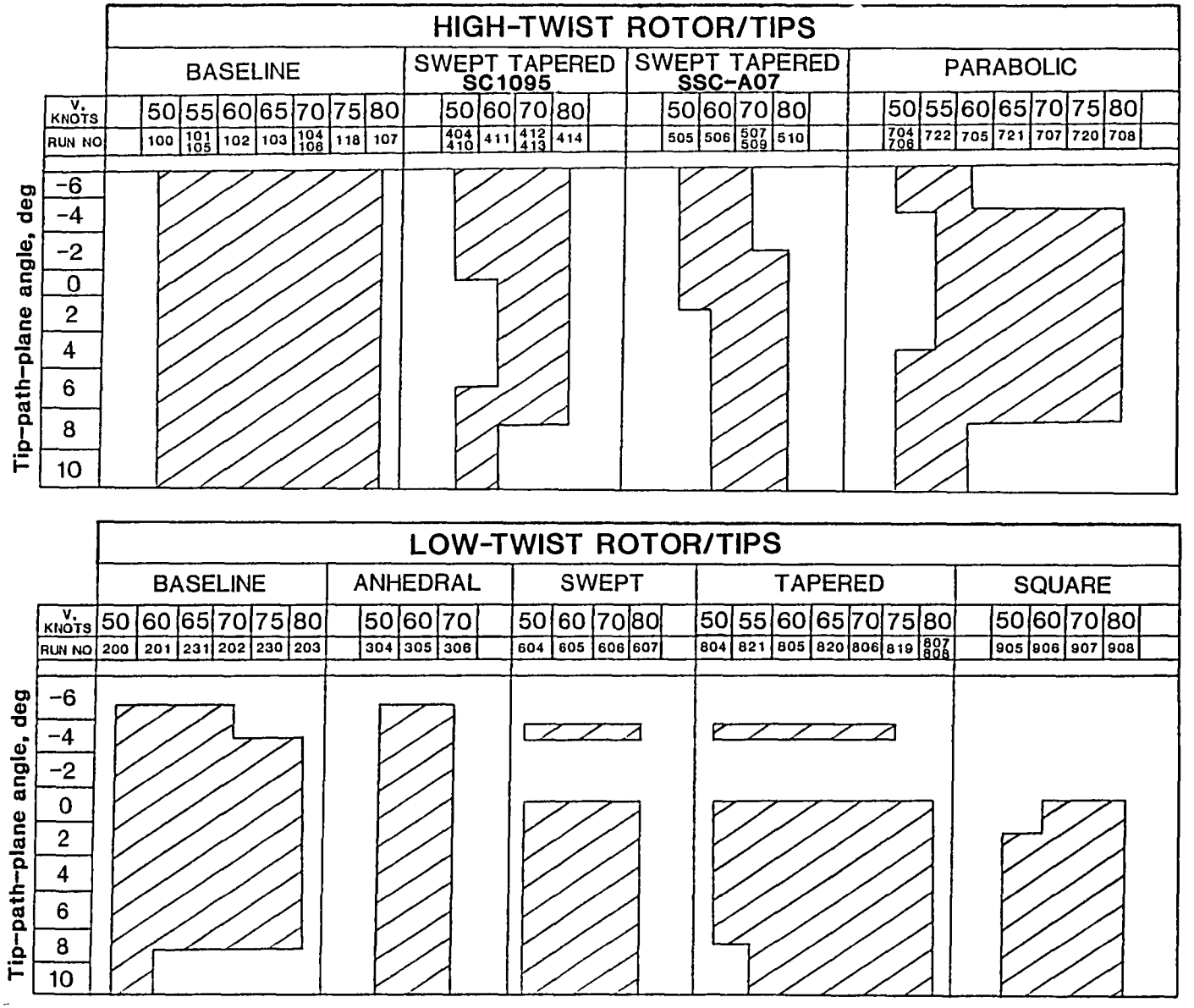

Figure 5.- Matrix diagram of test conditions for each rotor and tip combination.

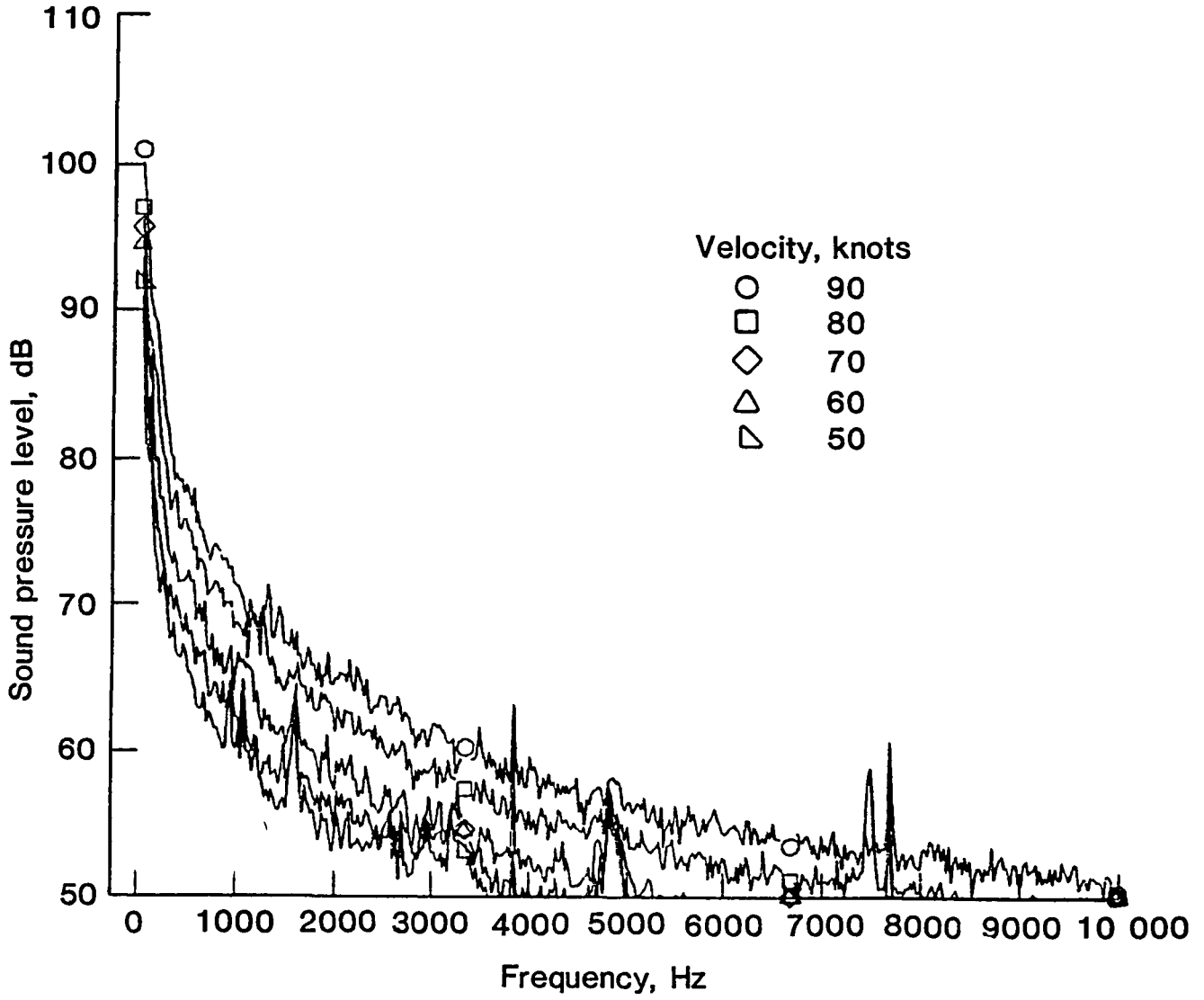

Figure 6.- Typical inflow background noise spectra in the Langley 4- by 7-Meter Tunnel. Microphone 3; 24-Hz bandwidth.

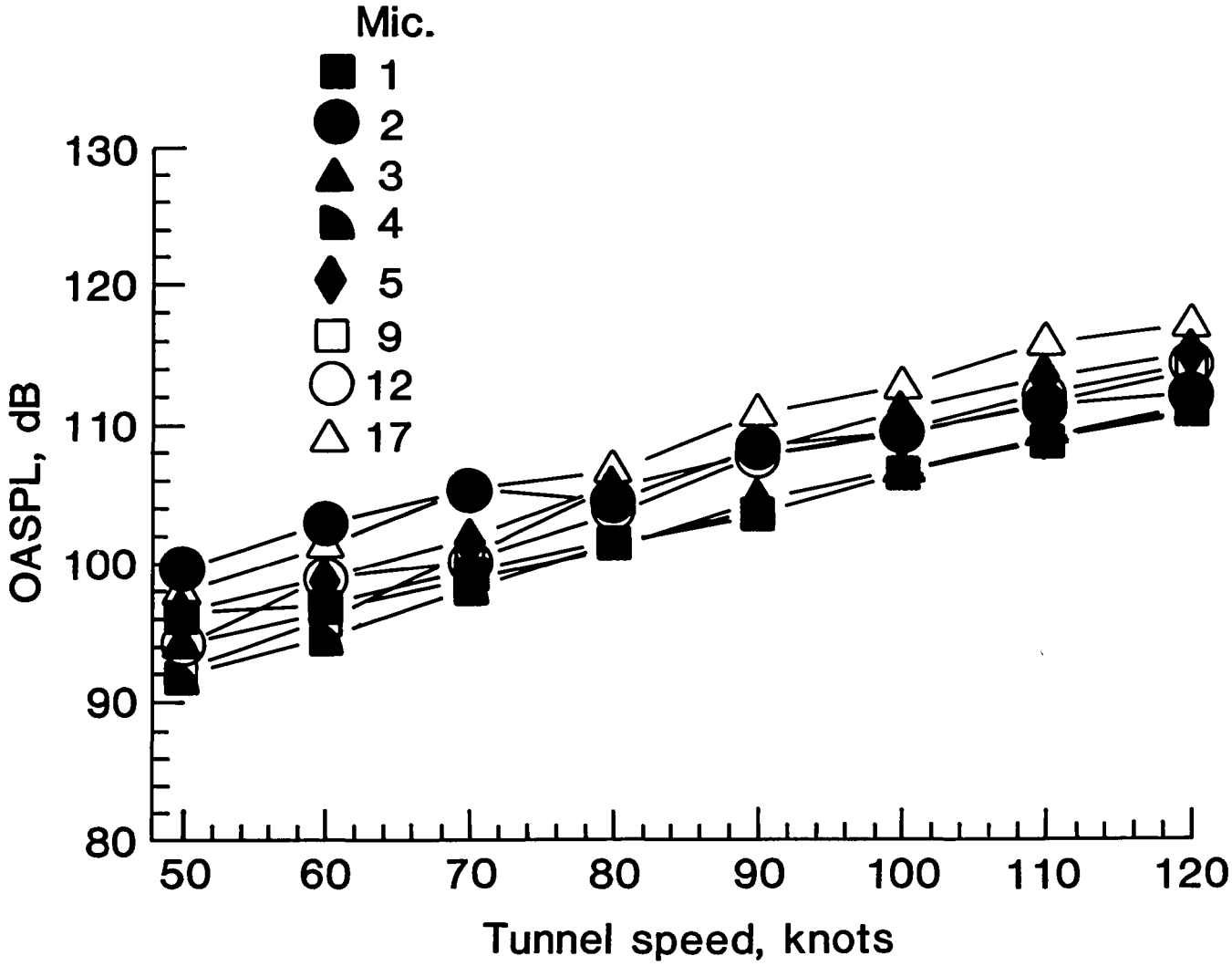

Figure 7.- Overall background noise levels of the Langley 4- by 7-Meter Tunnel as a function of tunnel airspeed for ITS locations.

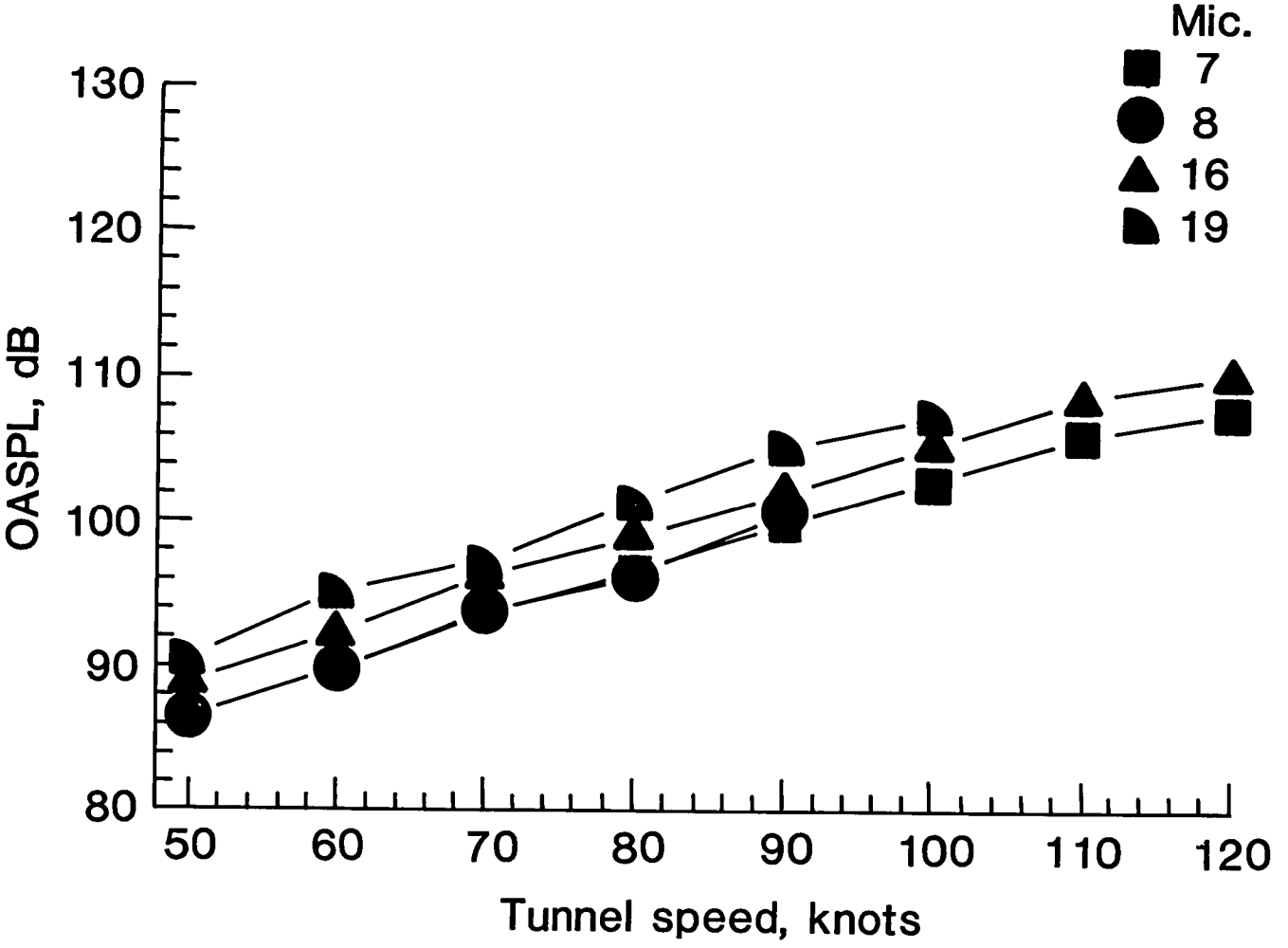

(a) Lowest noise level locations.

Figure 8.- Overall background noise levels of the Langley 4- by 7-Meter Tunnel as a function of tunnel airspeed for OTS locations.

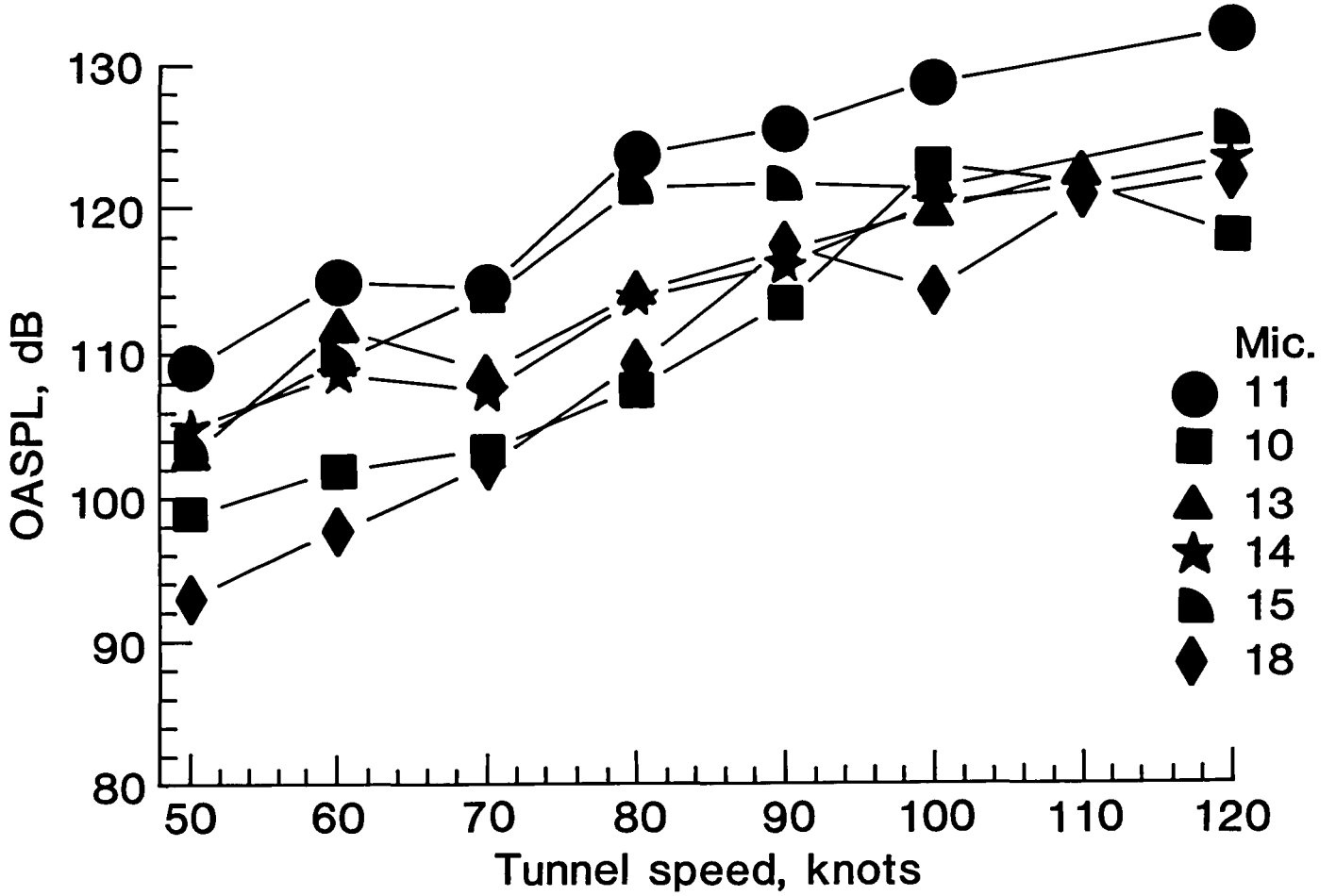

(b) Highest noise level locations.

Figure 8.- Concluded.

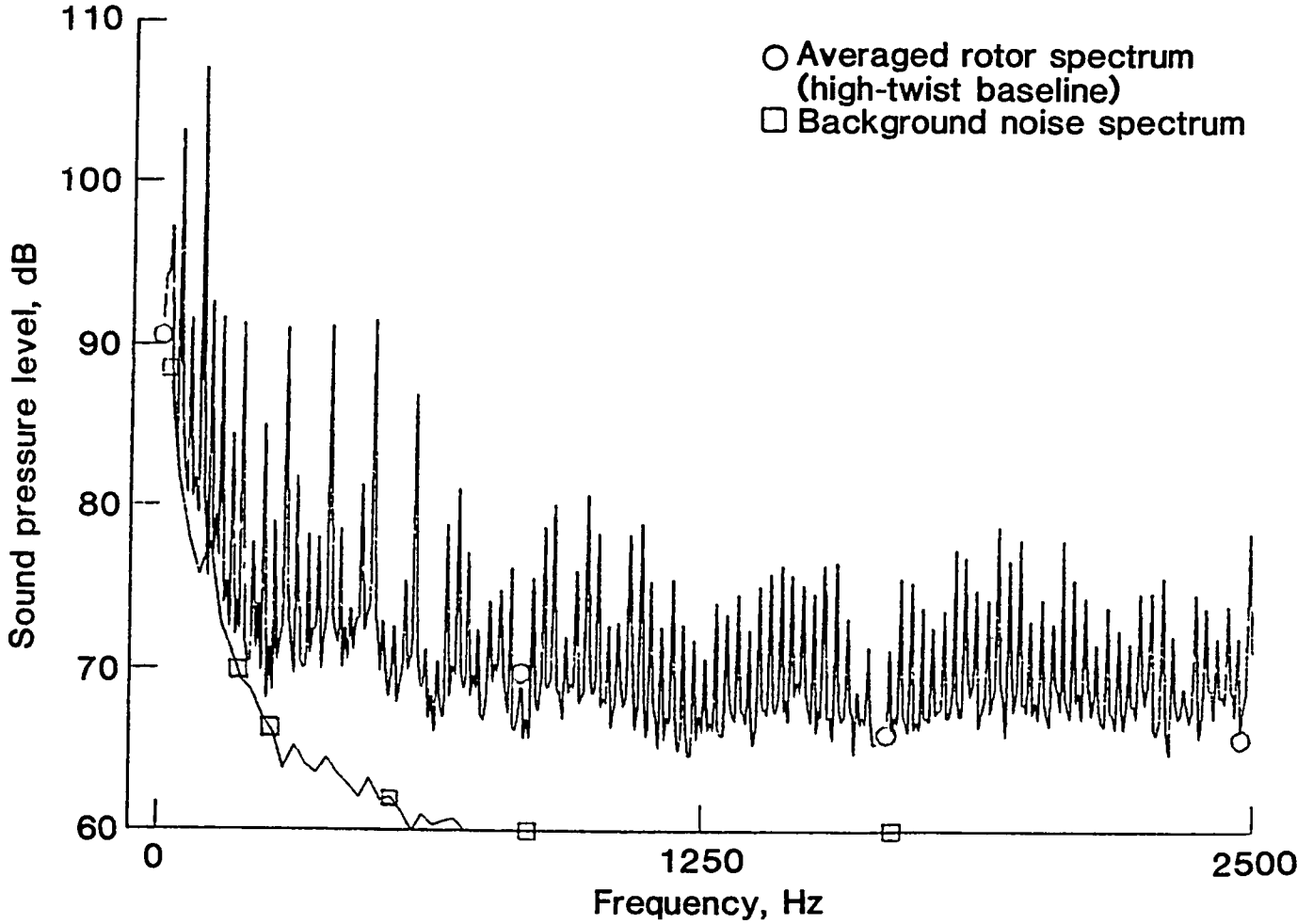

Figure 9.- Typical rotor noise spectrum compared with background noise spectrum of the Langley 4- by 7-Meter Tunnel. Microphone 3; V = 60 knots; α = -6°.

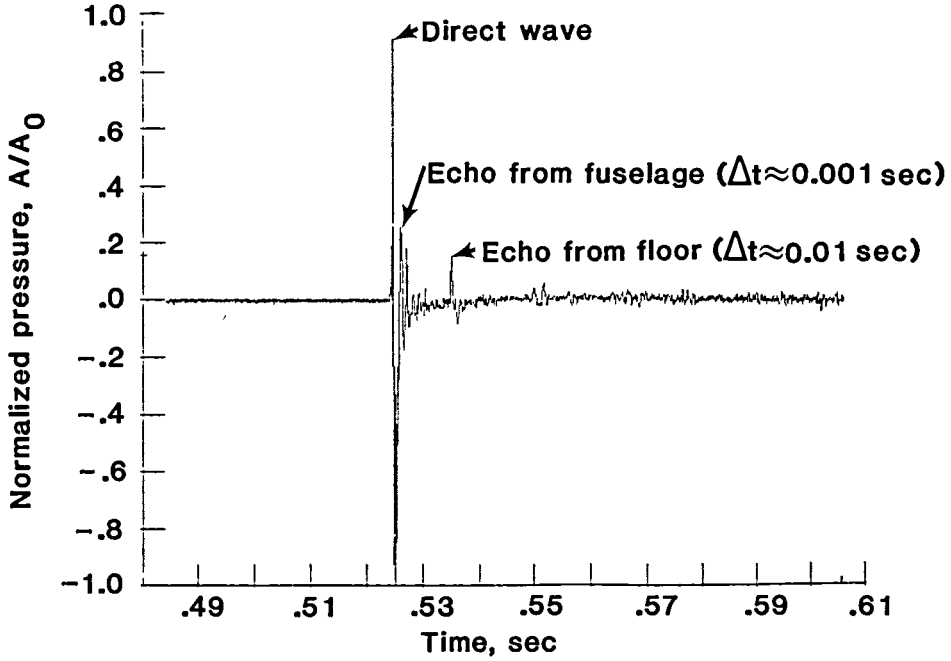

(a) Microphone 1.

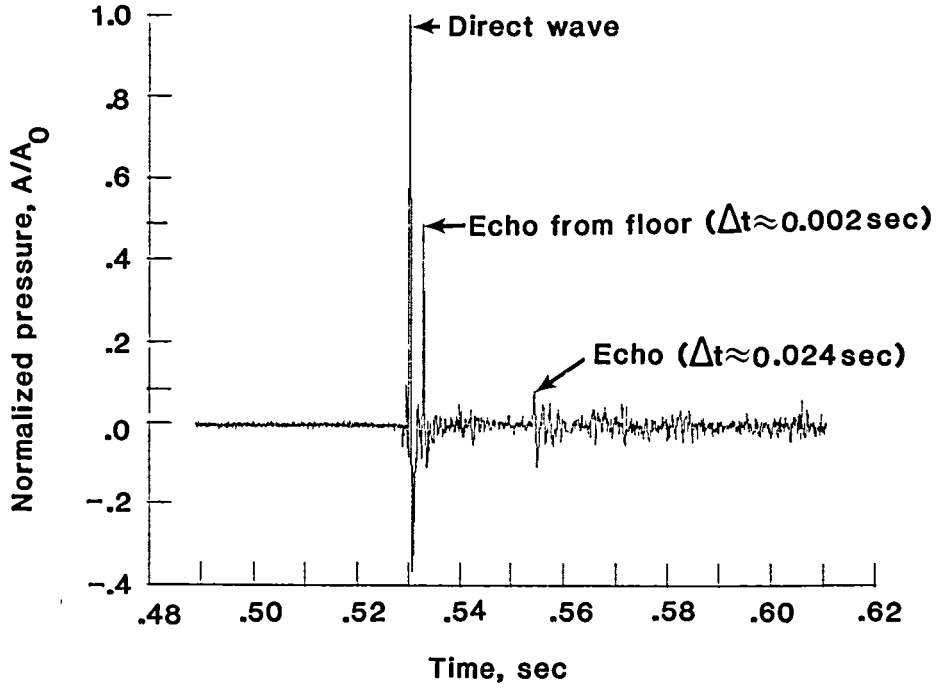

(b) Microphone 3.

Figure 10.- Examples of impulsive source calibration data with acoustic reflections. V = 0 knot.

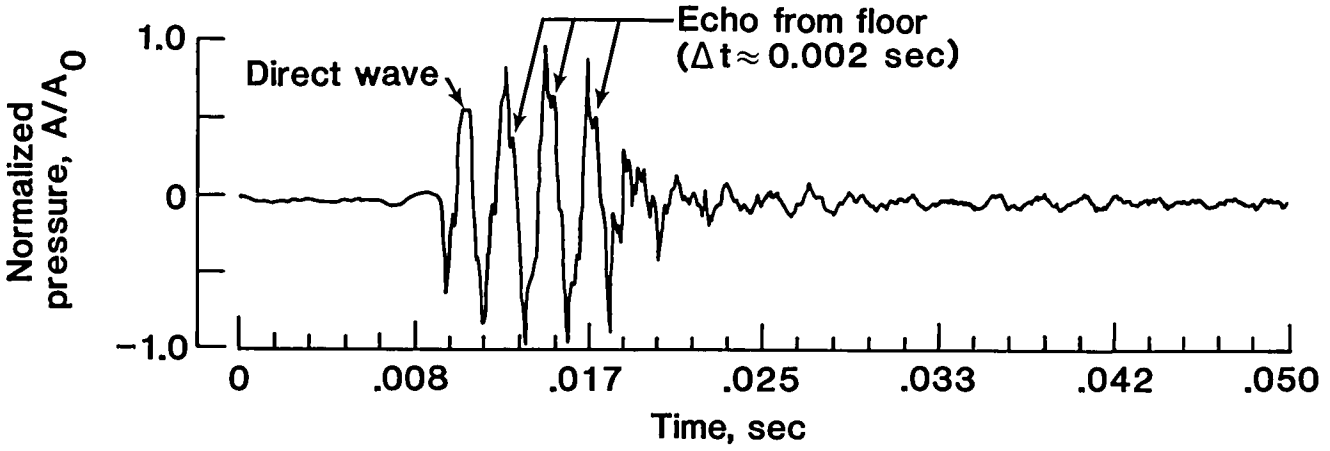

(a) Microphone 1. 1000-Hz tone burst.

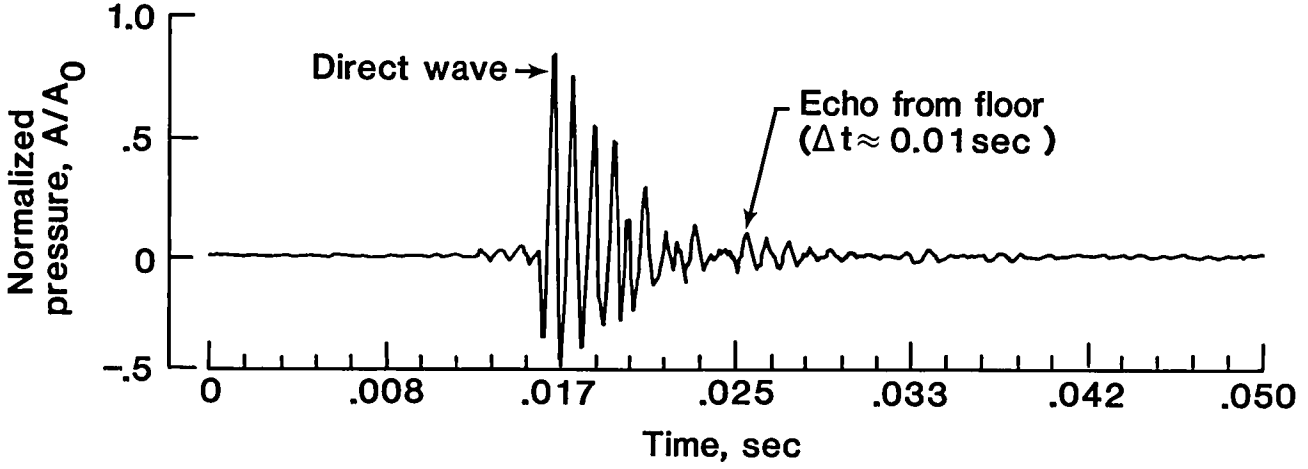

(b) Microphone 3. 500-Hz tone burst.

Figure 11.- Examples of tone burst calibration data with acoustic reflections.

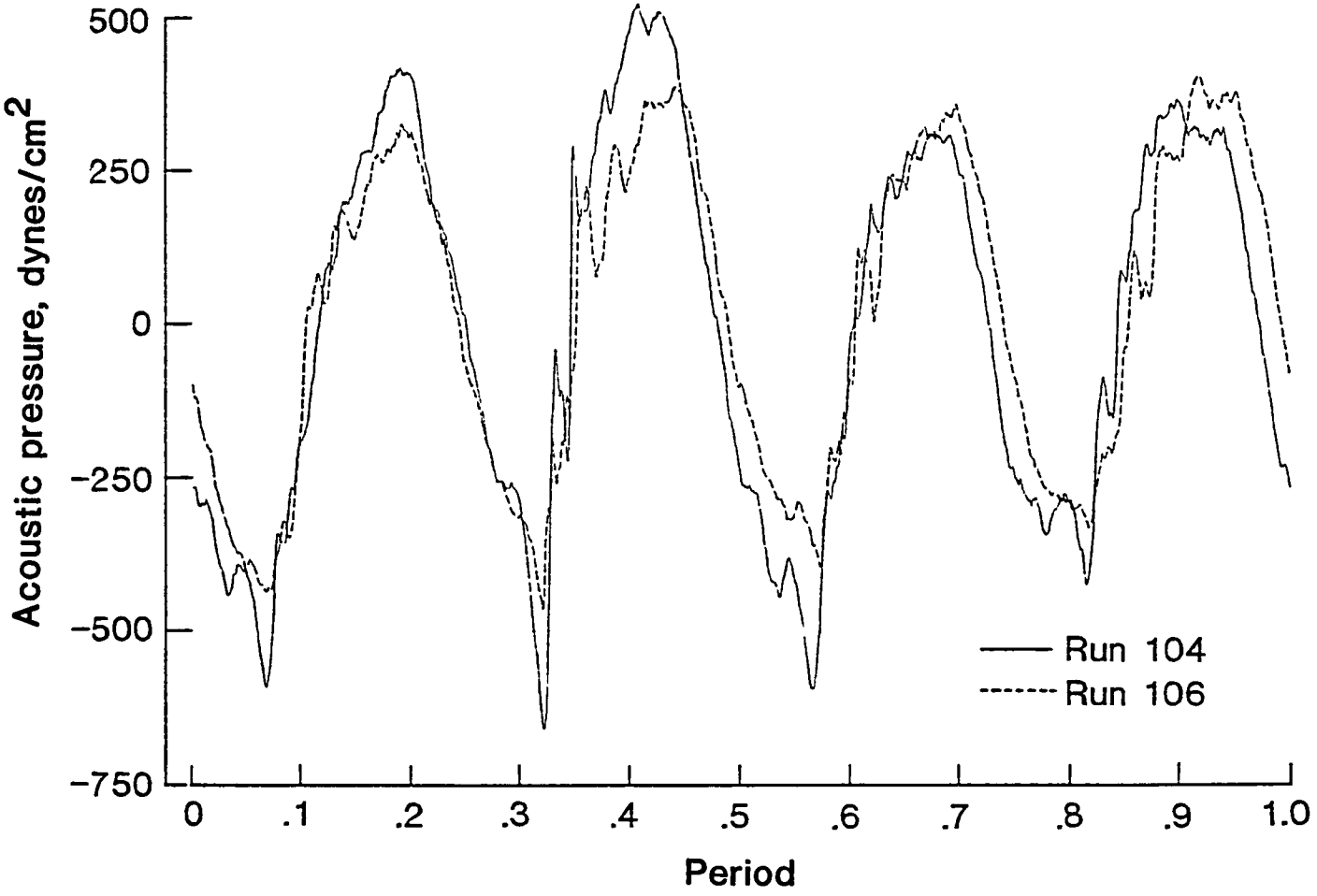

Figure 12.- Example of repeatability of averaged acoustic time history data. Microphone 1; V = 70 knots, $\alpha = 4°$.

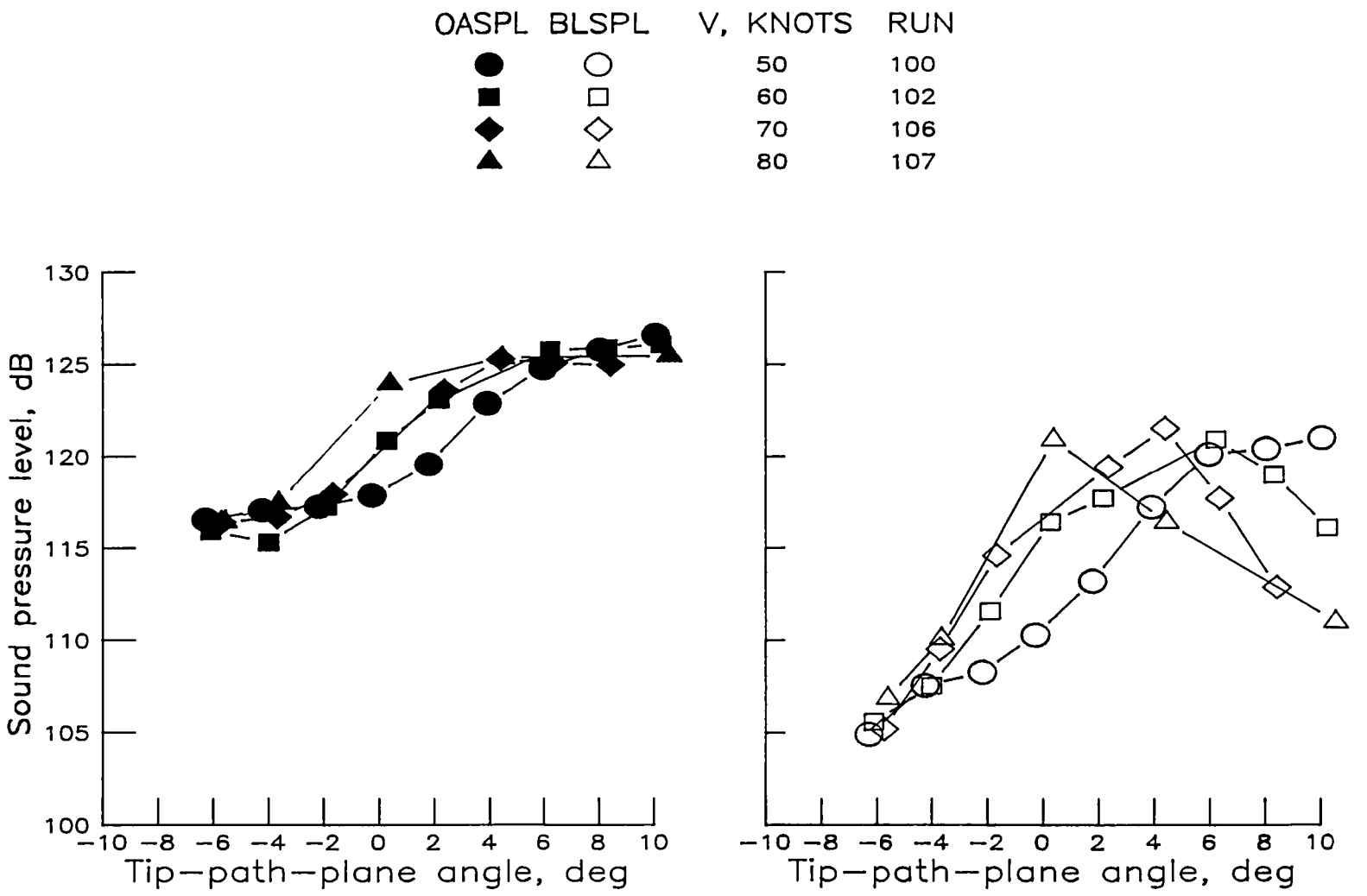

(a) High-twist standard tip.

Figure 13.- Overall and band-limited noise levels as a function of tip-path-plane angle over velocity range from 50 to 80 knots for microphone 1.

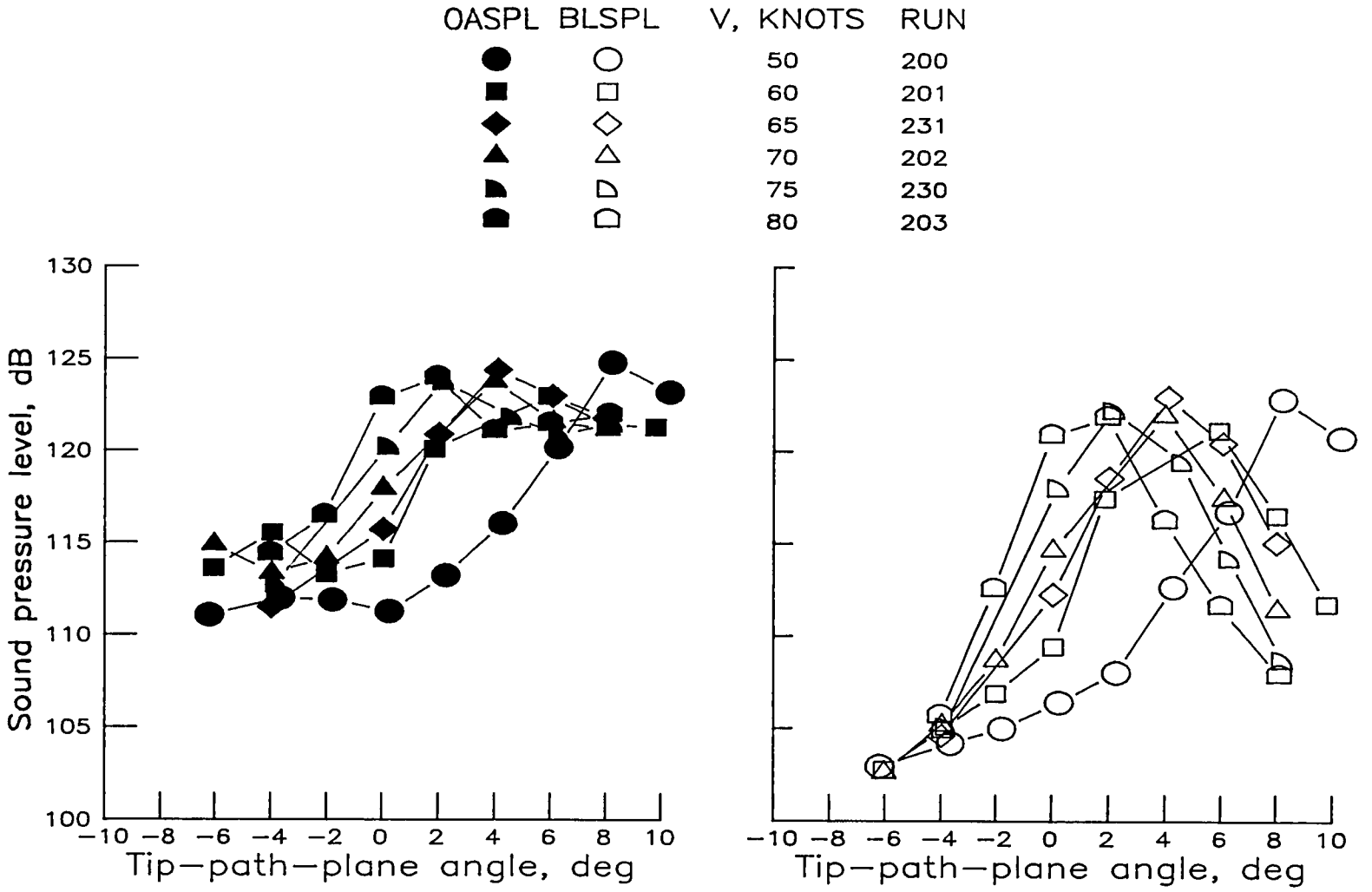

(b) Low-twist standard tip.

Figure 13.- Concluded.

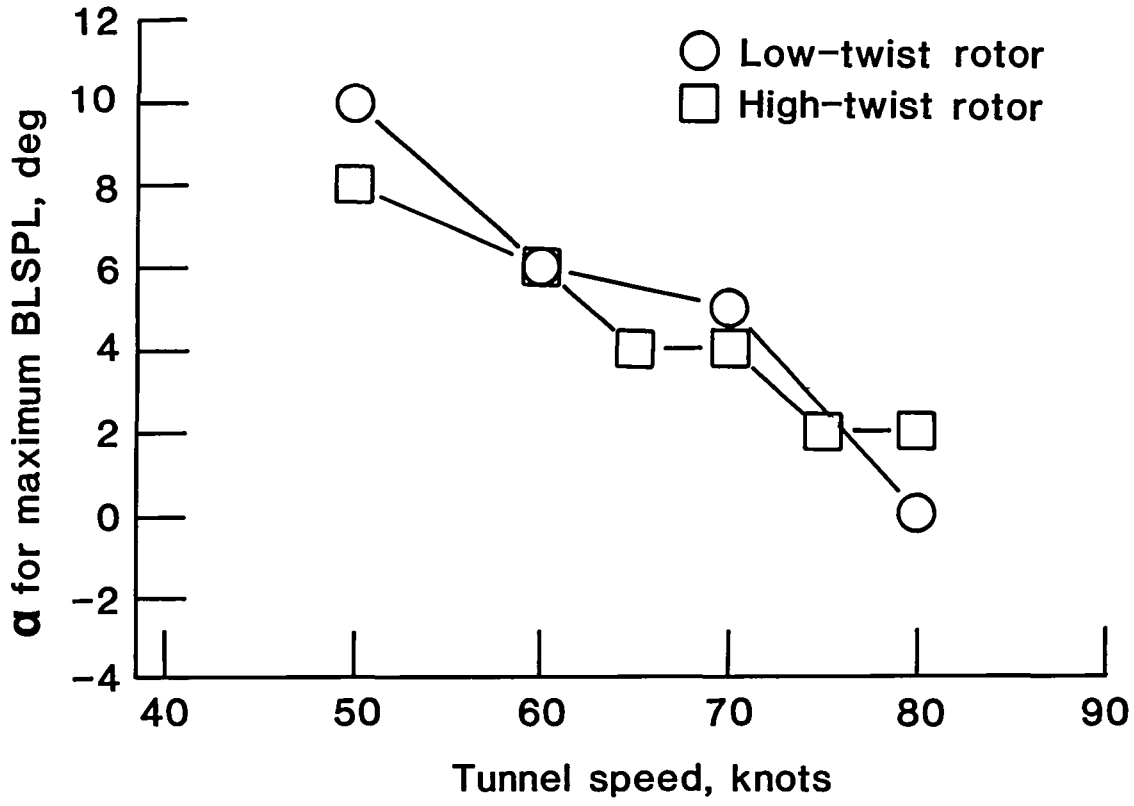

Figure 14.- Tip-path-plane angle for maximum band-limited sound pressure level plotted against tunnel speed for high- and low-twist baseline rotors for microphone 1.

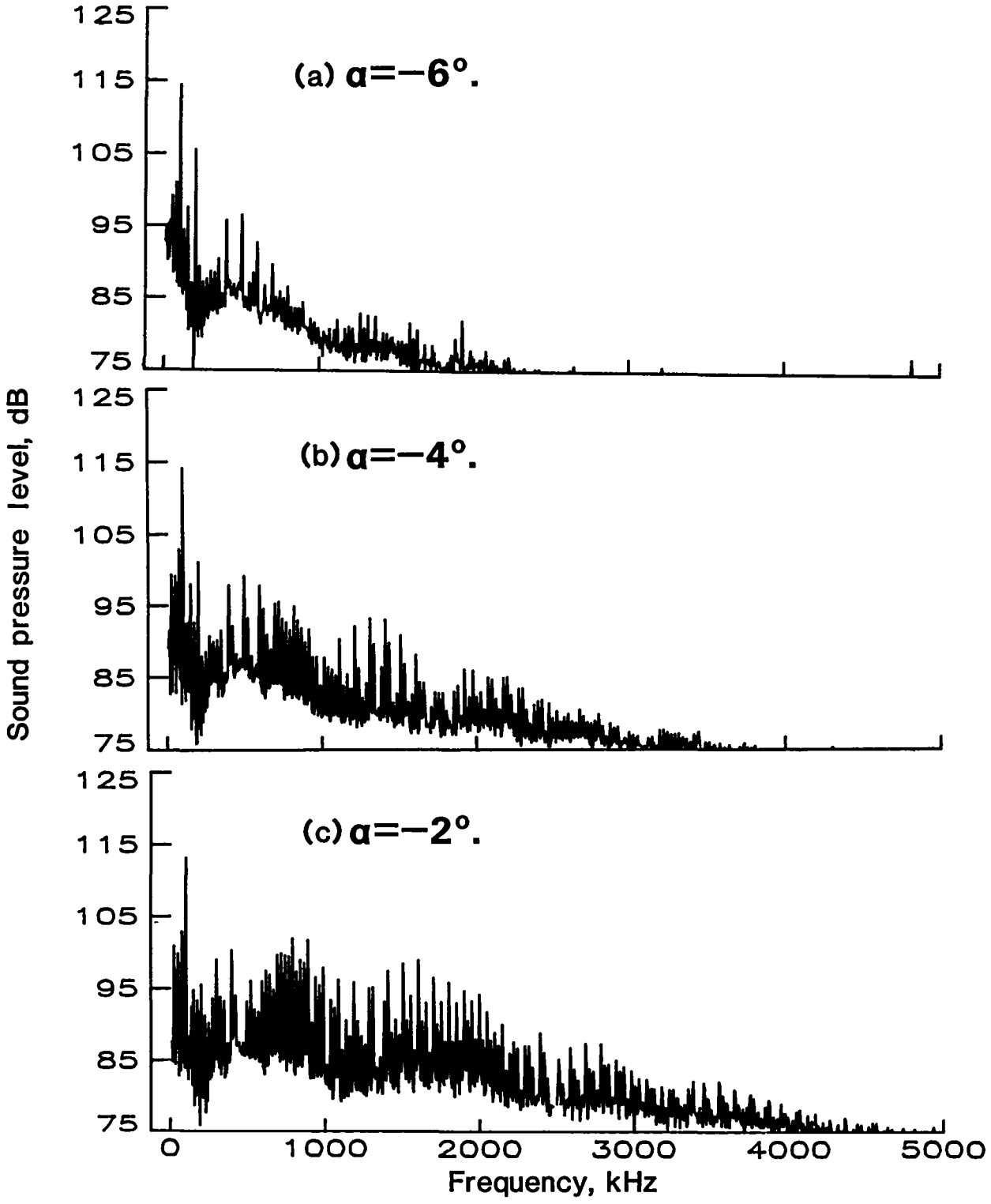

Figure 15.- Averaged narrowband spectra for high-twist standard tip at 70 knots, over range of tip-path-plane angle. Microphone 1; run 106.

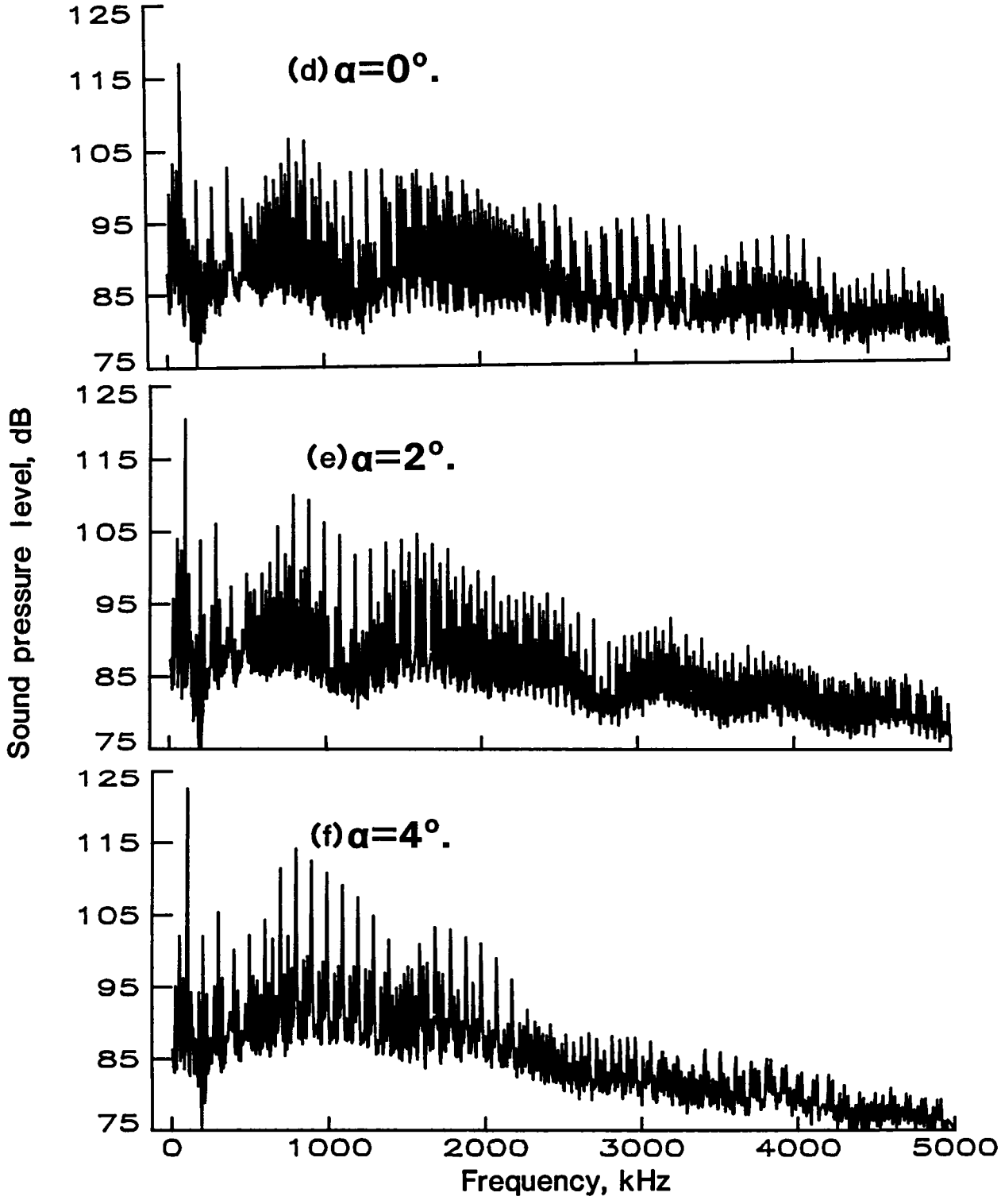

Figure 15.- Continued.

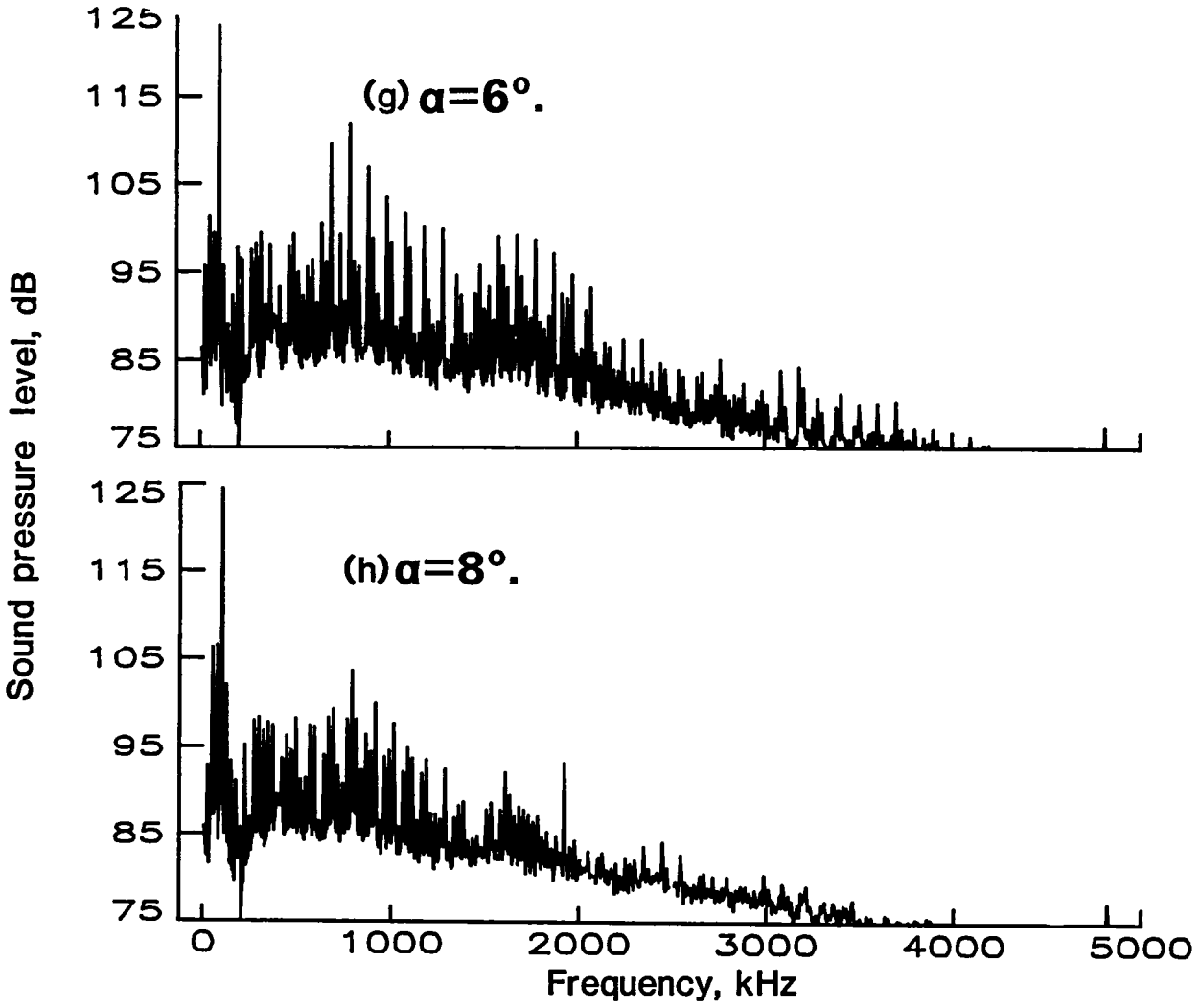

Figure 15.- Concluded.

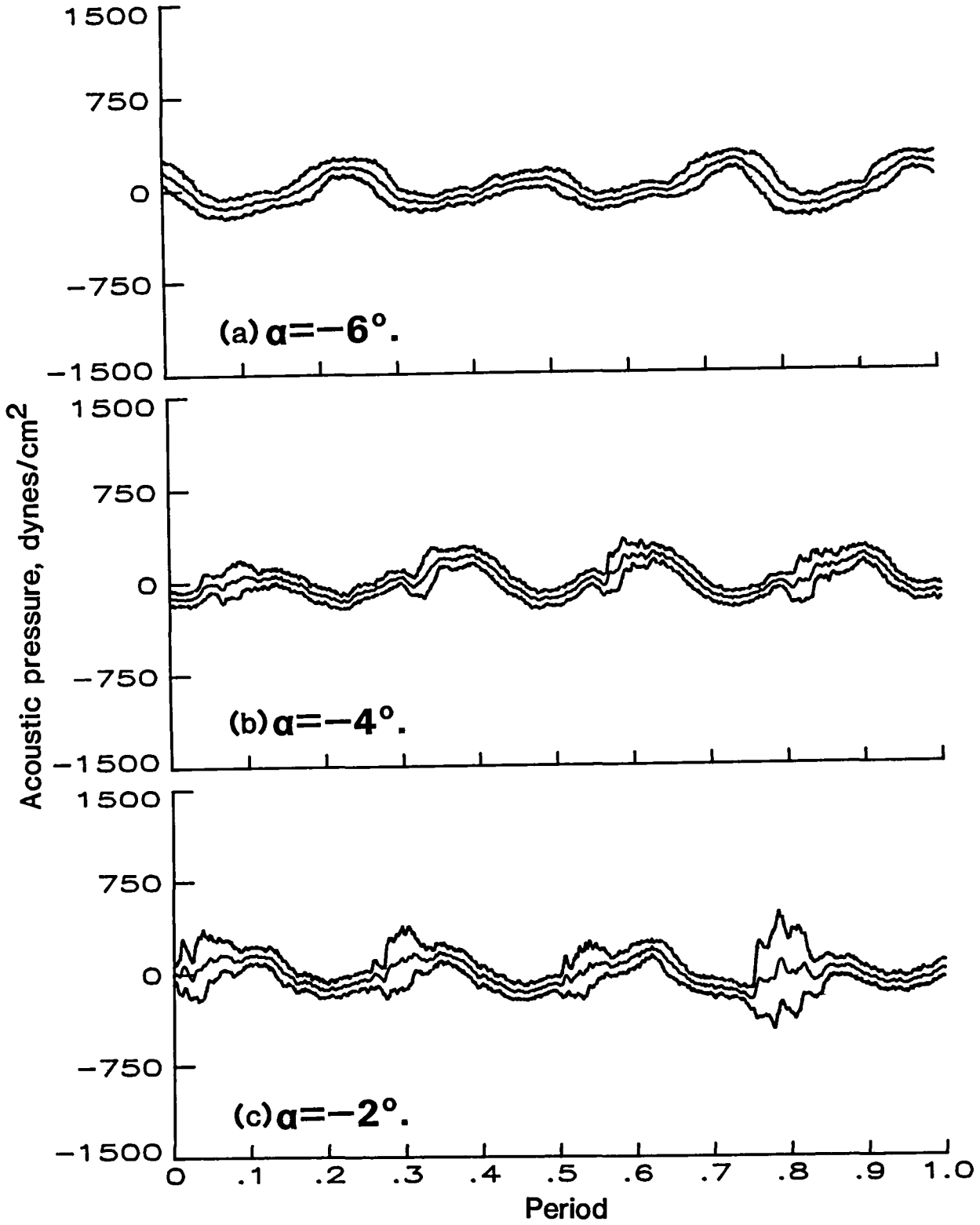

Figure 16.- Averaged time histories for high-twist standard tip at 70 knots over range of tip-path-plane angle. Middle curve is mean time history; upper and lower curves represent standard deviation about the mean; microphone 1; run 106.

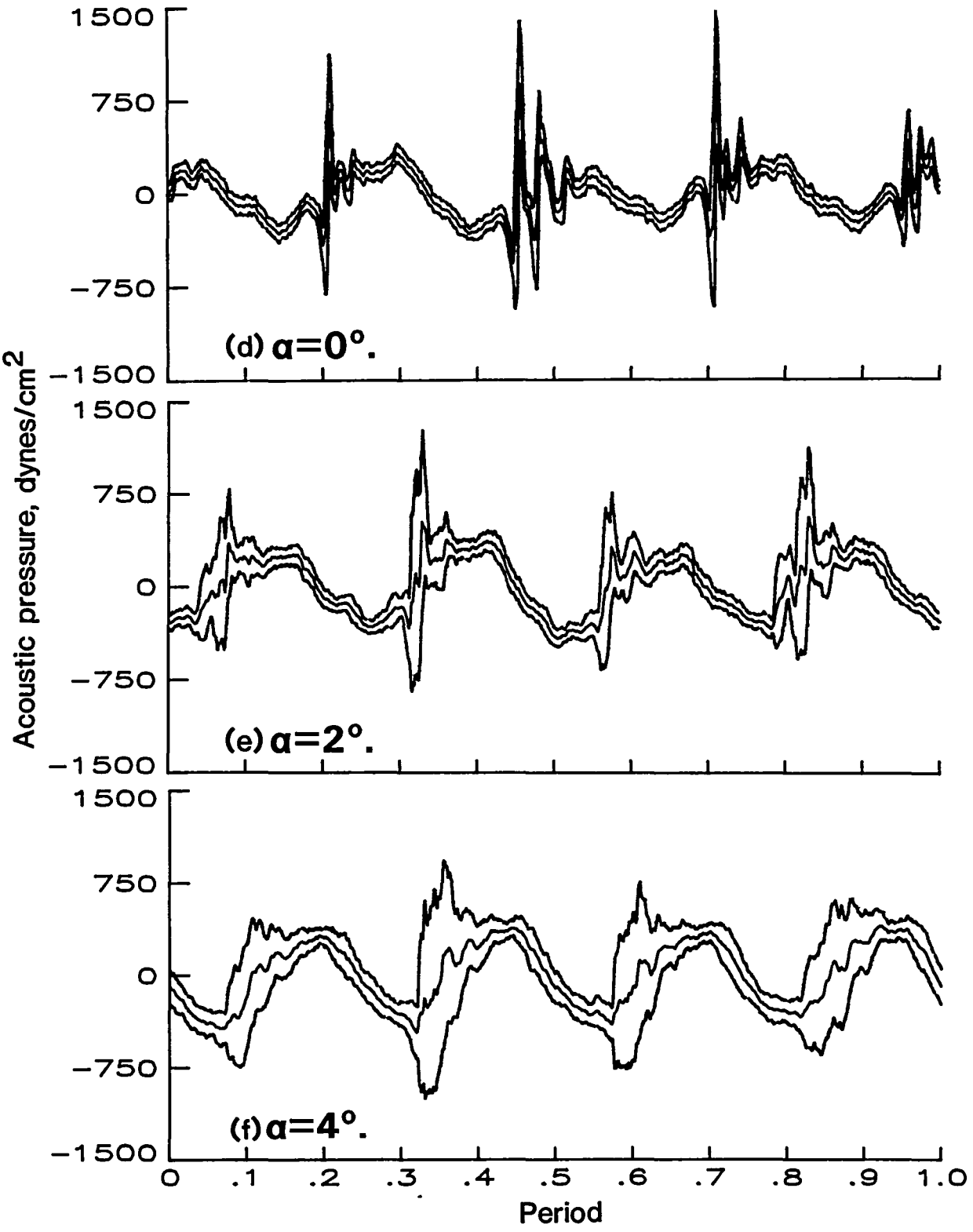

Figure 16.- Continued.

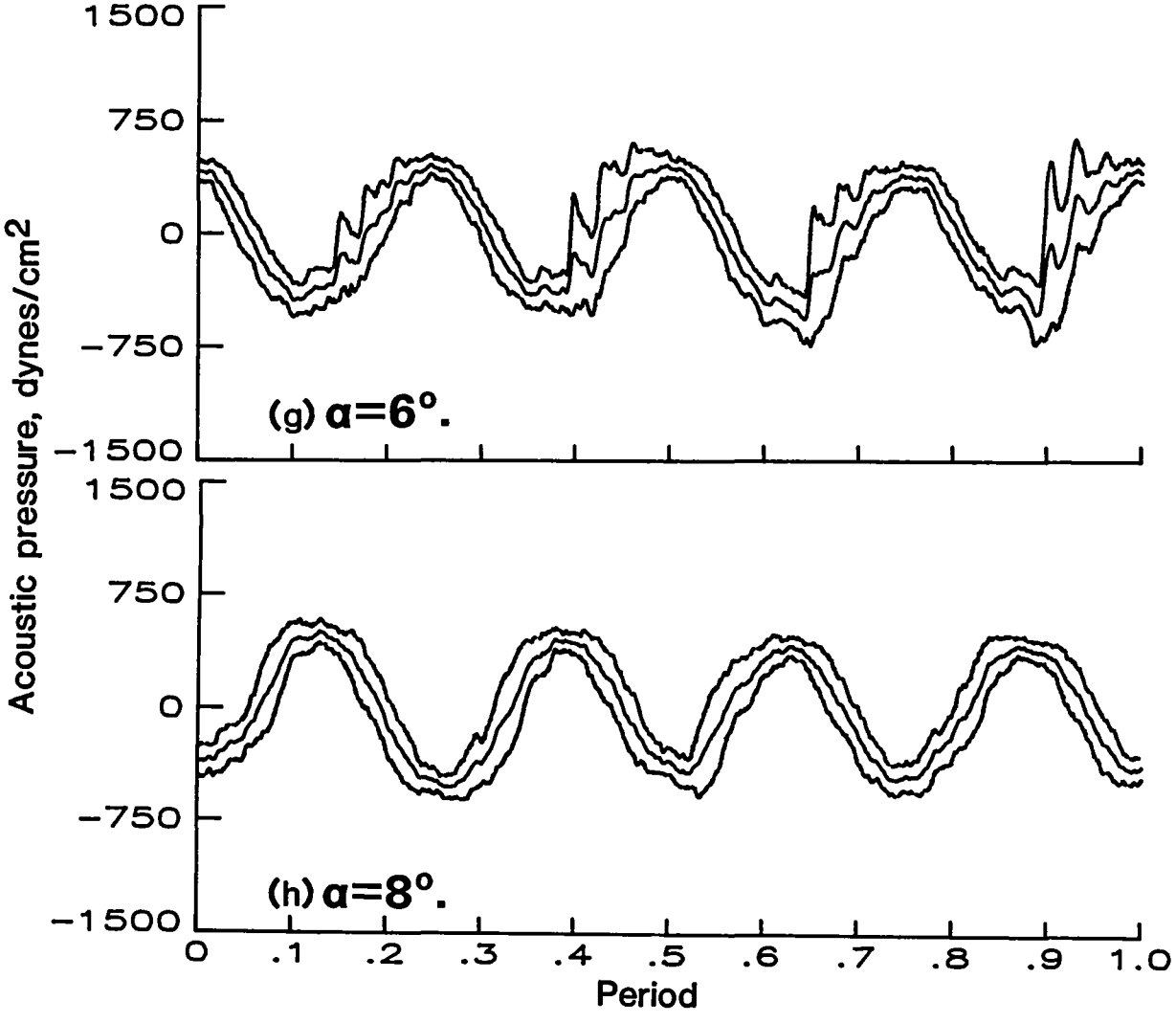

Figure 16.- Concluded.

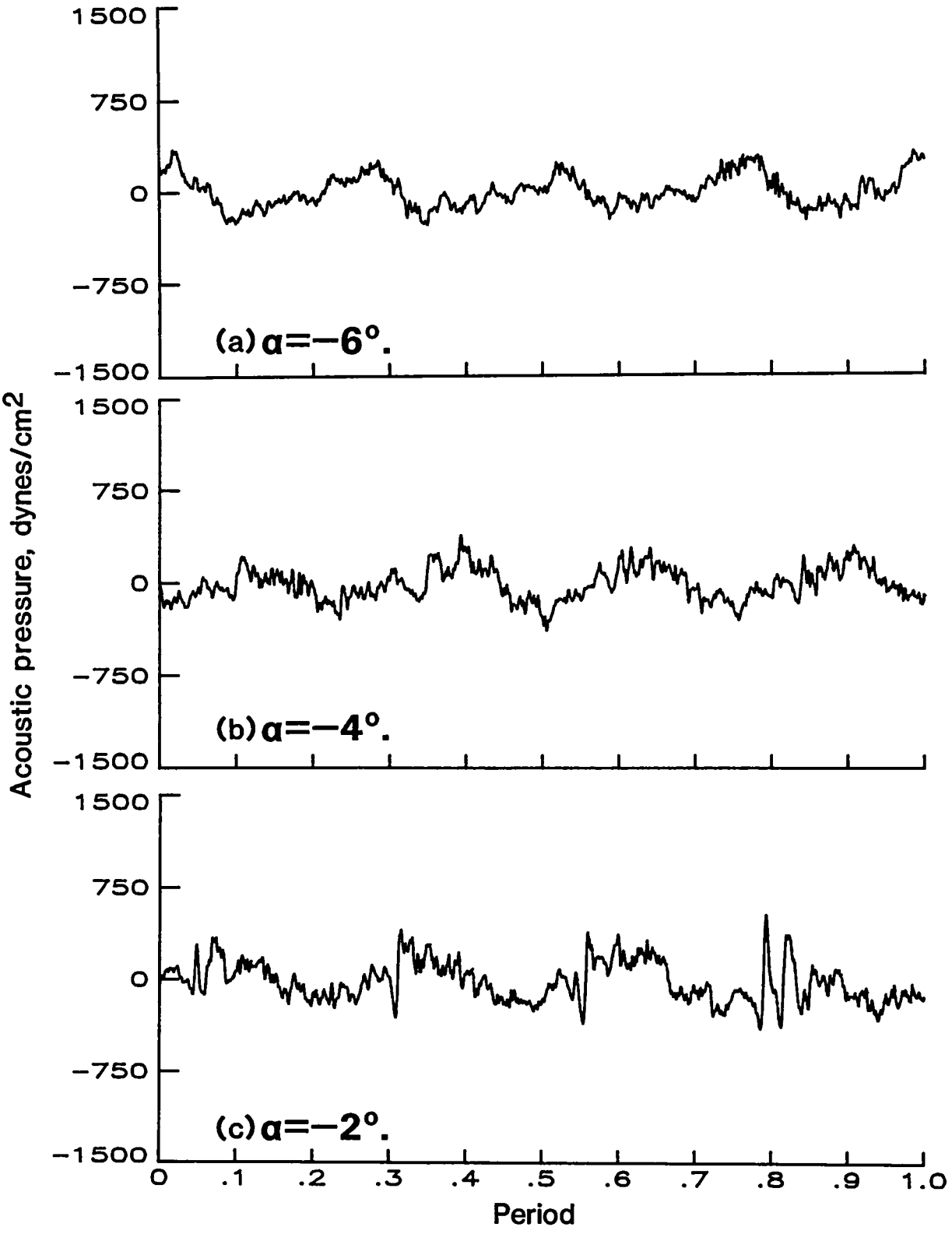

Figure 17.- Instantaneous time histories for high-twist standard tip at 70 knots for range of rotor angle of attack. Microphone 1; run 106.

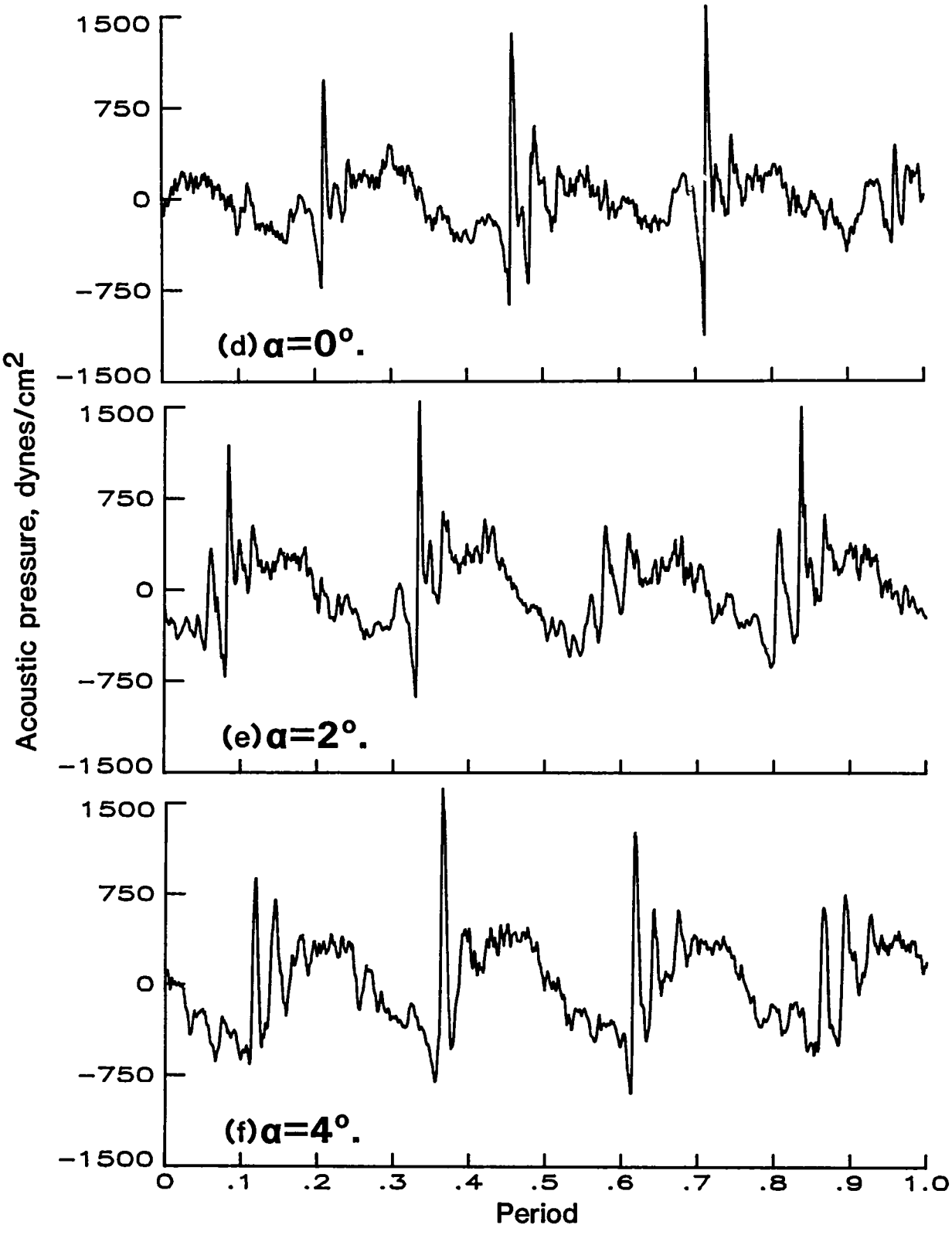

Figure 17.- Continued.

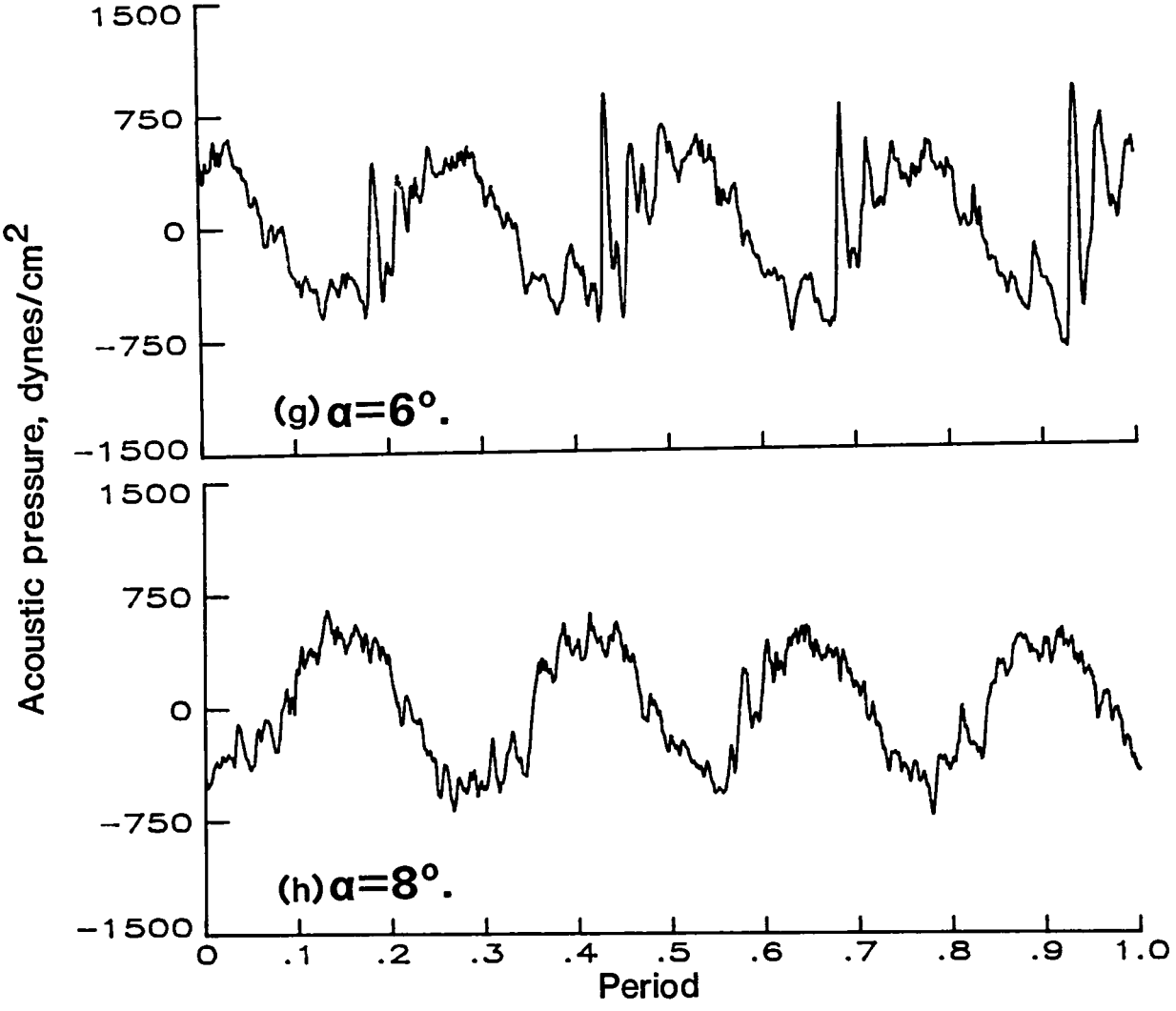

Figure 17.- Concluded.

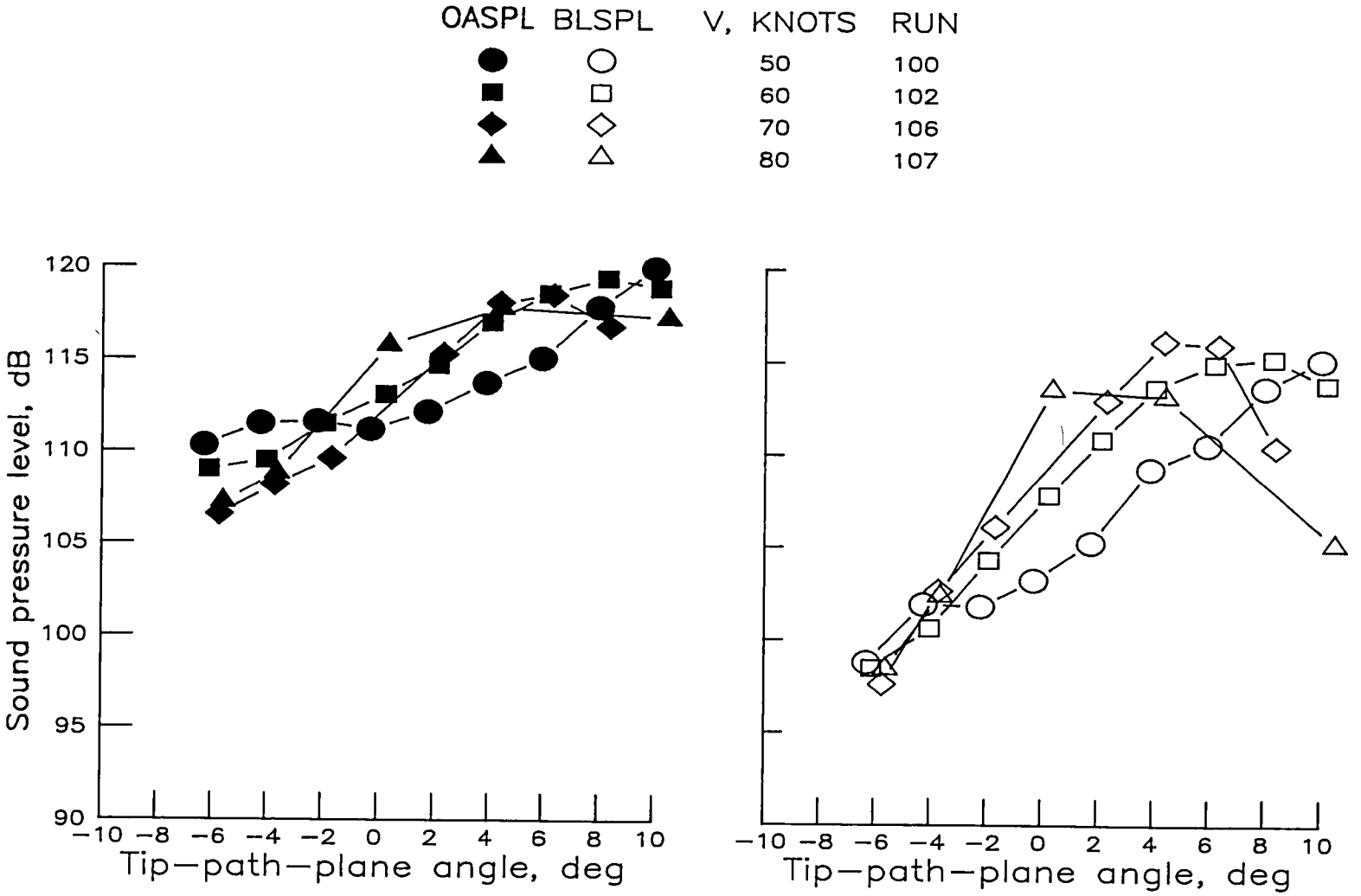

(a) High-twist standard tip.

Figure 18.- Overall and band-limited sound pressure levels as a function of tip-path-plane angle over velocity range from 50 to 80 knots for microphone 2.

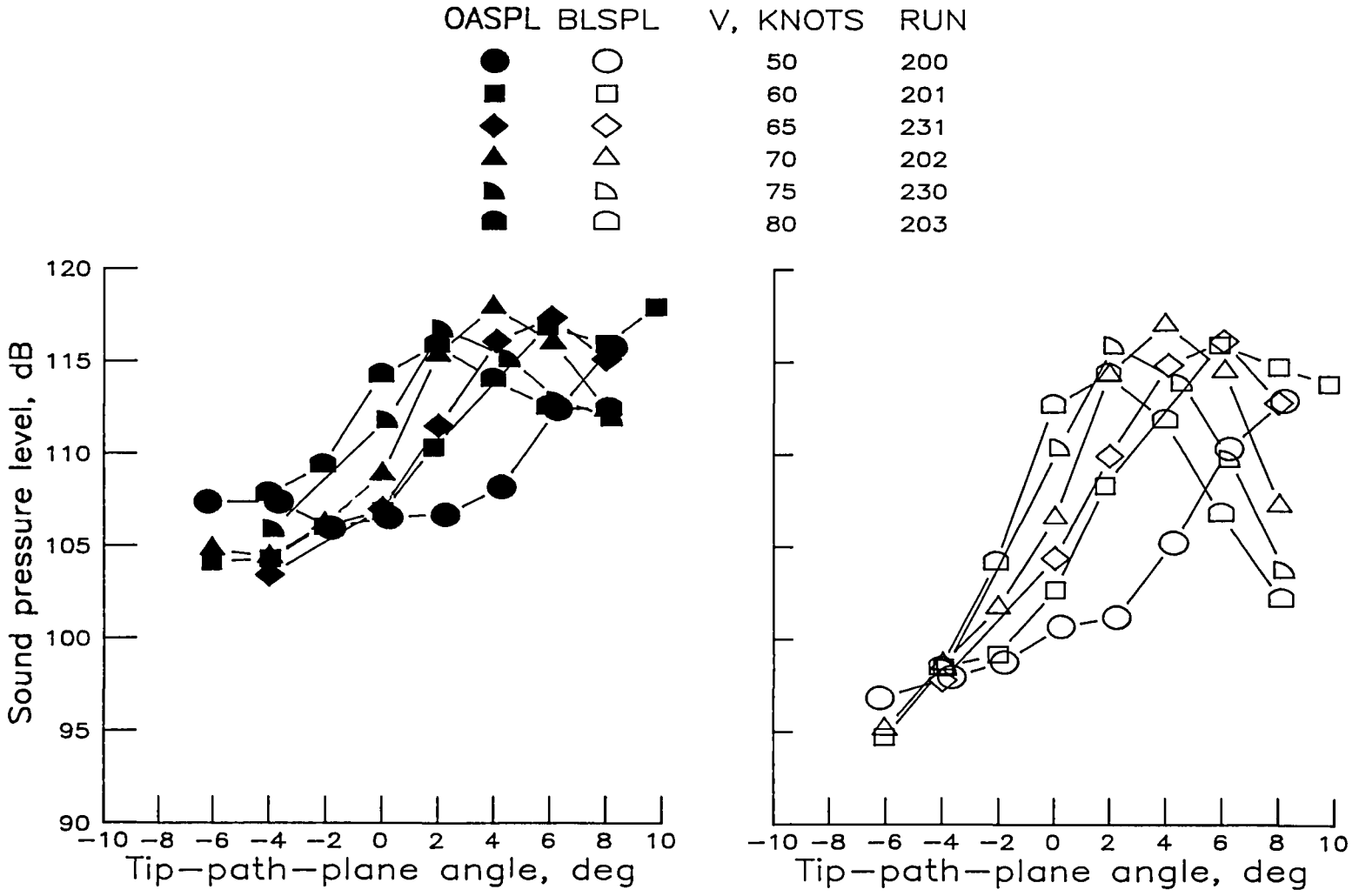

(b) Low-twist standard tip.

Figure 18.- Concluded.

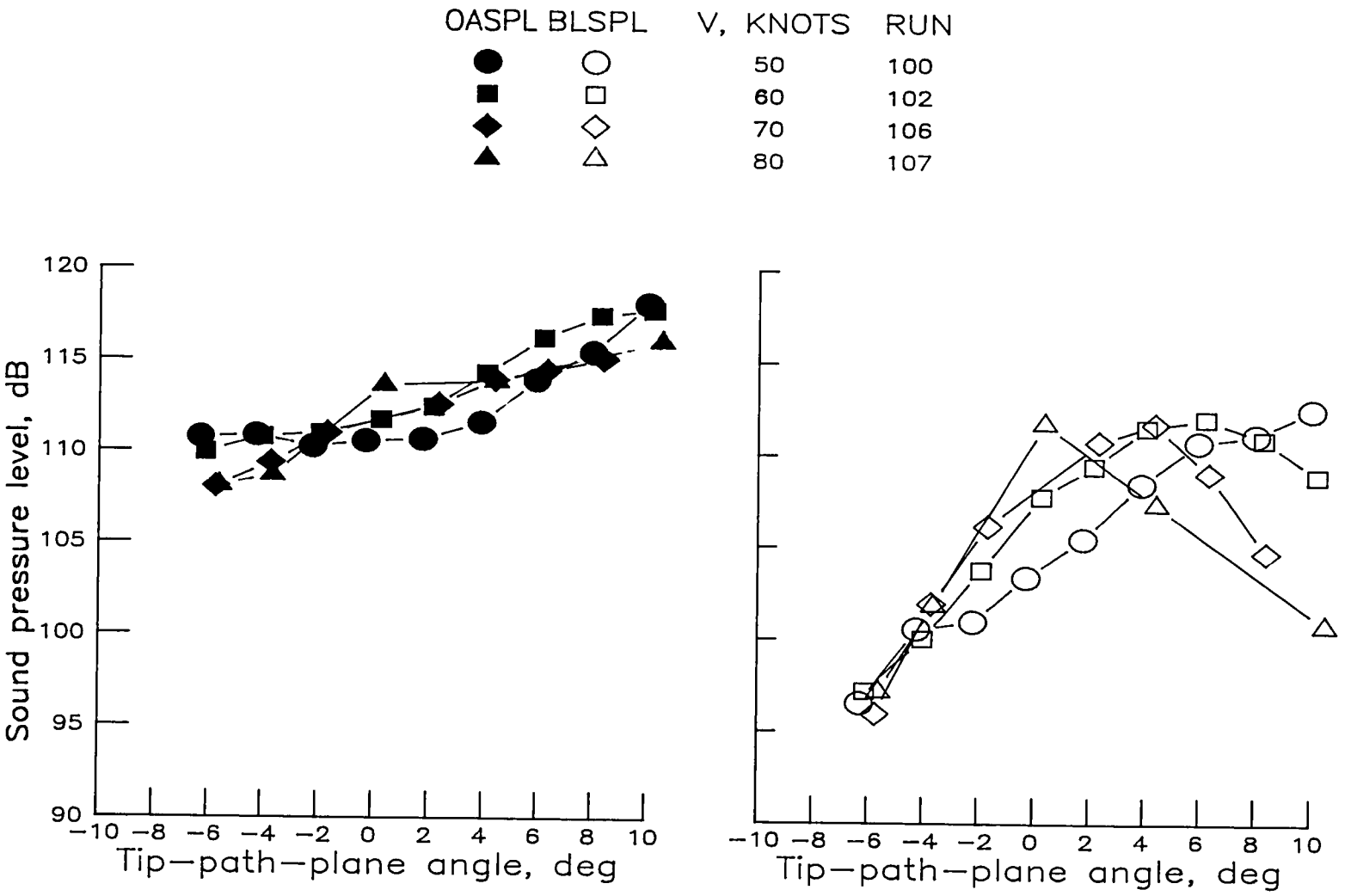

(a) High-twist standard tip.

Figure 19.- Overall and band-limited sound pressure levels as a function of tip-path-plane angle over velocity range from 50 to 80 knots for microphone 3.

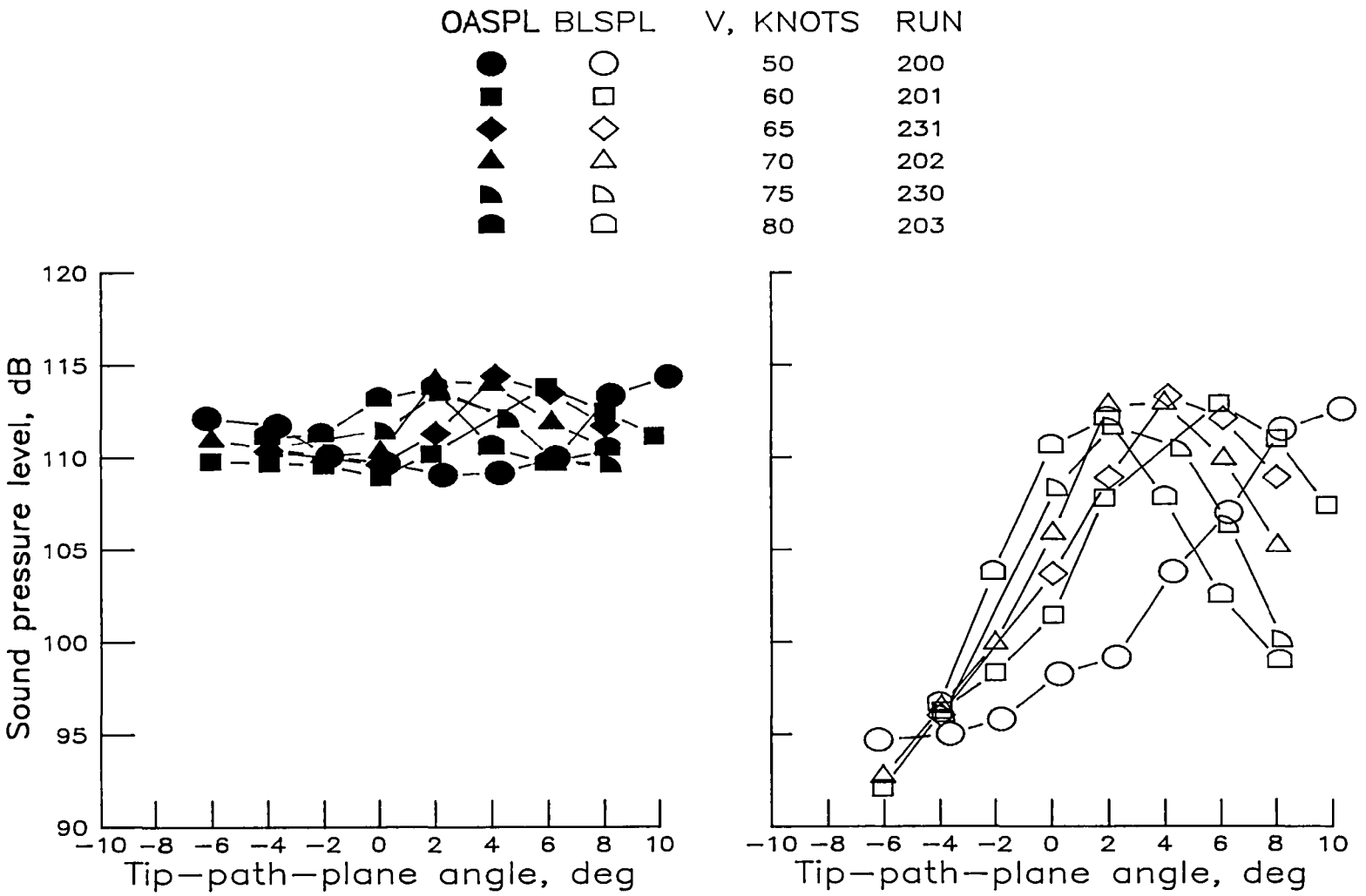

(b) Low-twist standard tip.

Figure 19.- Concluded.

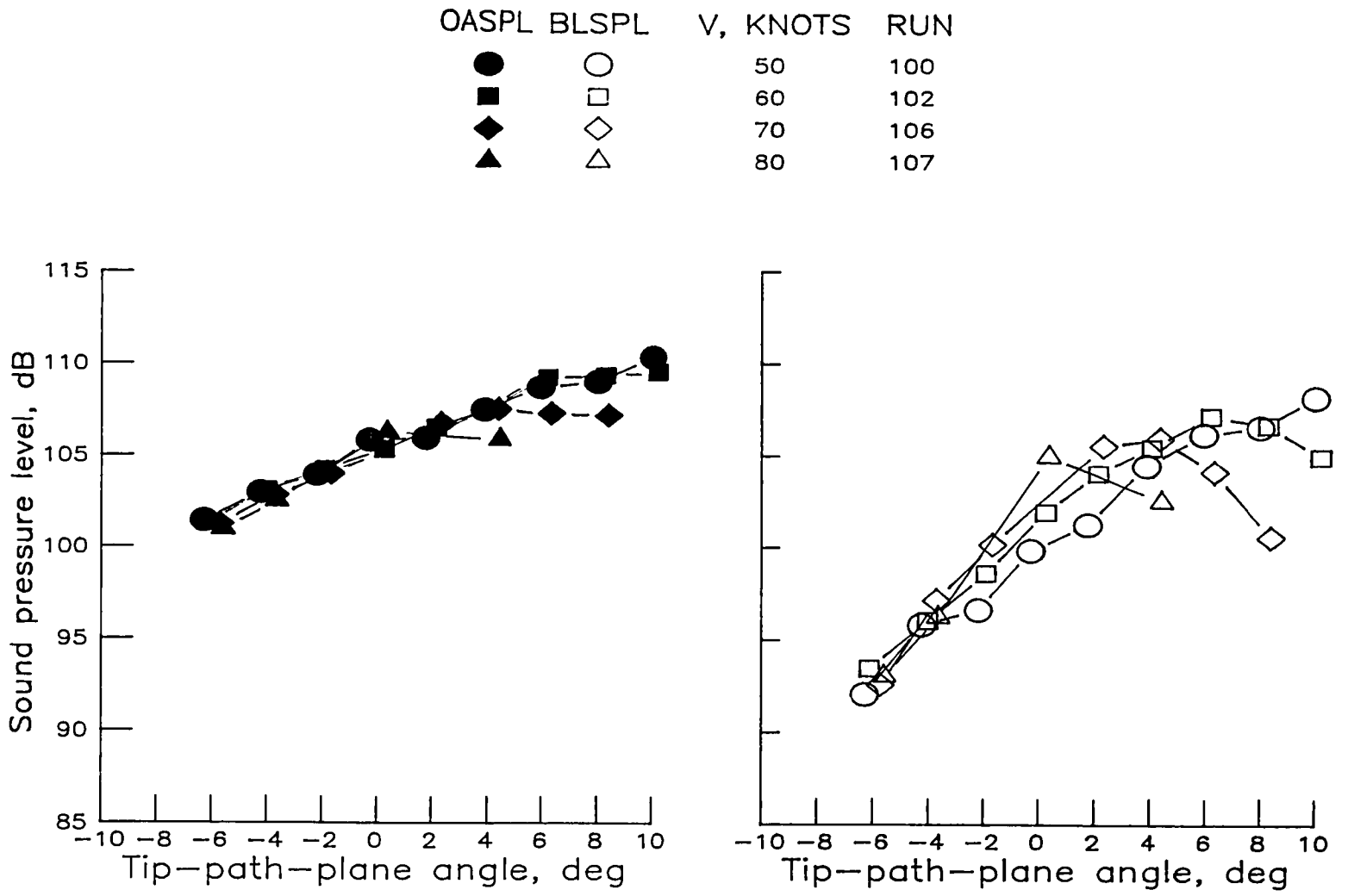

(a) High-twist standard tip.

Figure 20.- Overall and band-limited sound pressure levels as a function of tip-path-plane angle over velocity range from 50 to 80 knots for microphone 4.

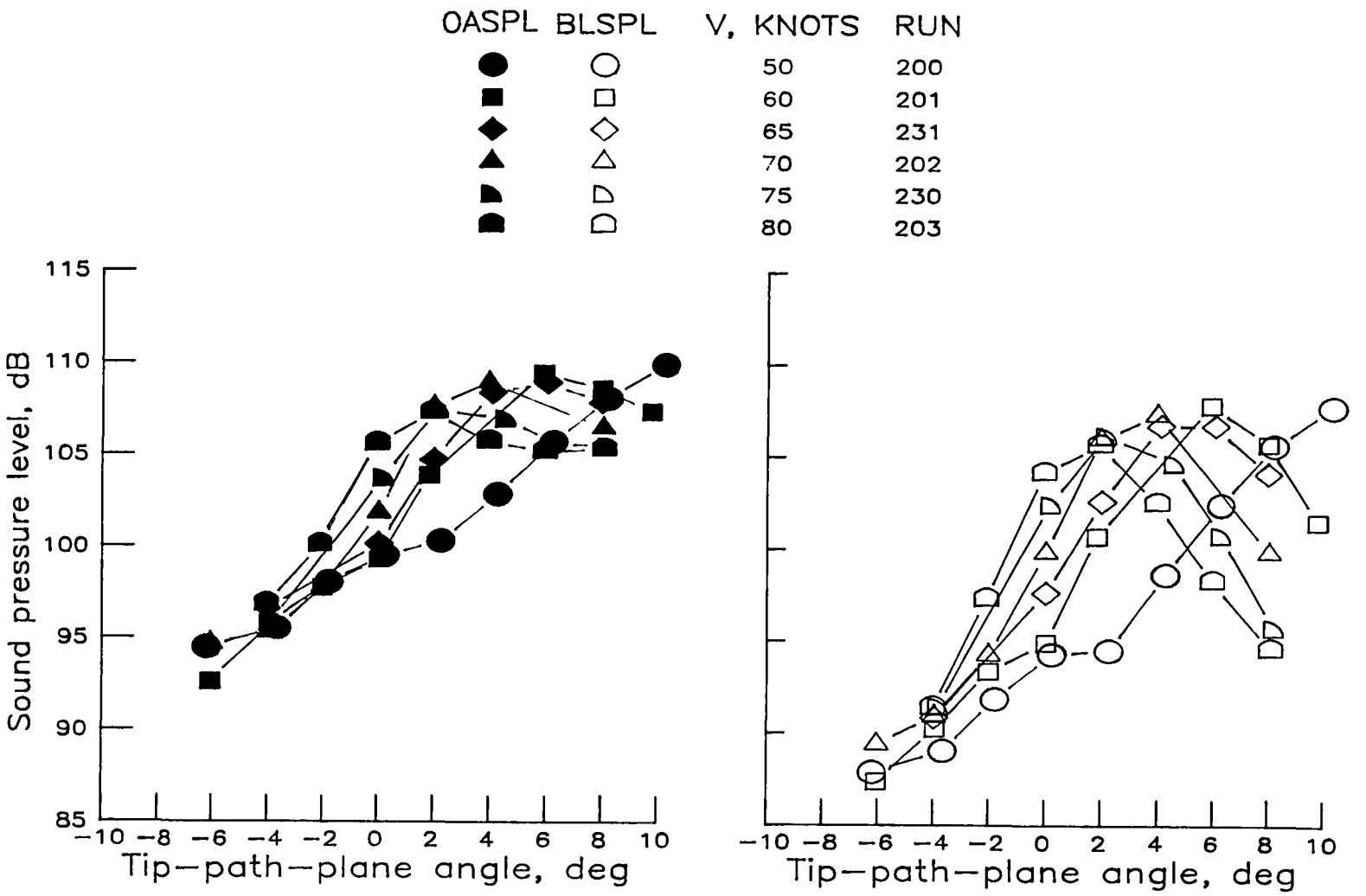

(b) Low-twist standard tip.

Figure 20.- Concluded.

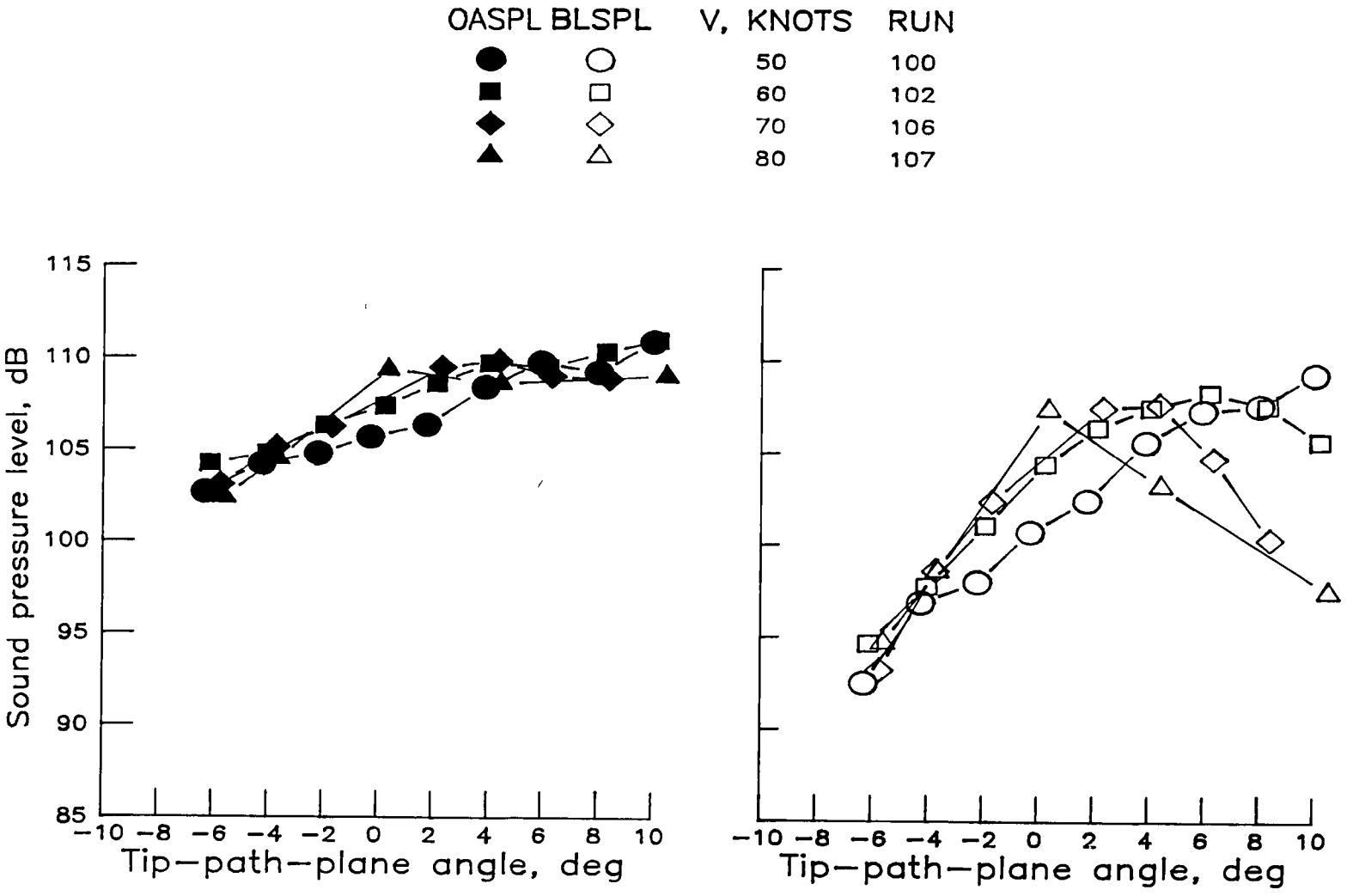

(a) High-twist standard tip.

Figure 21.- Overall and band-limited sound pressure levels as a function of tip-path-plane angle over velocity range from 50 to 80 knots for microphone 5.

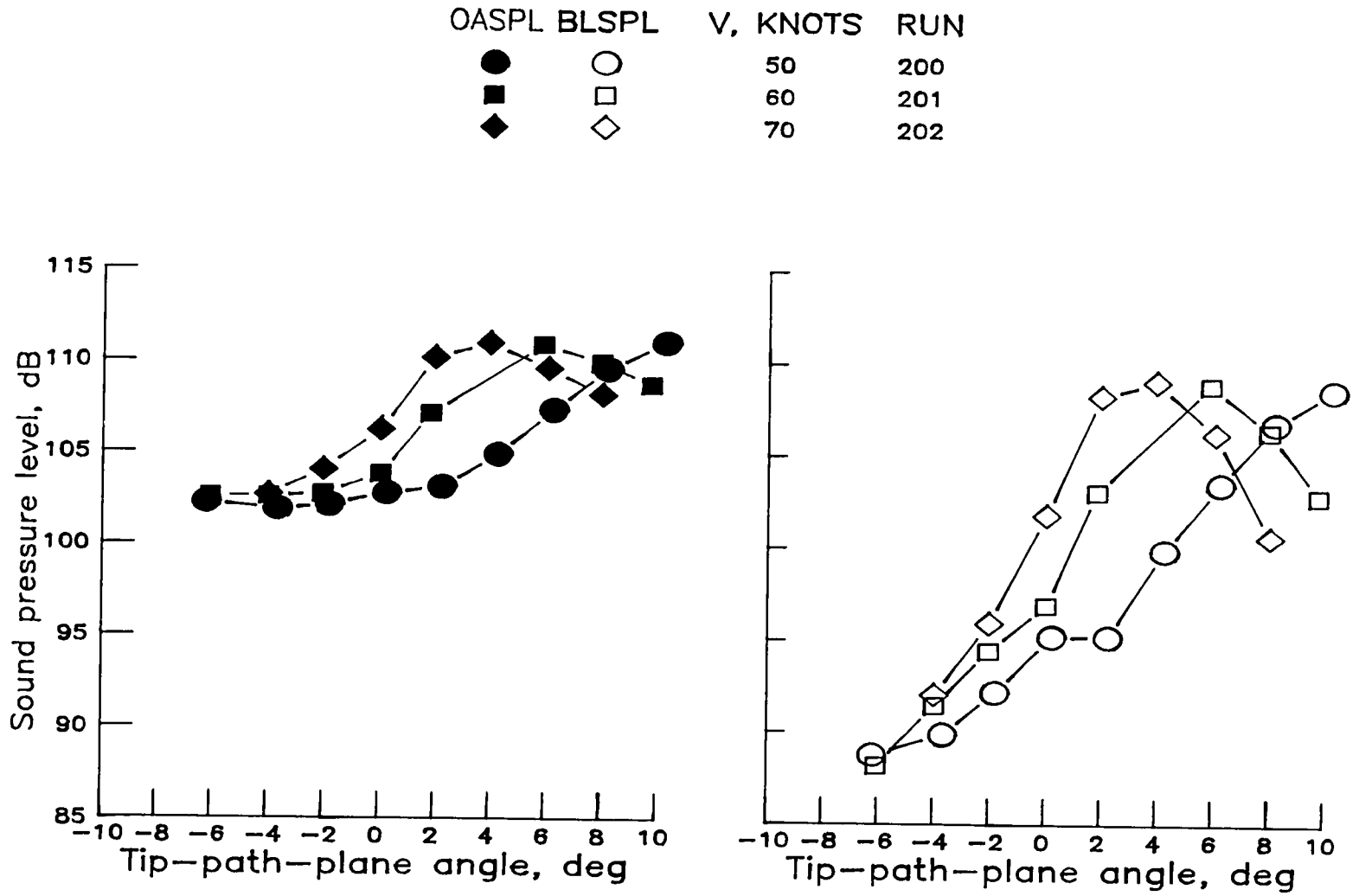

(b) Low-twist standard tip.

Figure 21.- Concluded.

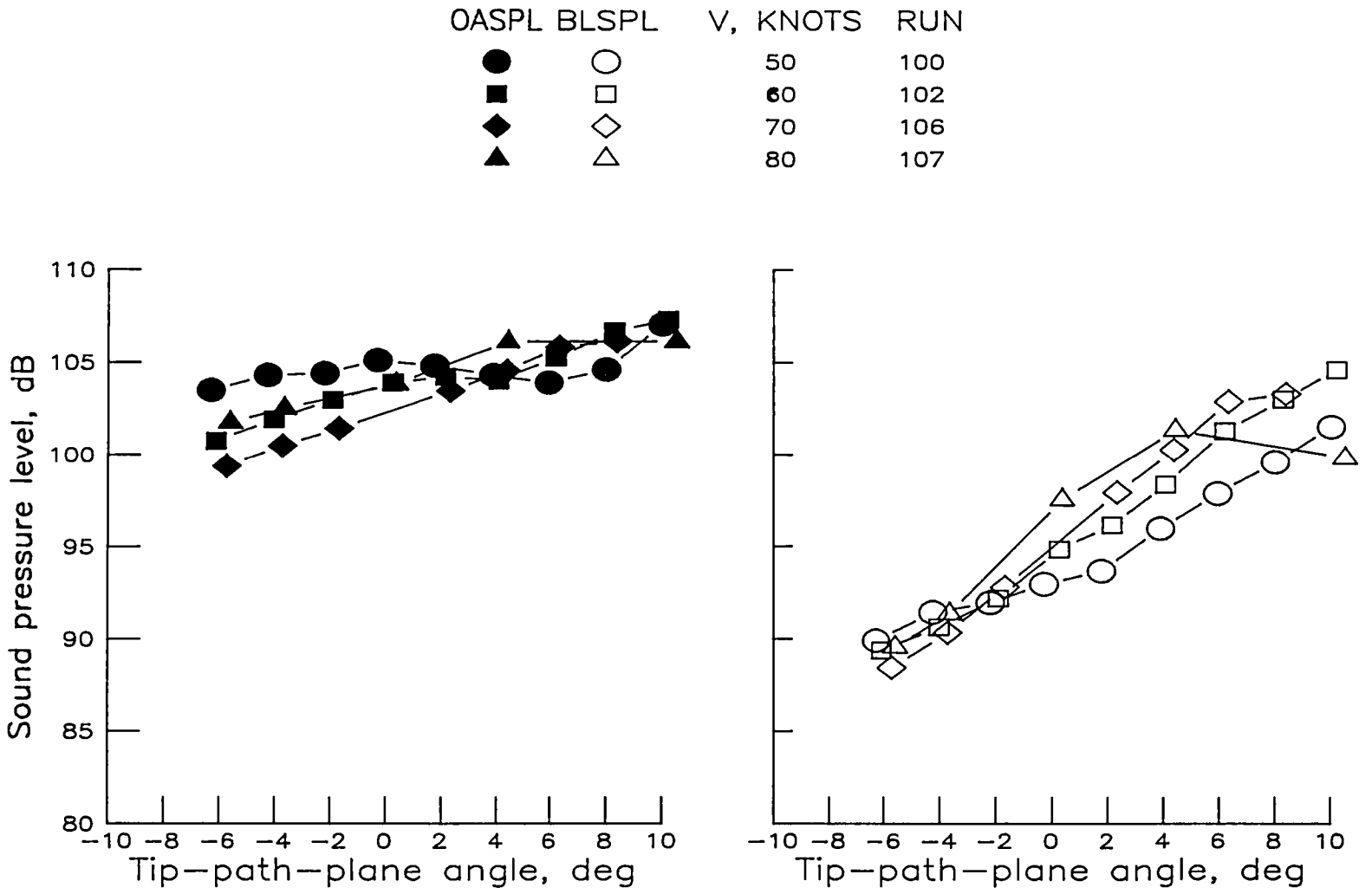

(a) High-twist standard tip.

Figure 22.- Overall and band-limited sound pressure levels as a function of tip-path-plane angle over velocity range from 50 to 80 knots for microphone 7.

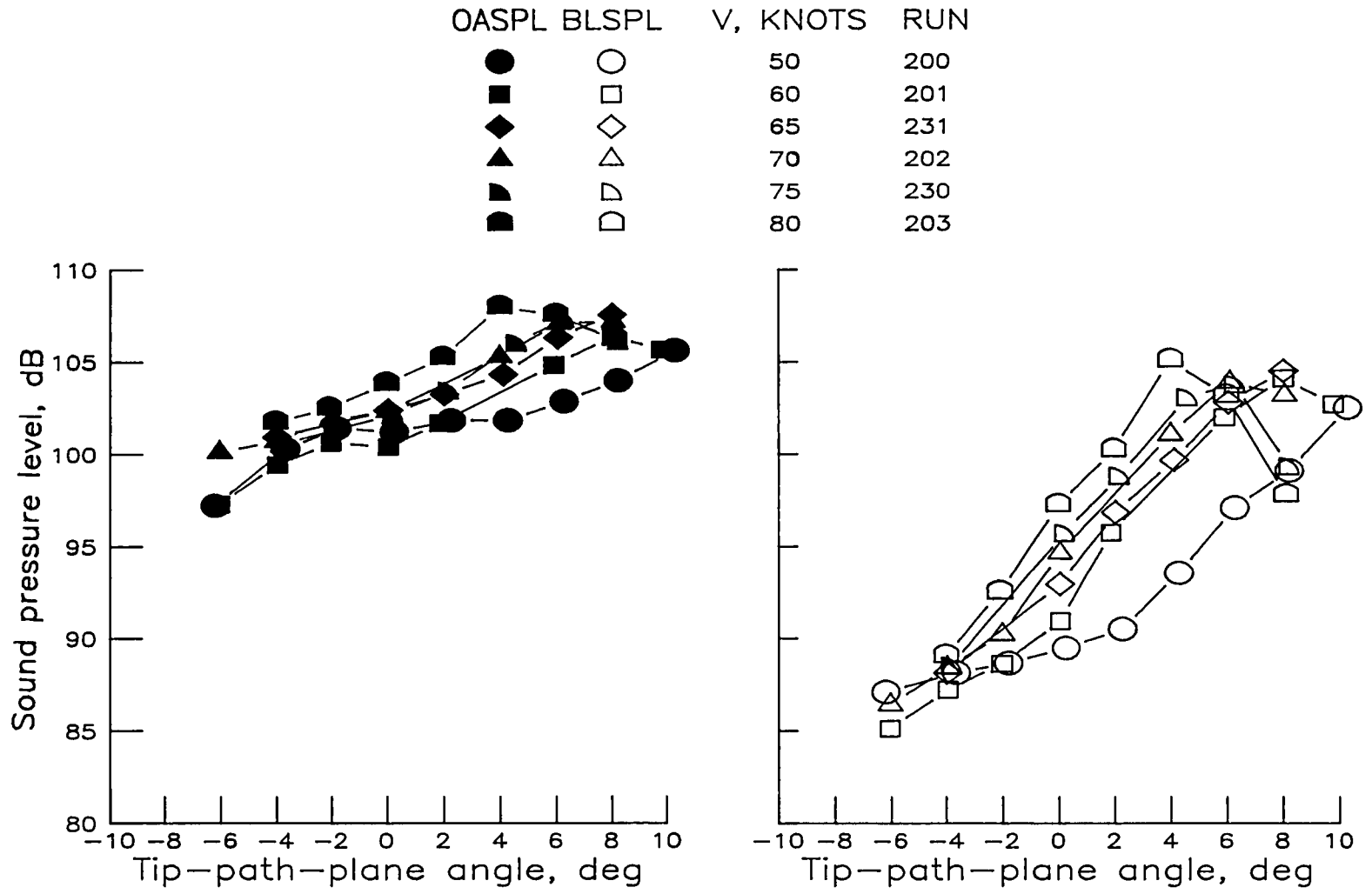

(b) Low-twist standard tip.

Figure 22.- Concluded.

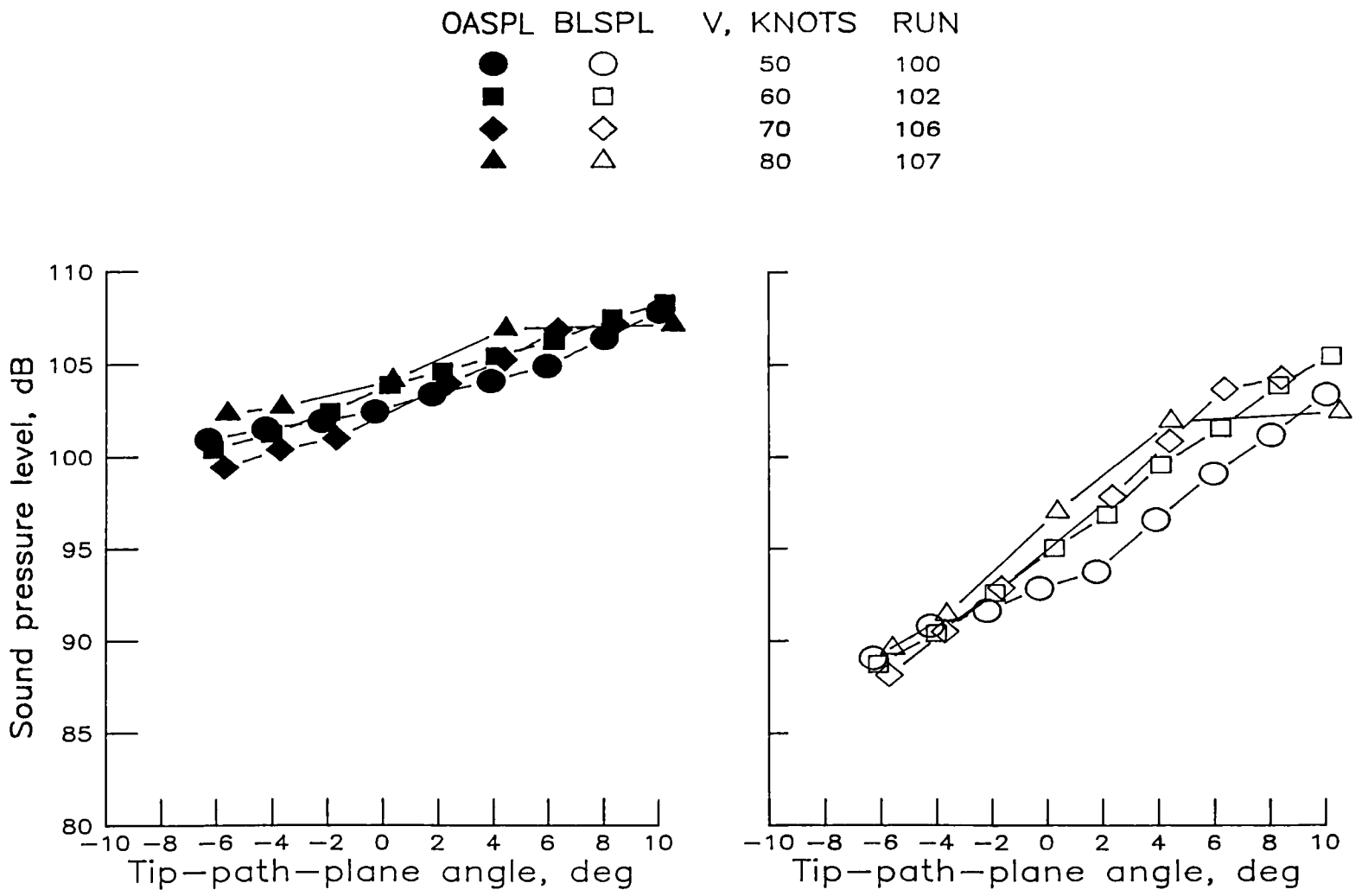

(a) High-twist standard tip.

Figure 23.- Overall and band-limited sound pressure levels as a function of tip-path-plane angle over velocity range from 50 to 80 knots for microphone 8.

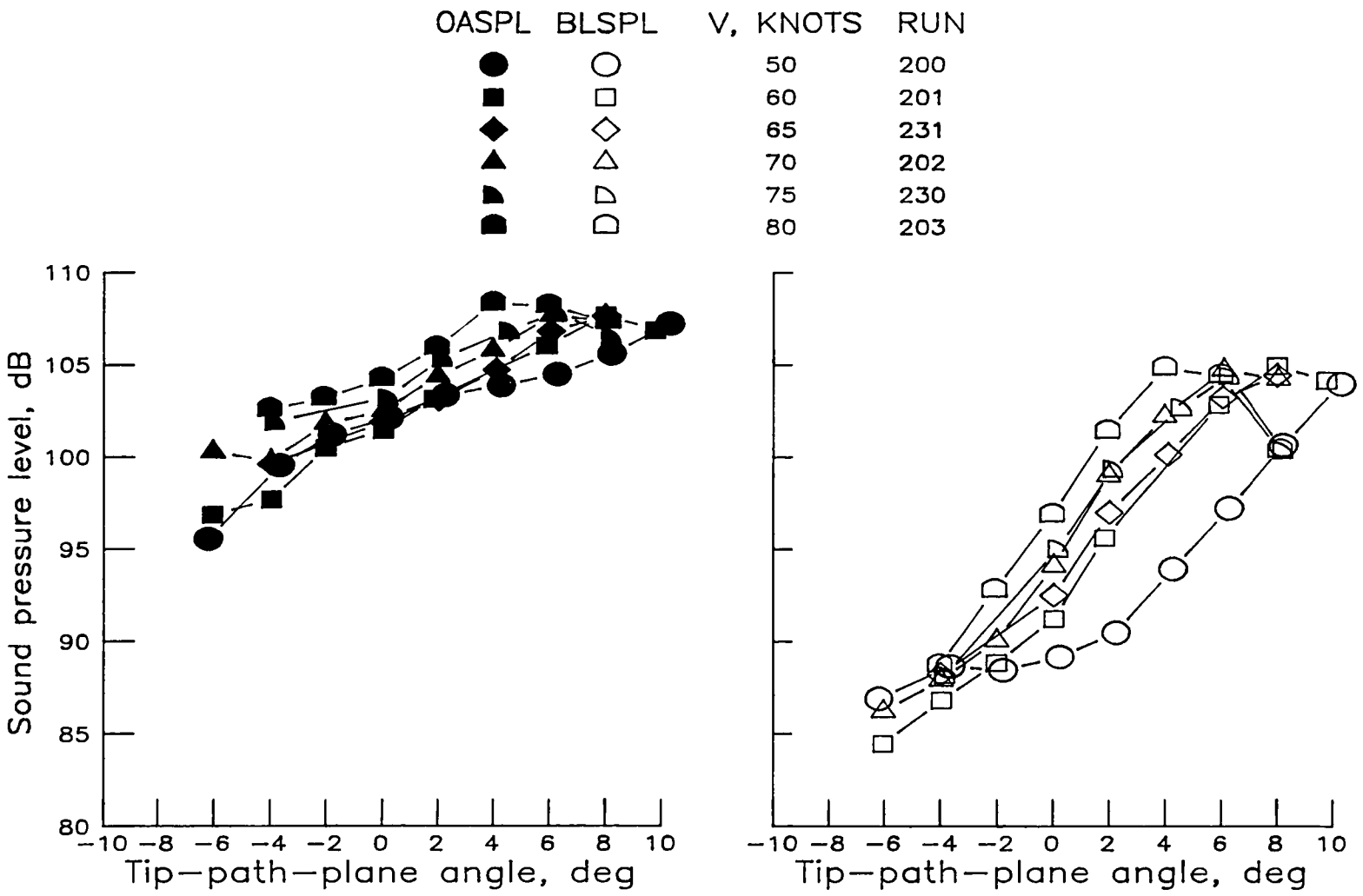

(b) Low-twist standard tip.

Figure 23.- Concluded.

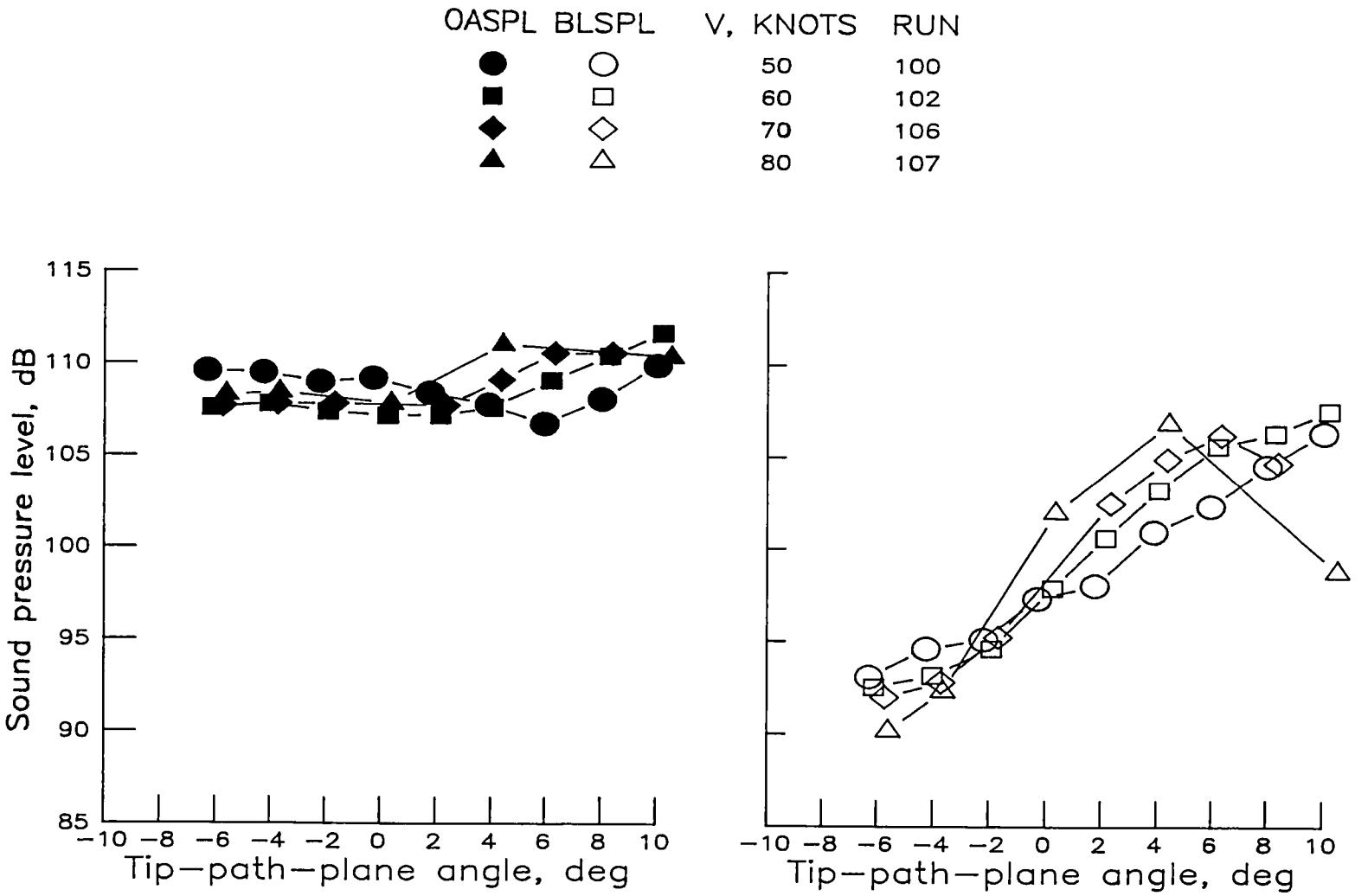

(a) High-twist standard tip.

Figure 24.- Overall and band-limited sound pressure levels as a function of tip-path-plane angle over velocity range from 50 to 80 knots for microphone 9.

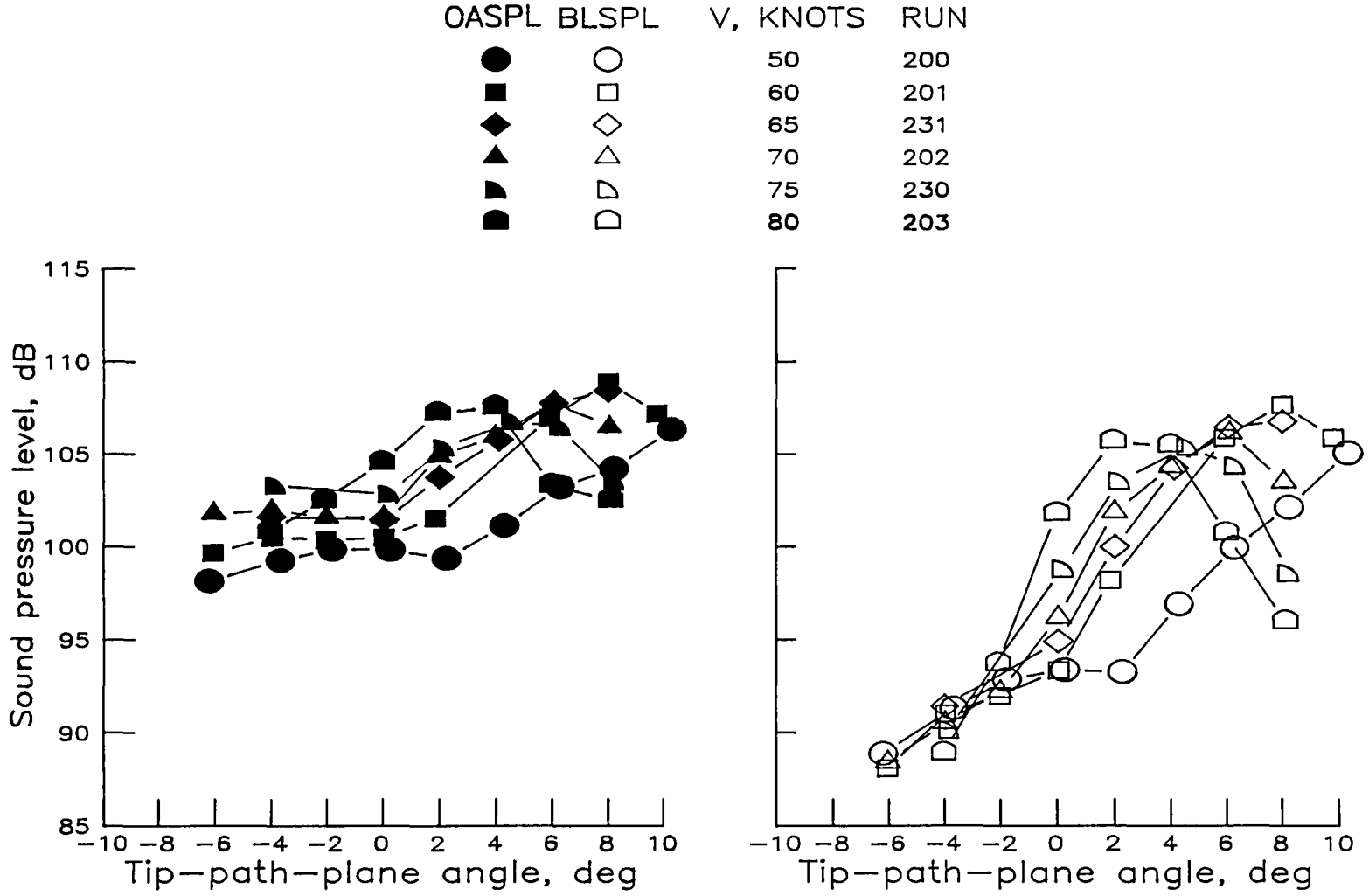

(b) Low-twist standard tip.

Figure 24.- Concluded.

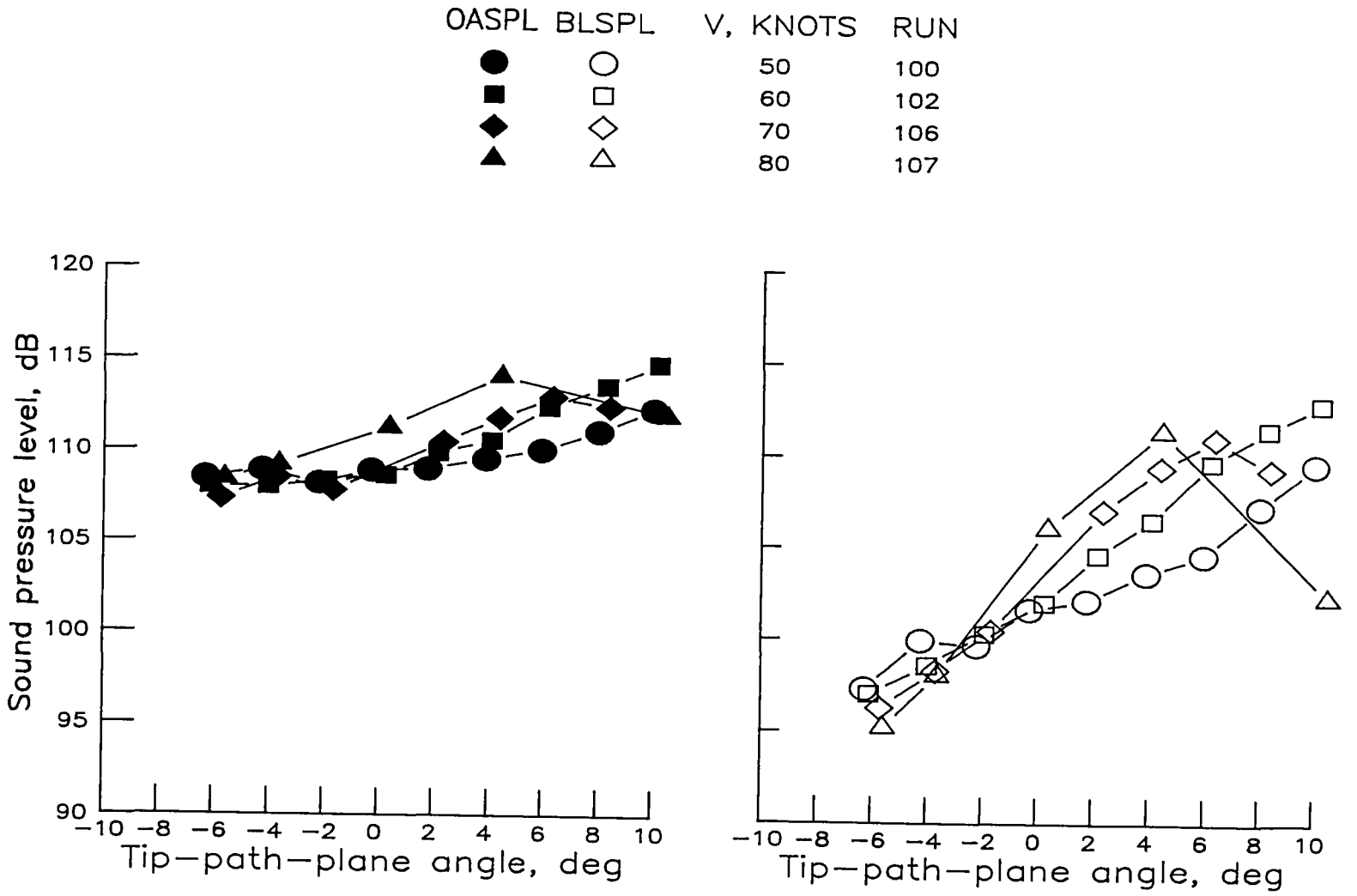

(a) High-twist standard tip.

Figure 25.- Overall and band-limited sound pressure levels as a function of tip-path-plane angle over velocity range from 50 to 80 knots for microphone 12.

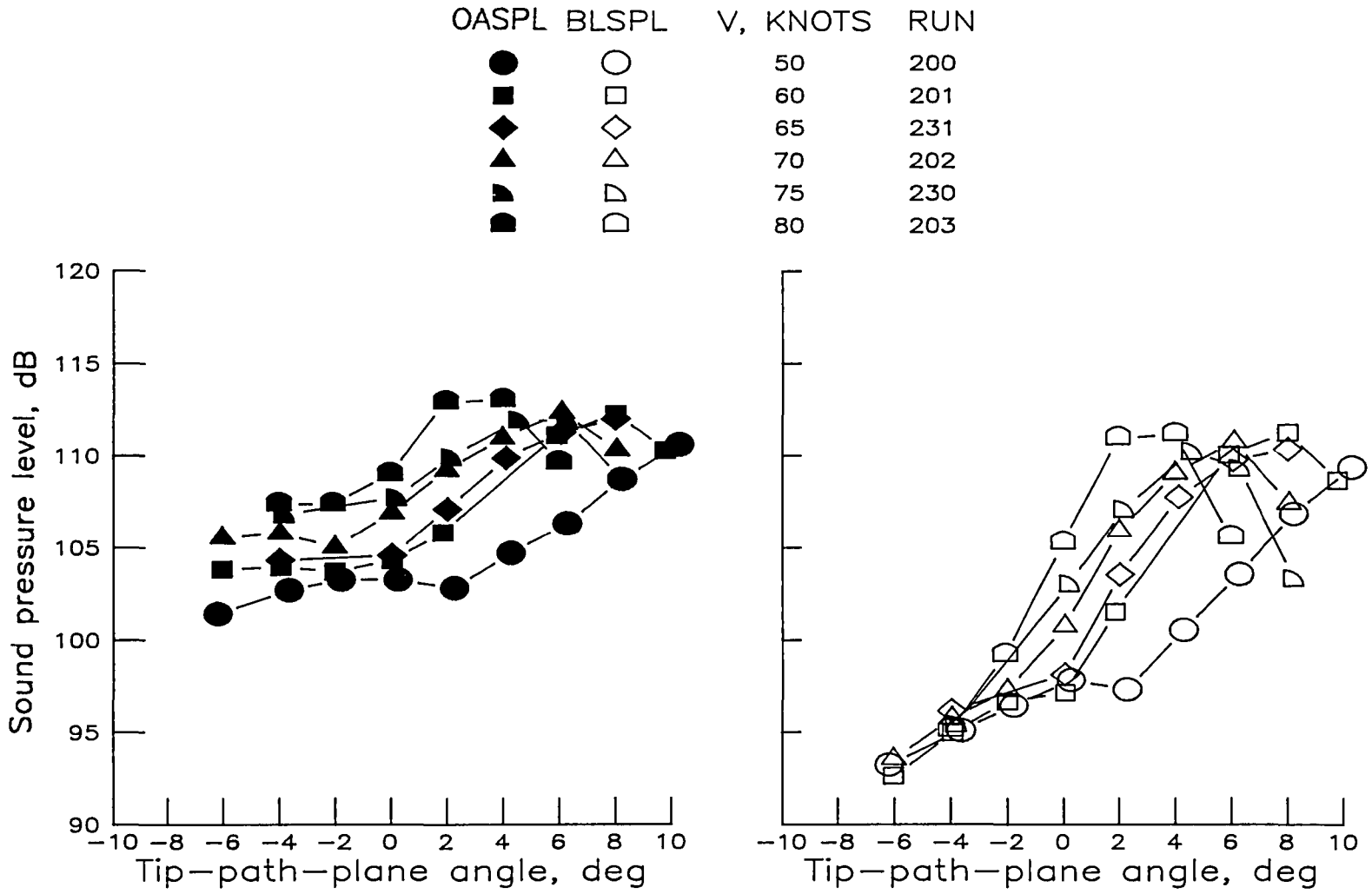

(b) Low-twist standard tip.

Figure 25.- Concluded.

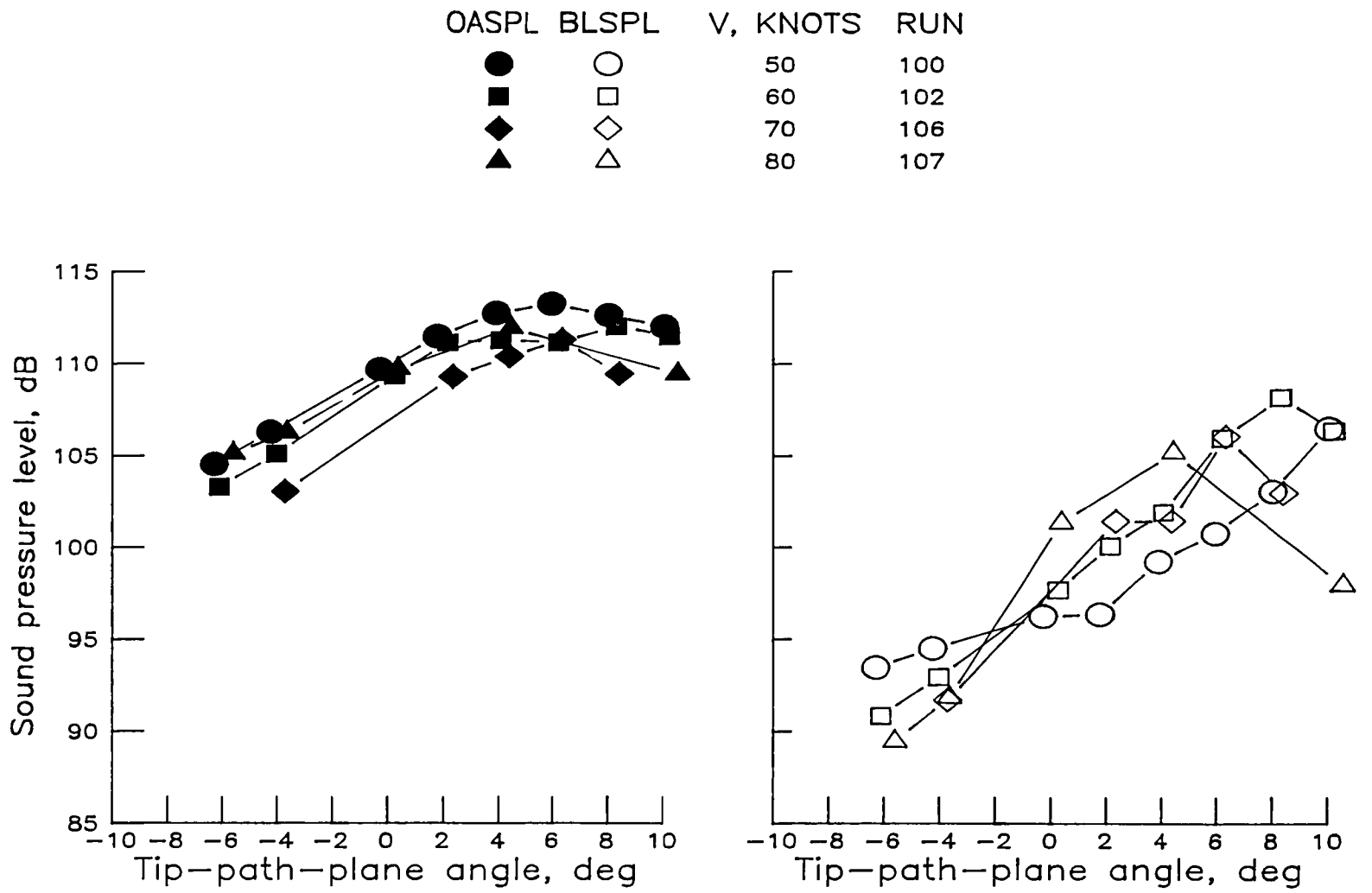

(a) High-twist standard tip.

Figure 26.- Overall and band-limited sound pressure levels as a function of tip-path-plane angle over velocity range from 50 to 80 knots for microphone 17.

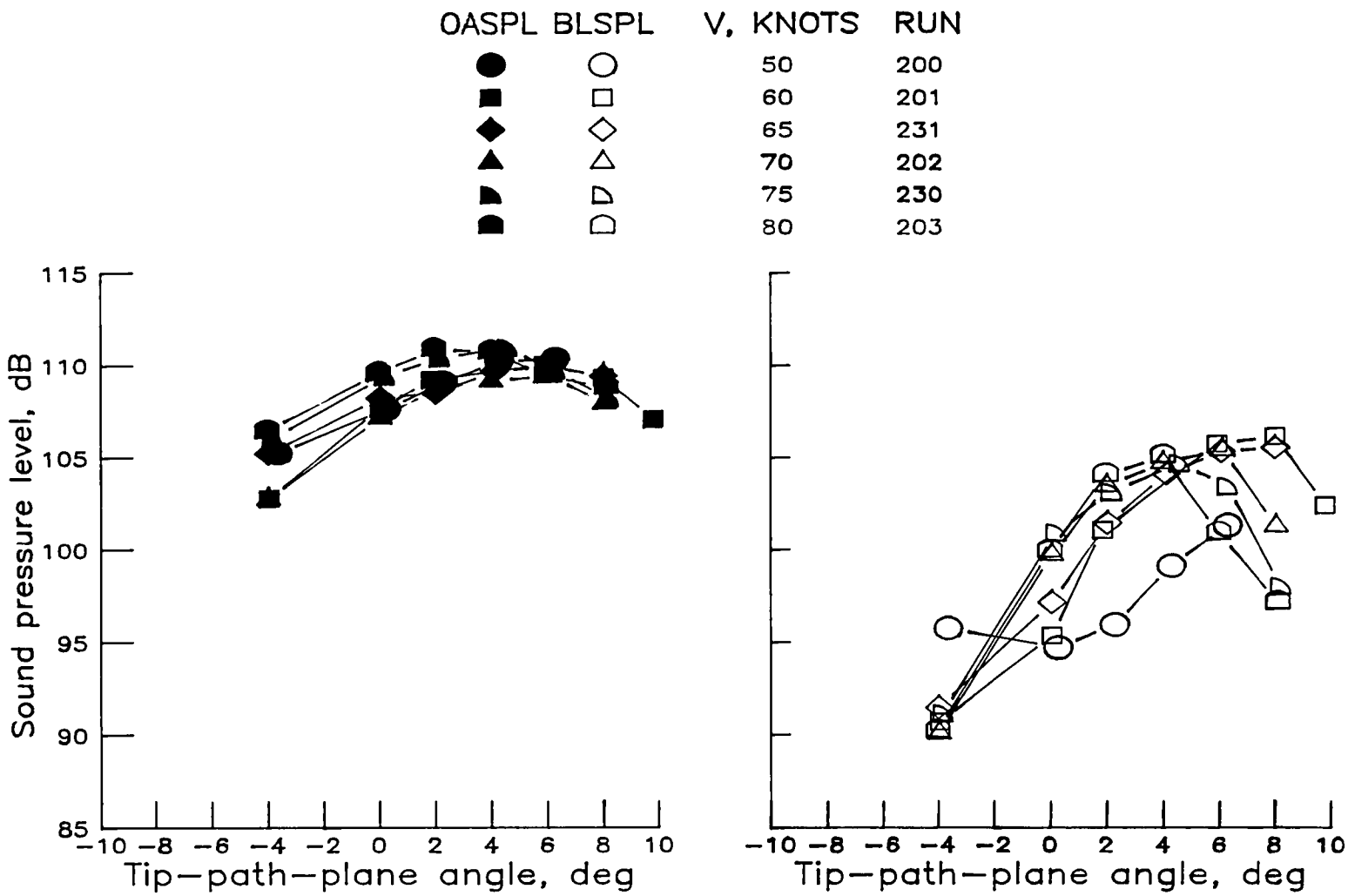

(b) Low-twist standard tip.

Figure 26.- Concluded.

APPENDIX A

COMPARISON OF OVERALL ACOUSTIC LEVELS FROM TWO ANALYSIS METHODS

The figures presented in this appendix show two sound metrics plotted against tip-path-plane angle as a function of forward velocity. Each figure presents two metrics (OASPL and BLSPL) for each of the unique rotor configurations shown in figure 4. Each curve in the figure is for a constant velocity. The solid symbols represent the OASPL data and the open symbols represent the BLSPL data. The plots for each microphone are made to the same decibel range, and all the plots are made with the same scale of decibels per major division to aid in cross comparisons. Each figure includes nine plots, one for each rotor configuration.

Because of problems encountered during either data acquisition or reduction, there is a paucity of data for the following: microphones 2, 4, and 7 for the high-twist swept tapered tip with the new airfoil (500-series runs), and microphone 17 for the high-twist parabolic tip (700-series runs) and the low-twist tapered and square tips (800- and 900-series runs).

The data base presented here may be furnished to interested researchers in the form of a computer listing or on digital tape by contacting the authors.

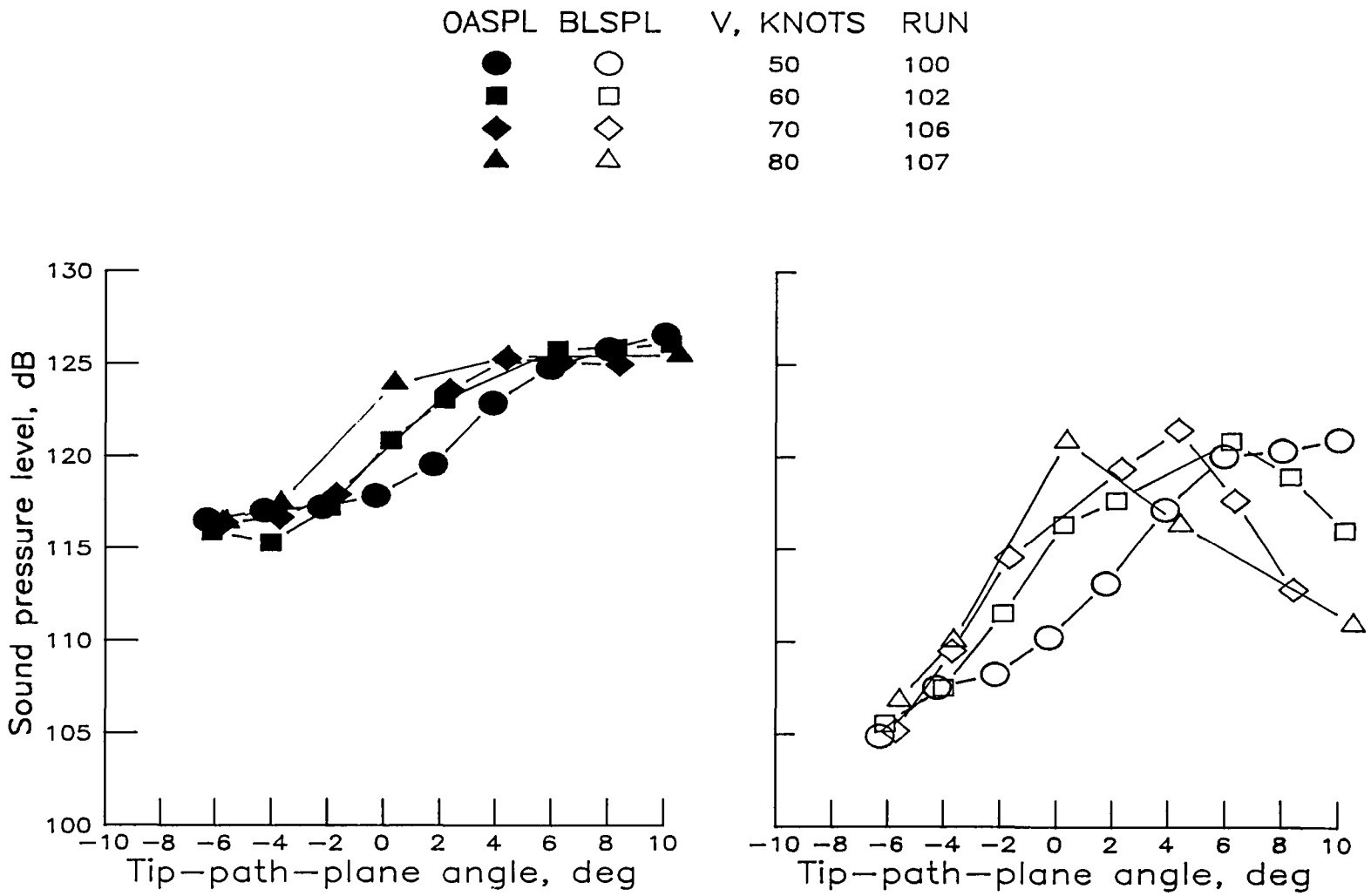

(a) High-twist standard tip (fig. 13(a)).

Figure A1.- Overall and band-limited noise levels as a function of tip-path-plane angle over velocity range from 50 to 80 knots for microphone 1.

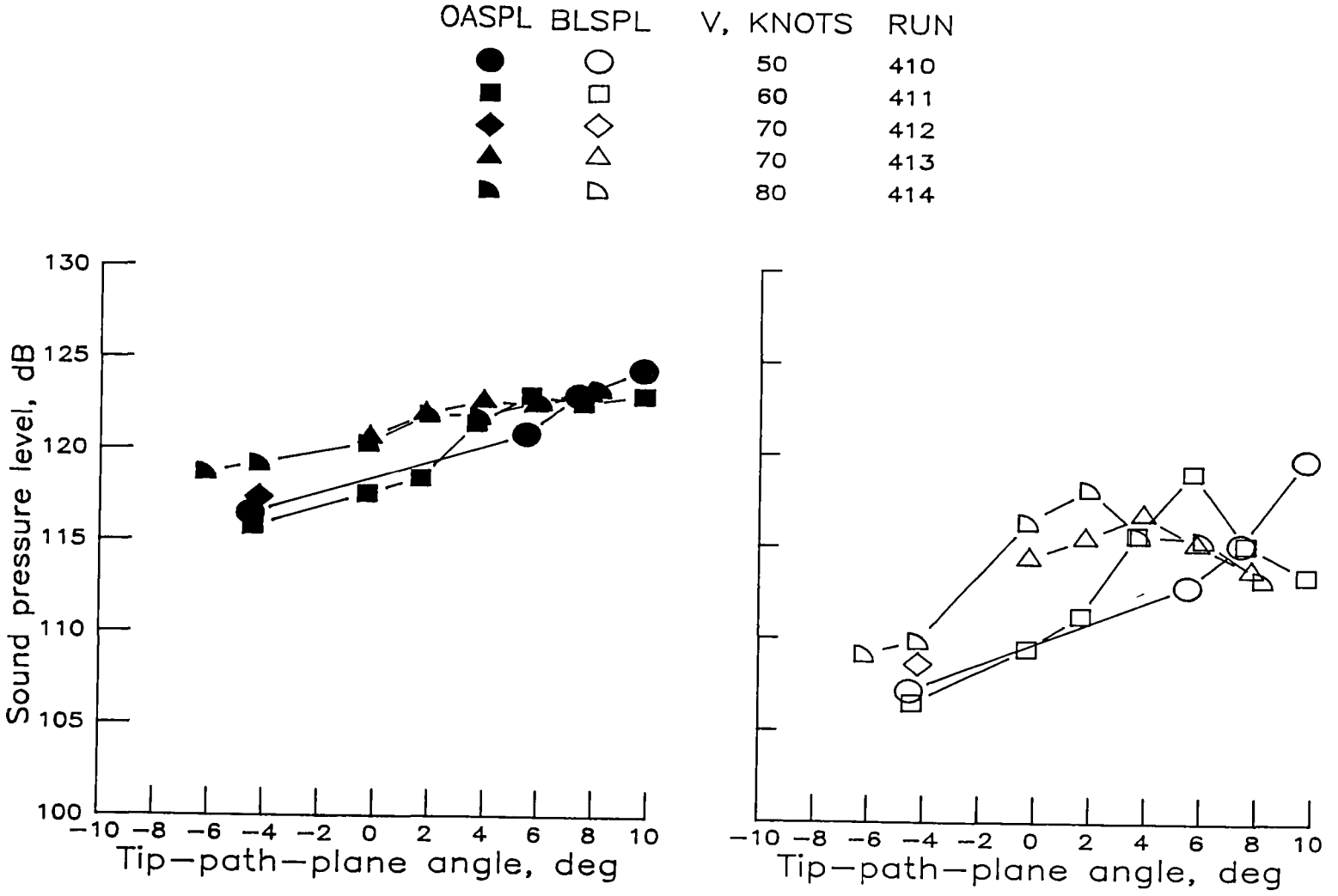

(b) High-twist swept tapered tip (SC1095 airfoil).

Figure A1.- Continued.

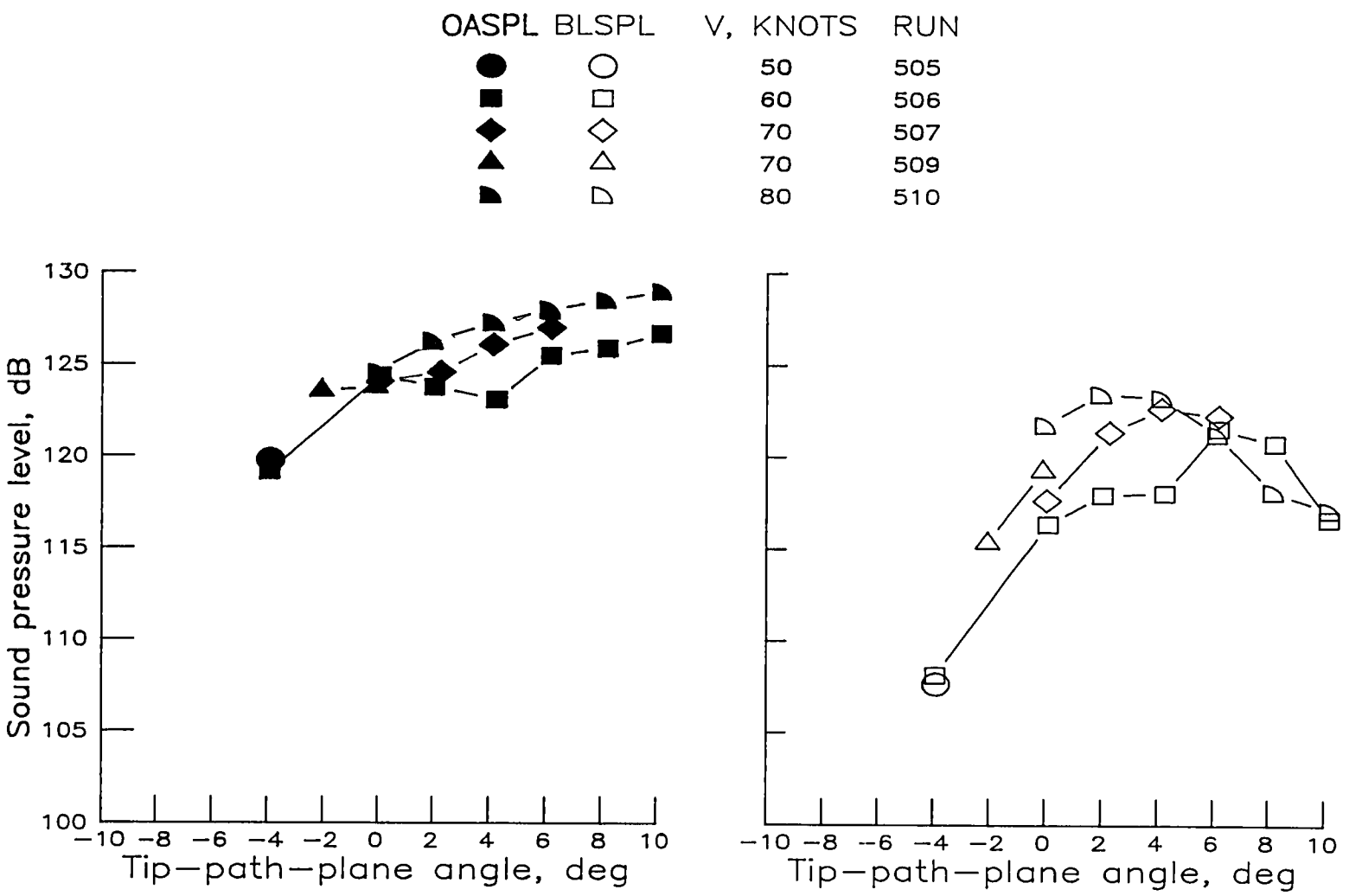

(c) High-twist swept tapered tip (SSC-A07 airfoil).

Figure A1.- Continued.

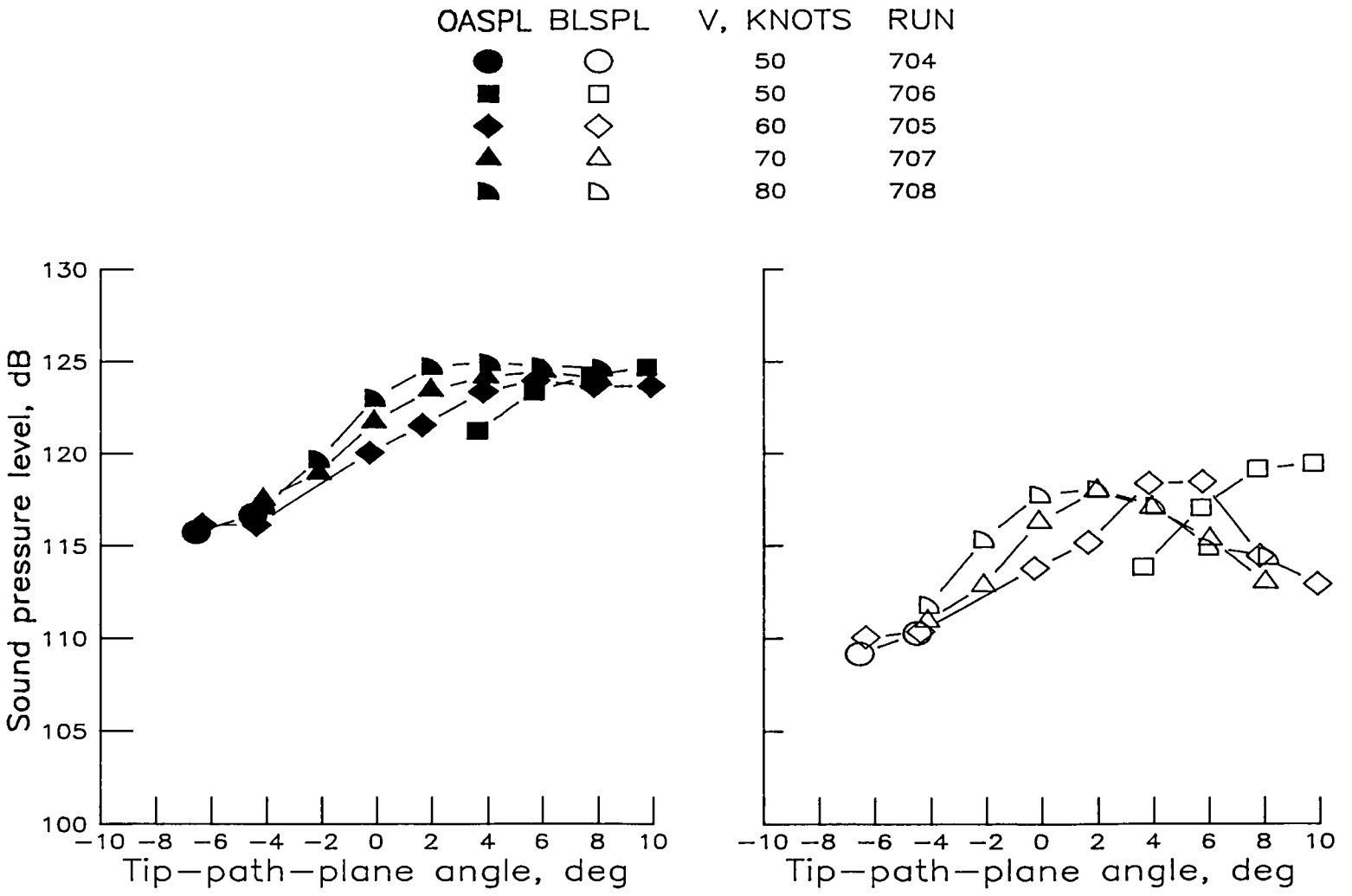

(d) High-twist parabolic tip.

Figure A1.- Continued.

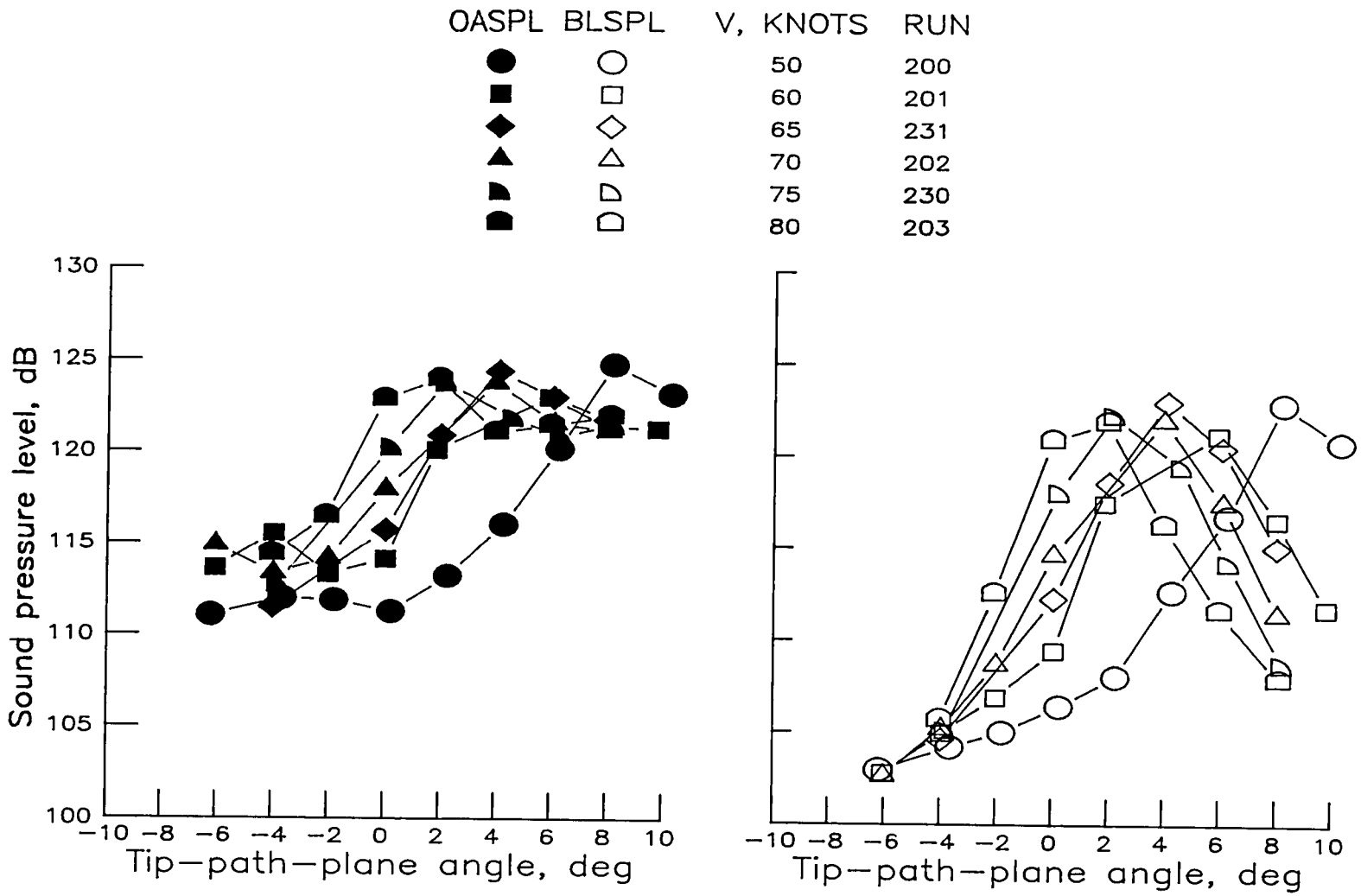

(e) Low-twist standard tip (fig. 13(b)).

Figure A1.- Continued.

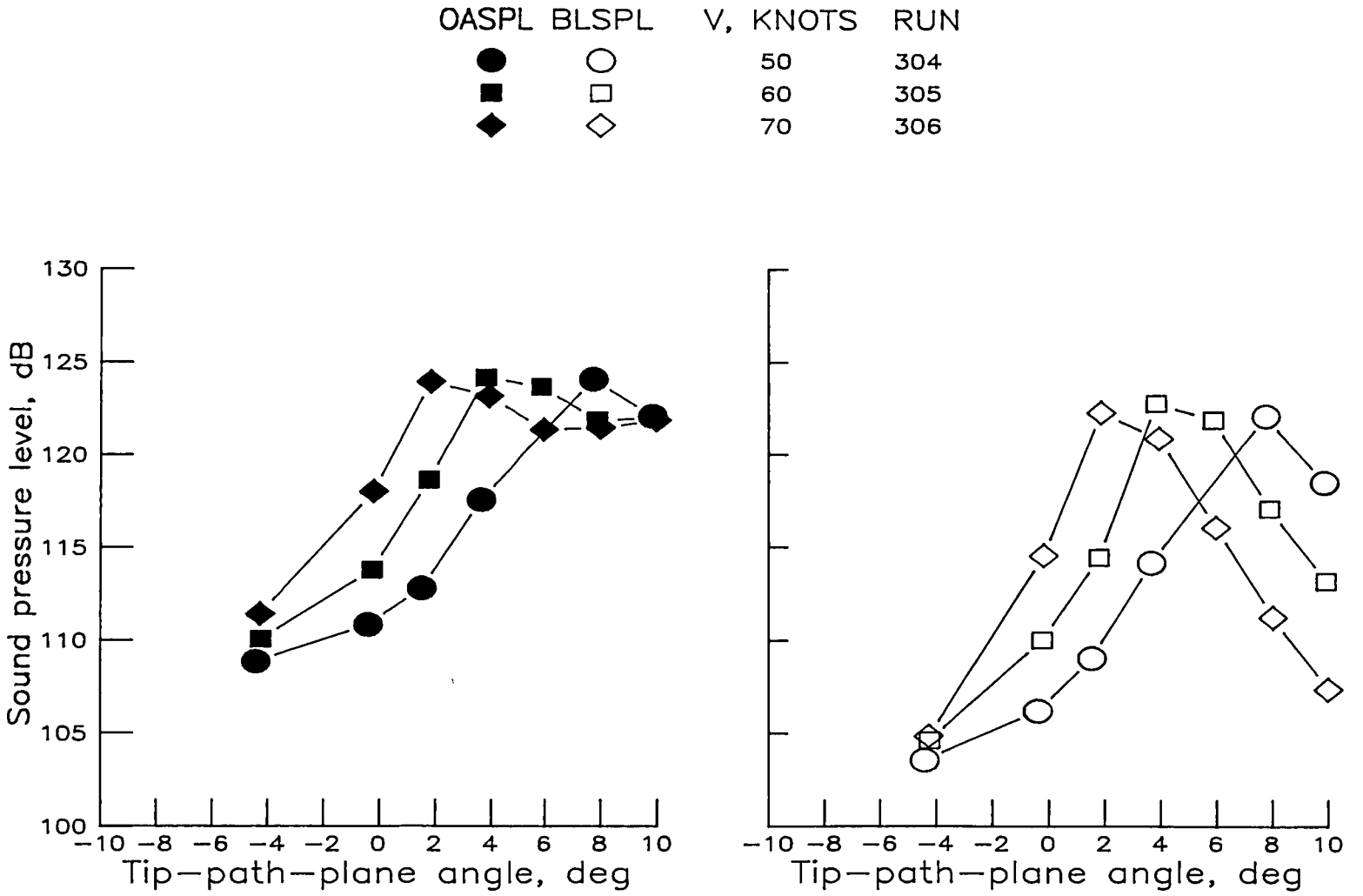

(f) Low-twist anhedral tip.

Figure A1.- Continued.

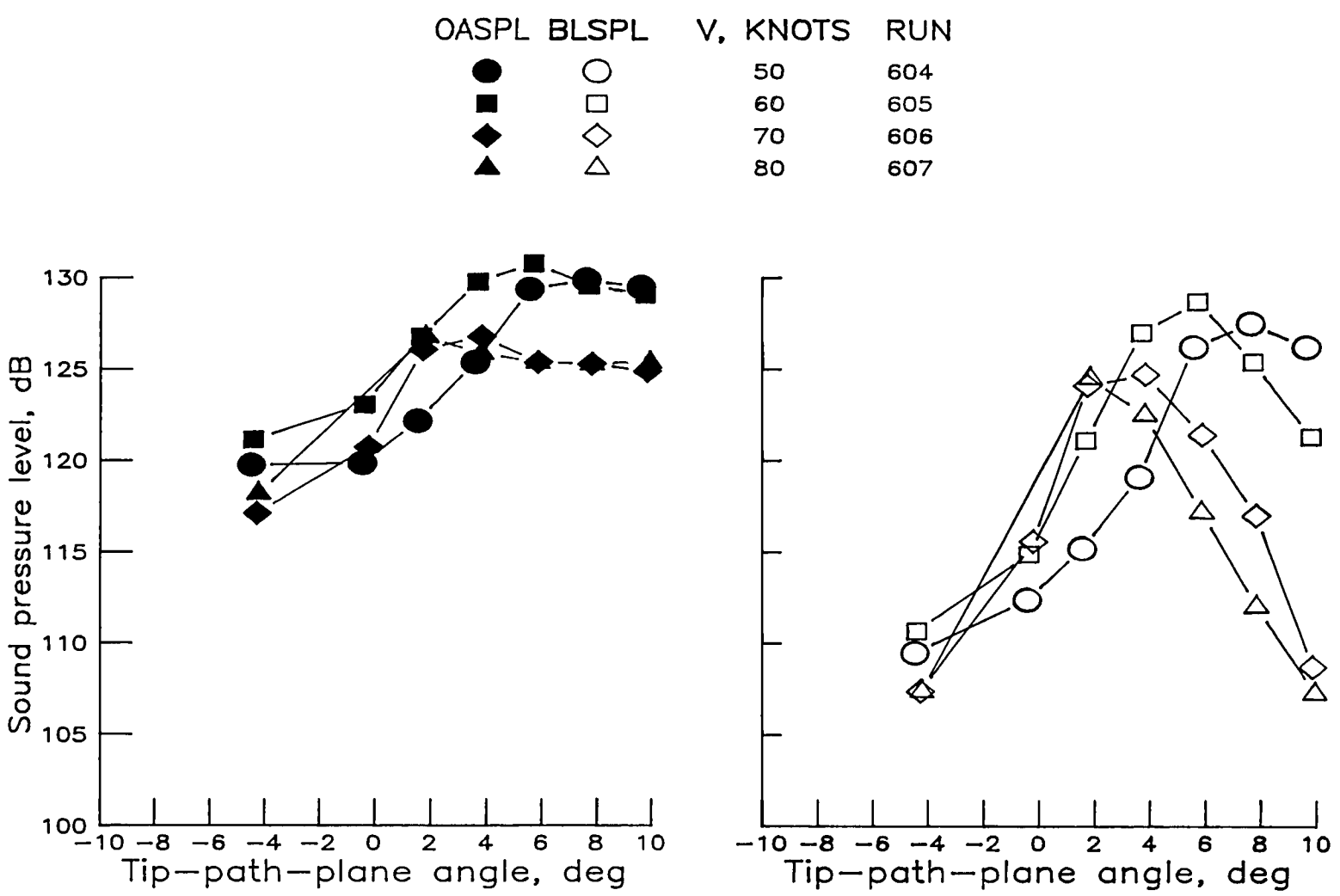

(g) Low-twist swept tip.

Figure A1.- Continued.

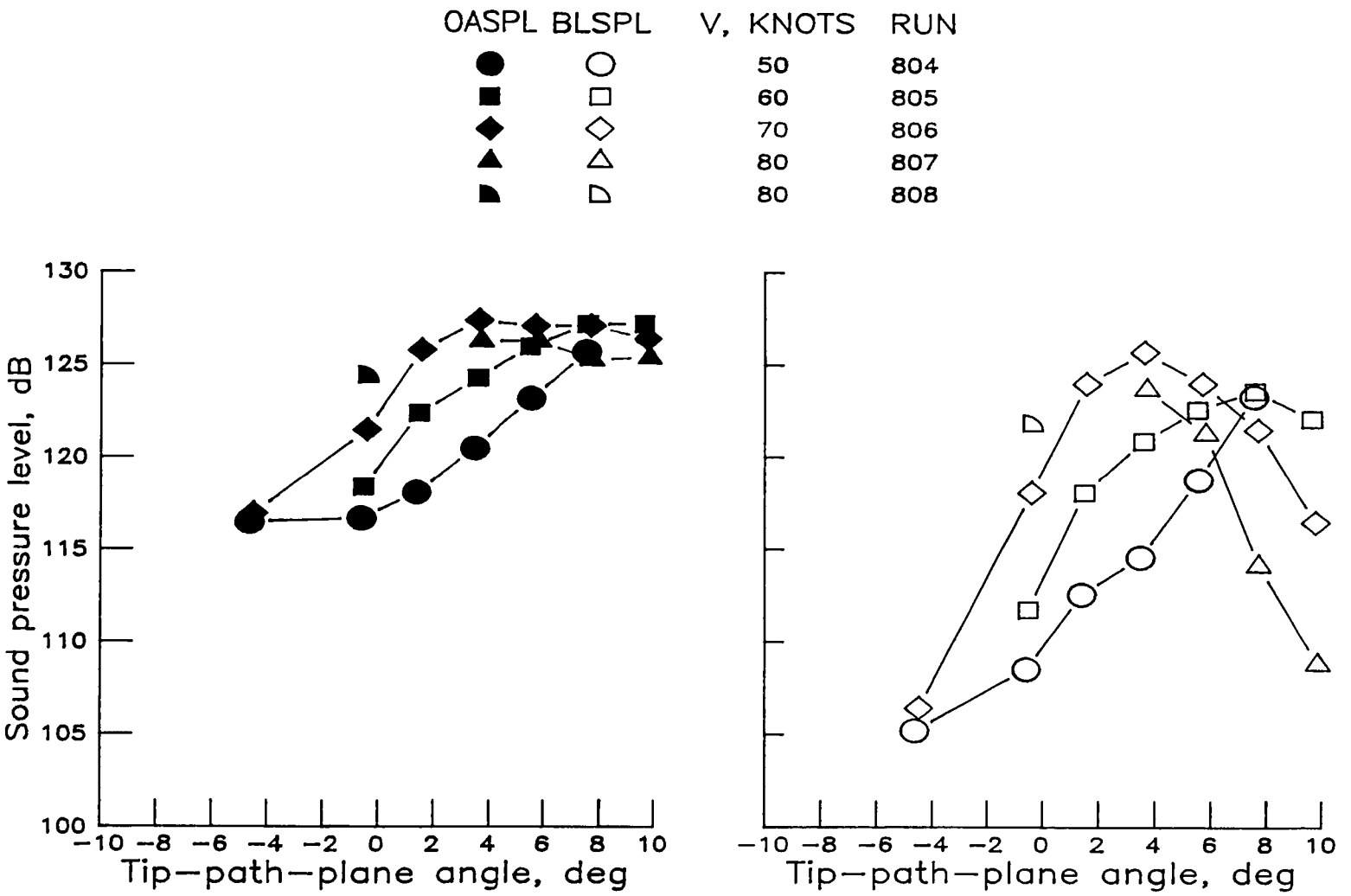

(h) Low-twist tapered tip.

Figure A1.- Continued.

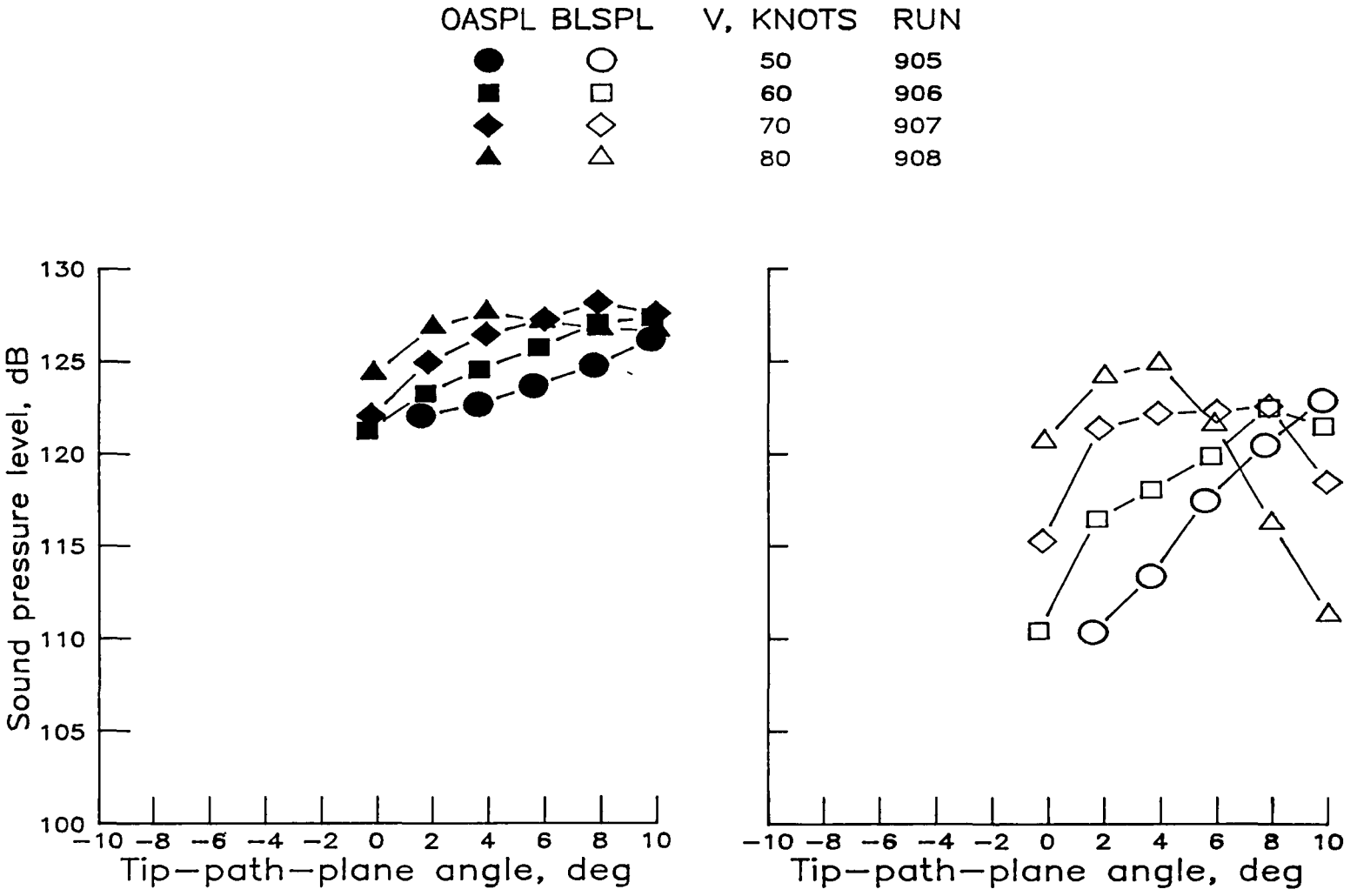

(1) Low-twist square tip.

Figure A1.- Concluded.

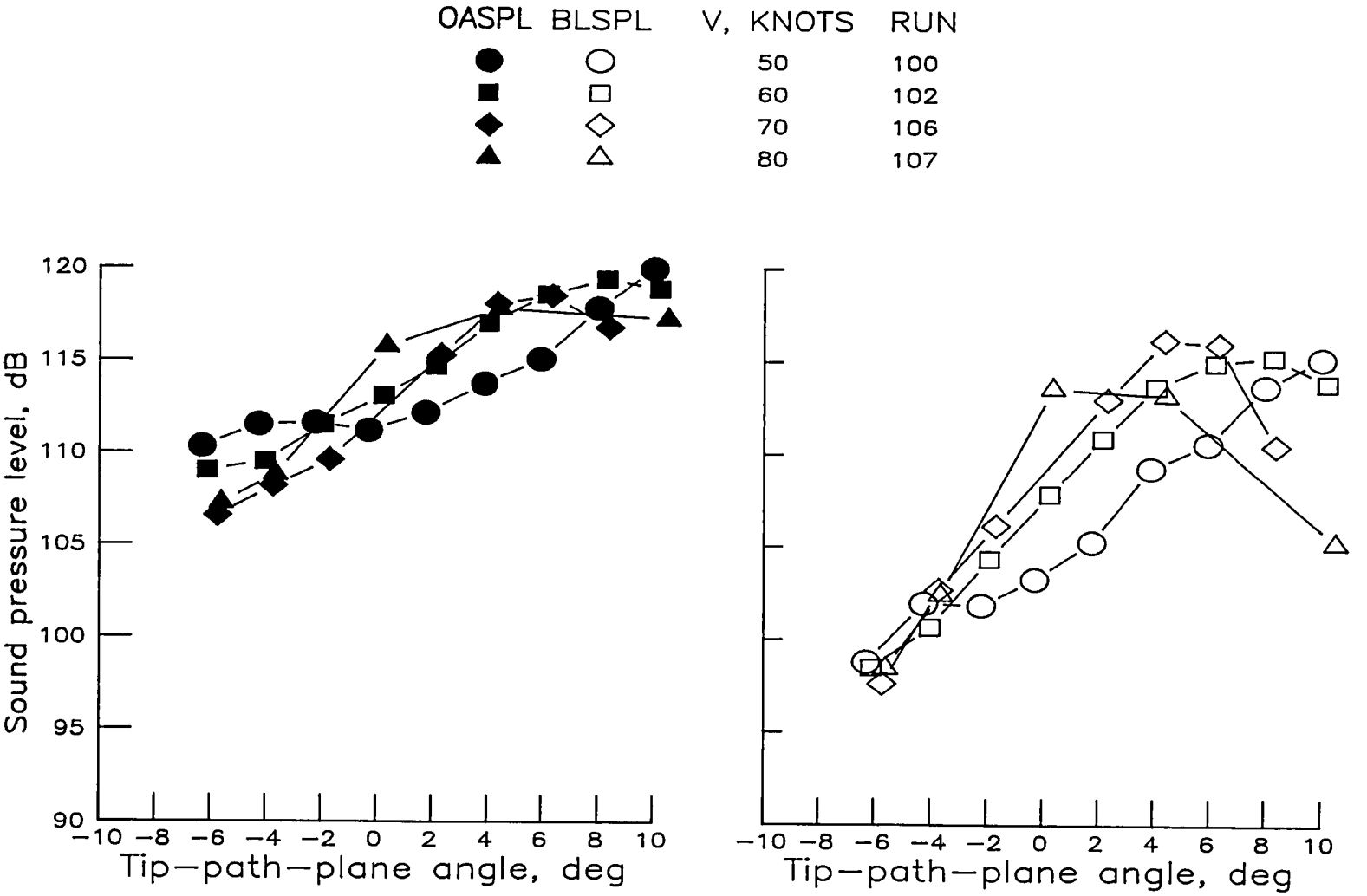

(a) High-twist standard tip (fig. 18(a)).

Figure A2.- Overall and band-limited sound pressure levels as a function of tip-path-plane angle over velocity range from 50 to 80 knots for microphone 2.

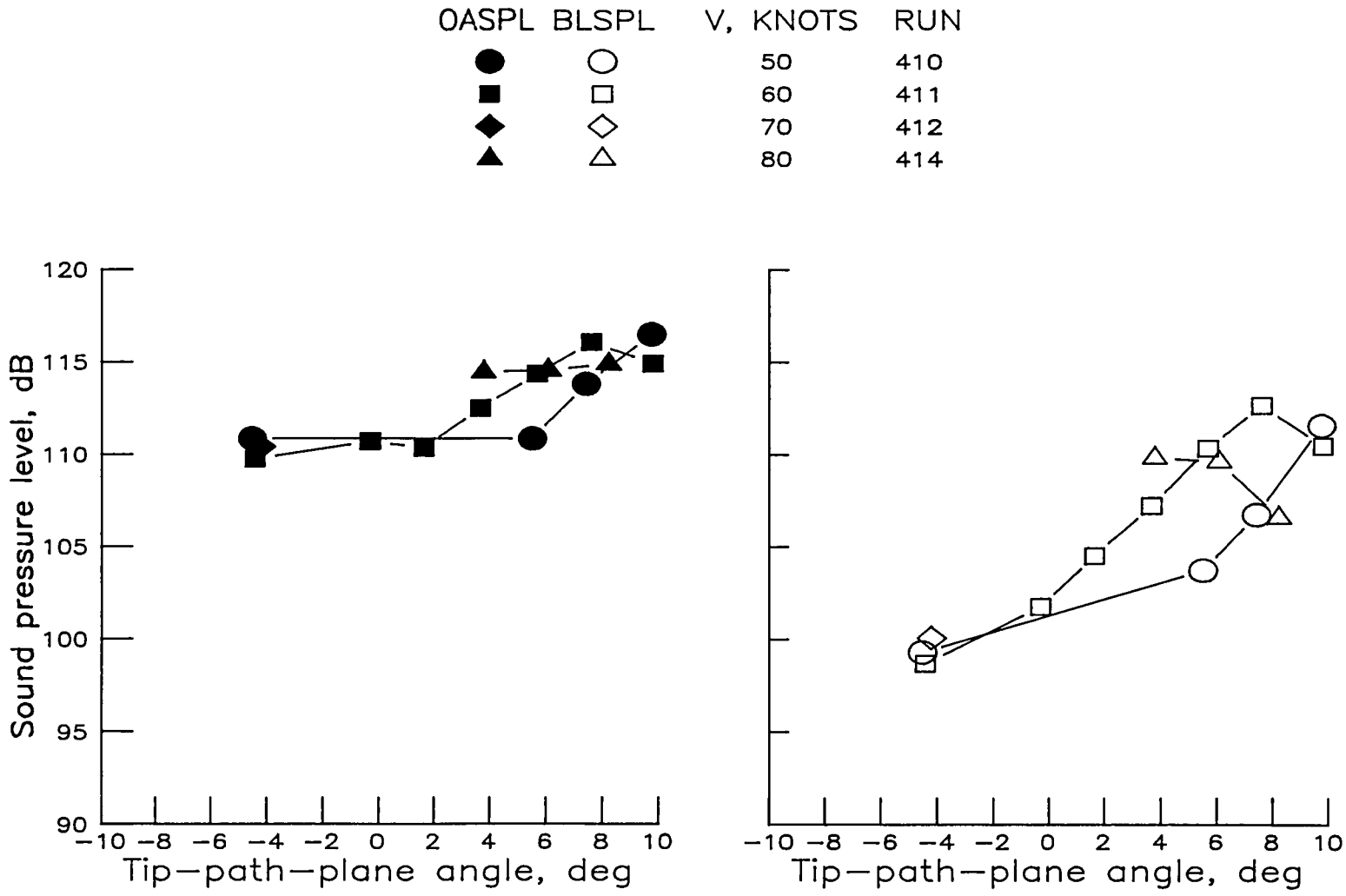

(b) High-twist swept tapered tip (SC1095 airfoil).

Figure A2.- Continued.

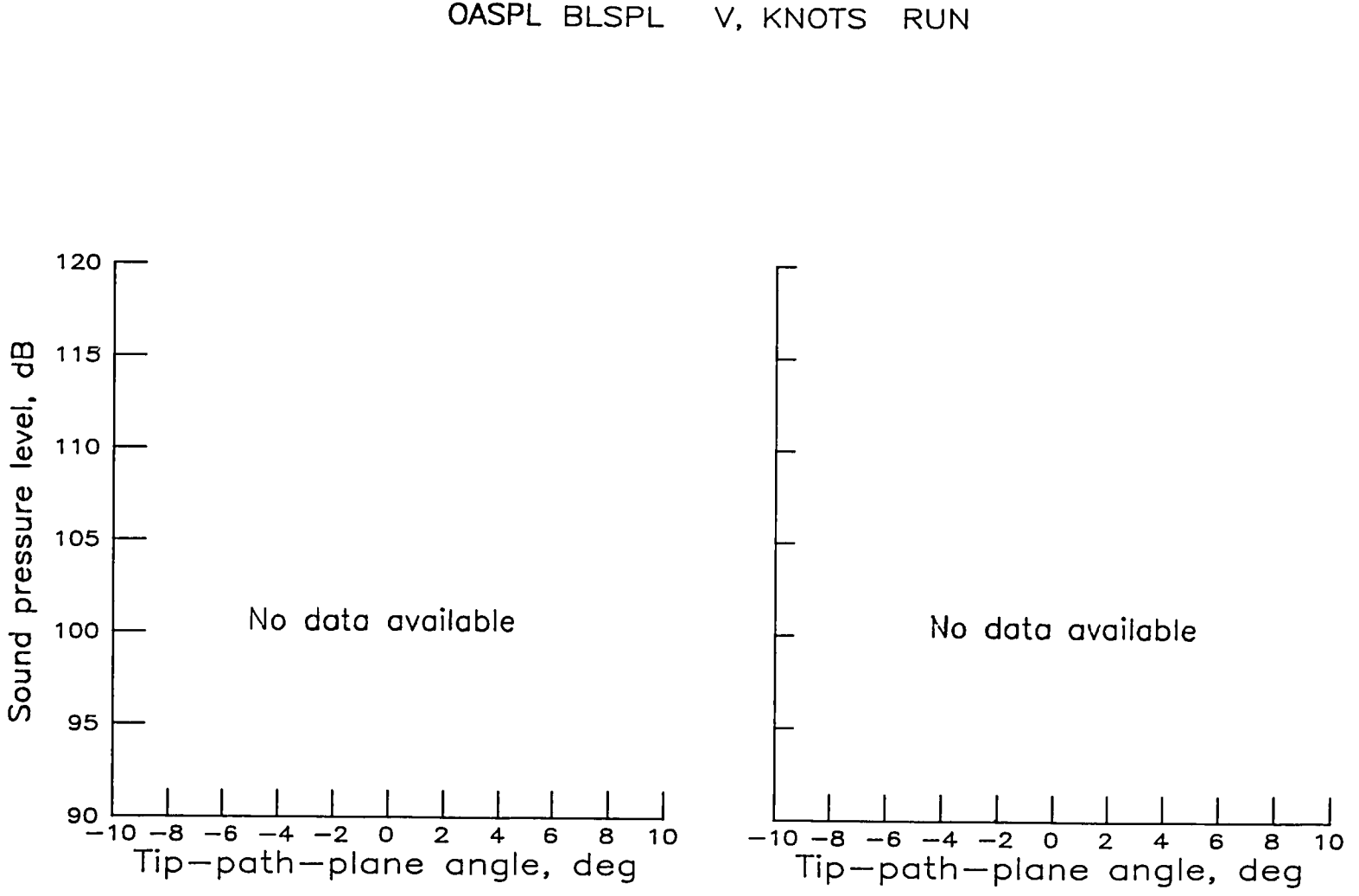

(c) High-twist swept tapered tip (SSC-A07 airfoil).

Figure A2.- Continued.

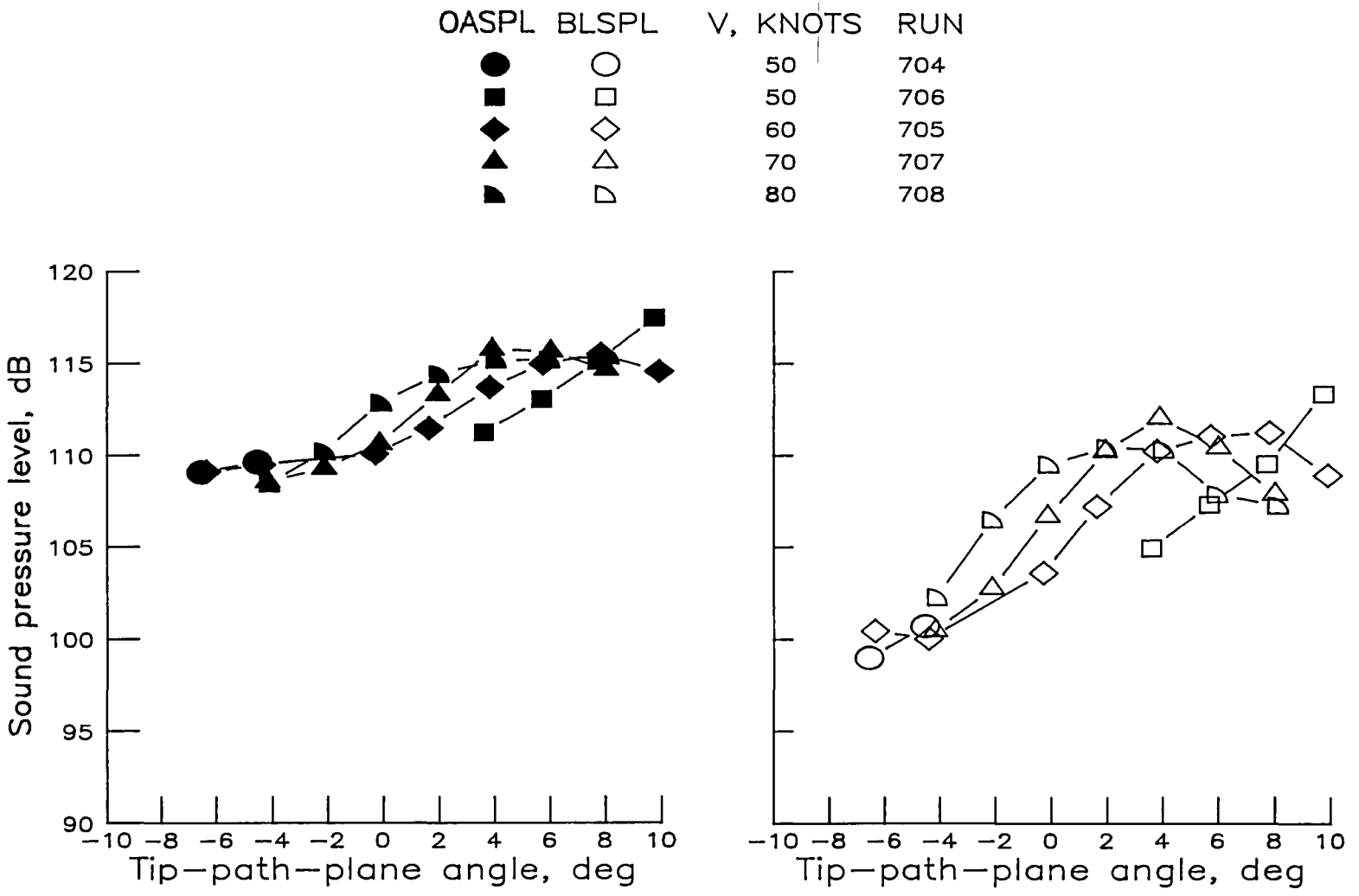

(d) High-twist parabolic tip.

Figure A2.- Continued.

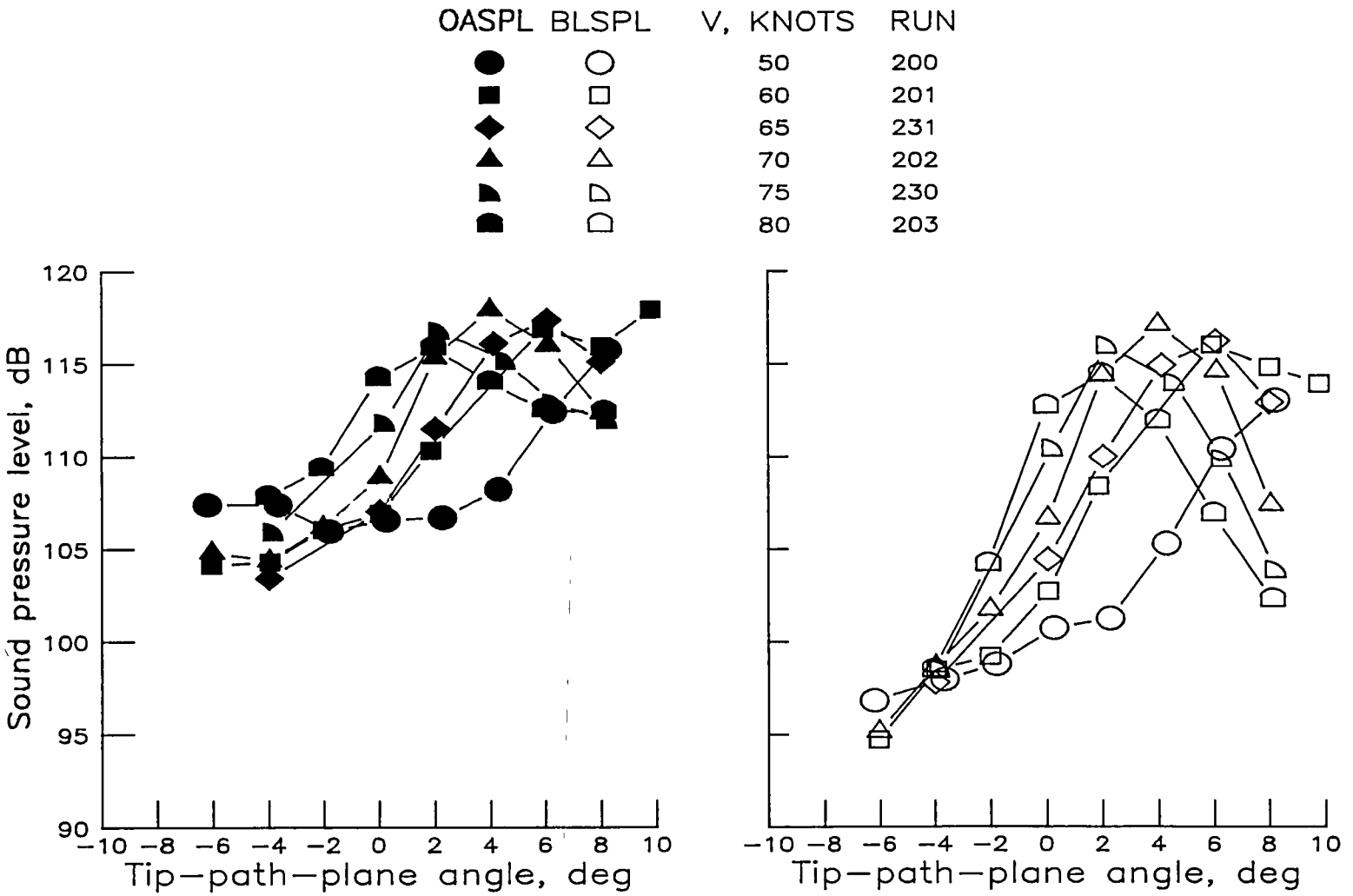

(e) Low-twist standard tip (fig. 18(b)).

Figure A2.- Continued.

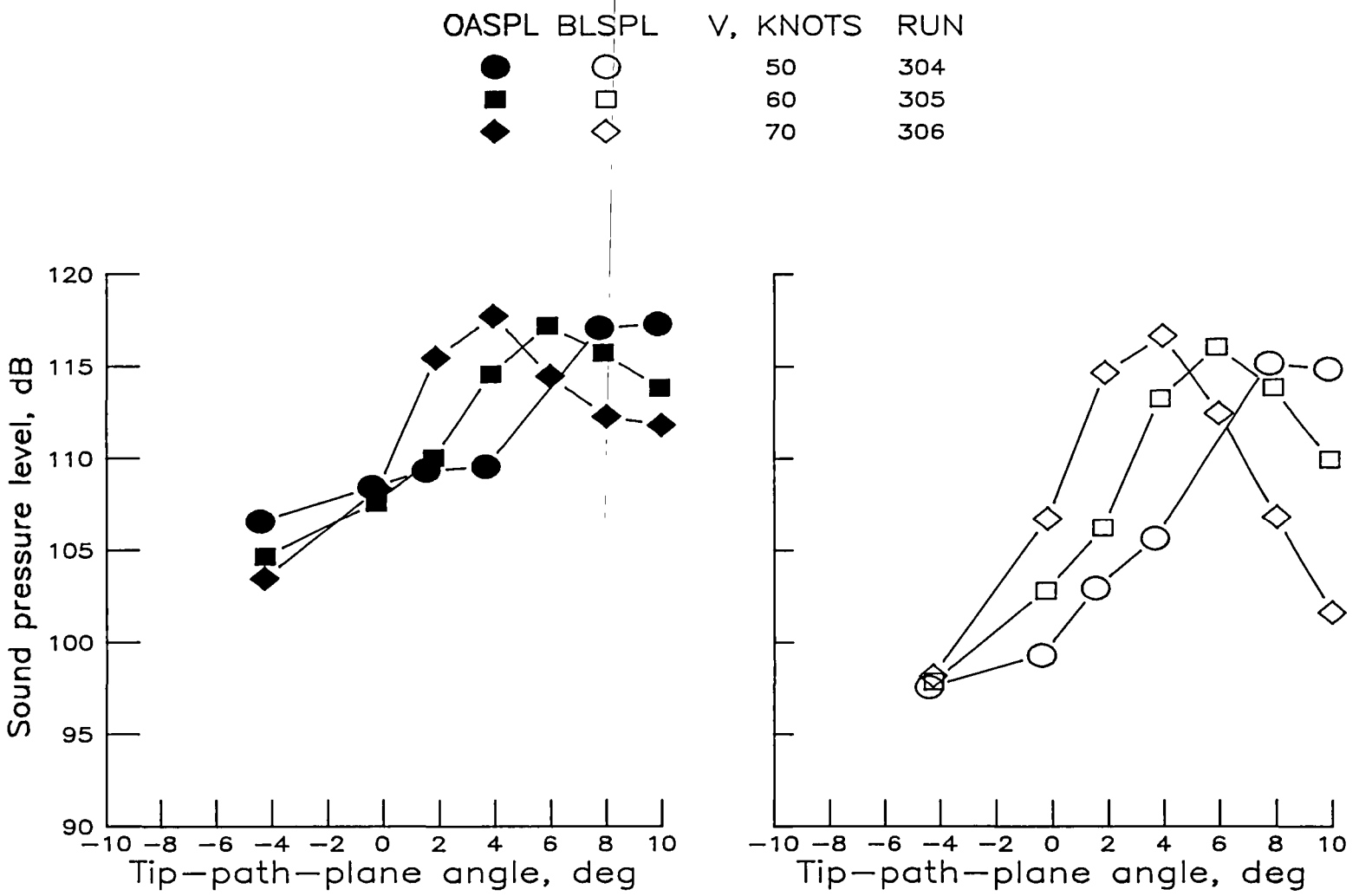

(f) Low-twist anhedral tip.

Figure A2.- Continued.

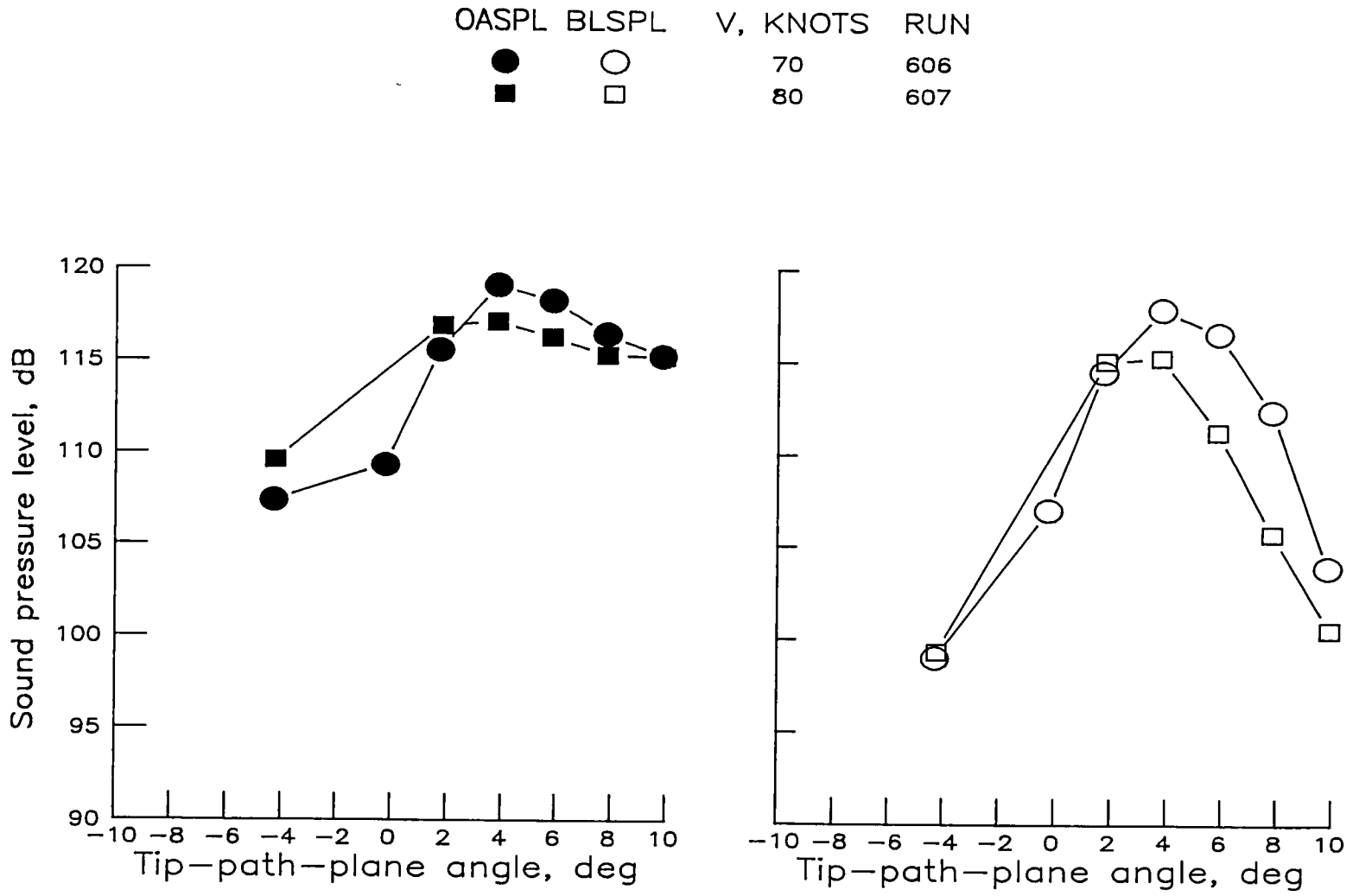

(g) Low-twist swept tip.

Figure A2.- Continued.

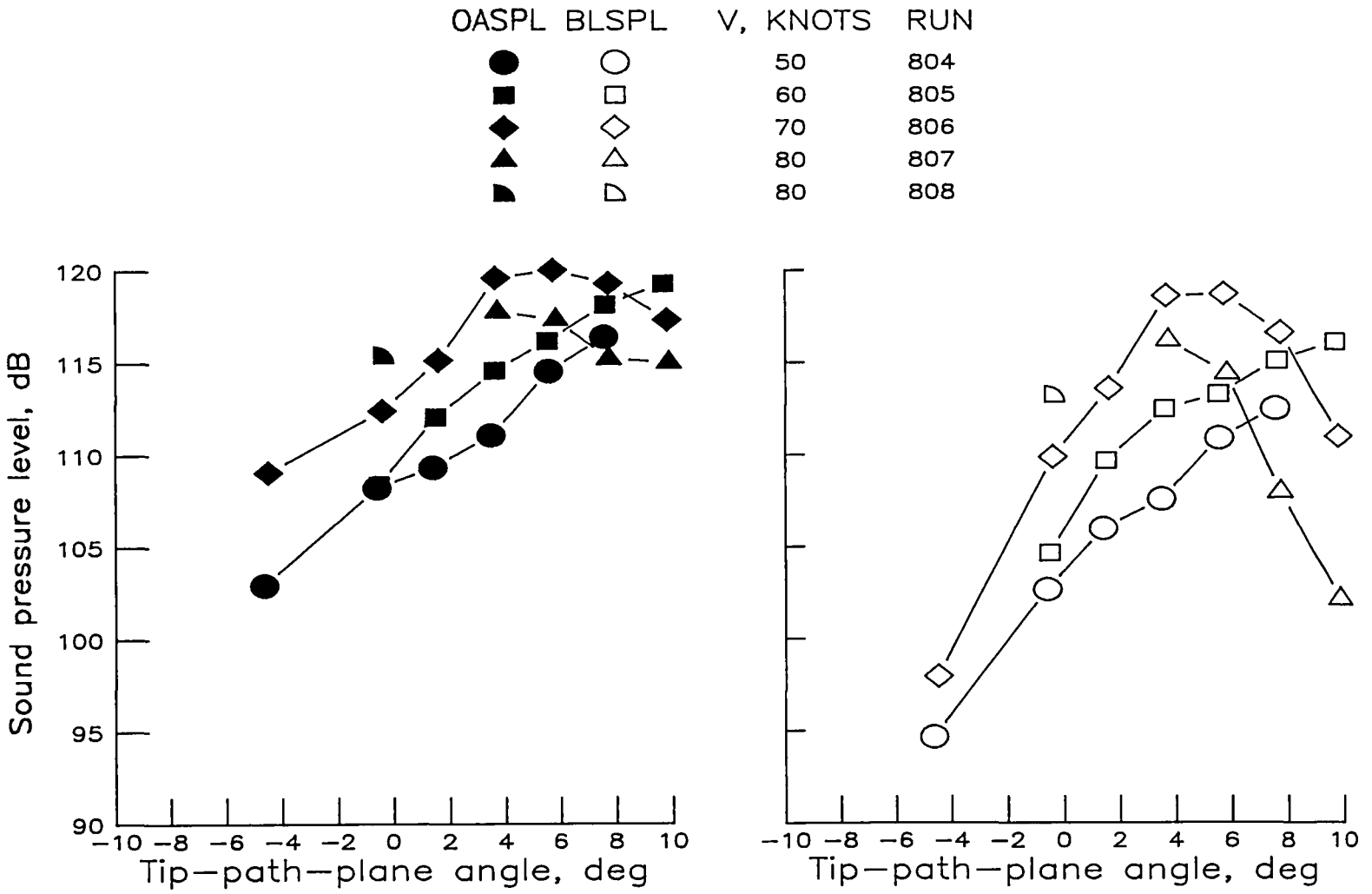

(h) Low-twist tapered tip.

Figure A2.- Continued.

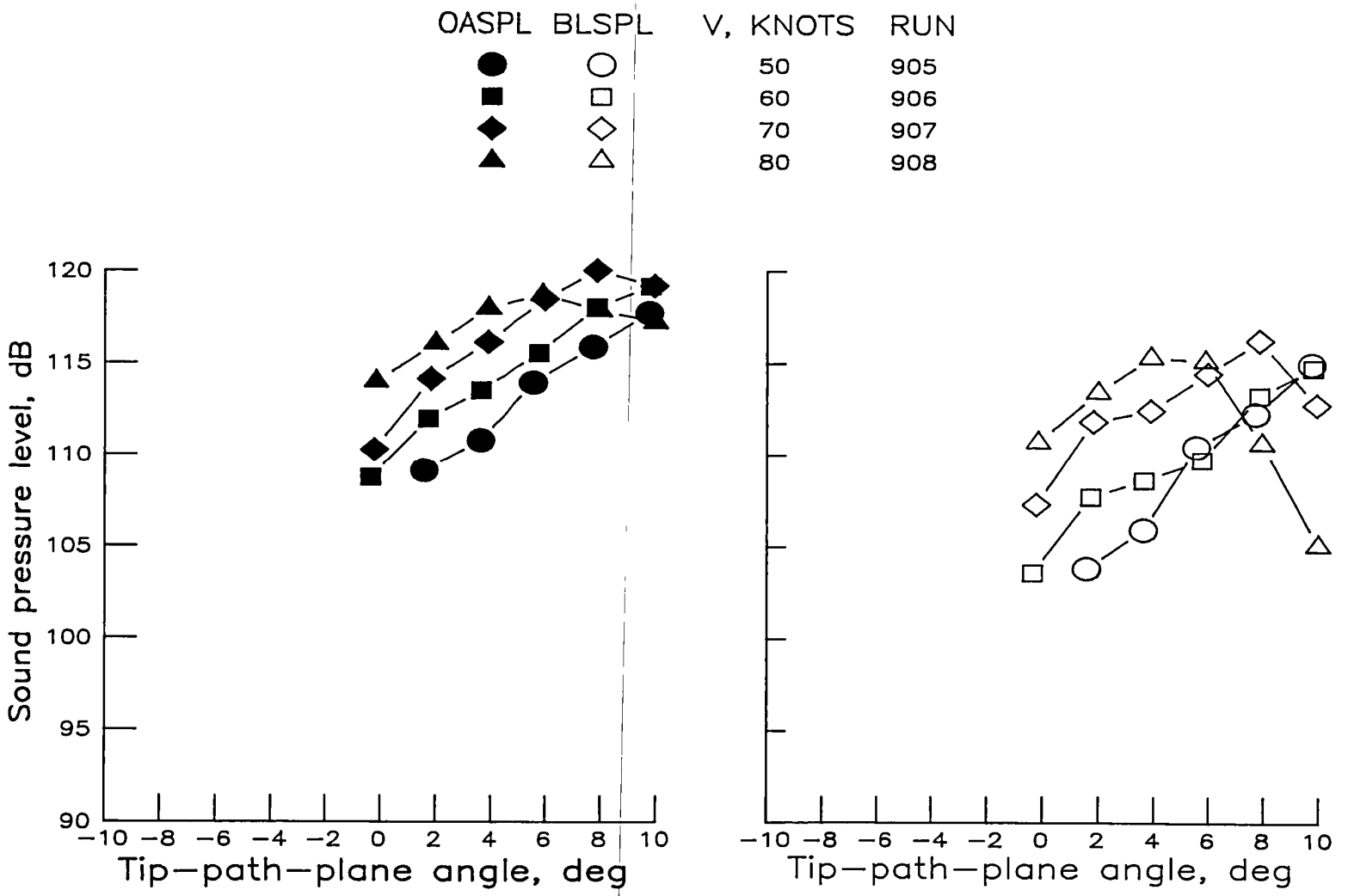

(i) Low-twist square tip.

Figure A2.- Concluded.

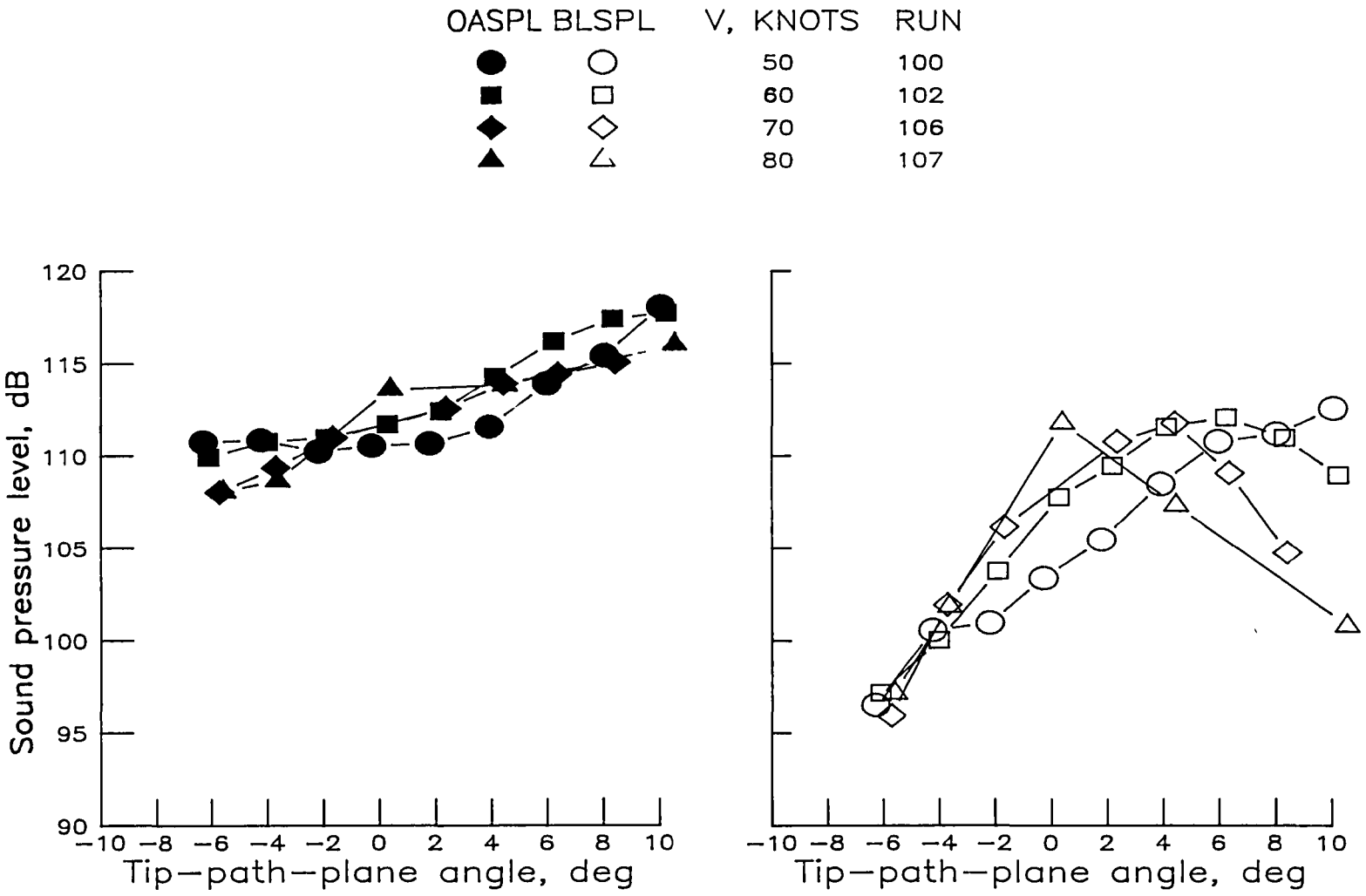

(a) High-twist standard tip (fig. 19(a)).

Figure A3.- Overall and band-limited sound pressure levels as a function of tip-path-plane angle over velocity range from 50 to 80 knots for microphone 3.

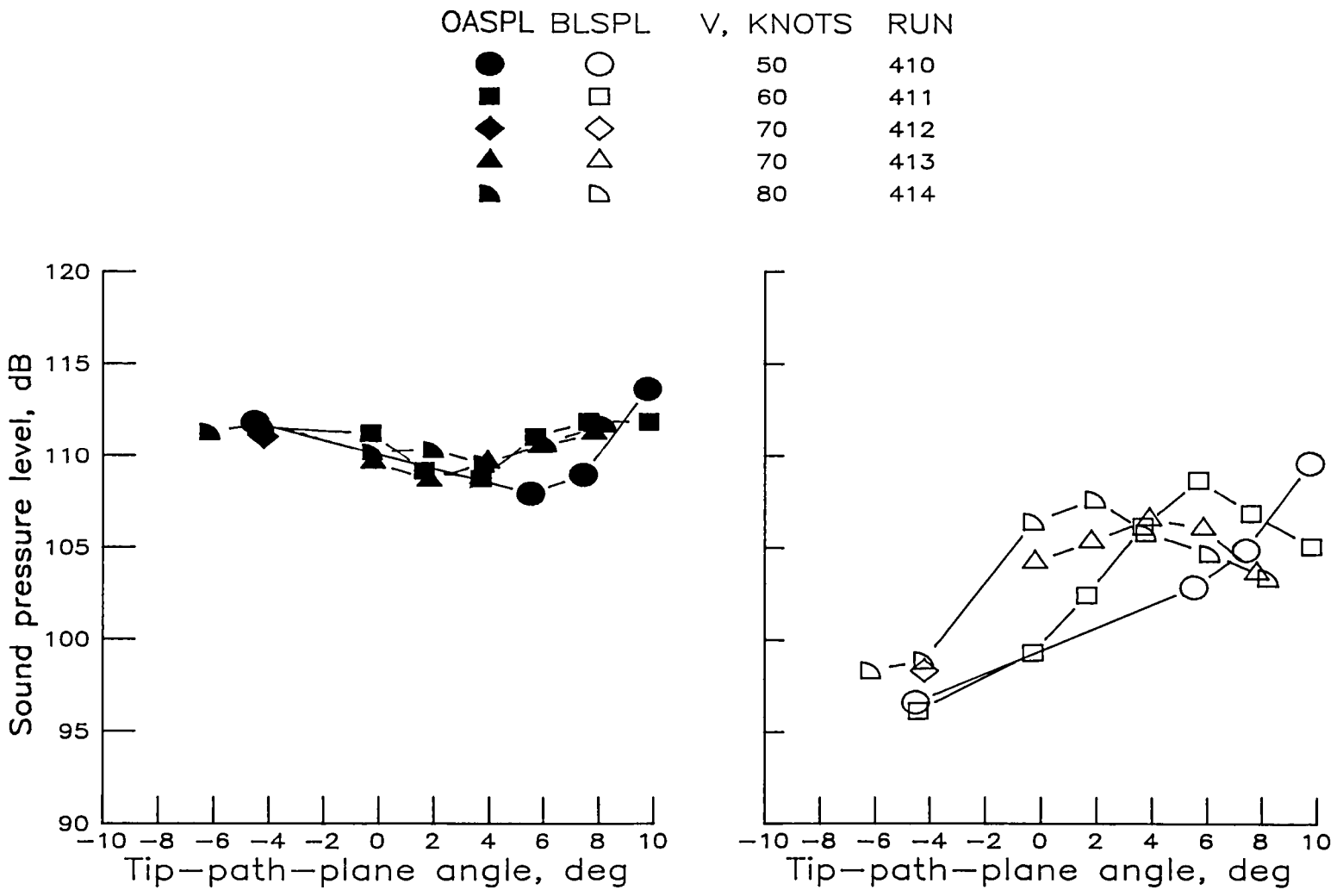

(b) High-twist swept tapered tip (SC1095 airfoil).

Figure A3.- Continued.

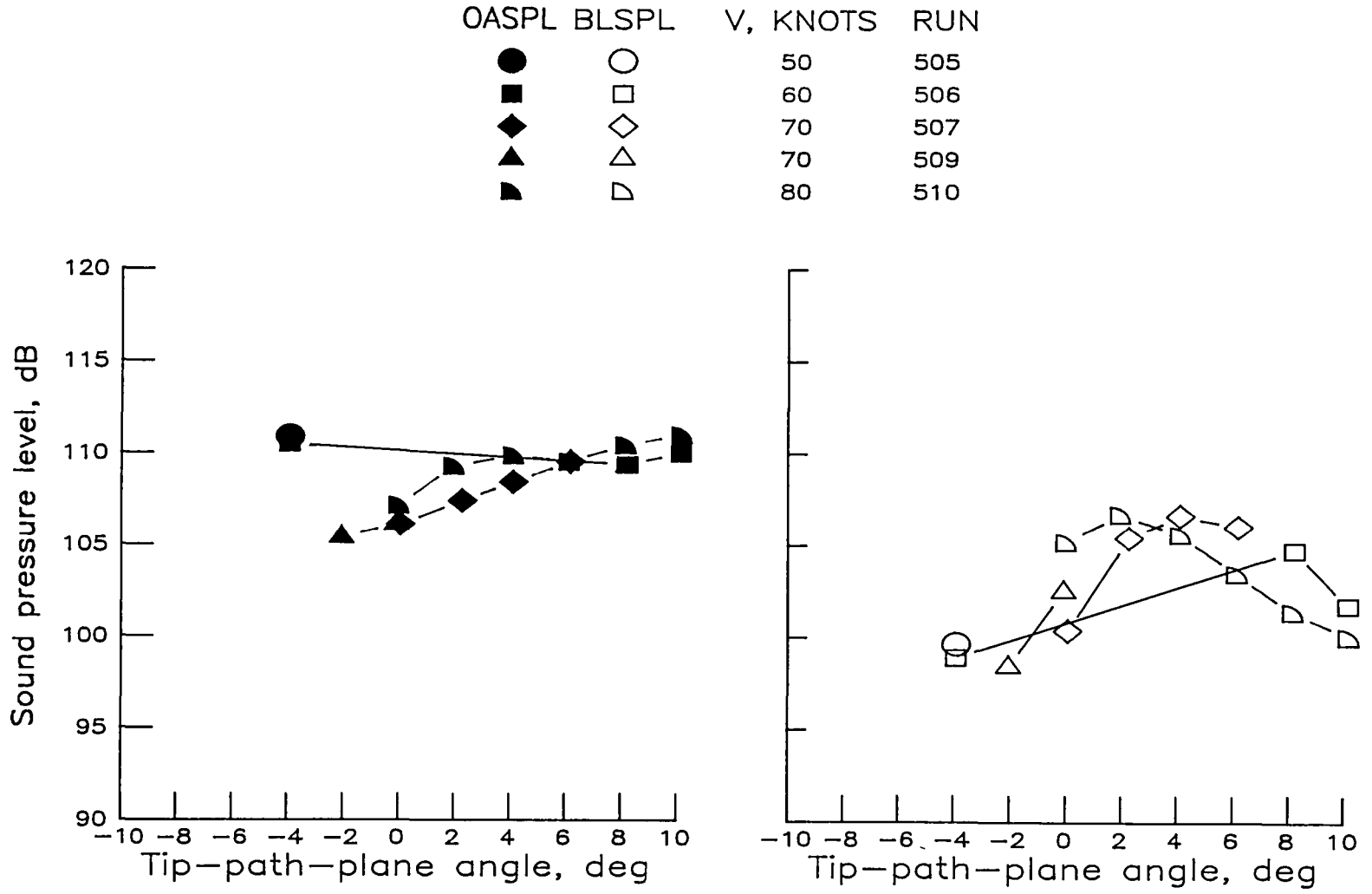

(c) High-twist swept tapered tip (SSC-A07 airfoil).

Figure A3.- Continued.

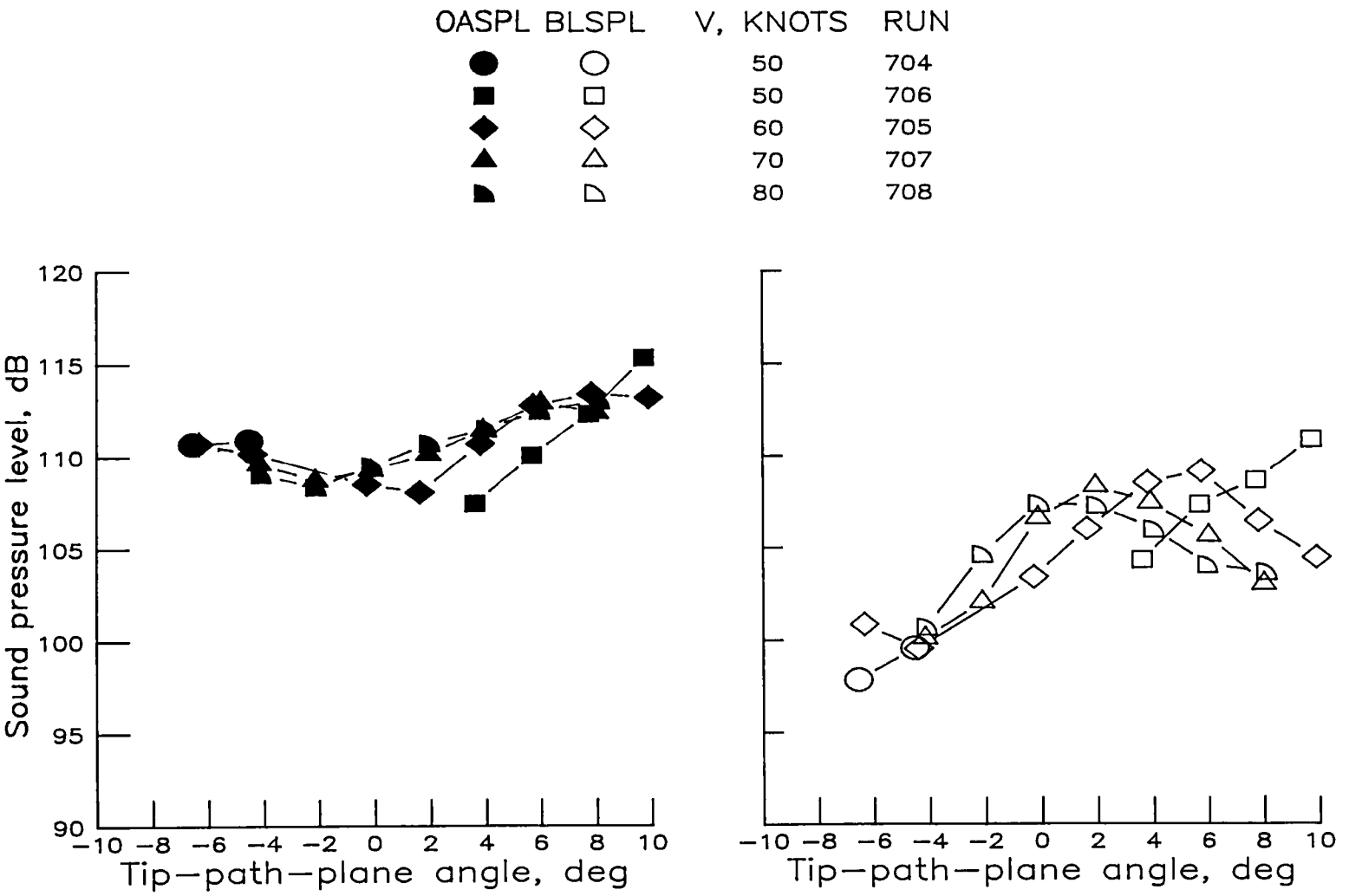

(d) High-twist parabolic tip.

Figure A3.- Continued.

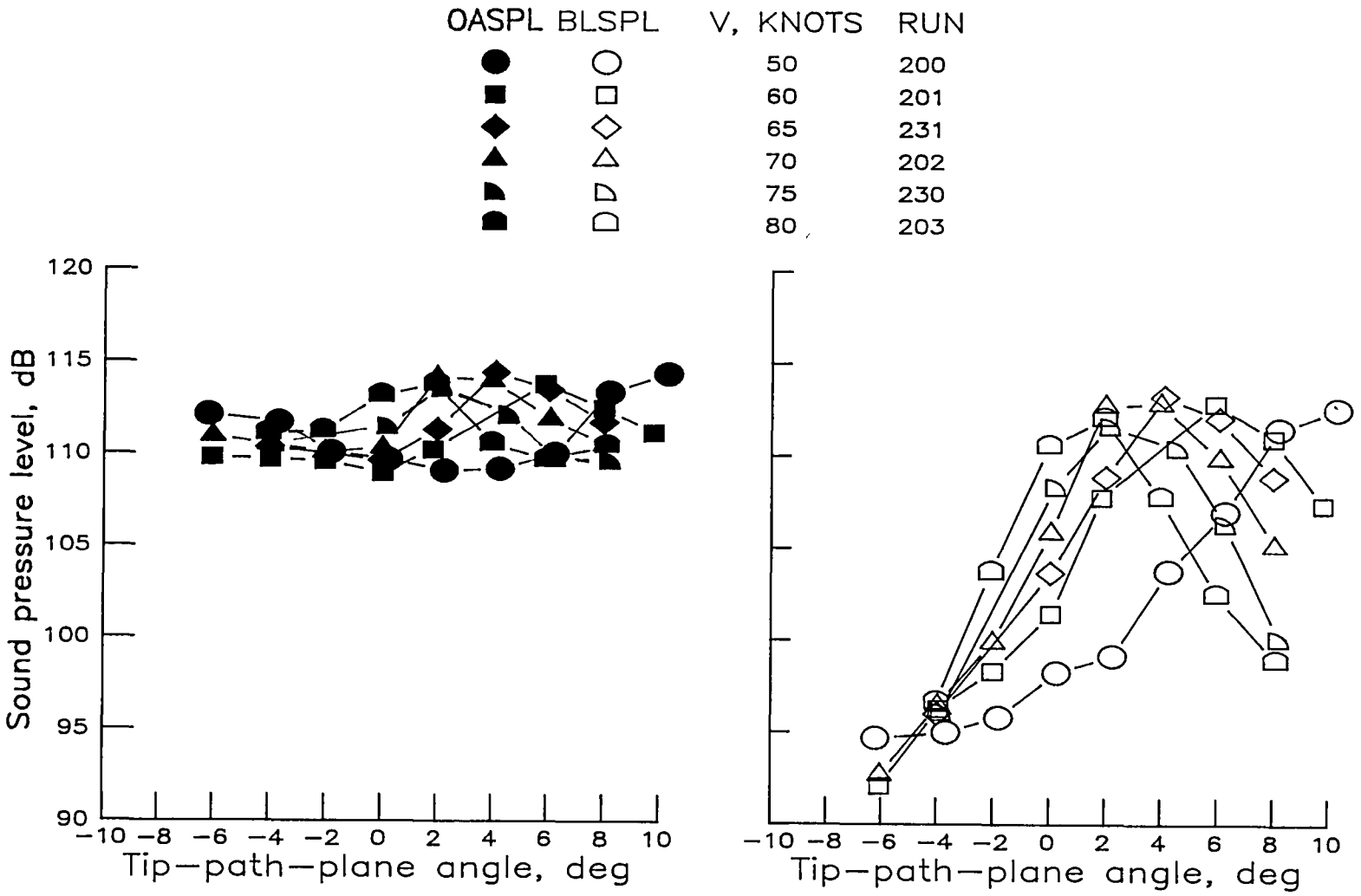

(e) Low-twist standard tip (fig. 19(b)).

Figure A3.- Continued.

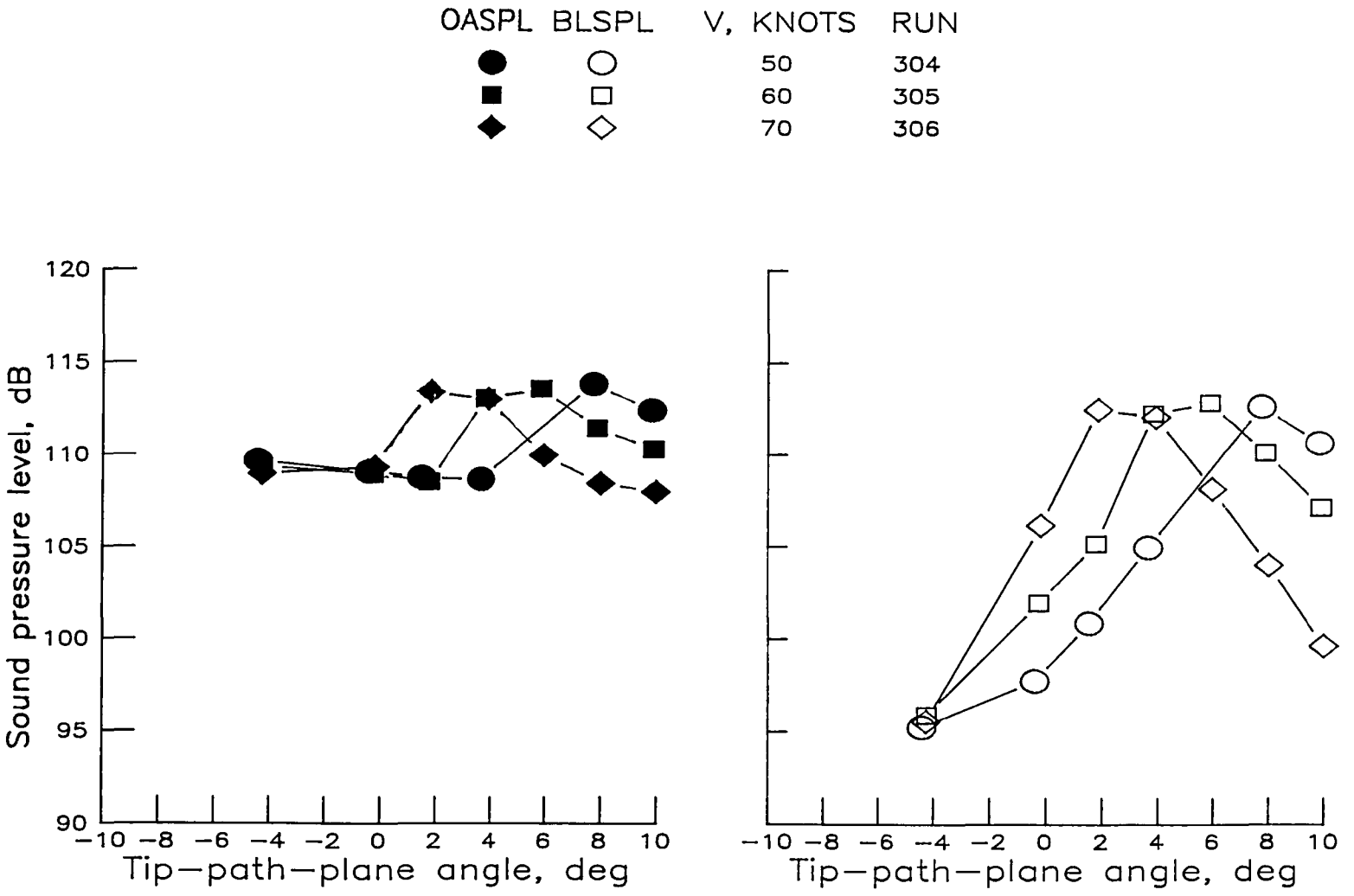

(f) Low-twist anhedral tip.

Figure A3.- Continued.

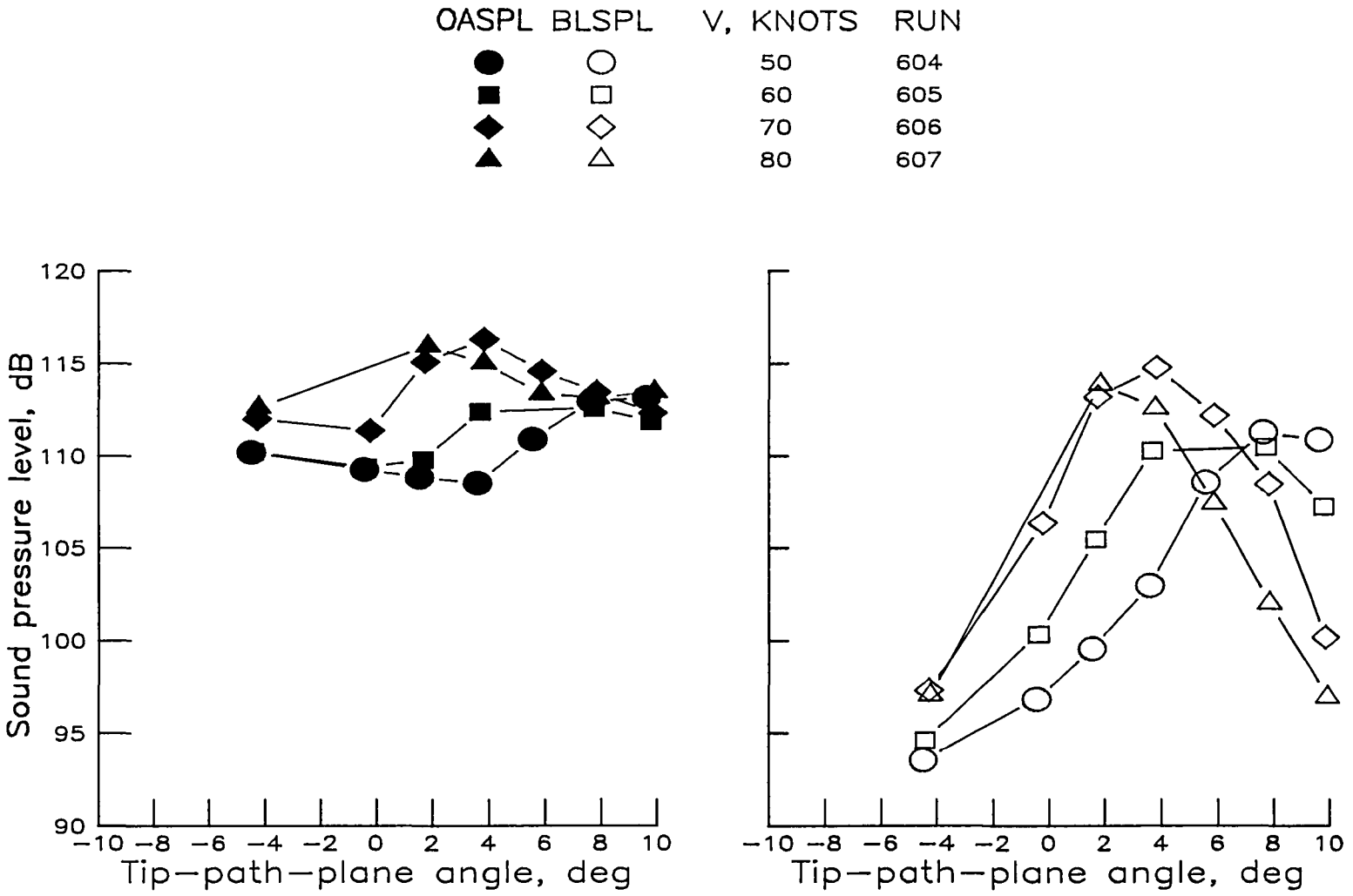

(g) Low-twist swept tip.

Figure A3.- Continued.

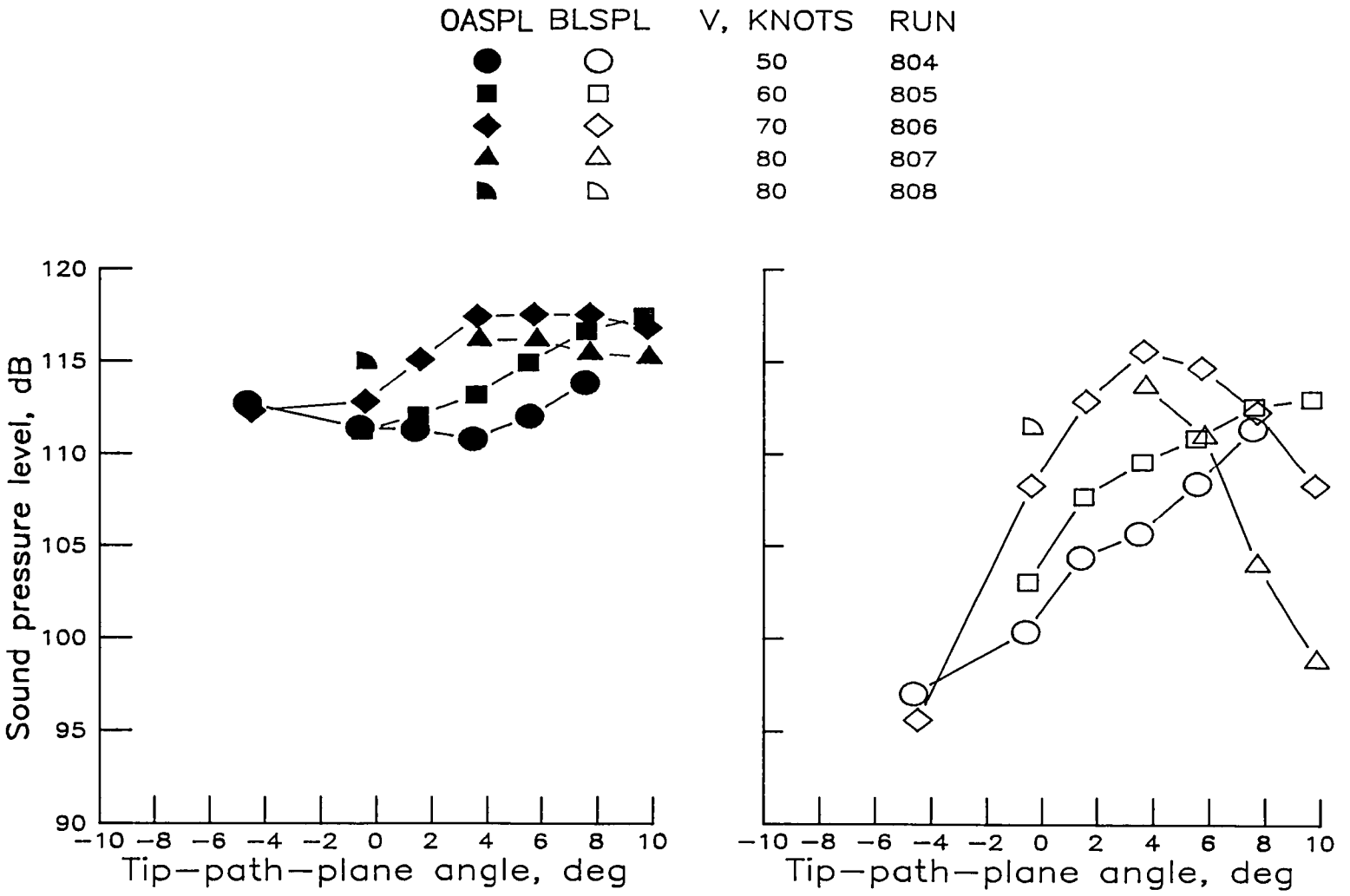

(h) Low-twist tapered tip.

Figure A3.- Continued.

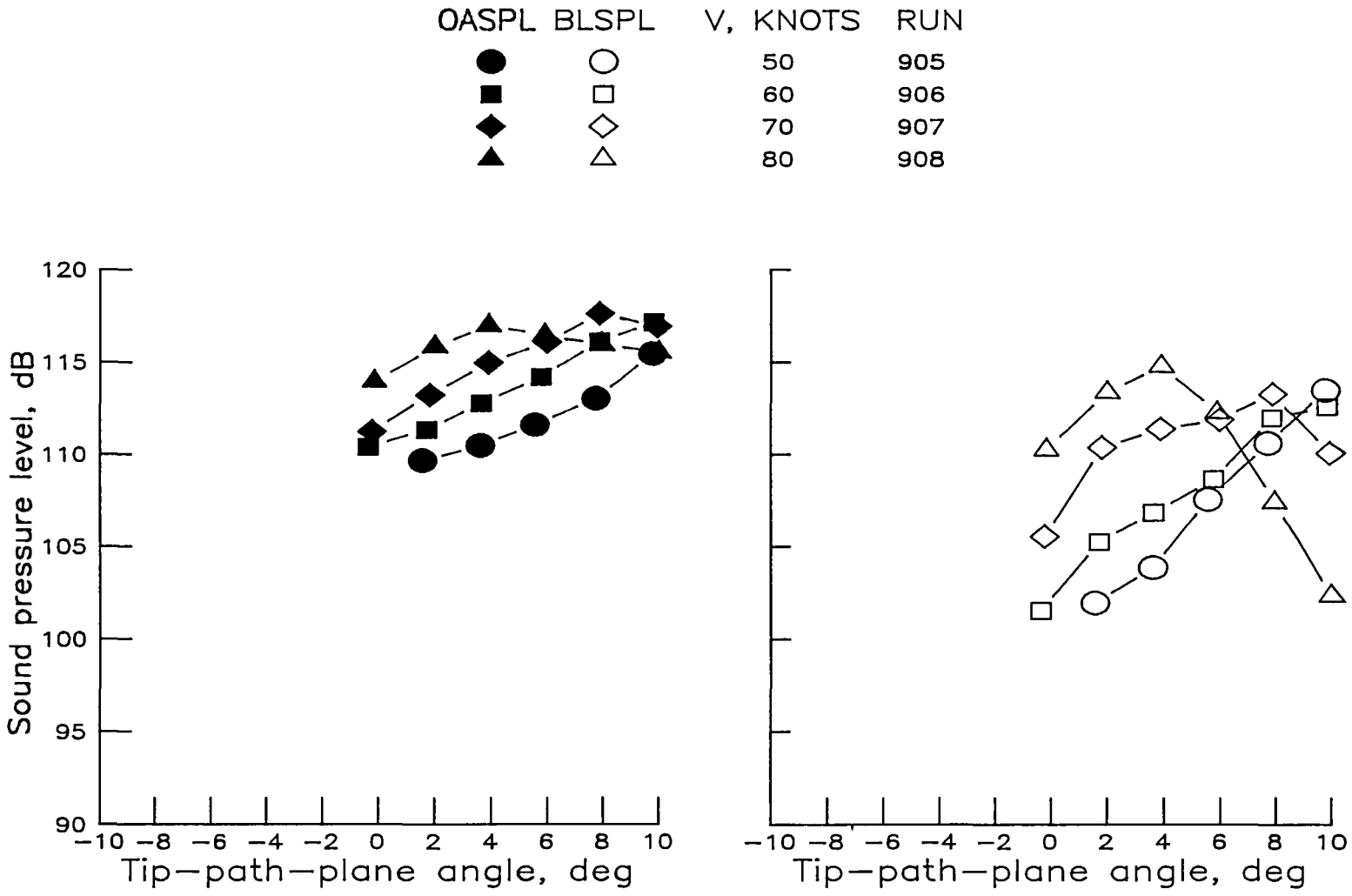

(1) Low-twist square tip.

Figure A3.- Concluded.

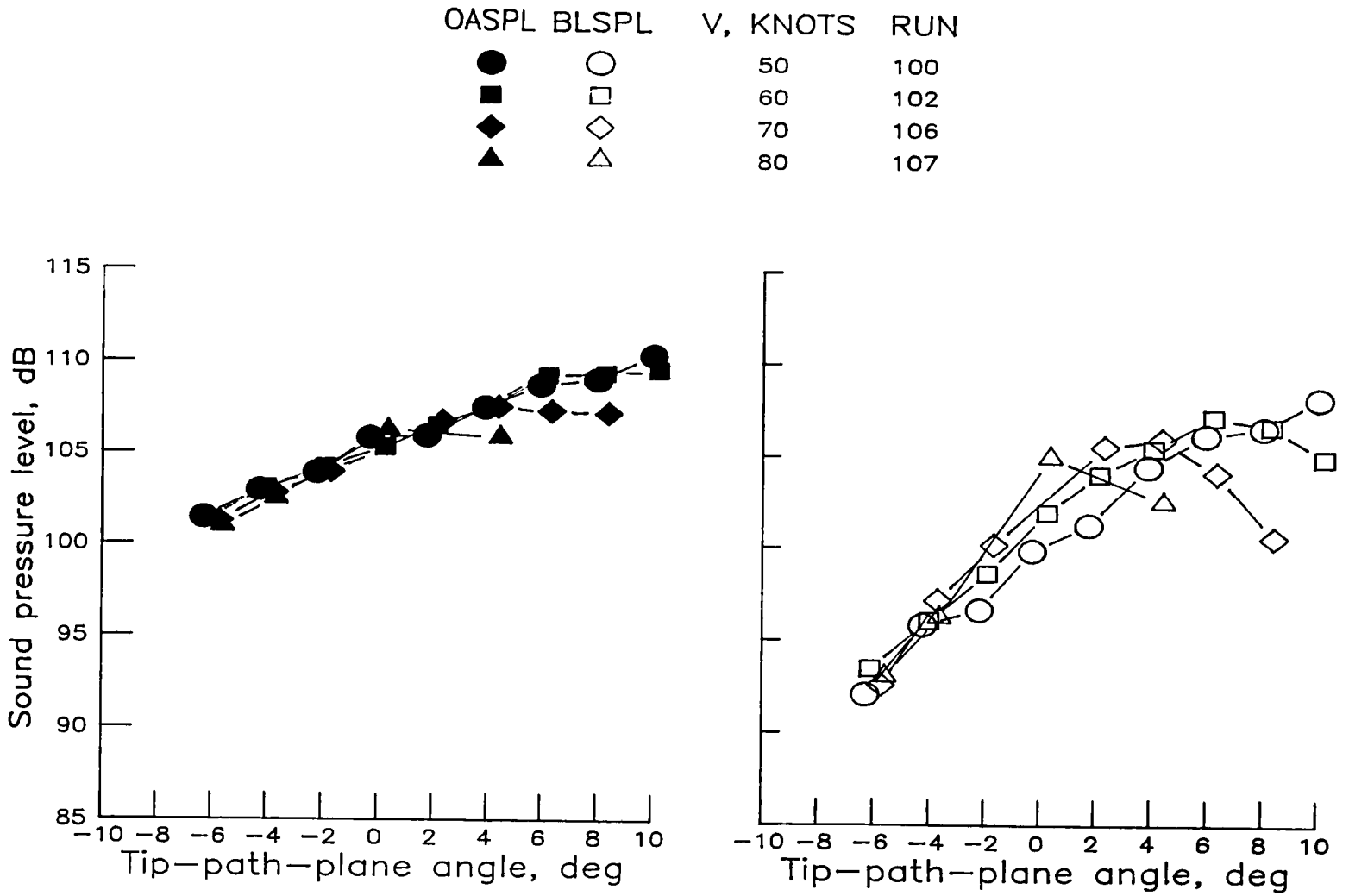

(a) High-twist standard tip (fig. 20(a)).

Figure A4.- Overall and band-limited sound pressure levels as a function of tip-path-plane angle over velocity range from 50 to 80 knots for microphone 4.

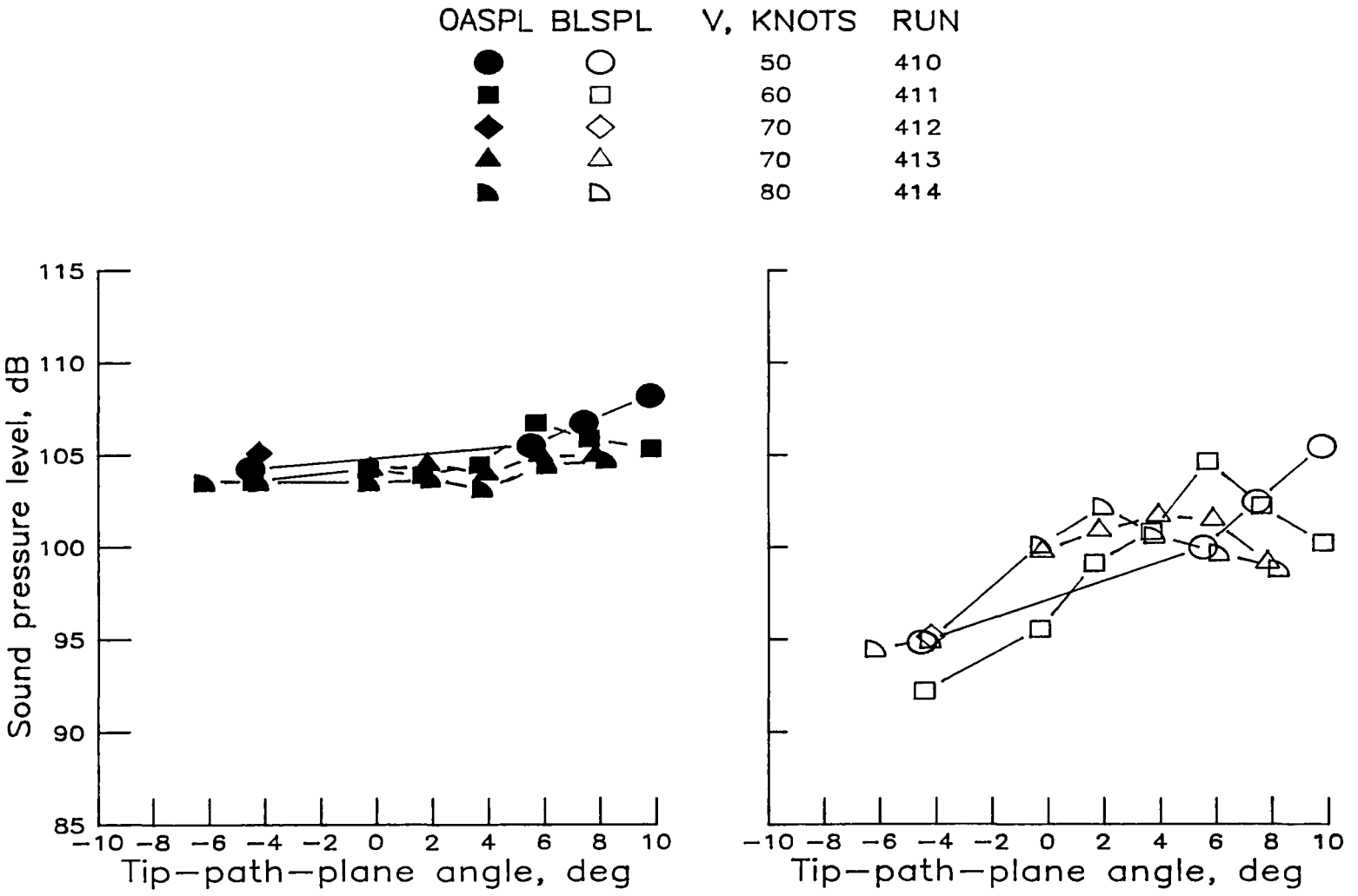

(b) High-twist swept tapered tip (SC1095 airfoil).

Figure A4.- Continued.

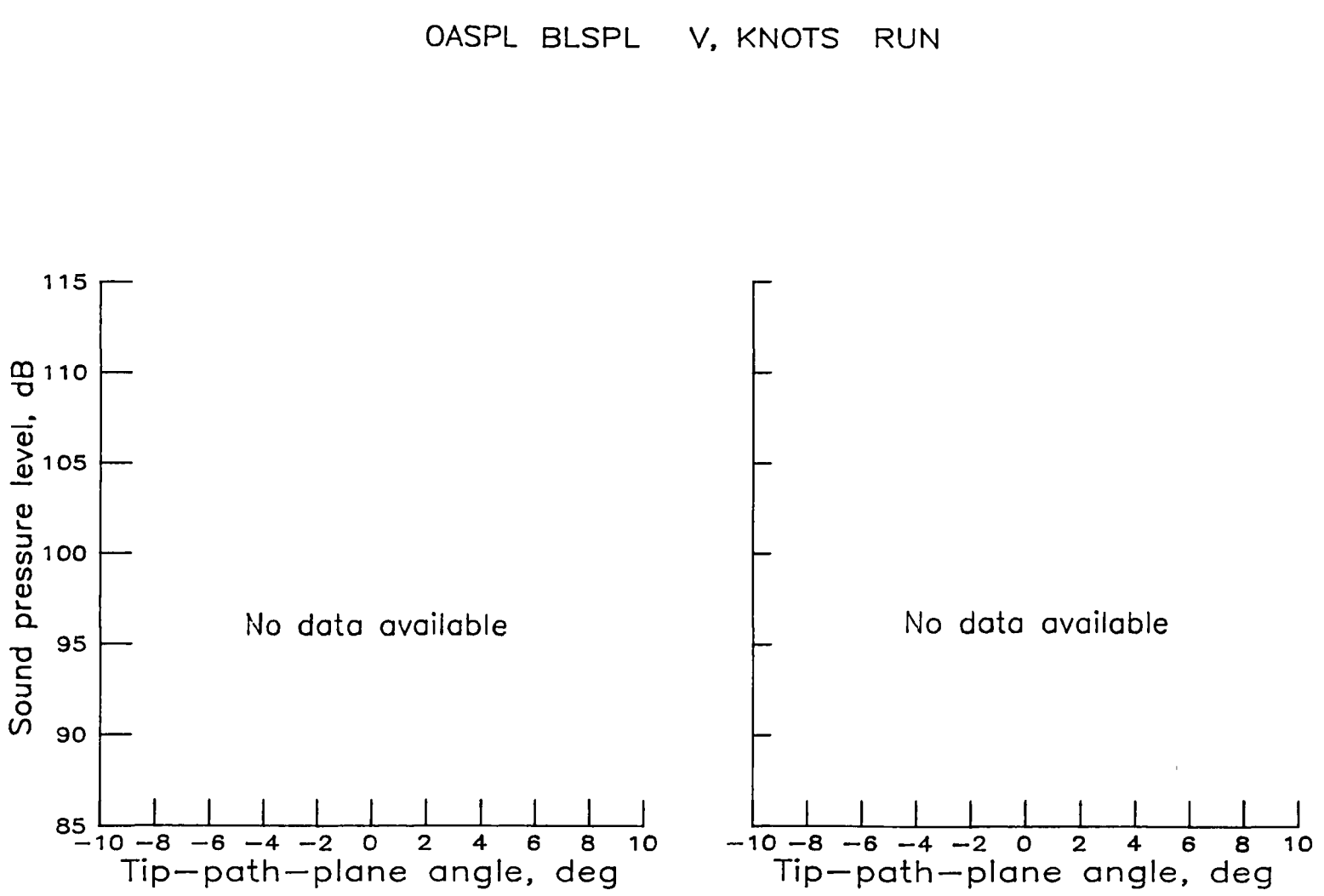

(c) High-twist swept tapered tip (SSC-A07 airfoil).

Figure A4.- Continued.

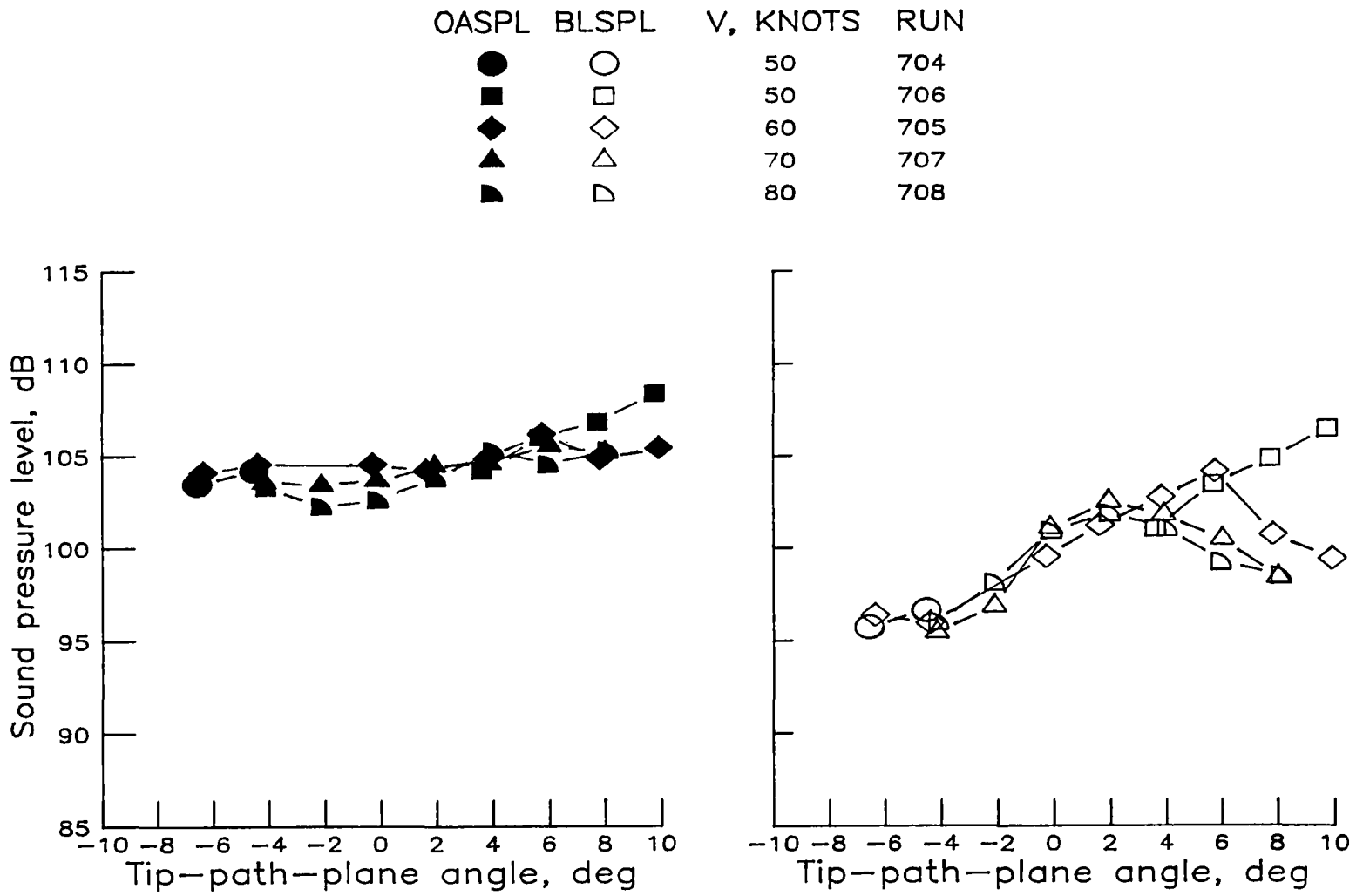

(d) High-twist parabolic tip.

Figure A4.- Continued.

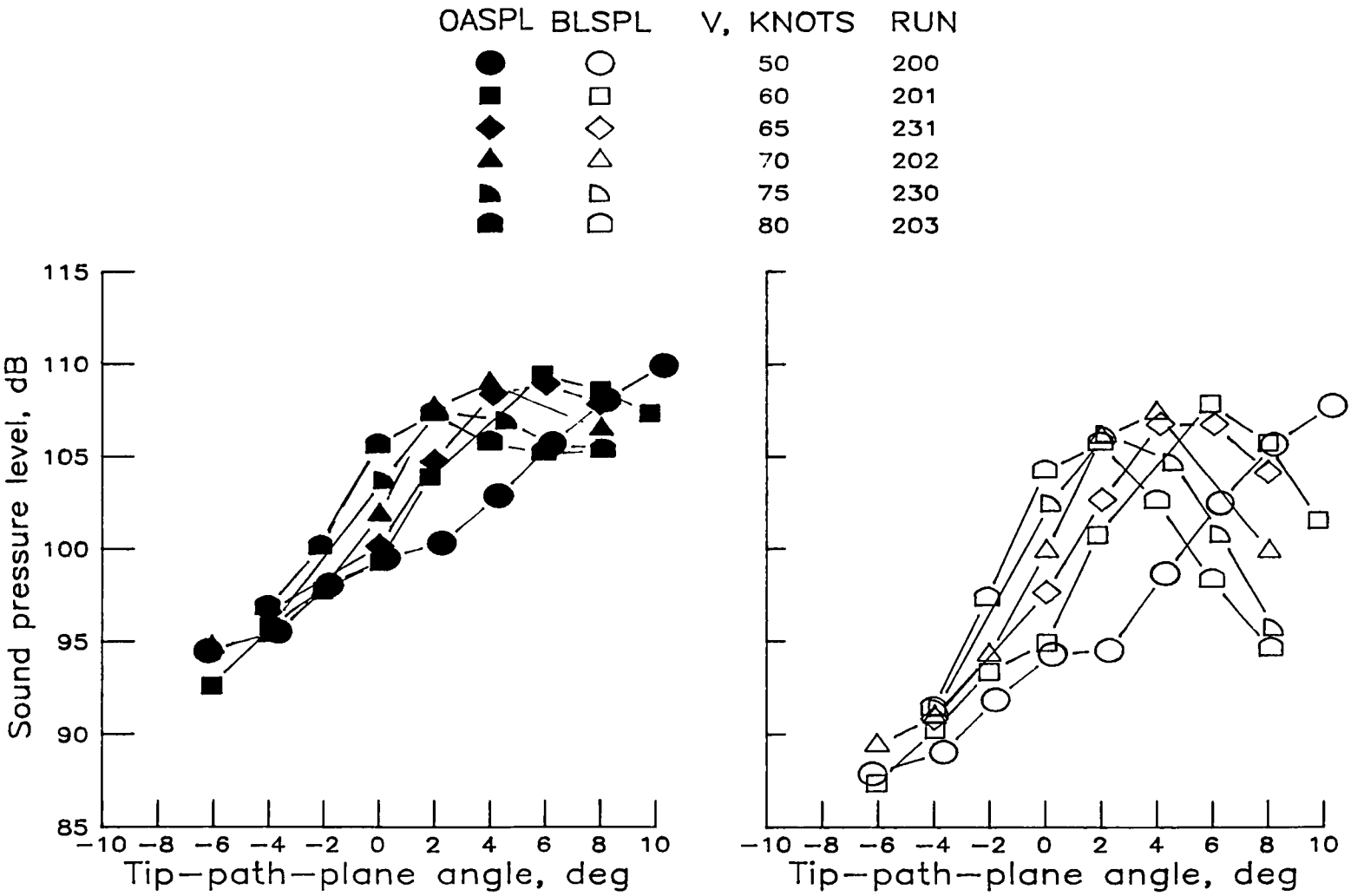

(e) Low-twist standard tip (fig. 20(b)).

Figure A4.- Continued.

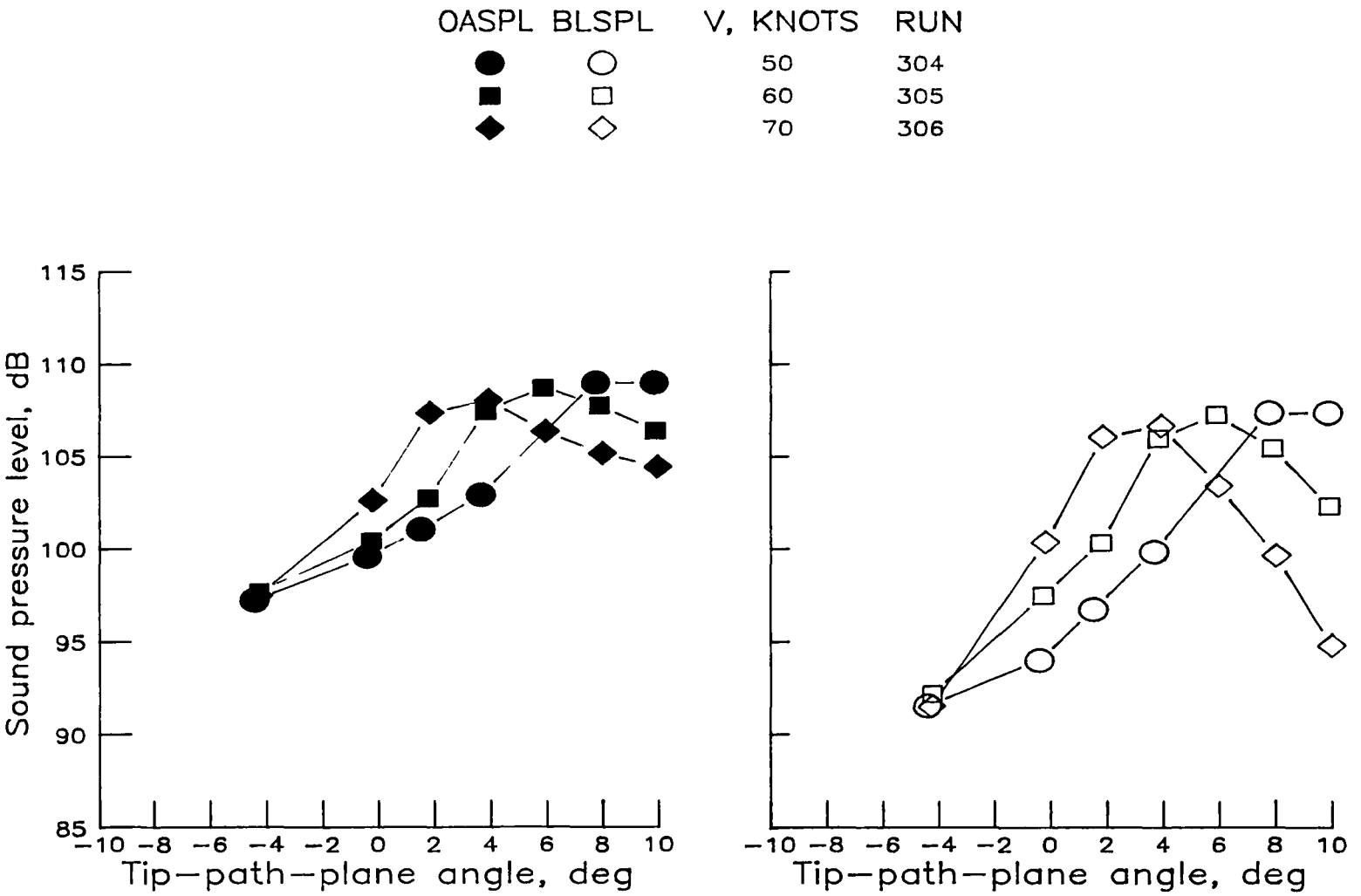

(f) Low-twist anhedral tip.

Figure A4.- Continued.

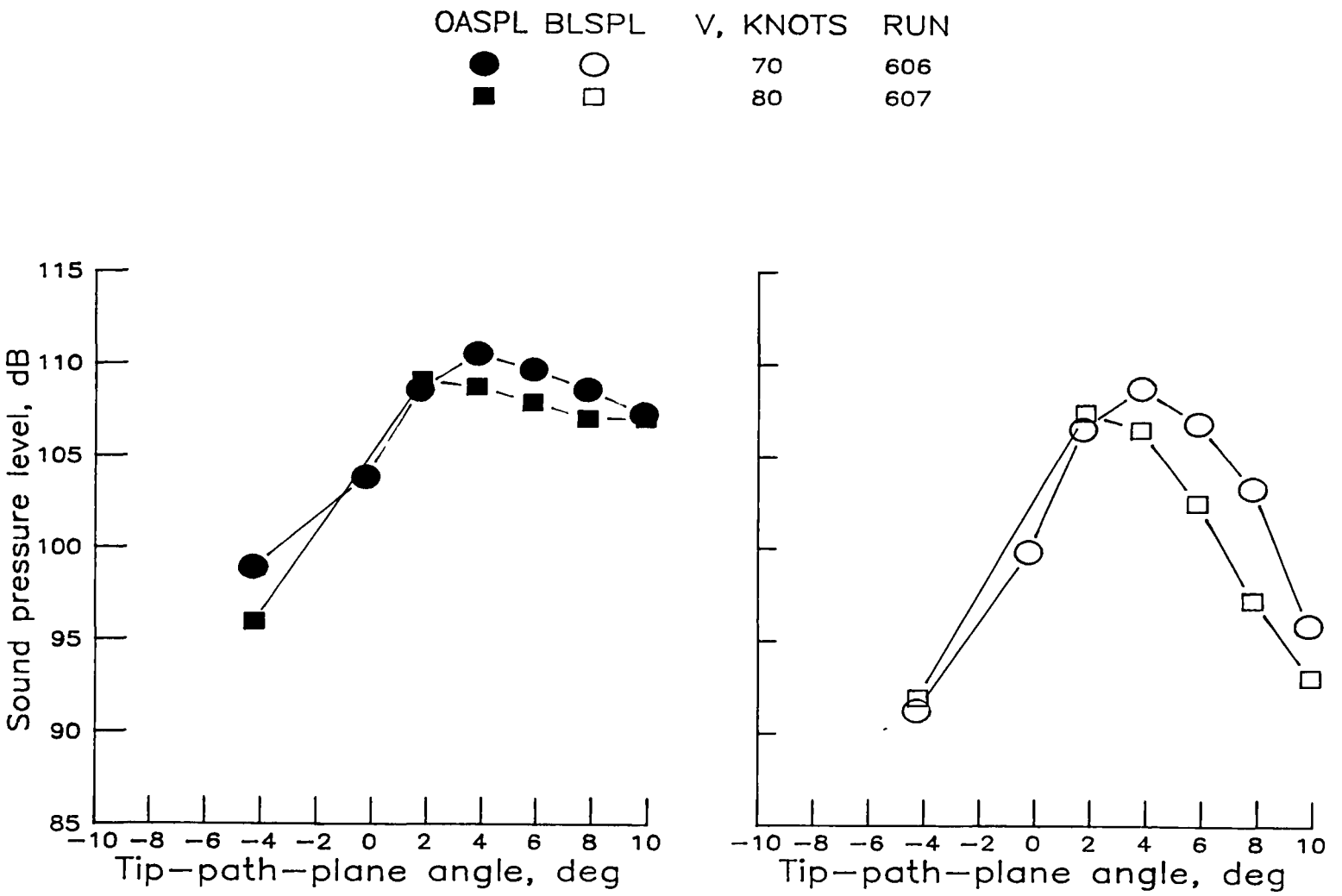

(g) Low-twist swept tip.

Figure A4.- Continued.

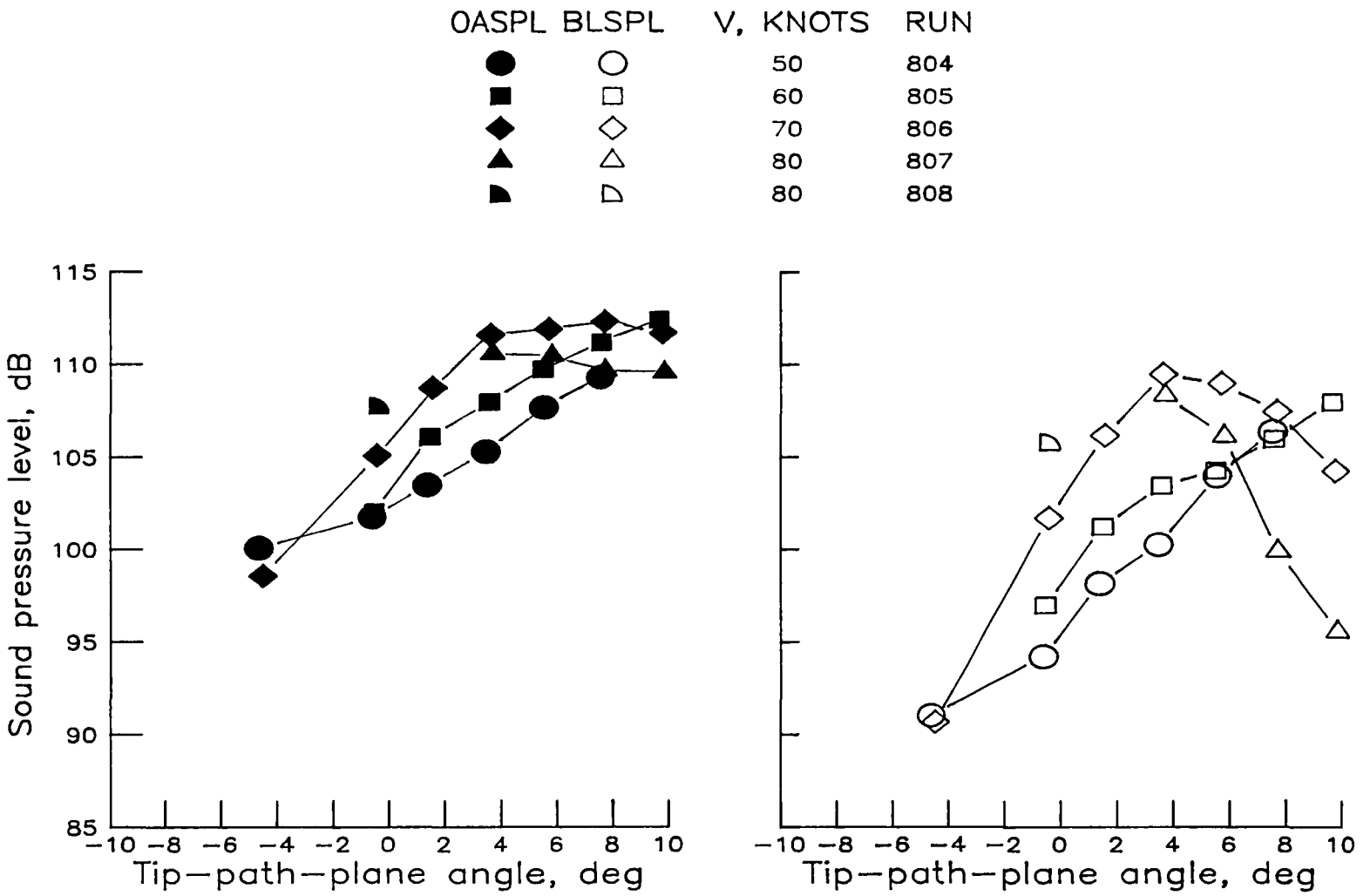

(h) Low-twist tapered tip.

Figure A4.- Continued.

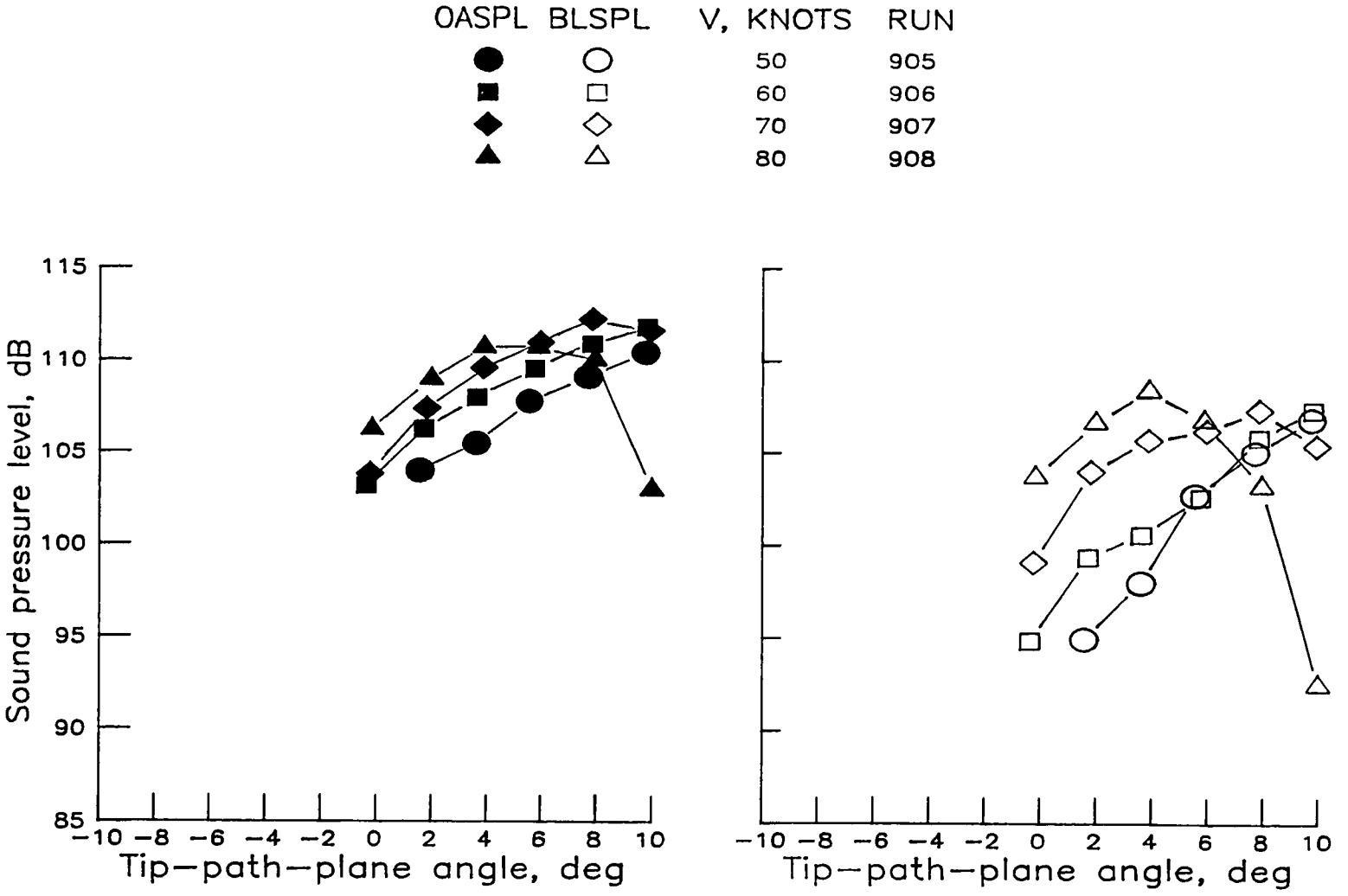

(i) Low-twist square tip.

Figure A4.- Concluded.

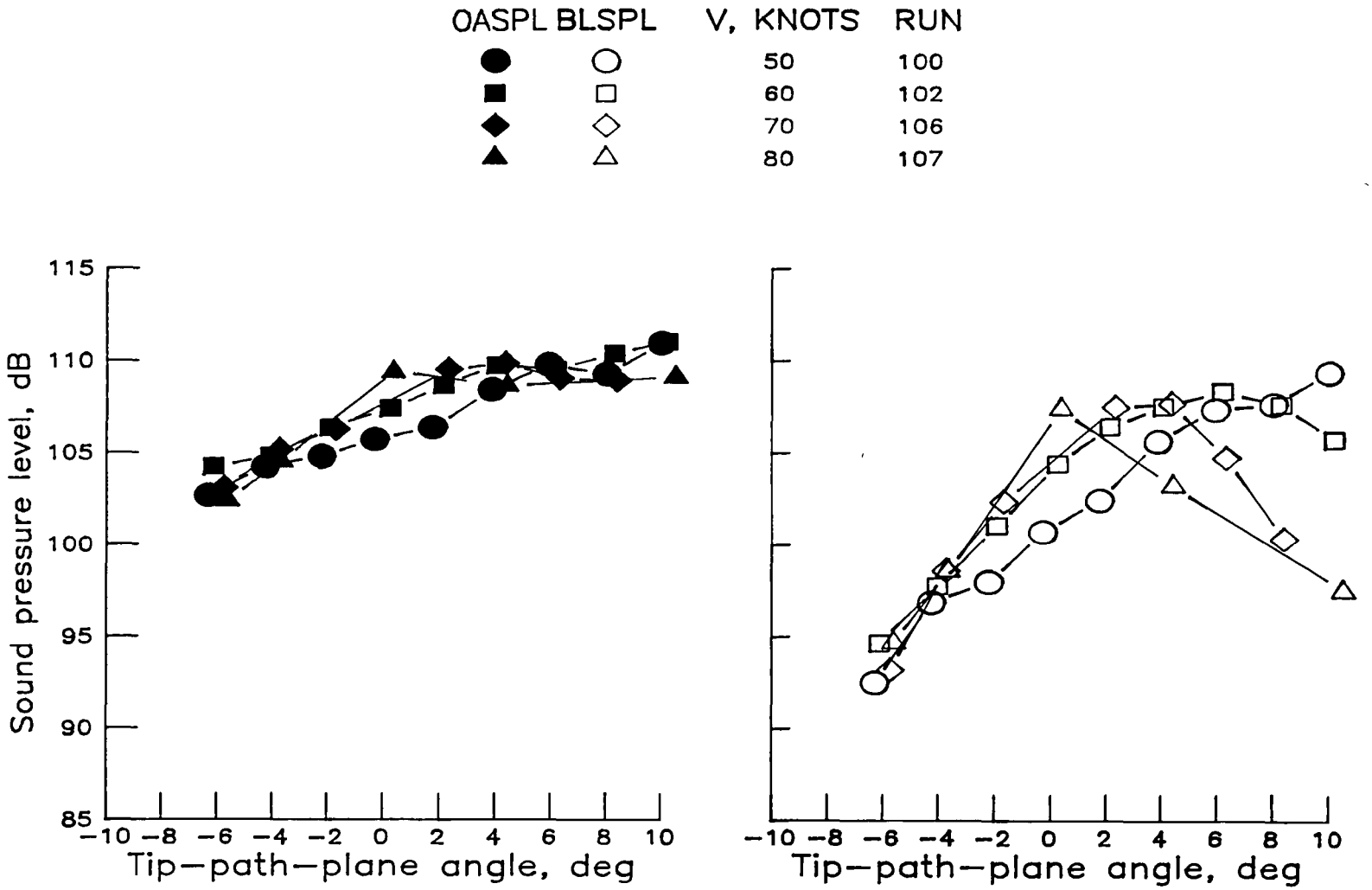

(a) High-twist standard tip (fig. 21(a)).

Figure A5.- Overall and band-limited sound pressure levels as a function of tip-path-plane angle over velocity from 50 to 80 knots for microphone 5.

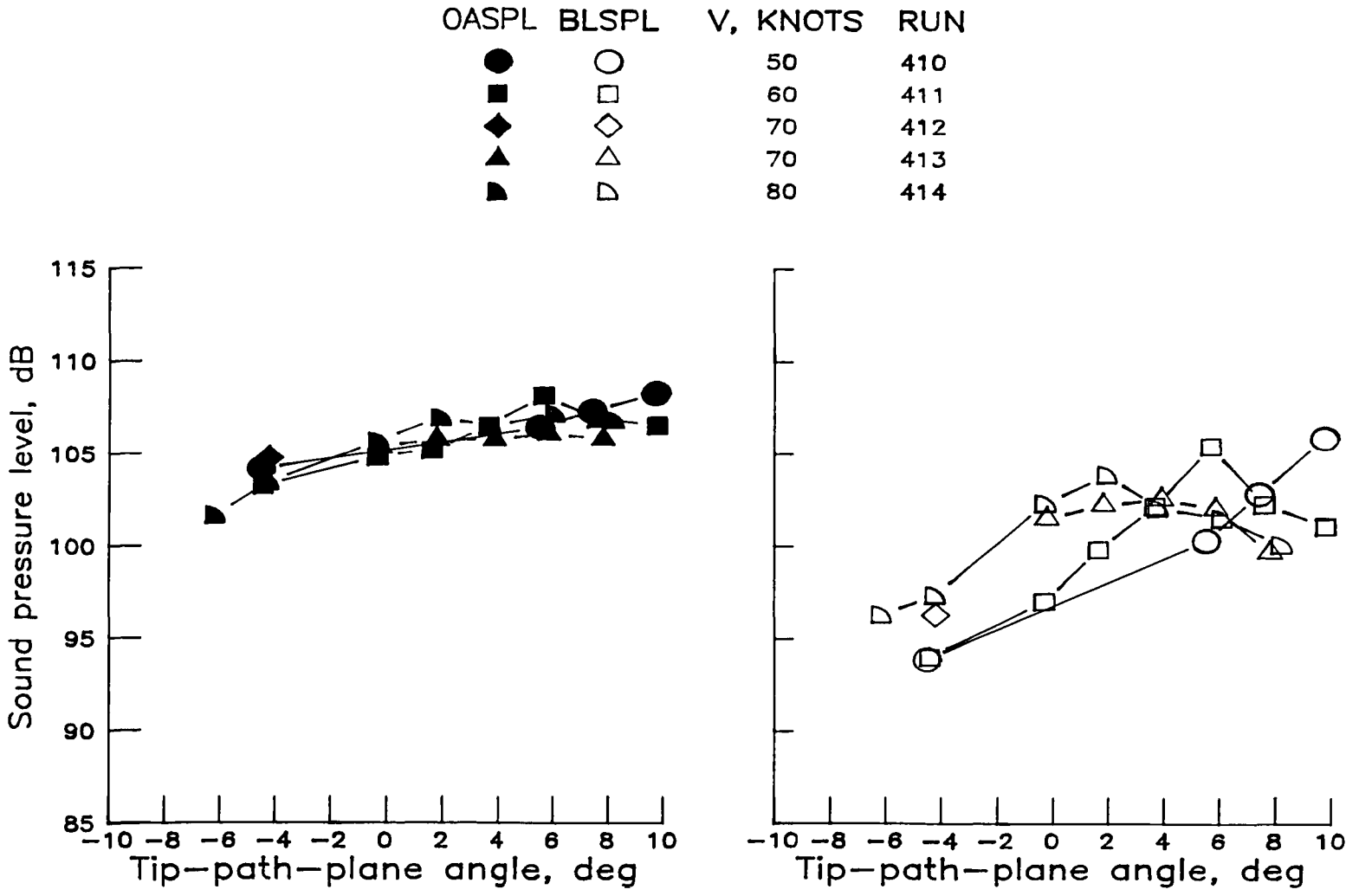

(b) High-twist swept tapered tip (SC1095 airfoil).

Figure A5.- Continued.

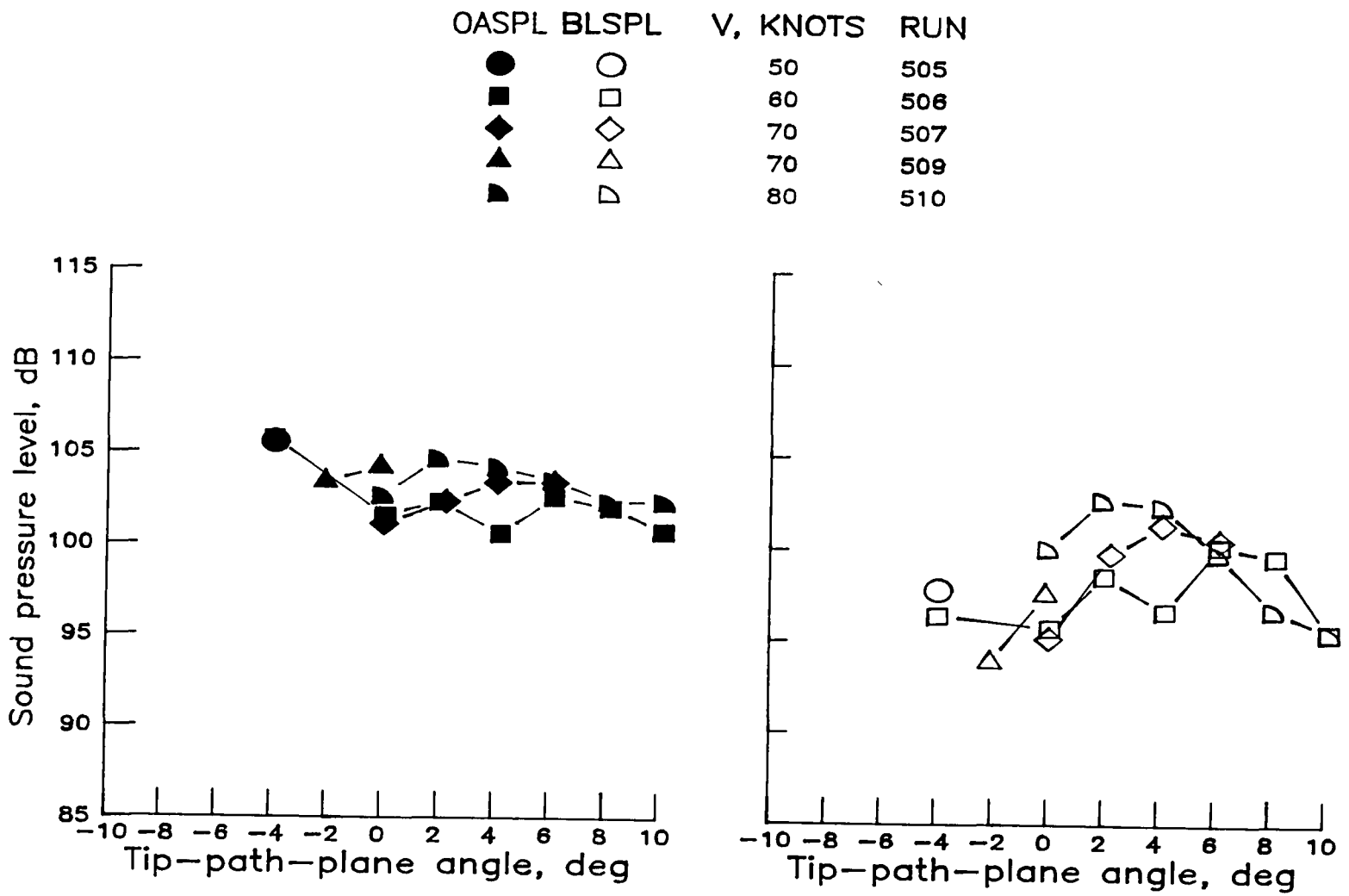

(c) High-twist swept tapered tip (SSC-A07 airfoil).

Figure A5.- Continued.

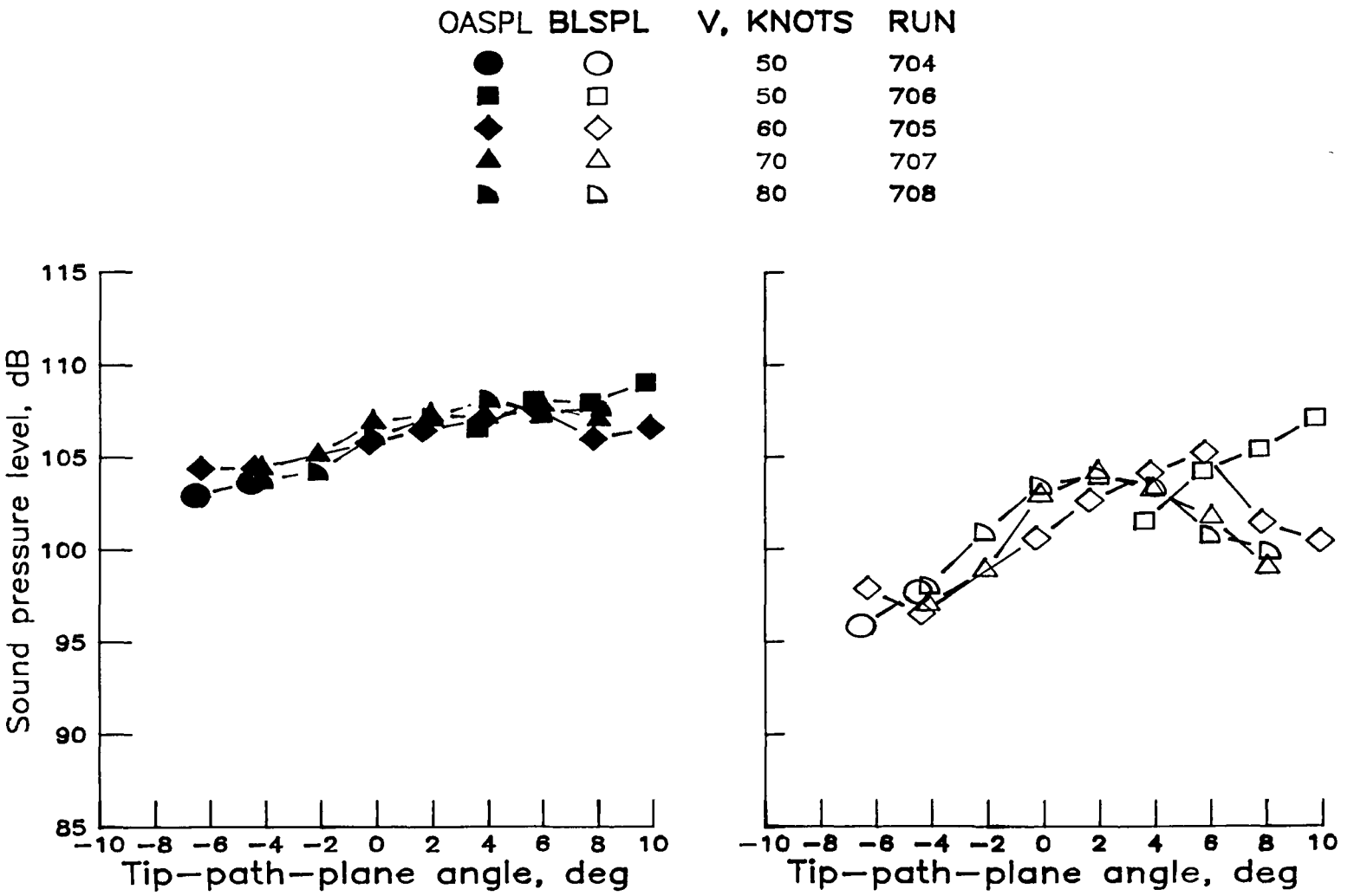

(d) High-twist parabolic tip.

Figure A5.- Continued.

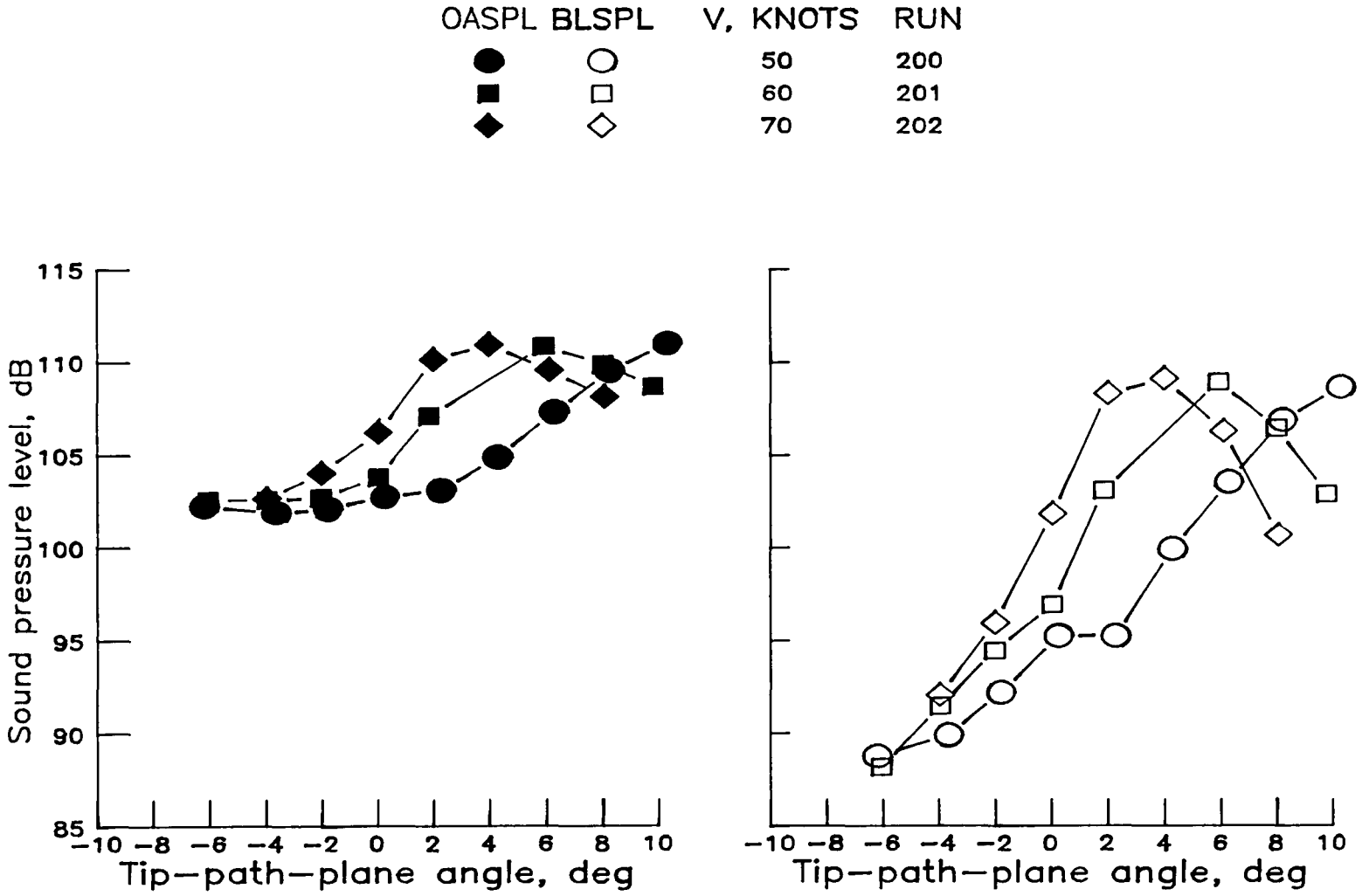

(e) Low-twist standard tip (fig. 21(b)).

Figure A5.- Continued.

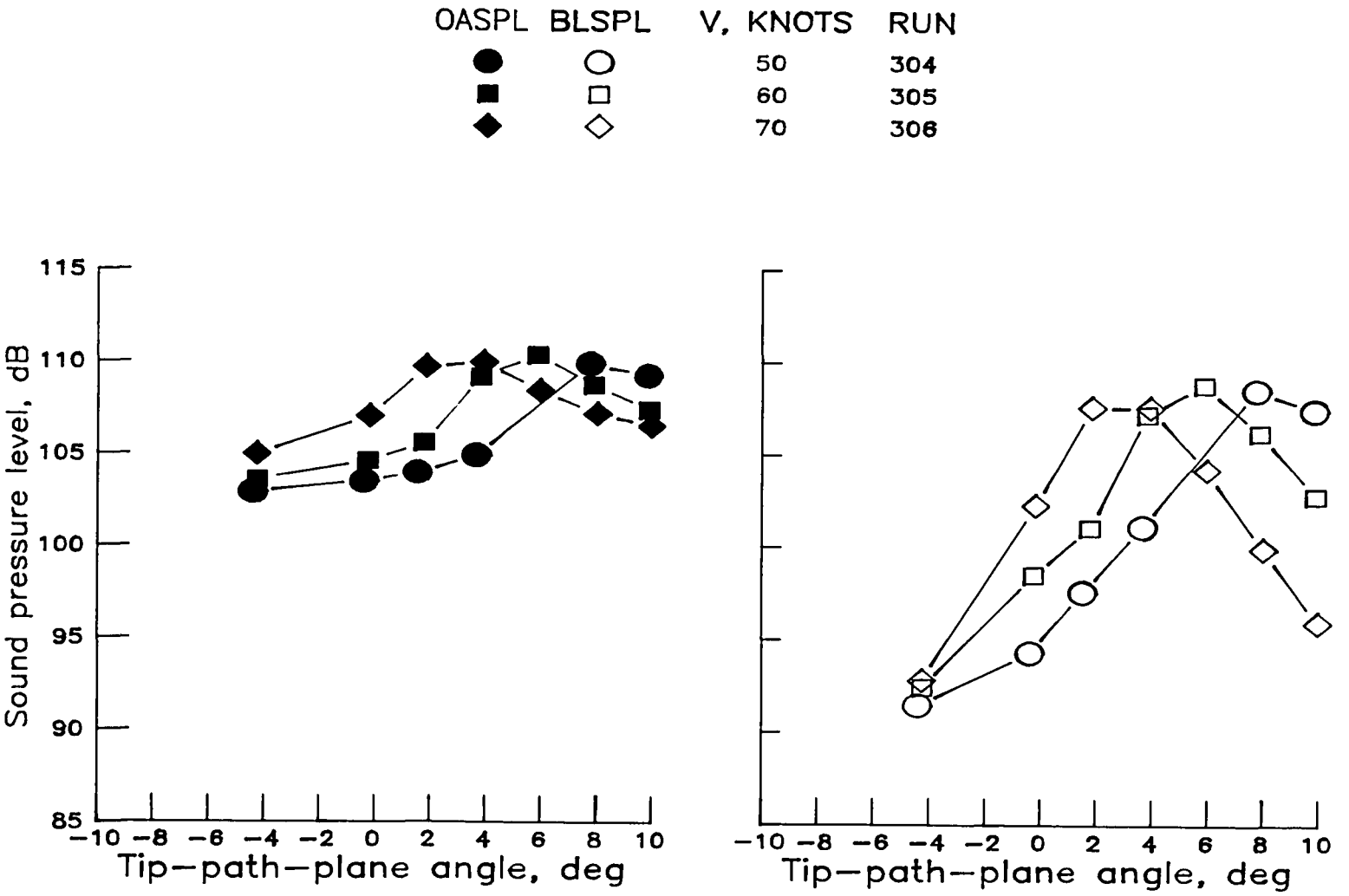

(f) Low-twist anhedral tip.

Figure A5.- Continued.

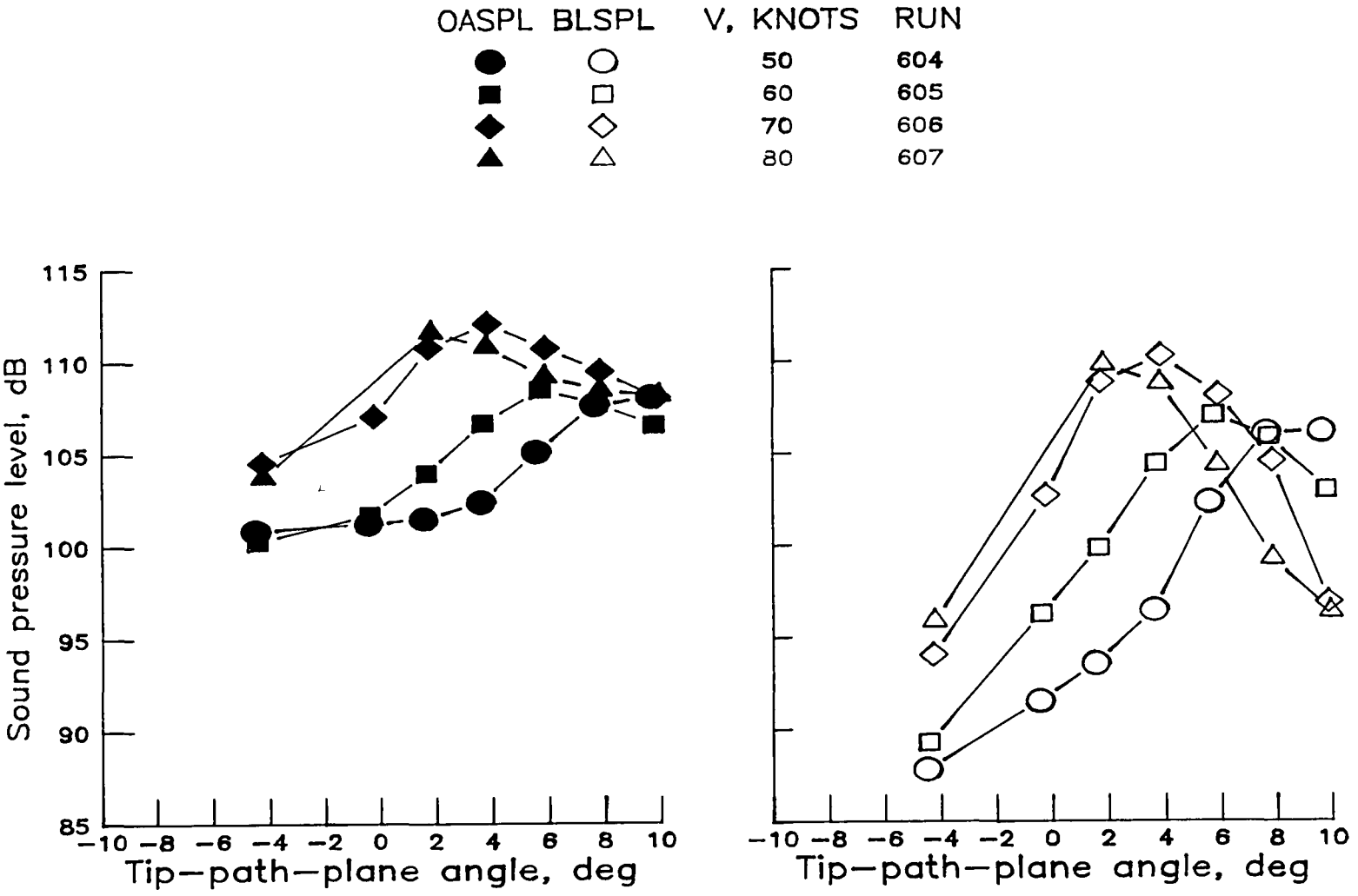

(g) Low-twist swept tip.

Figure A5.- Continued.

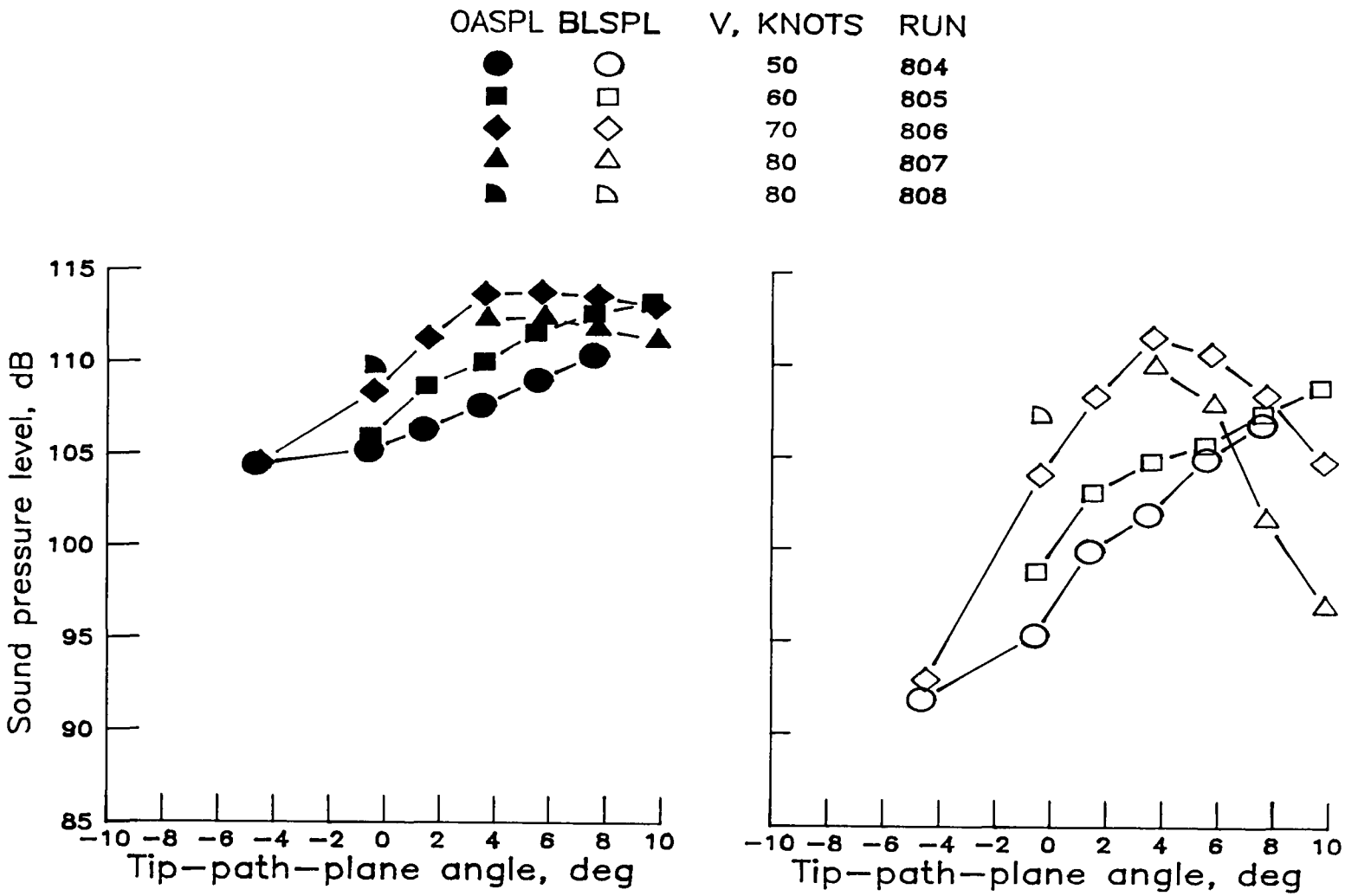

(h) Low-twist tapered tip.

Figure A5.- Continued.

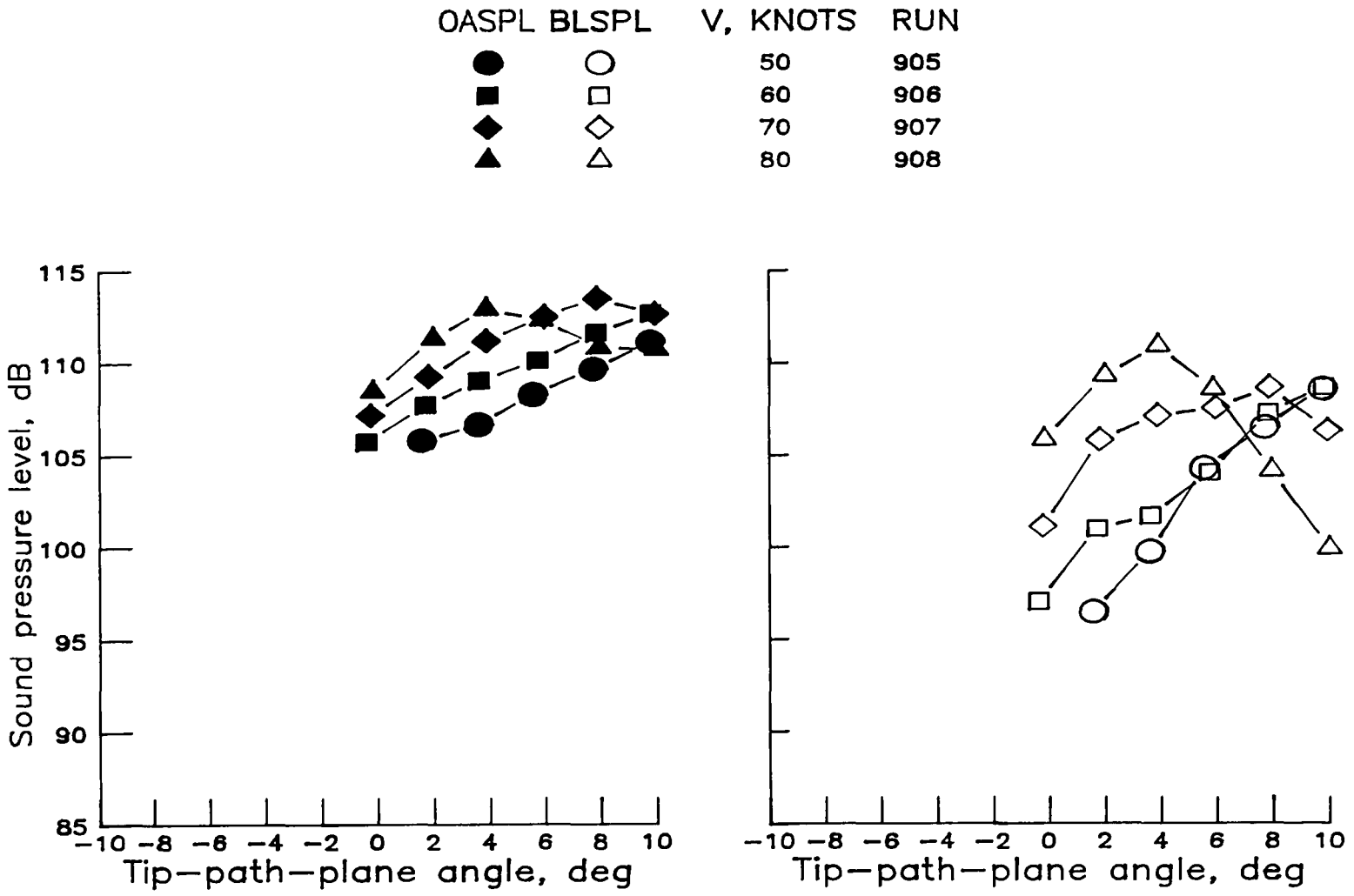

(i) Low-twist square tip.

Figure A5.- Concluded.

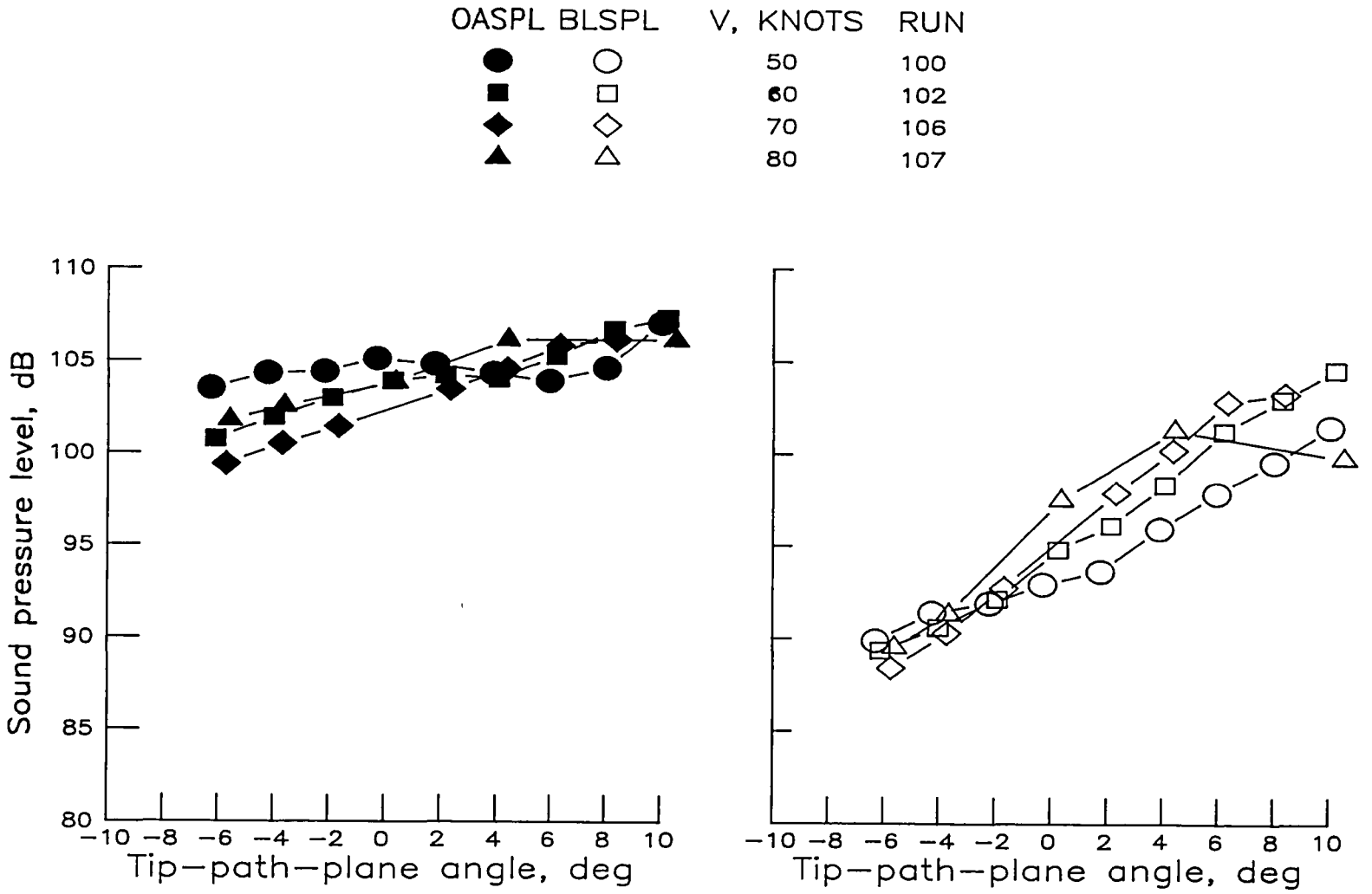

(a) High-twist standard tip (fig. 22(a)).

Figure A6.- Overall and band-limited sound pressure levels as a function of tip-path-plane angle over velocity range from 50 to 80 knots for microphone 7.

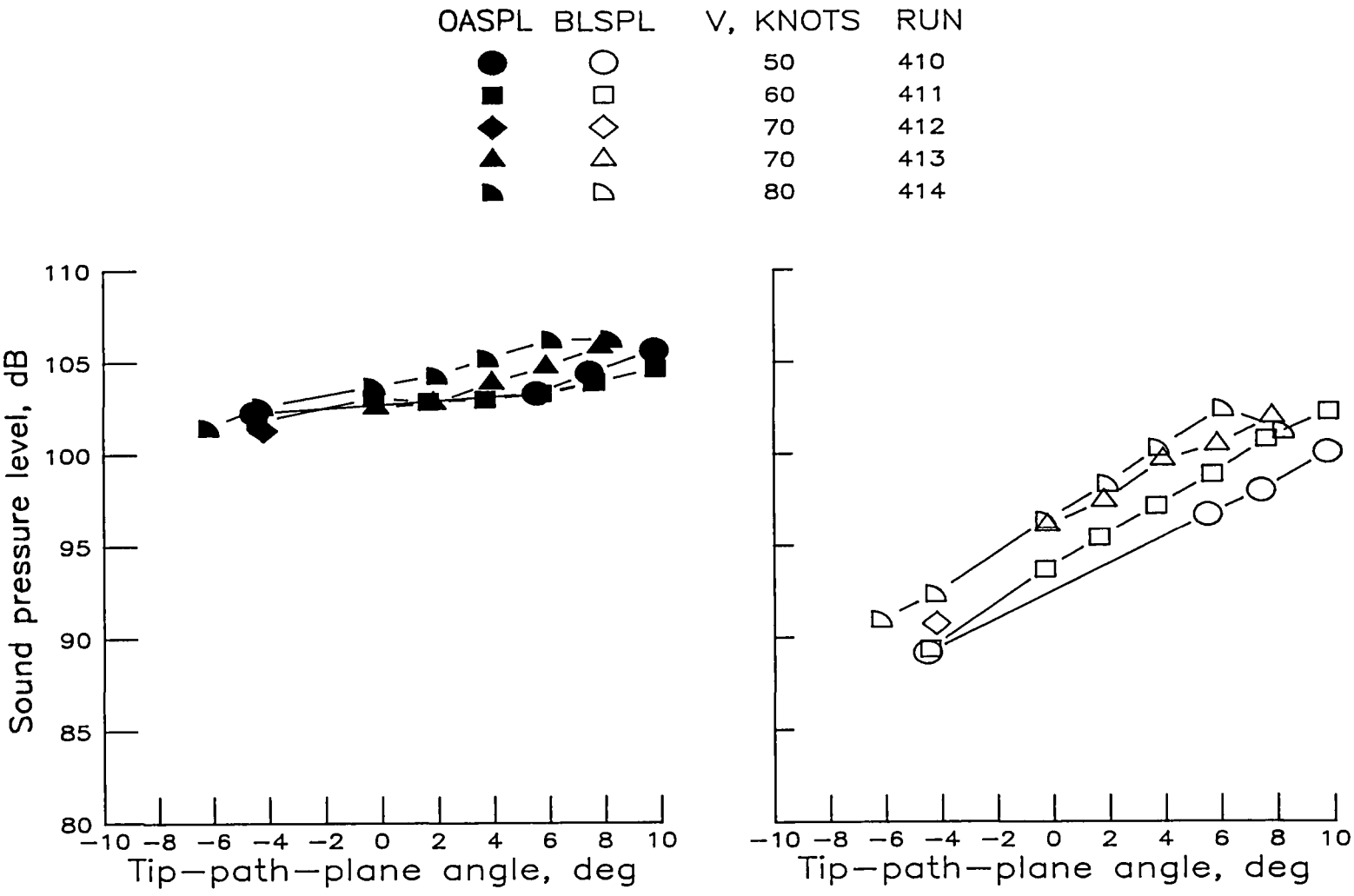

(b) High-twist swept tapered tip (SC1095 airfoil).

Figure A6.- Continued.

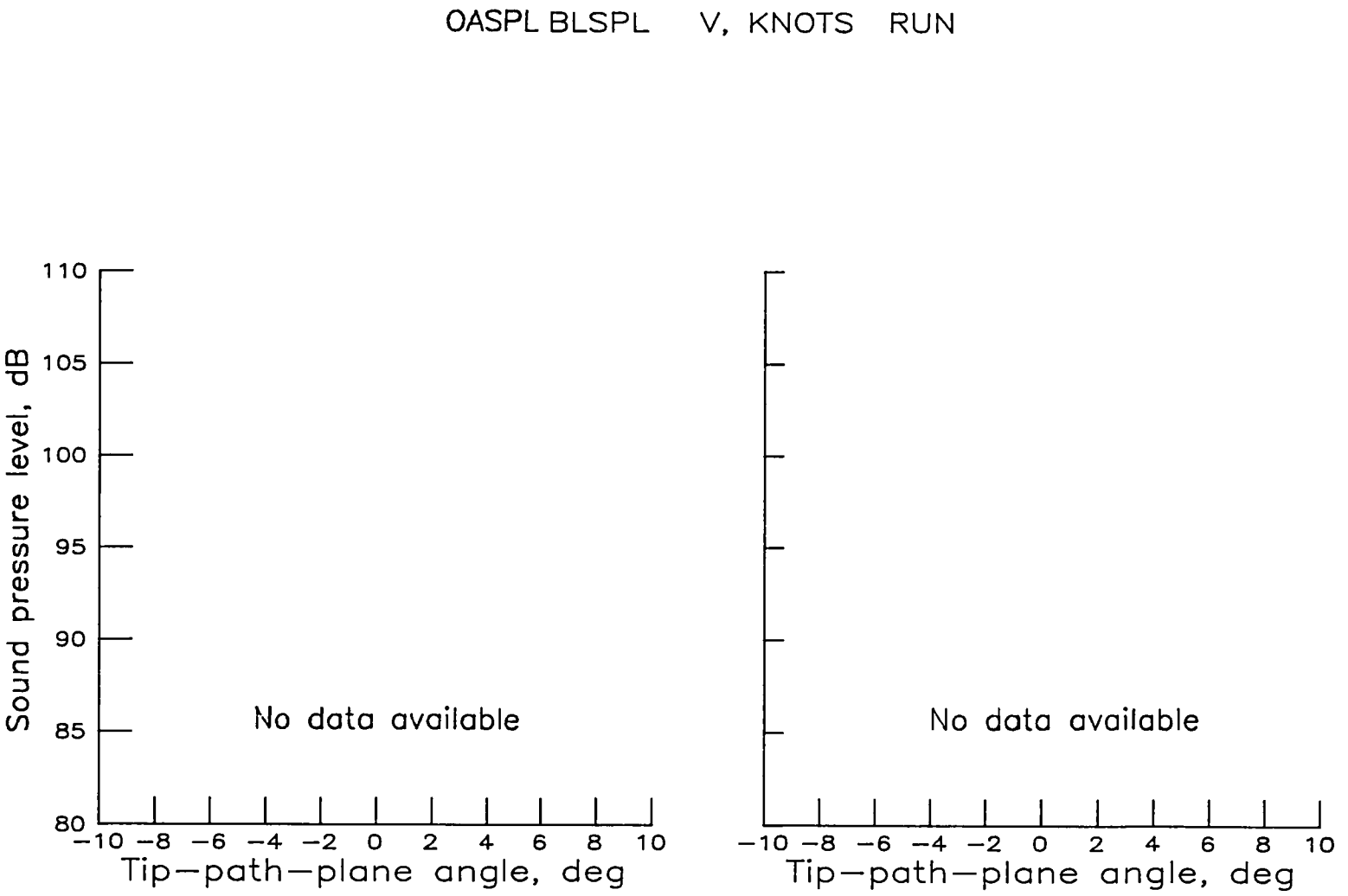

(c) High-twist swept tapered tip (SSC-A07 airfoil).

Figure A6.- Continued.

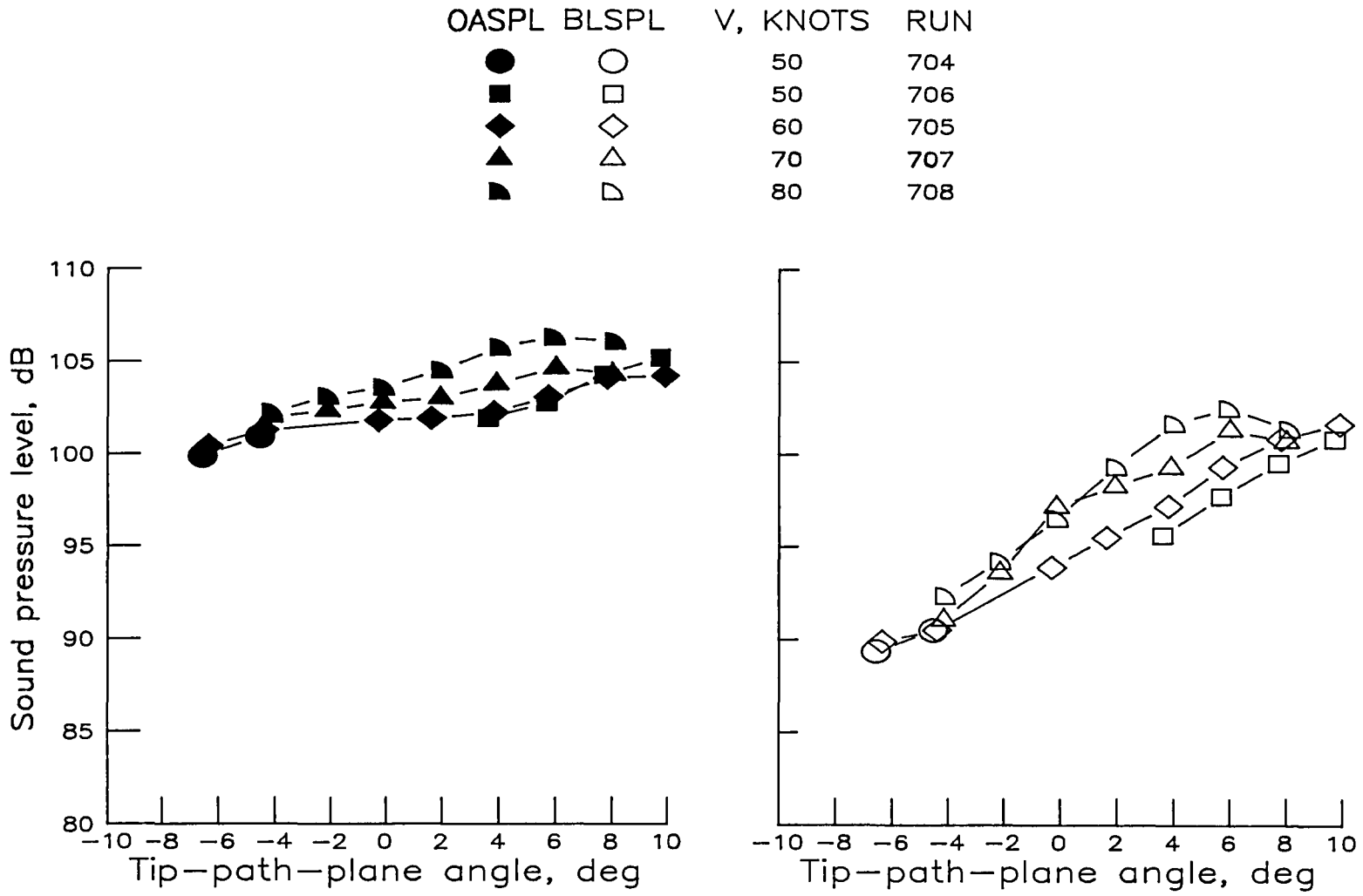

(d) High-twist parabolic tip.

Figure A6.- Continued.

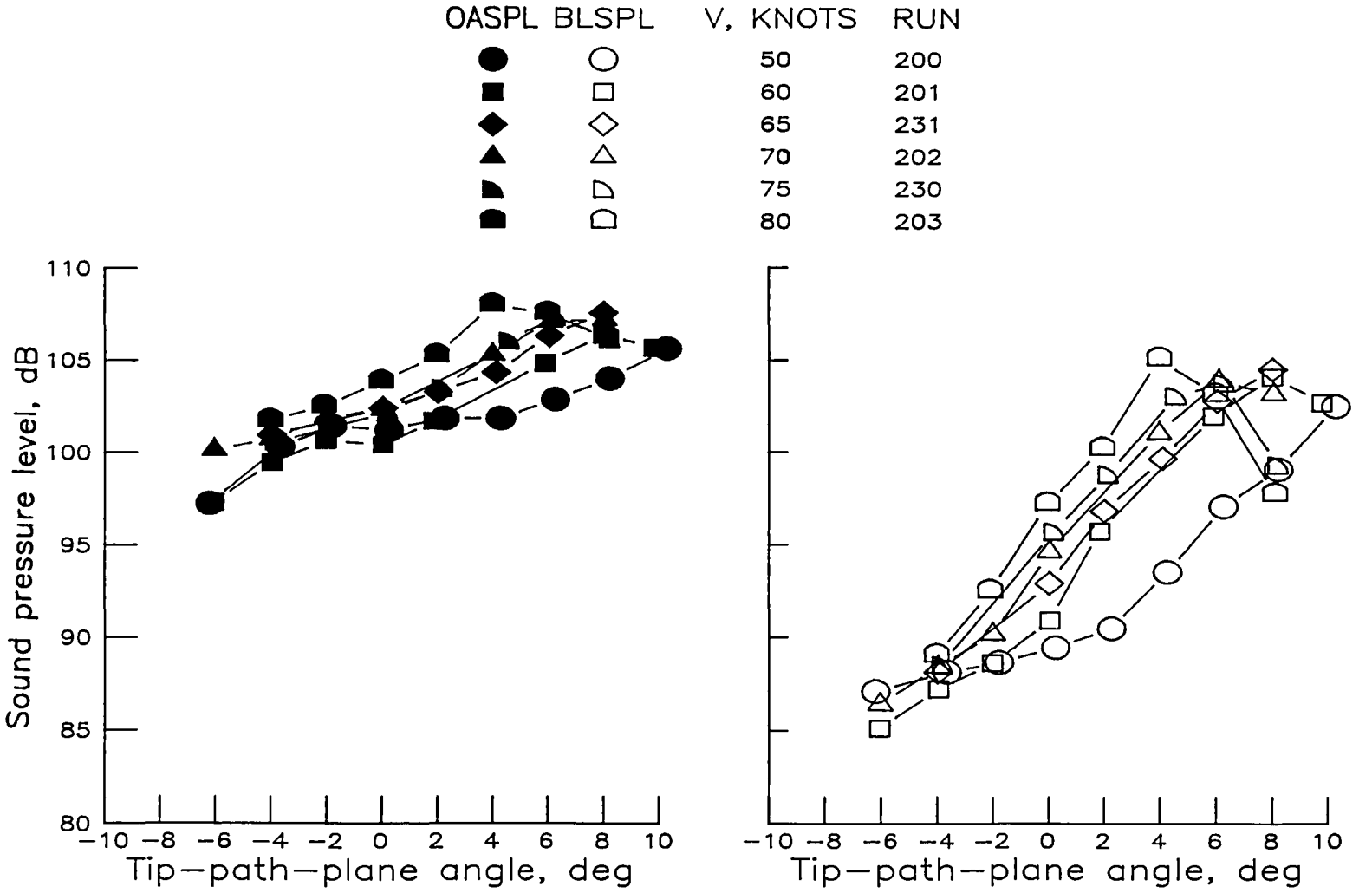

(e) Low-twist standard tip (fig. 22(b)).

Figure A6.- Continued.

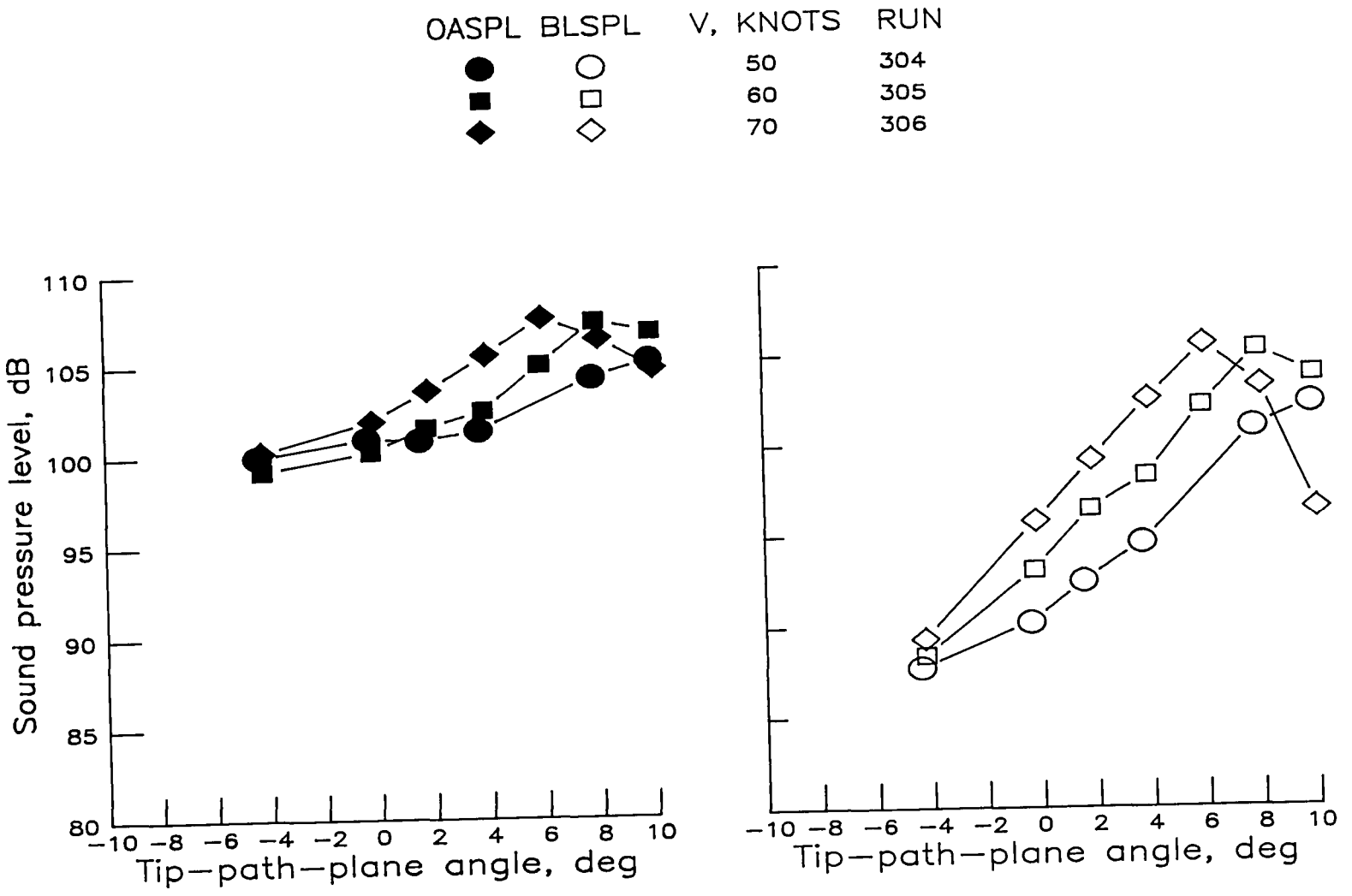

(f) Low-twist anhedral tip.

Figure A6.- Continued.

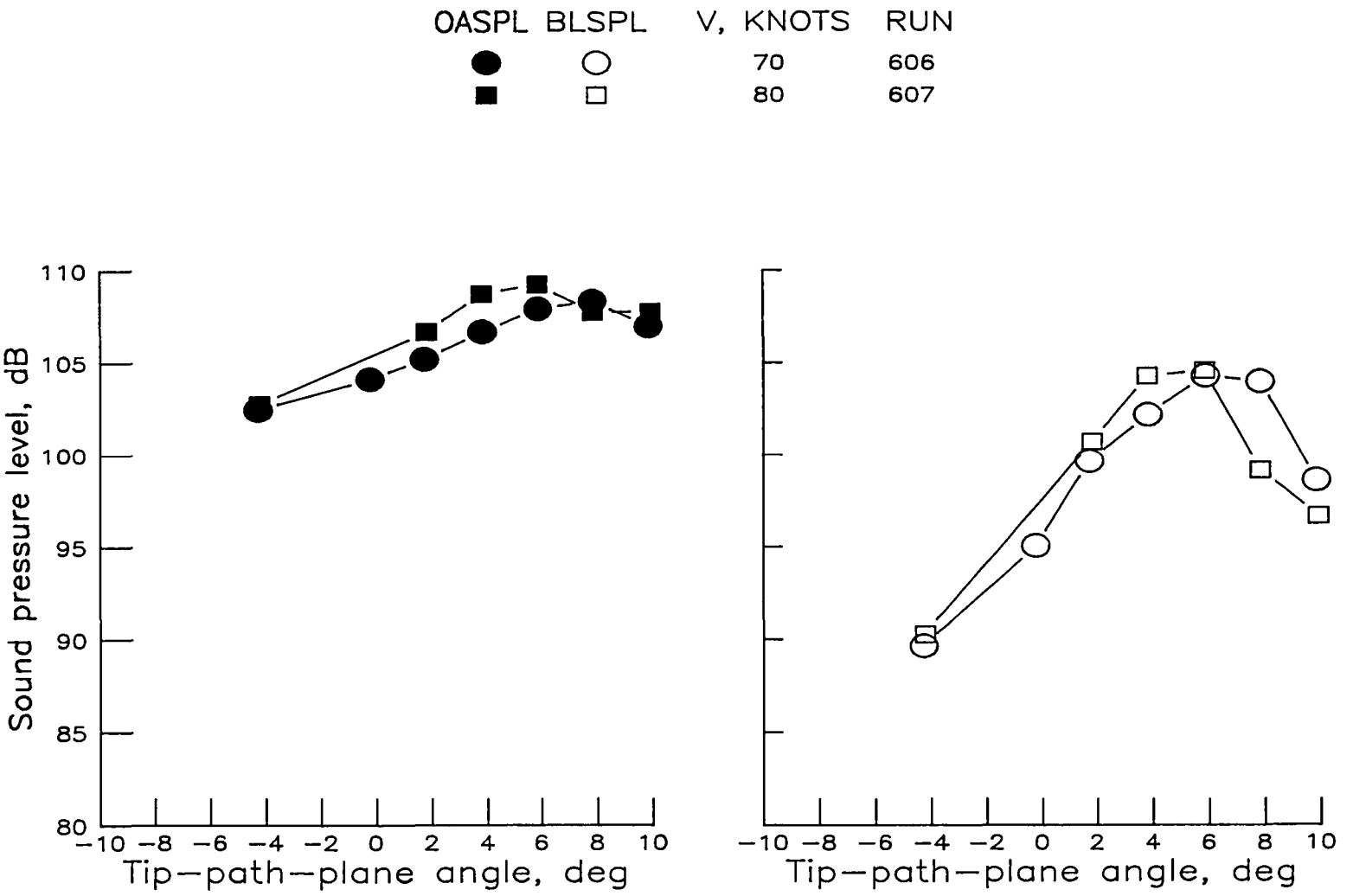

(g) Low-twist swept tip.

Figure A6.- Continued.

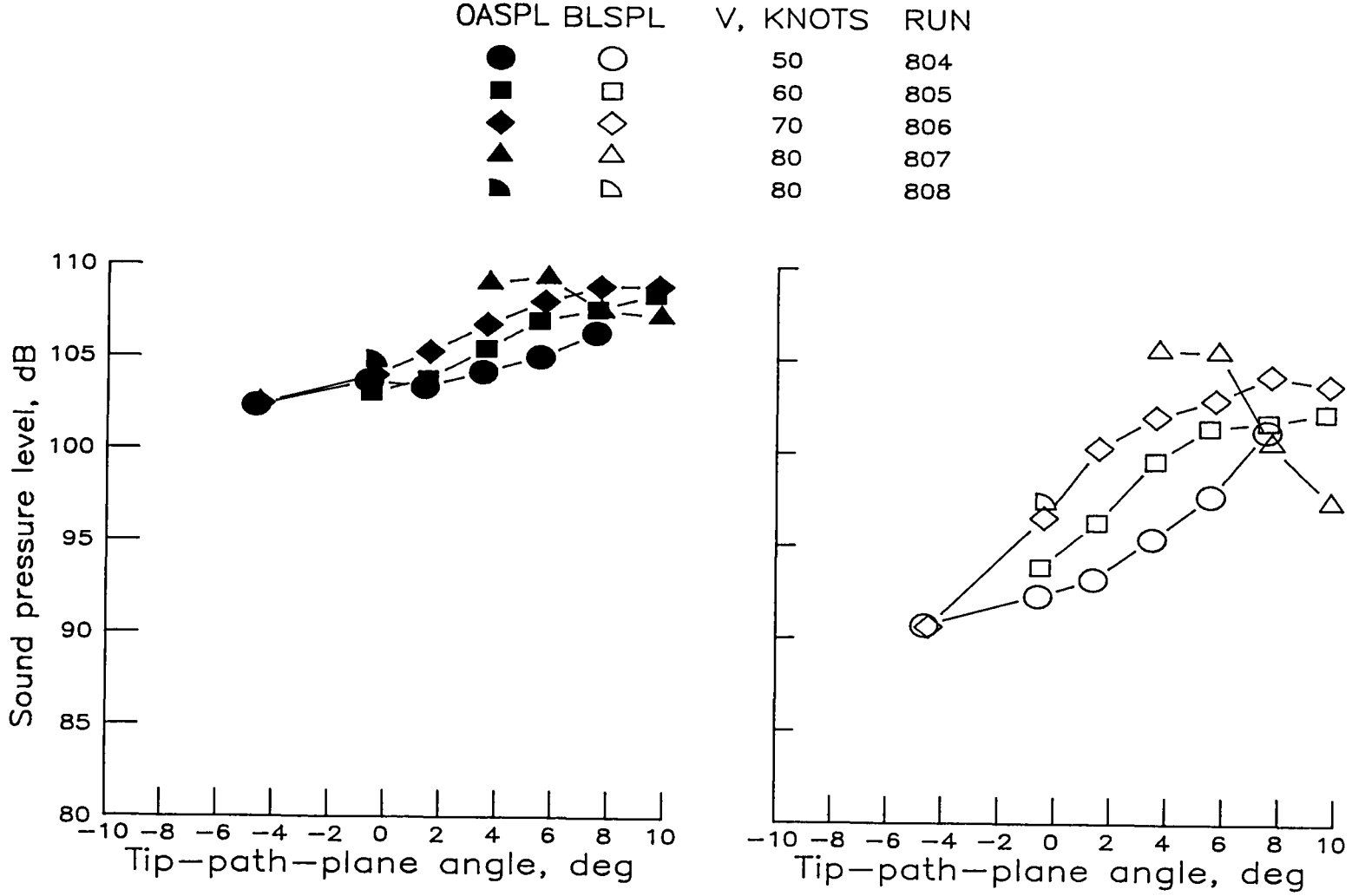

(h) Low-twist tapered tip.

Figure A6.- Continued.

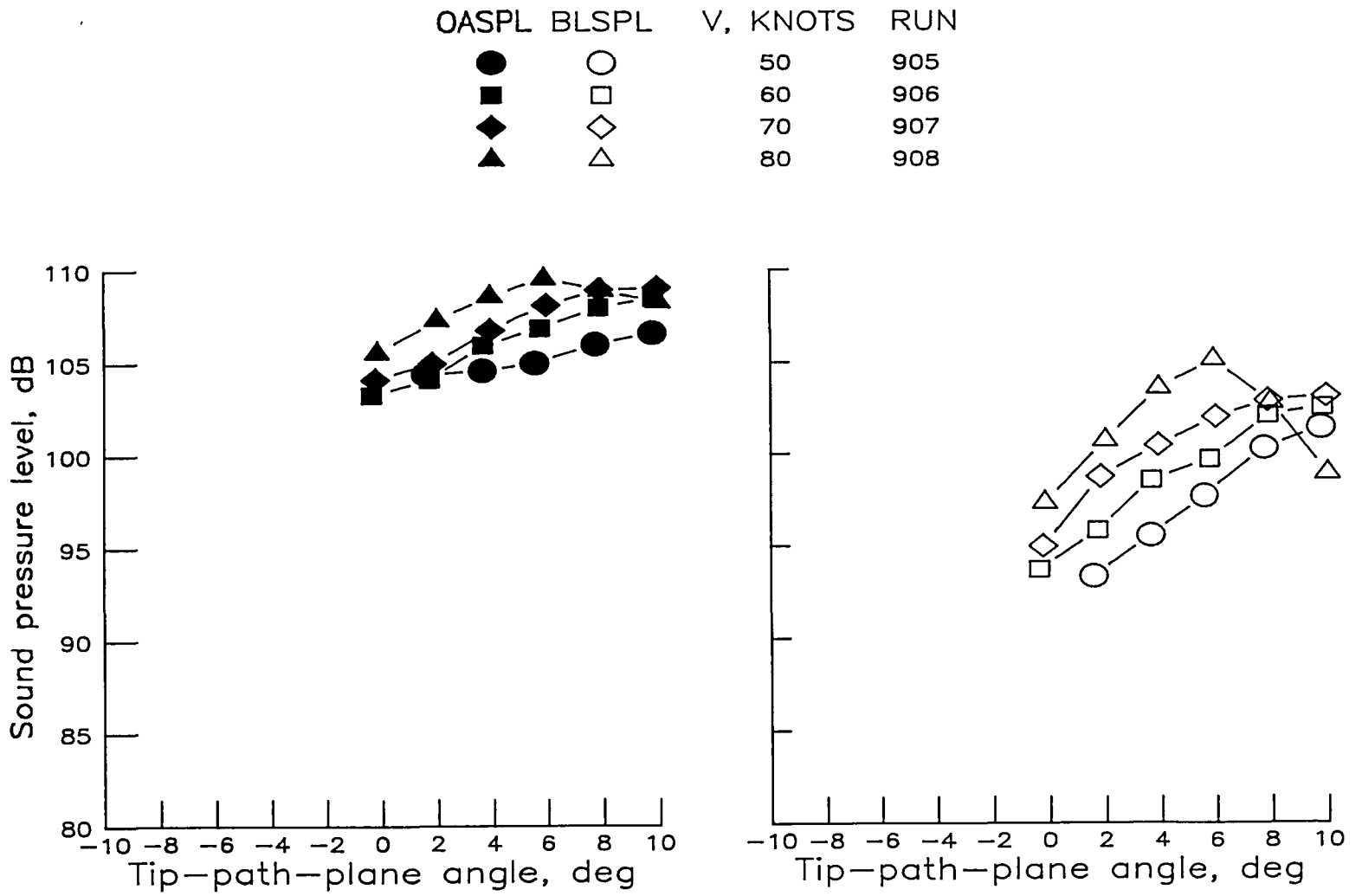

(1) Low-twist square tip.

Figure A6.- Concluded.

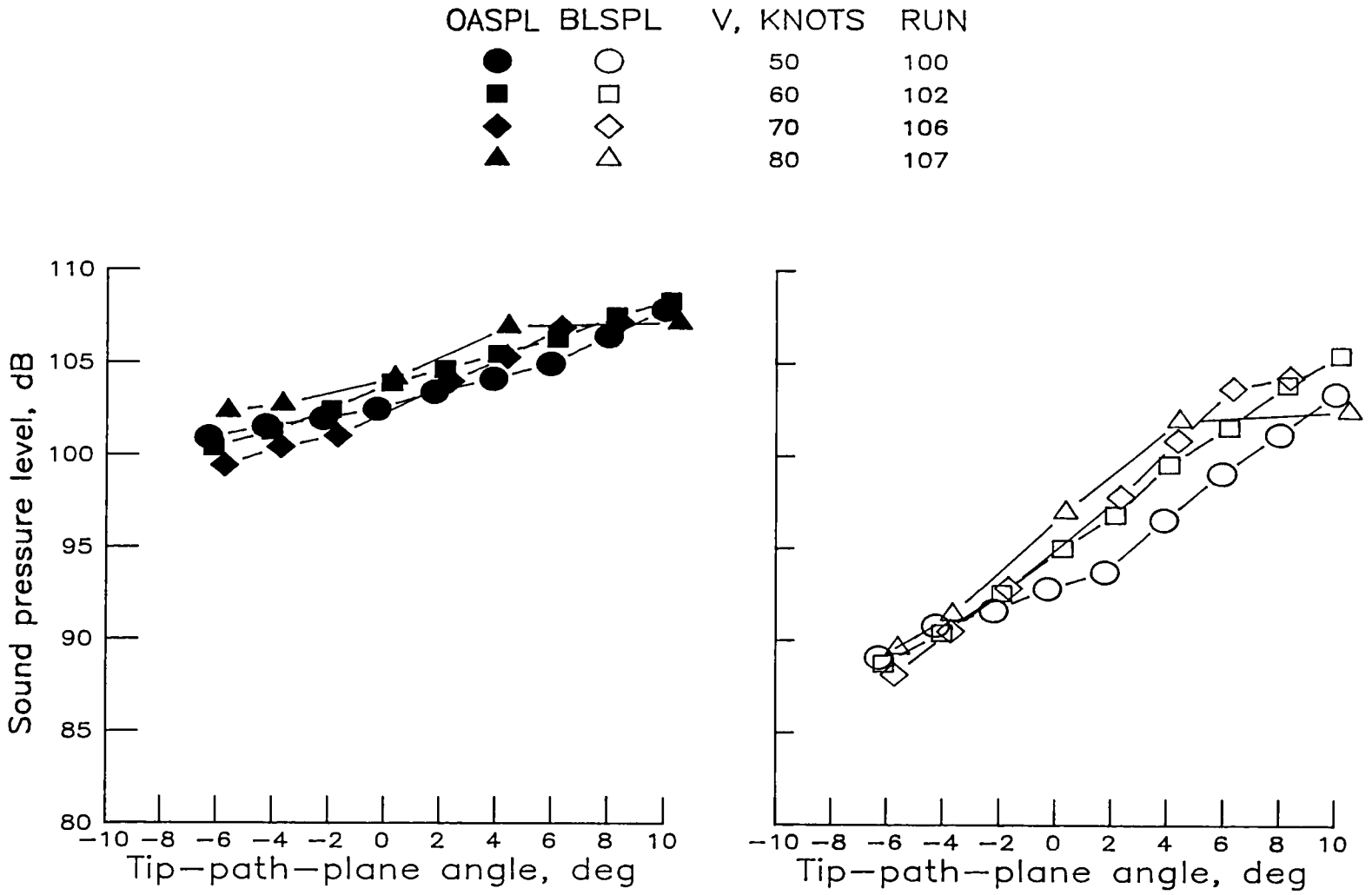

(a) High-twist standard tip (fig. 23(a)).

Figure A7.- Overall and band-limited sound pressure levels as a function of tip-path-plane angle over velocity range from 50 to 80 knots for microphone 8.

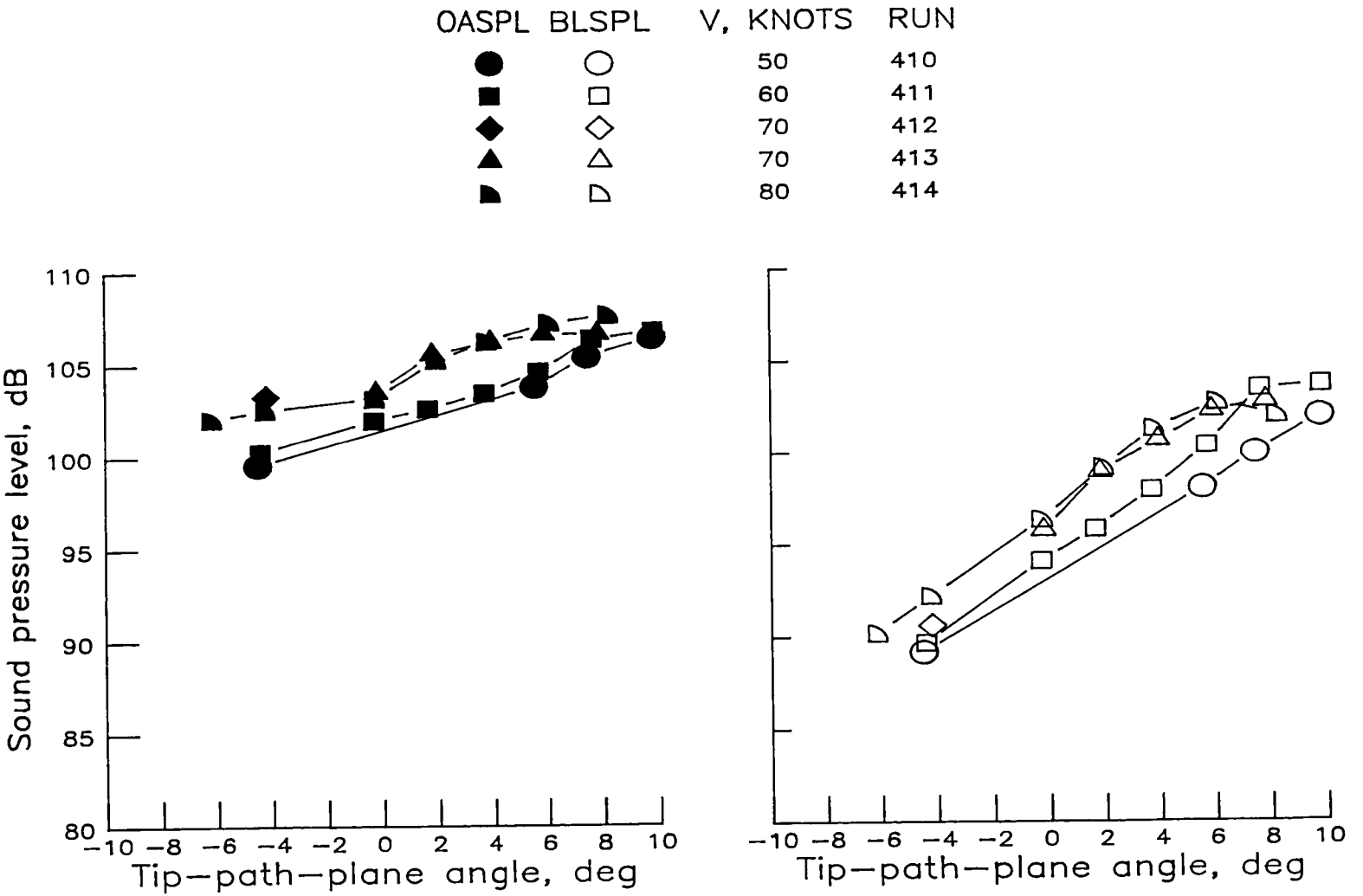

(b) High-twist swept tapered tip (SC1095 airfoil).

Figure A7.- Continued.

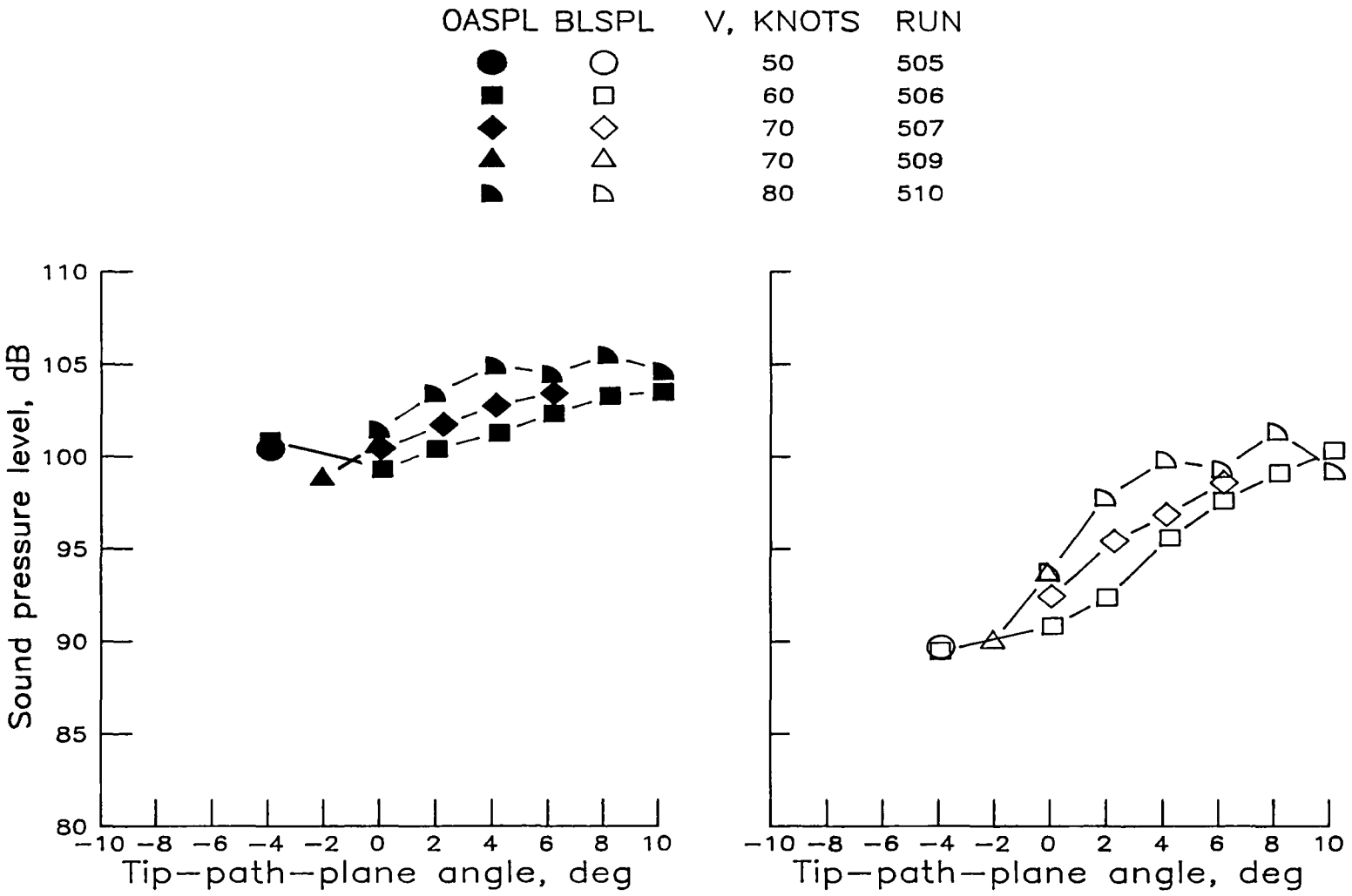

(c) High-twist swept tapered tip (SSC-A07 airfoil).

Figure A7.- Continued.

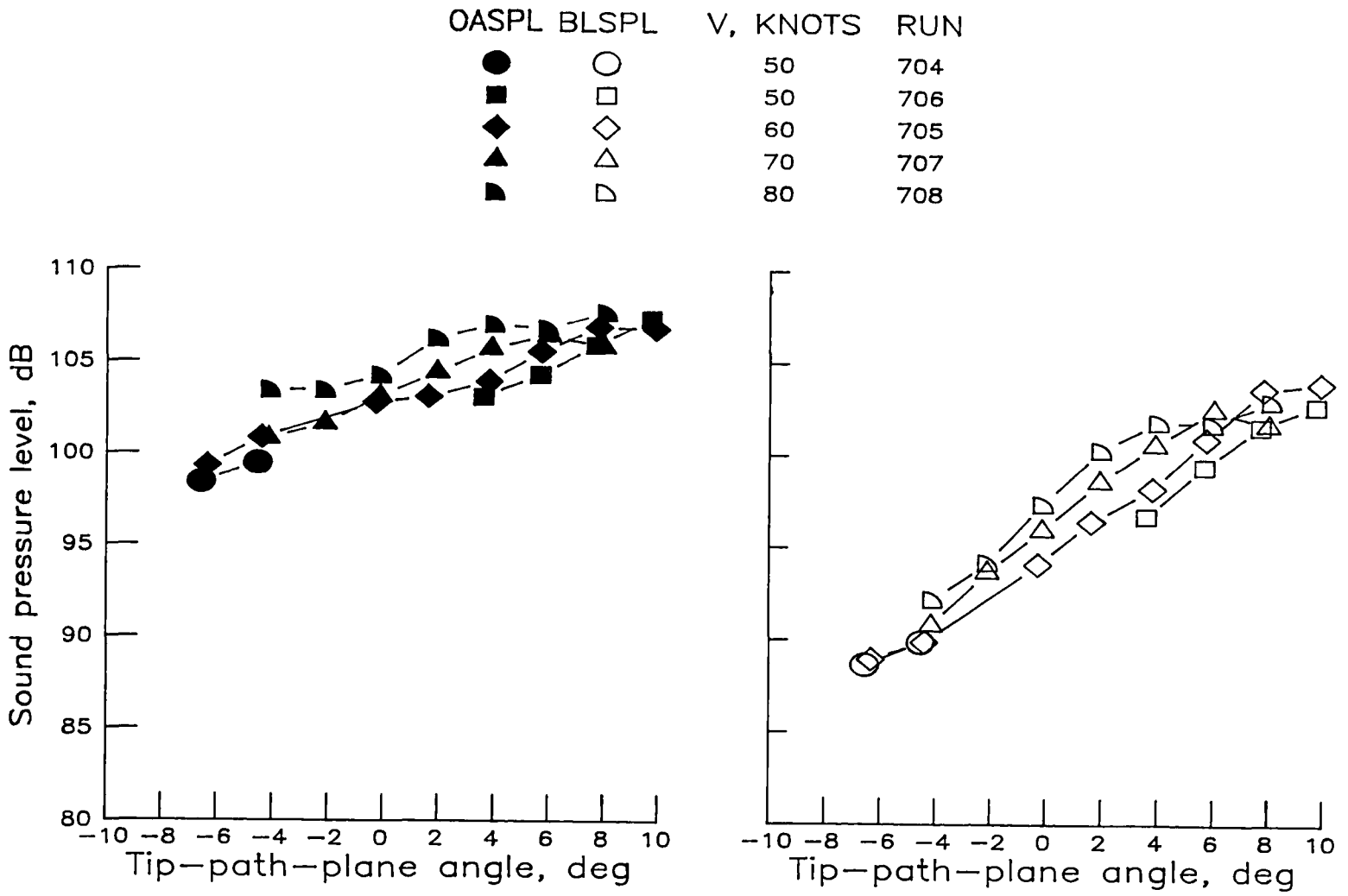

(d) High-twist parabolic tip.

Figure A7.- Continued.

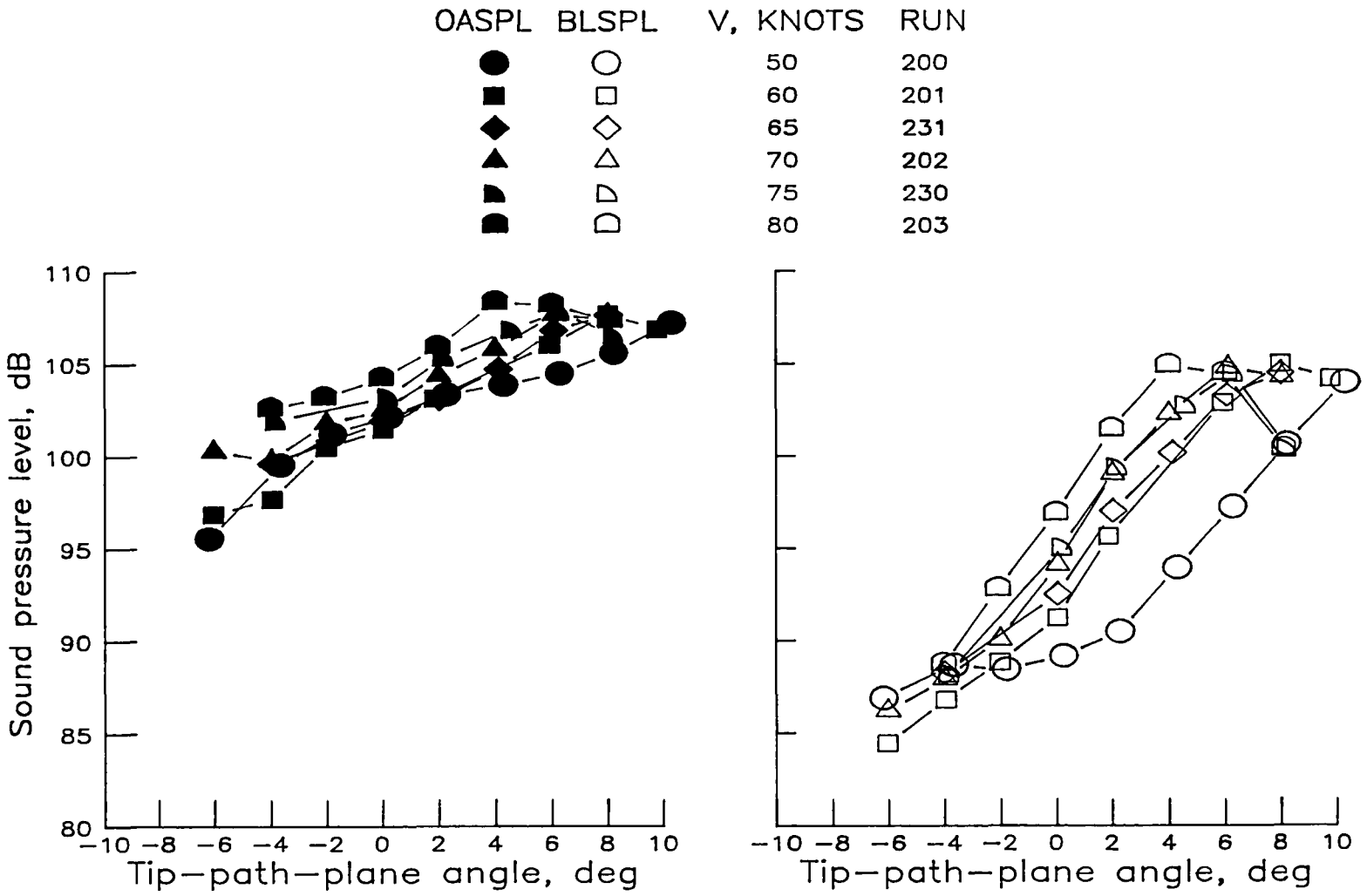

(e) Low-twist standard tip (fig. 23(b)).

Figure A7.- Continued.

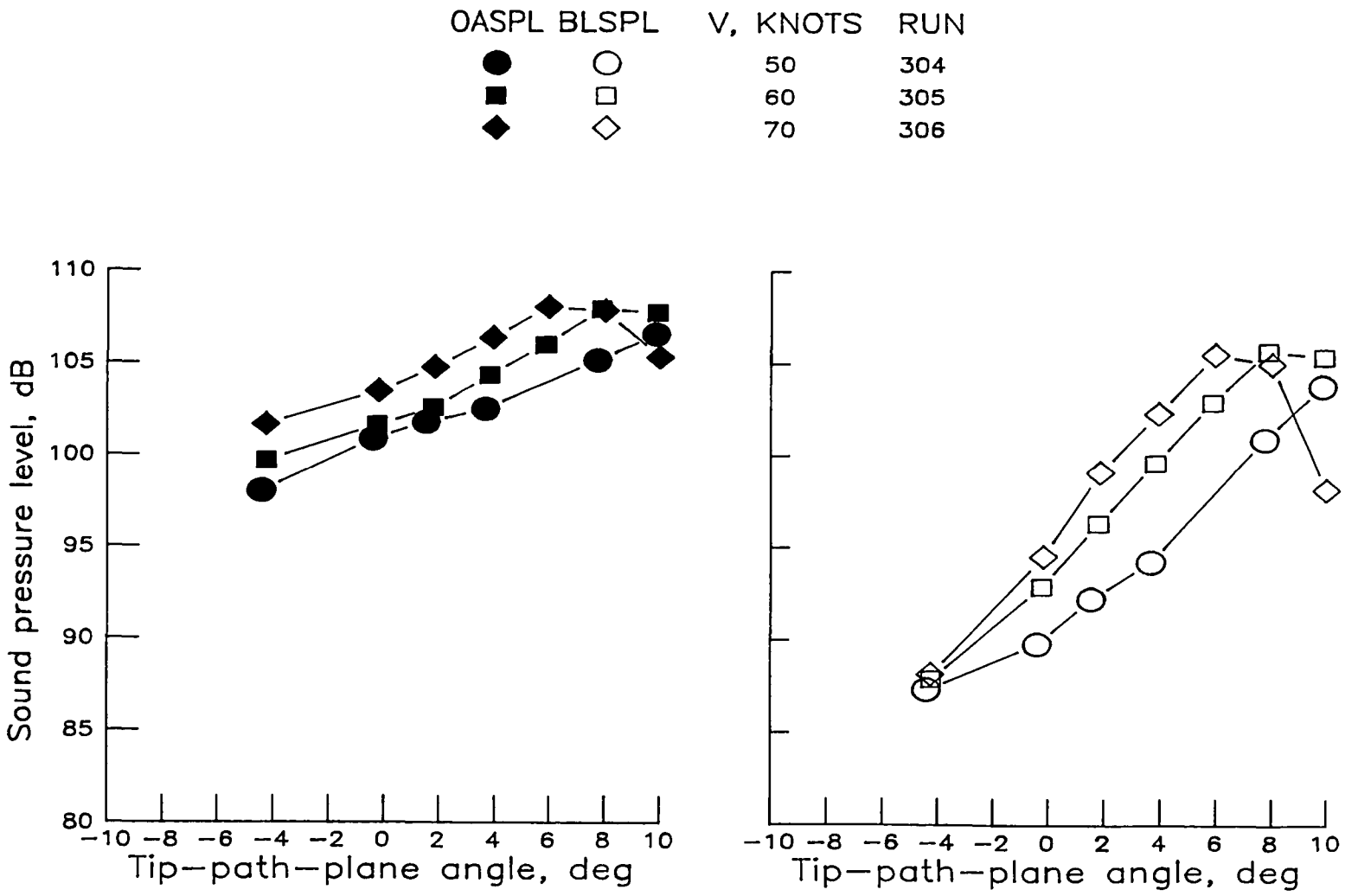

(f) Low-twist anhedral tip.

Figure A7.- Continued.

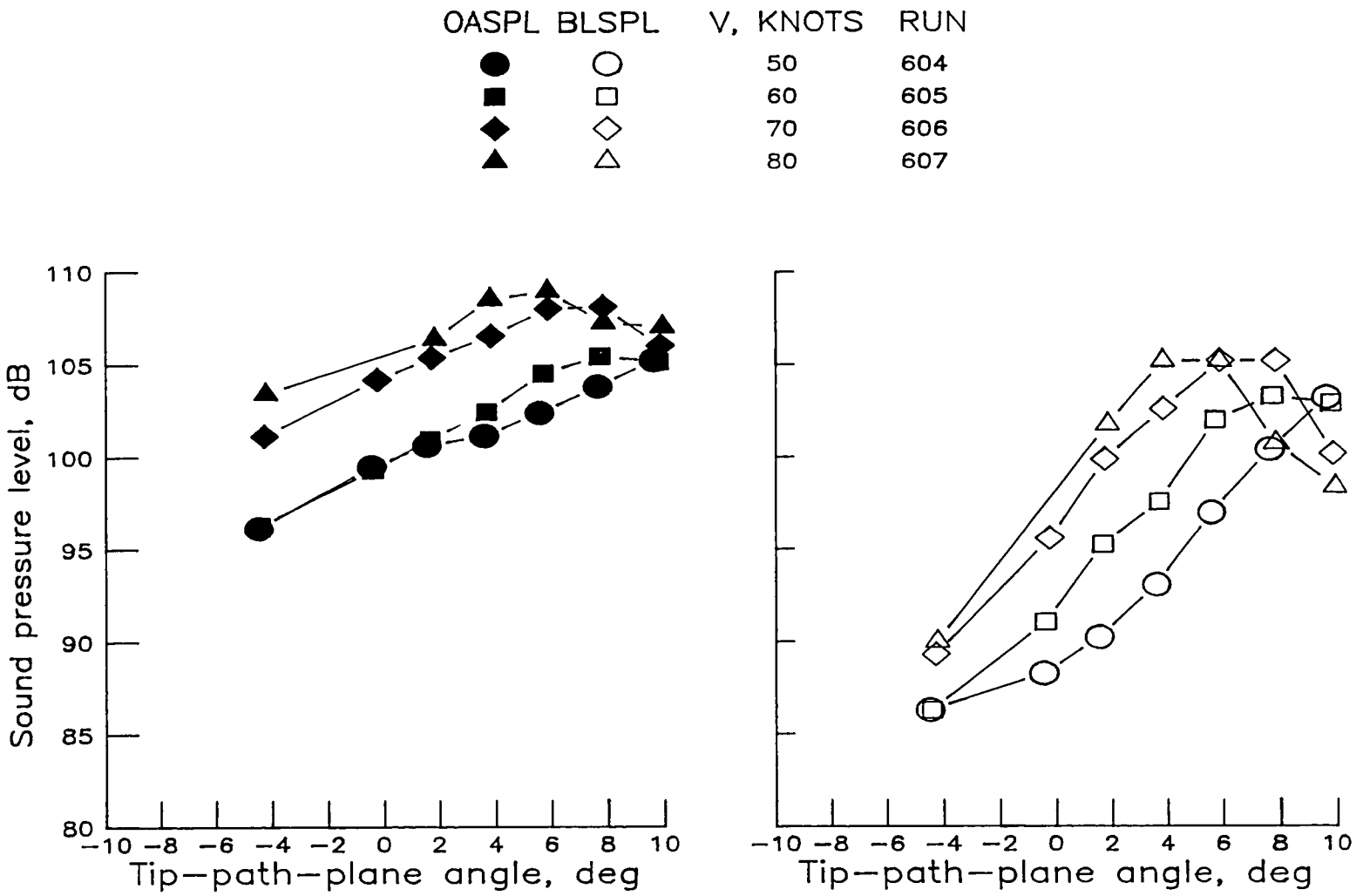

(g) Low-twist swept tip.

Figure A7.- Continued.

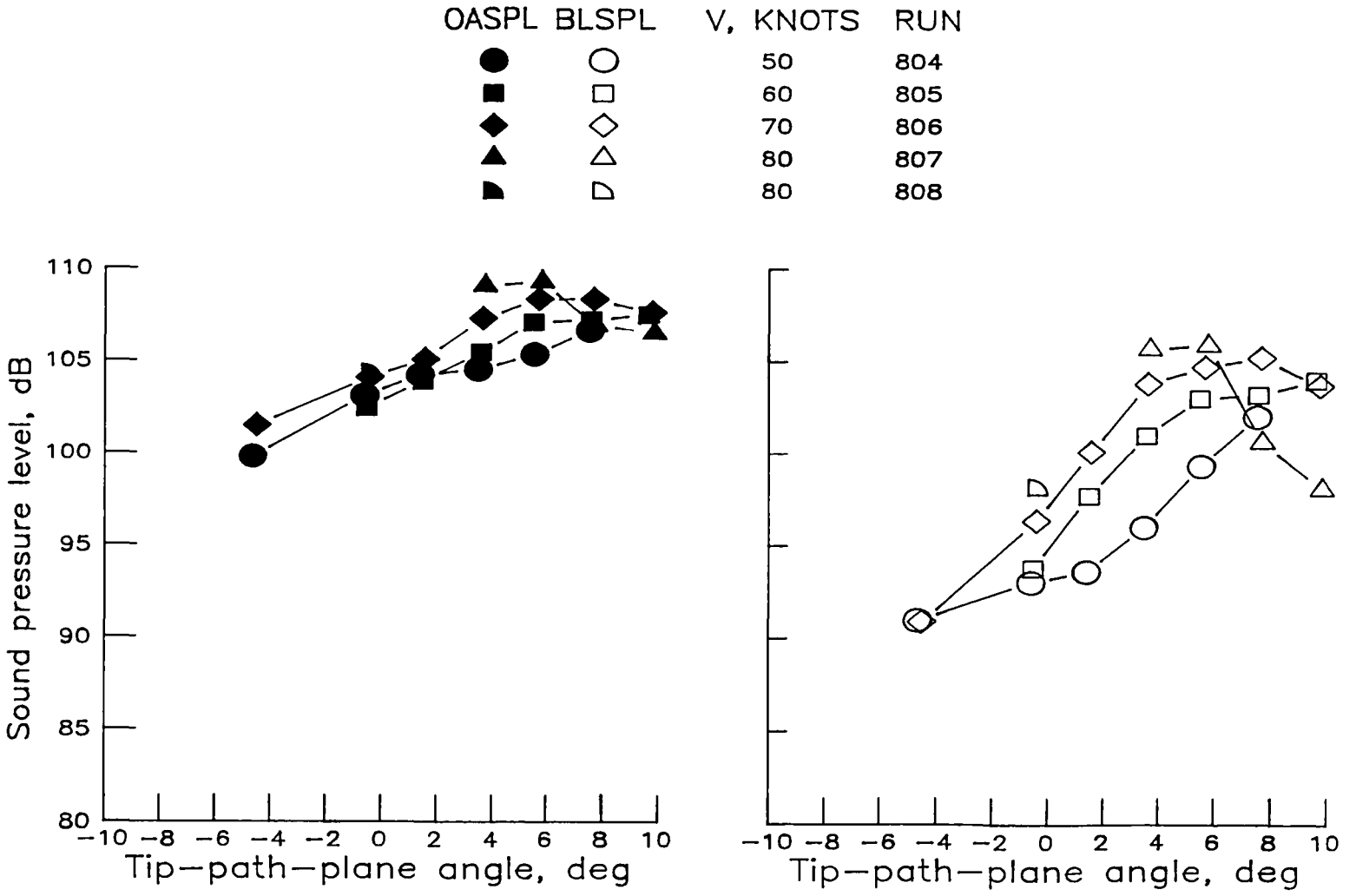

(h) Low-twist tapered tip.

Figure A7.- Continued.

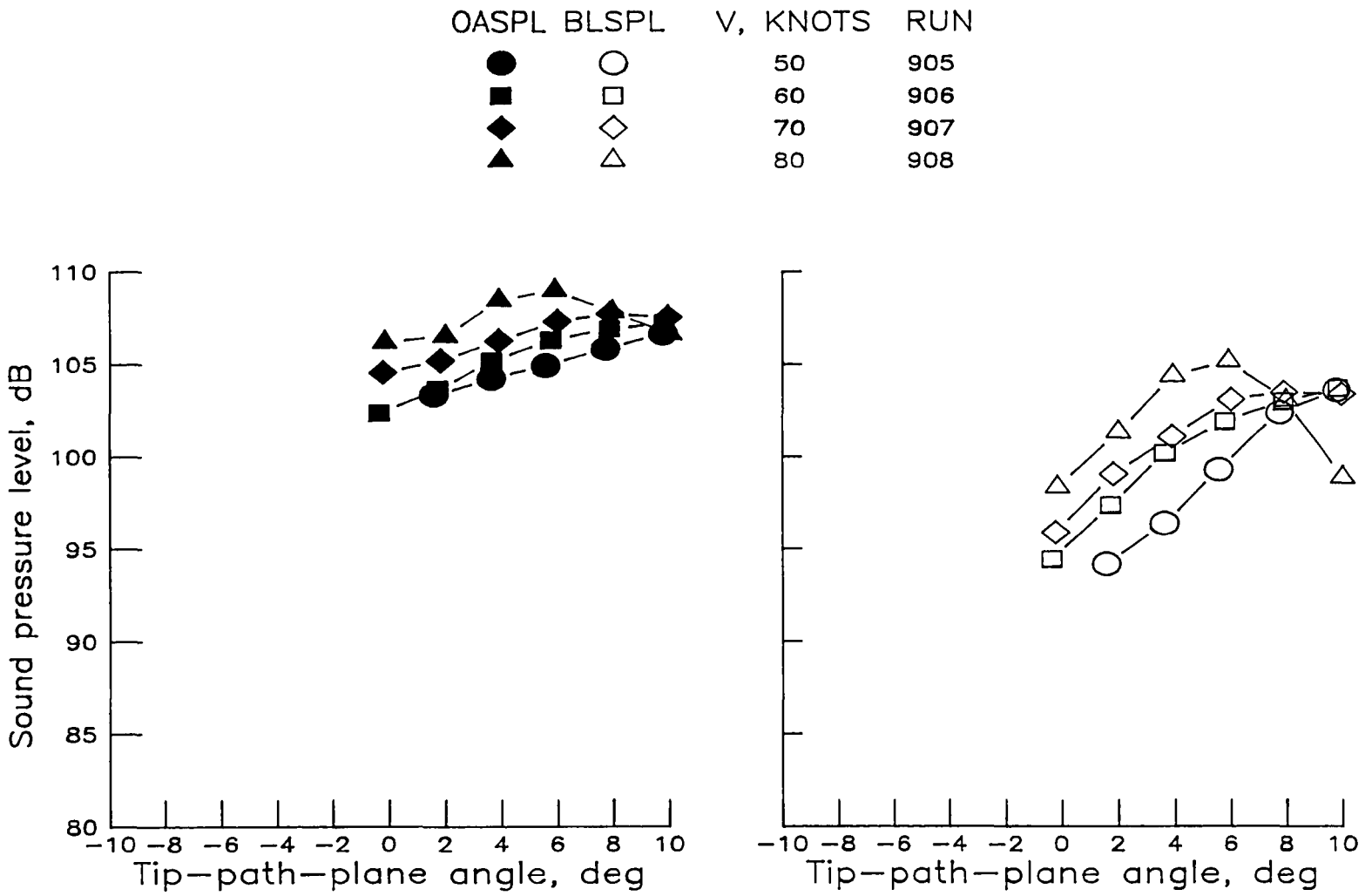

(1) Low-twist square tip.

Figure A7.- Concluded.

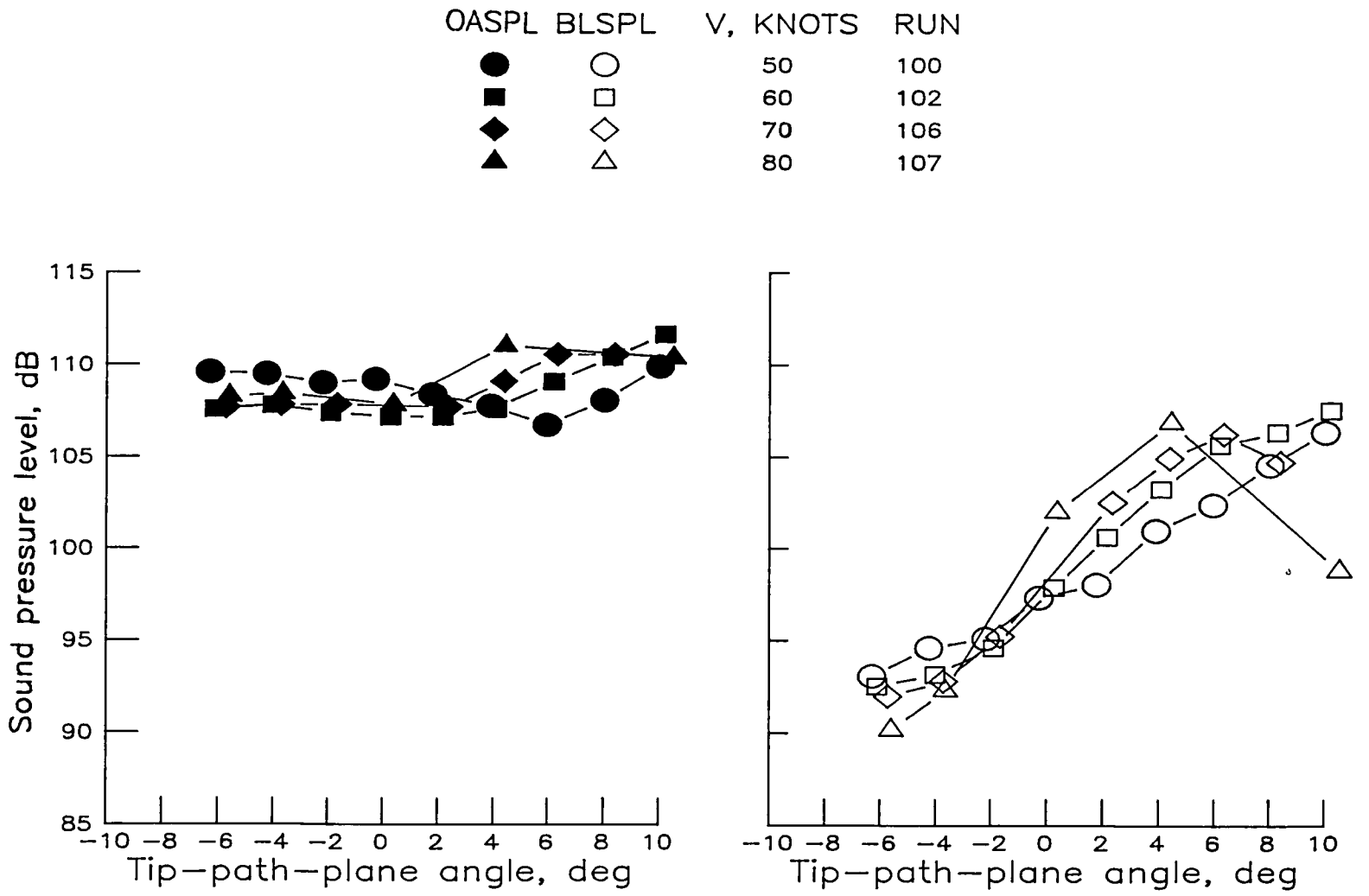

(a) High-twist standard tip (fig. 24(a)).

Figure A8.- Overall and band-limited sound pressure levels as a function of tip-path-plane angle over velocity range from 50 to 80 knots for microphone 9.

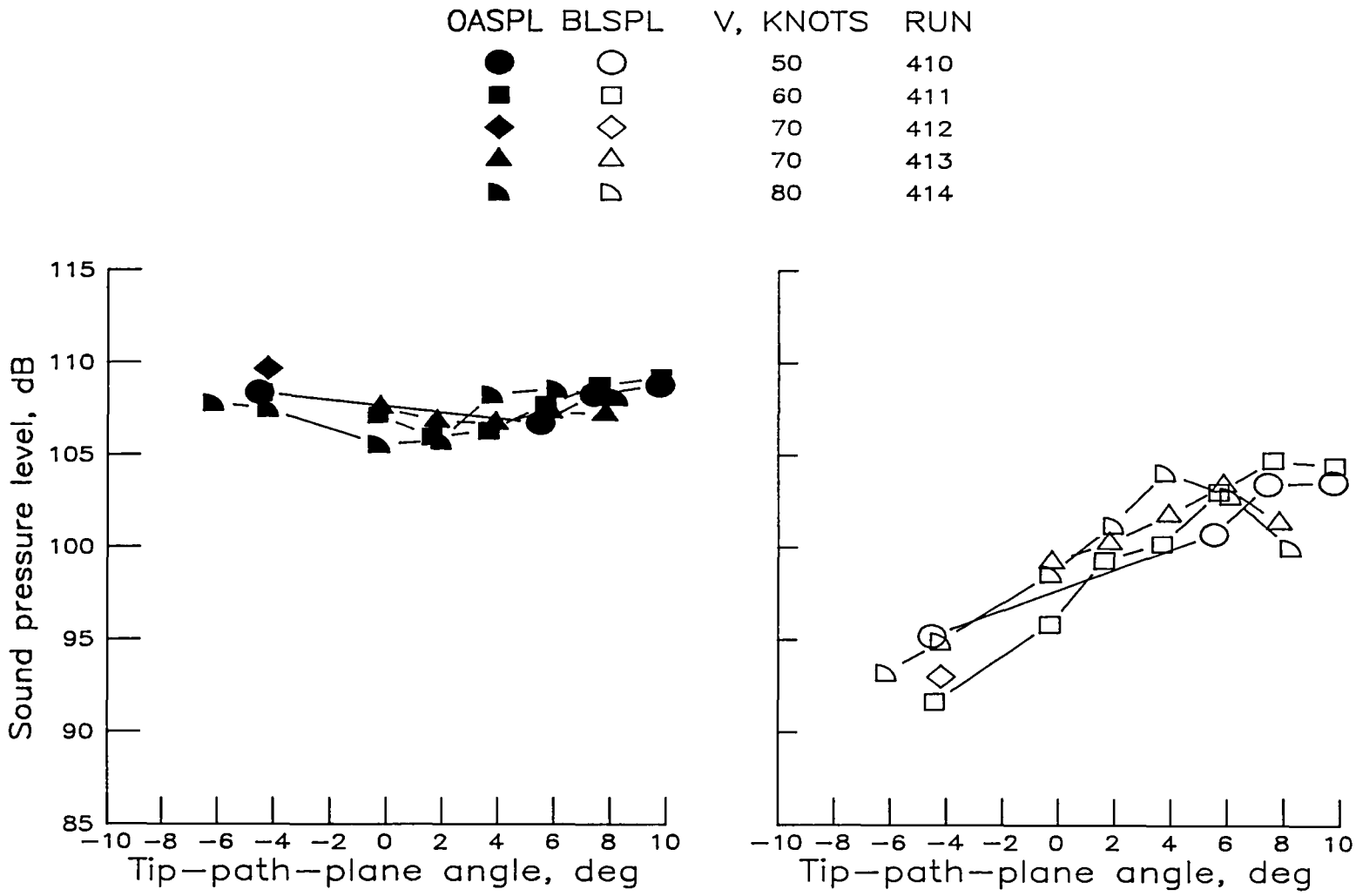

(b) High-twist swept tapered tip (SC1095 airfoil).

Figure A8.- Continued.

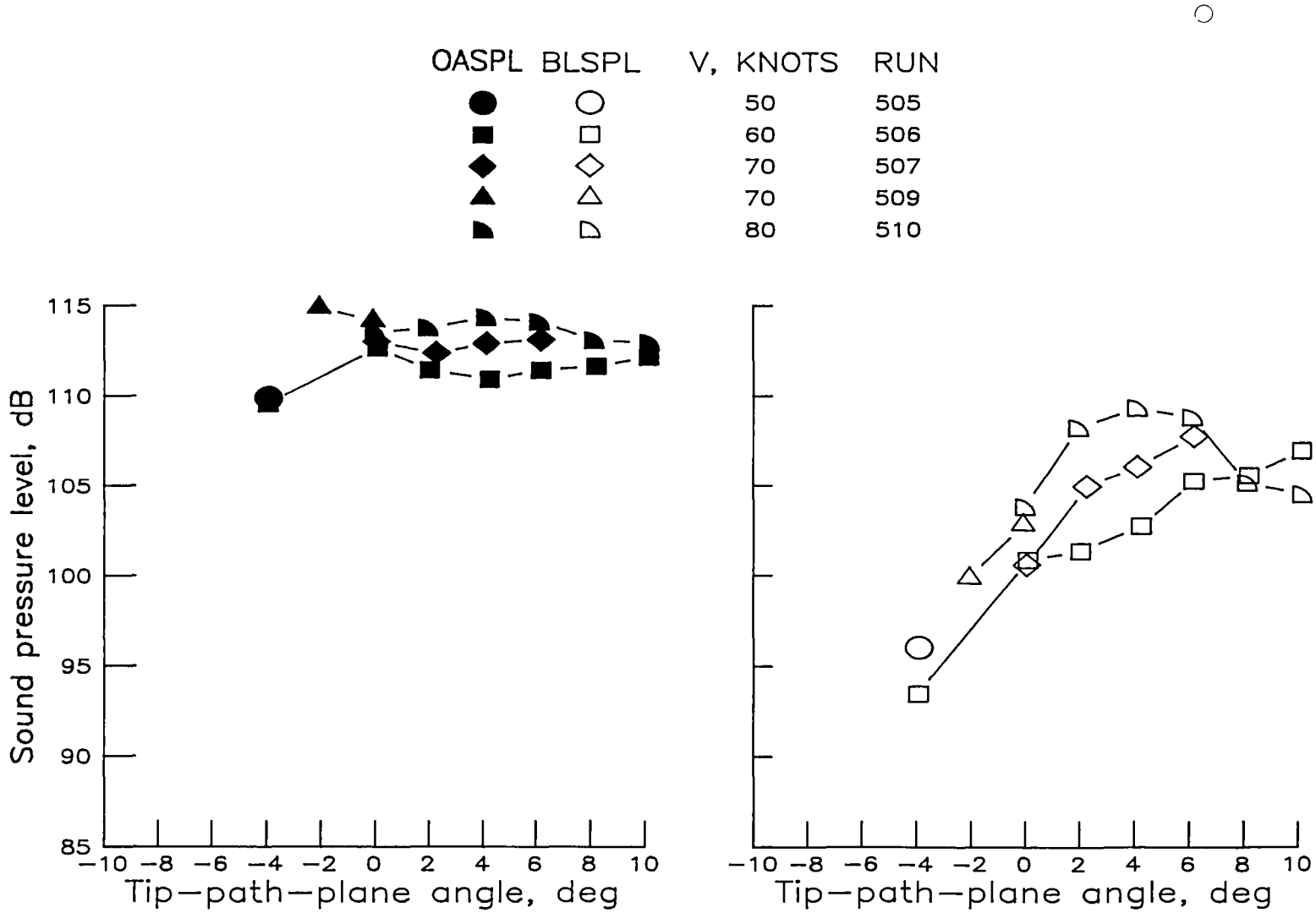

(c) High-twist swept tapered tip (SSC-A07 airfoil).

Figure A8.- Continued.

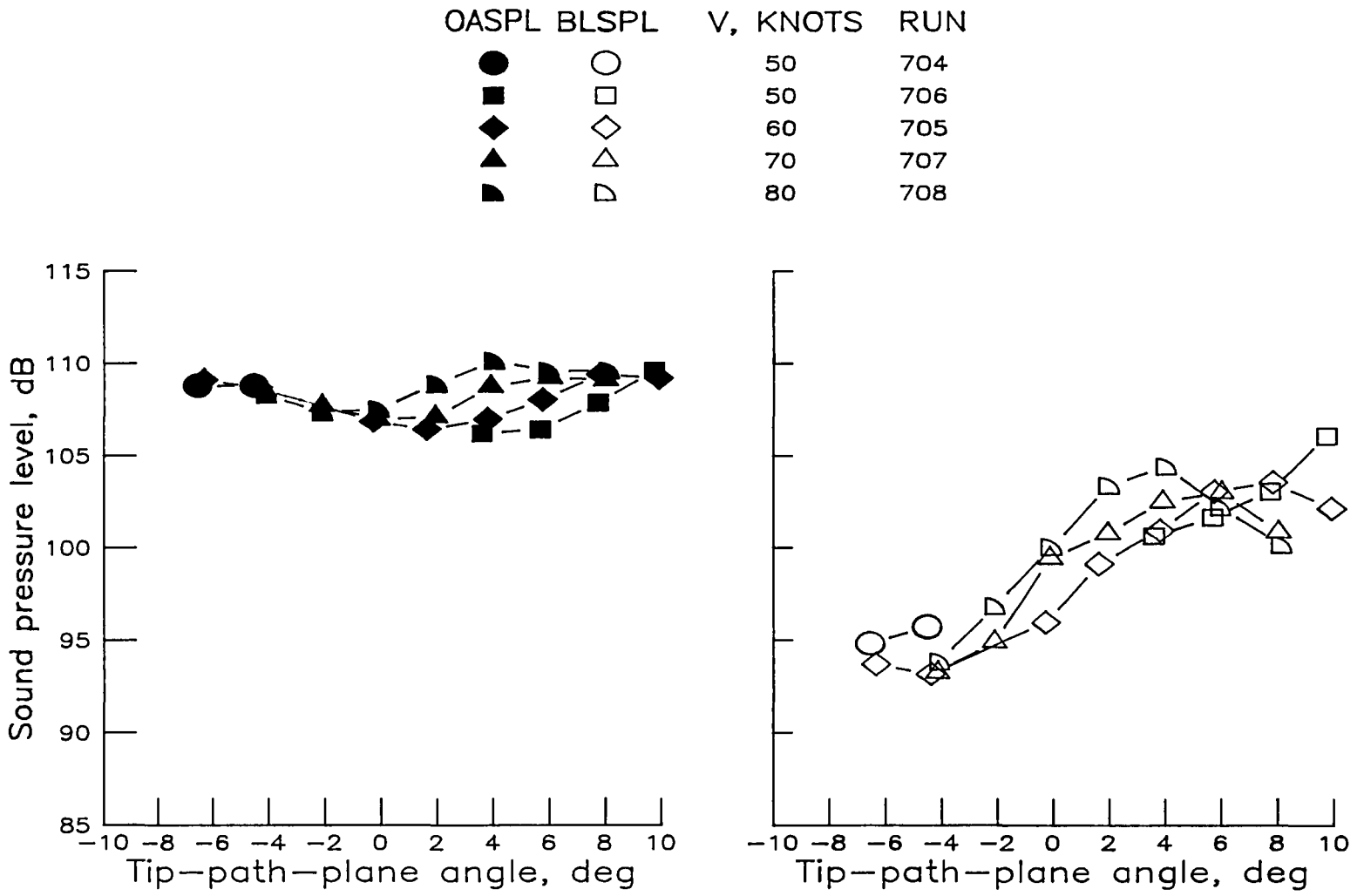

(d) High-twist parabolic tip.

Figure A8.- Continued.

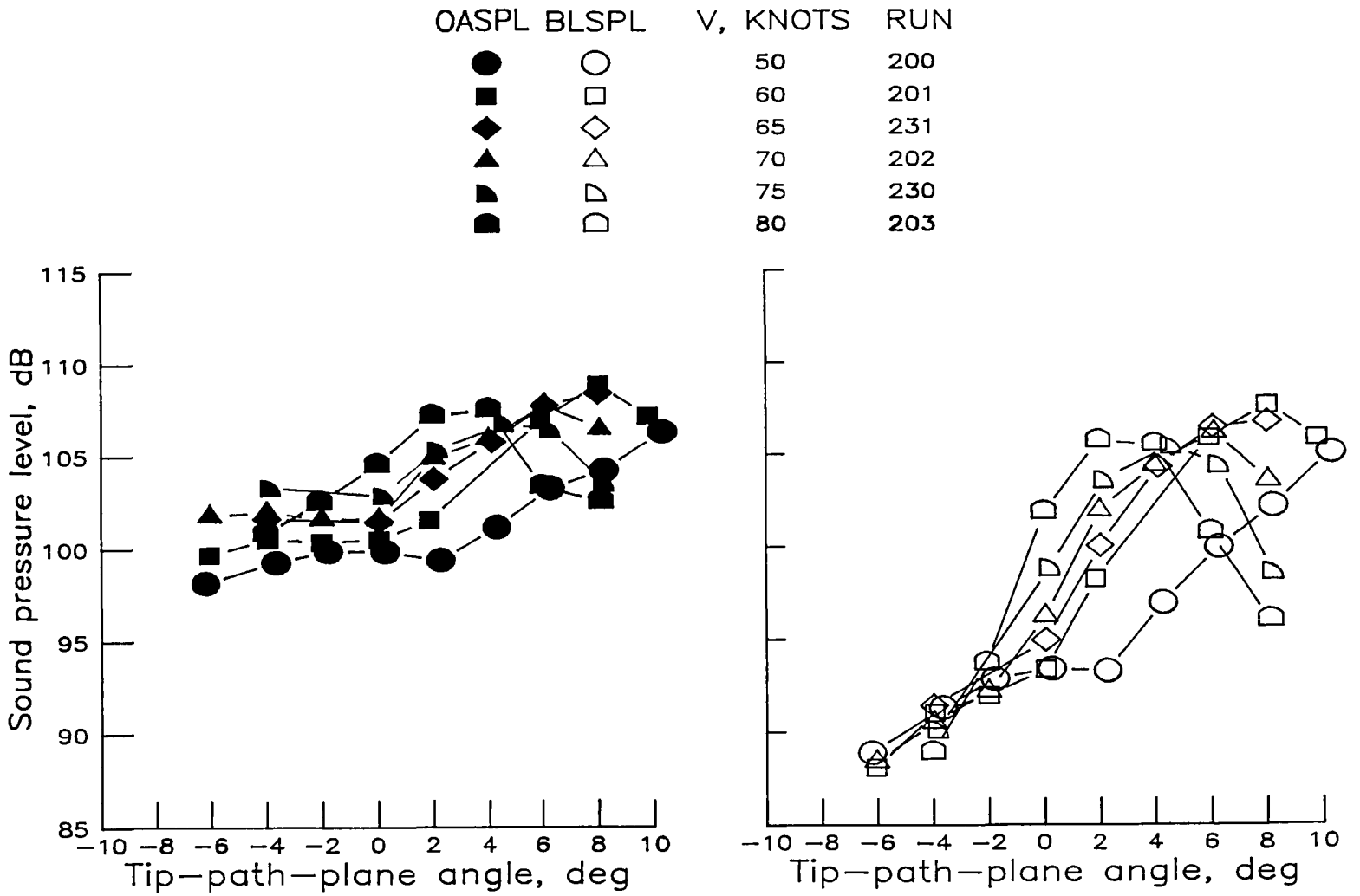

(e) Low-twist standard tip (fig. 24(b)).

Figure A8.- Continued.

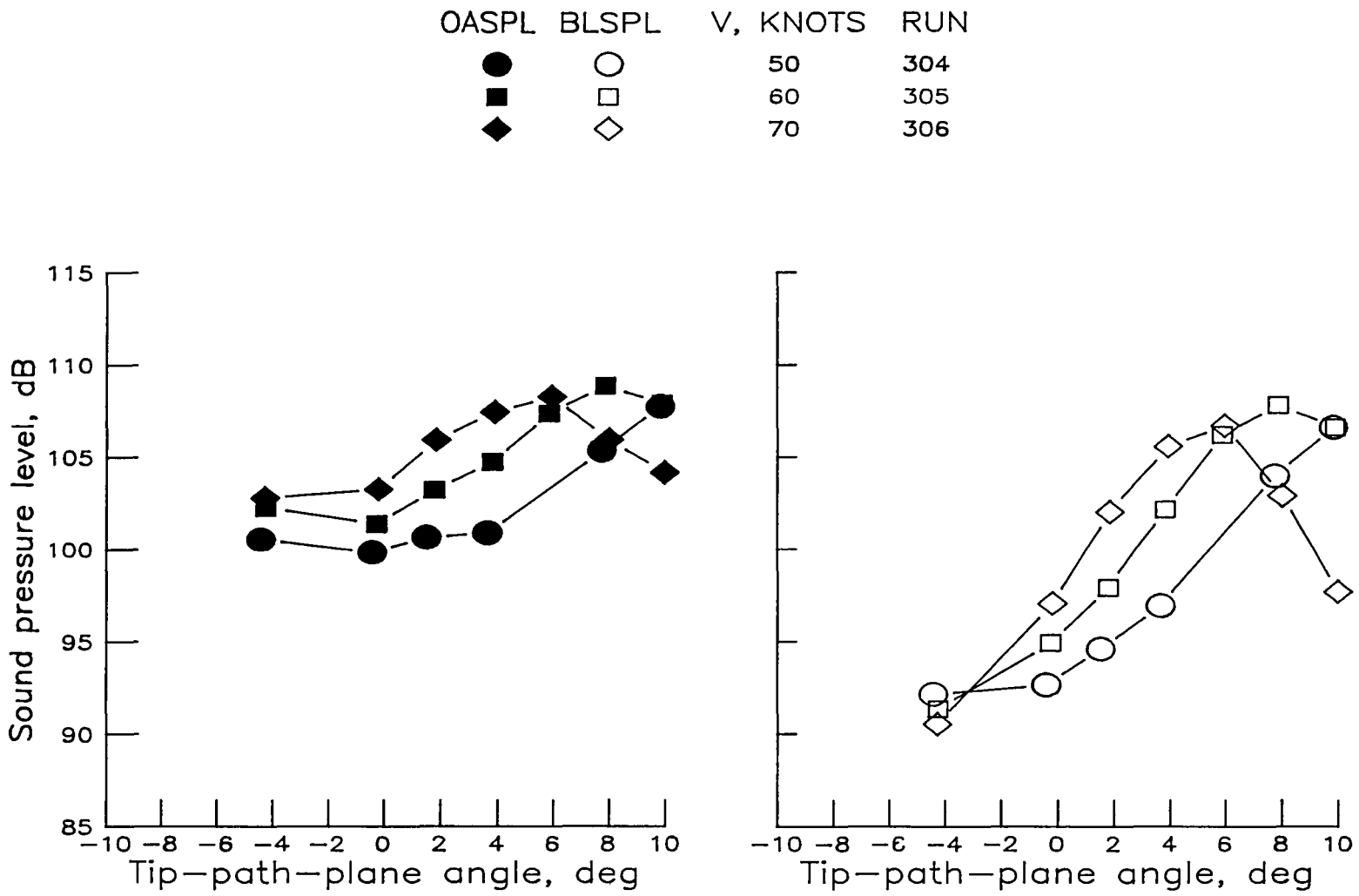

(f) Low-twist anhedral tip.

Figure A8.- Continued.

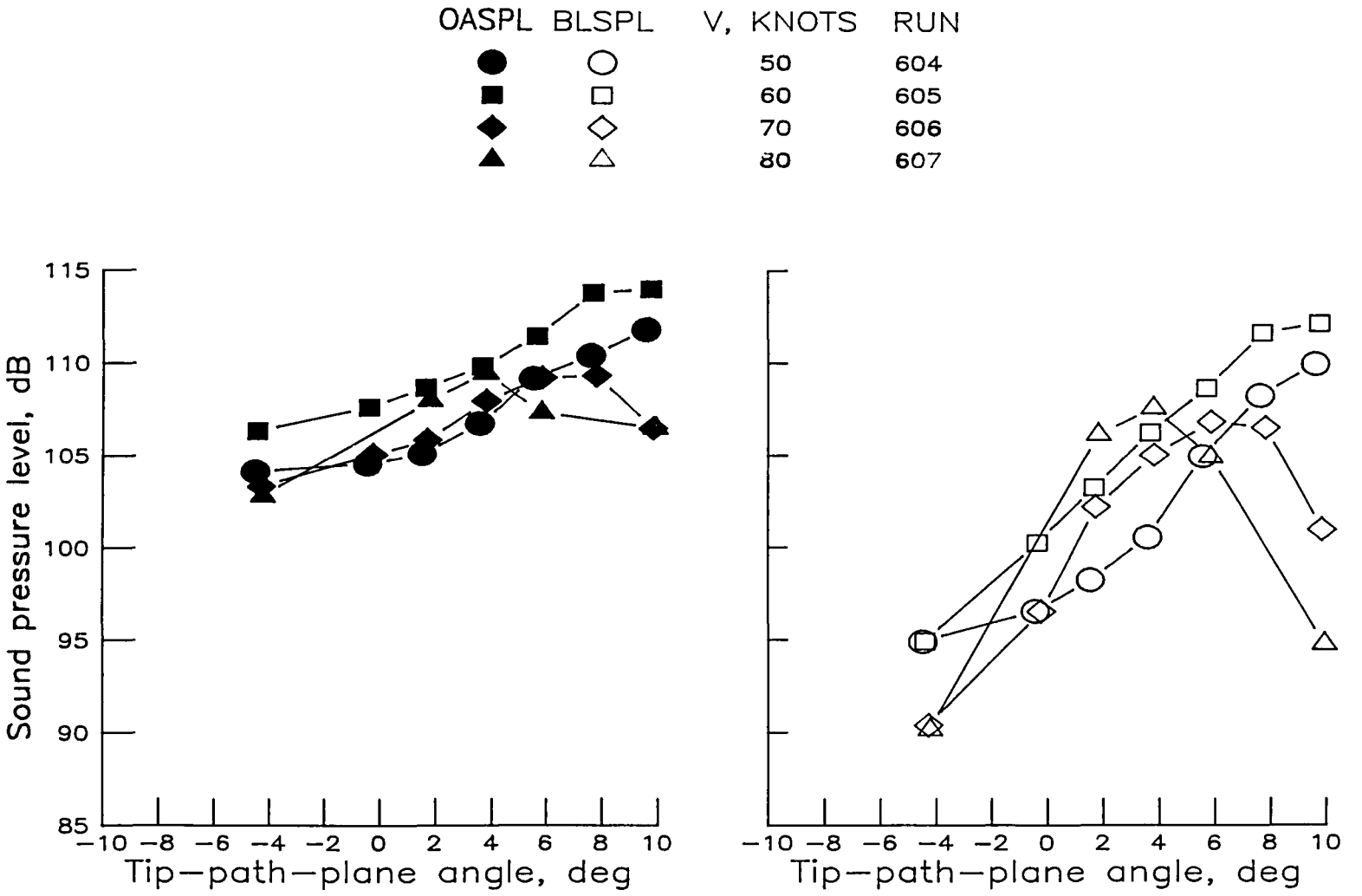

(g) Low-twist swept tip.

Figure A8.- Continued.

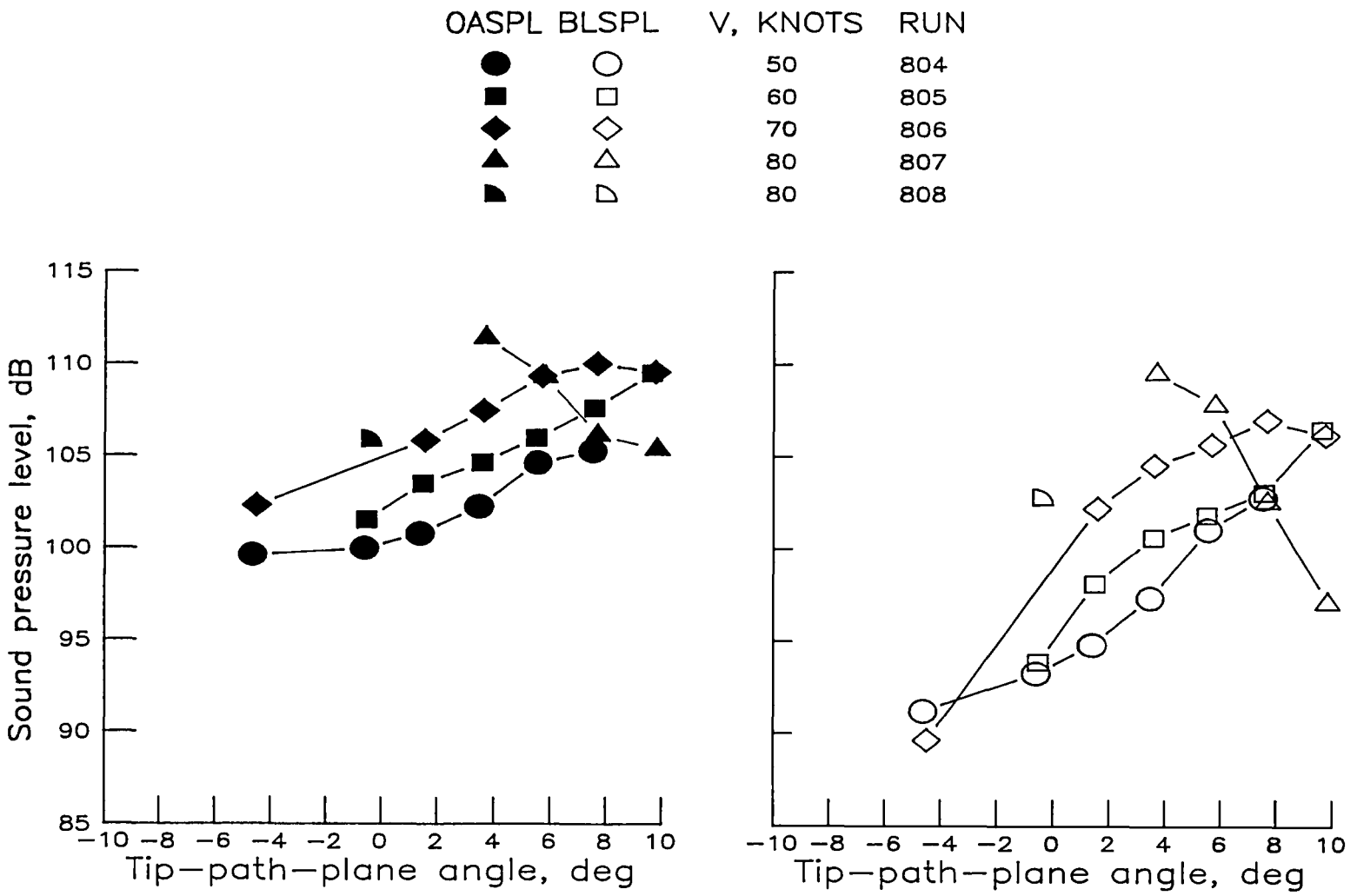

(h) Low-twist tapered tip.

Figure A8.- Continued.

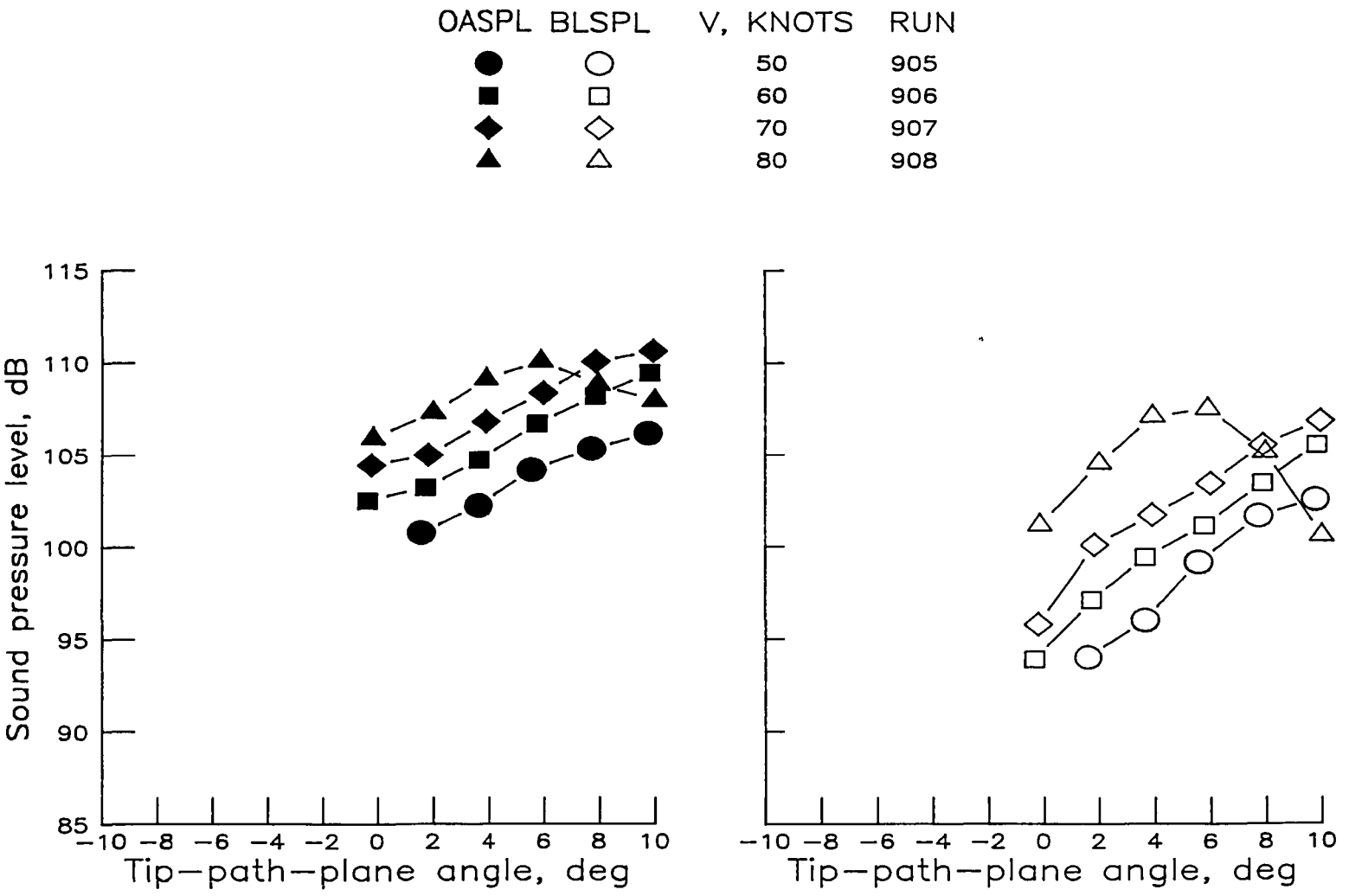

(i) Low-twist square tip.

Figure A8.- Concluded.

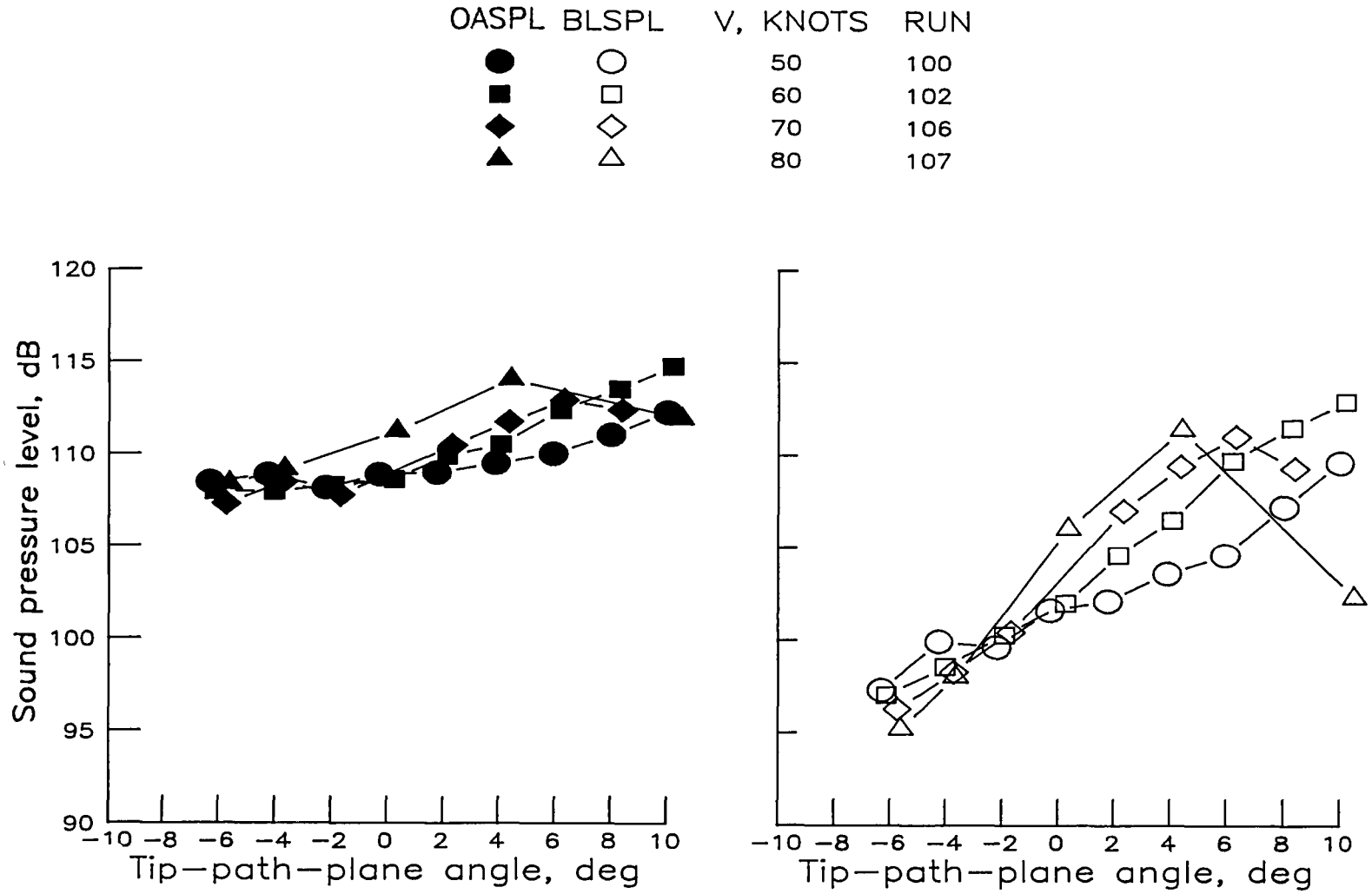

(a) High-twist standard tip (fig. 25(a)).

Figure A9.- Overall and band-limited sound pressure levels as a function of tip-path-plane angle over velocity range from 50 to 80 knots for microphone 12.

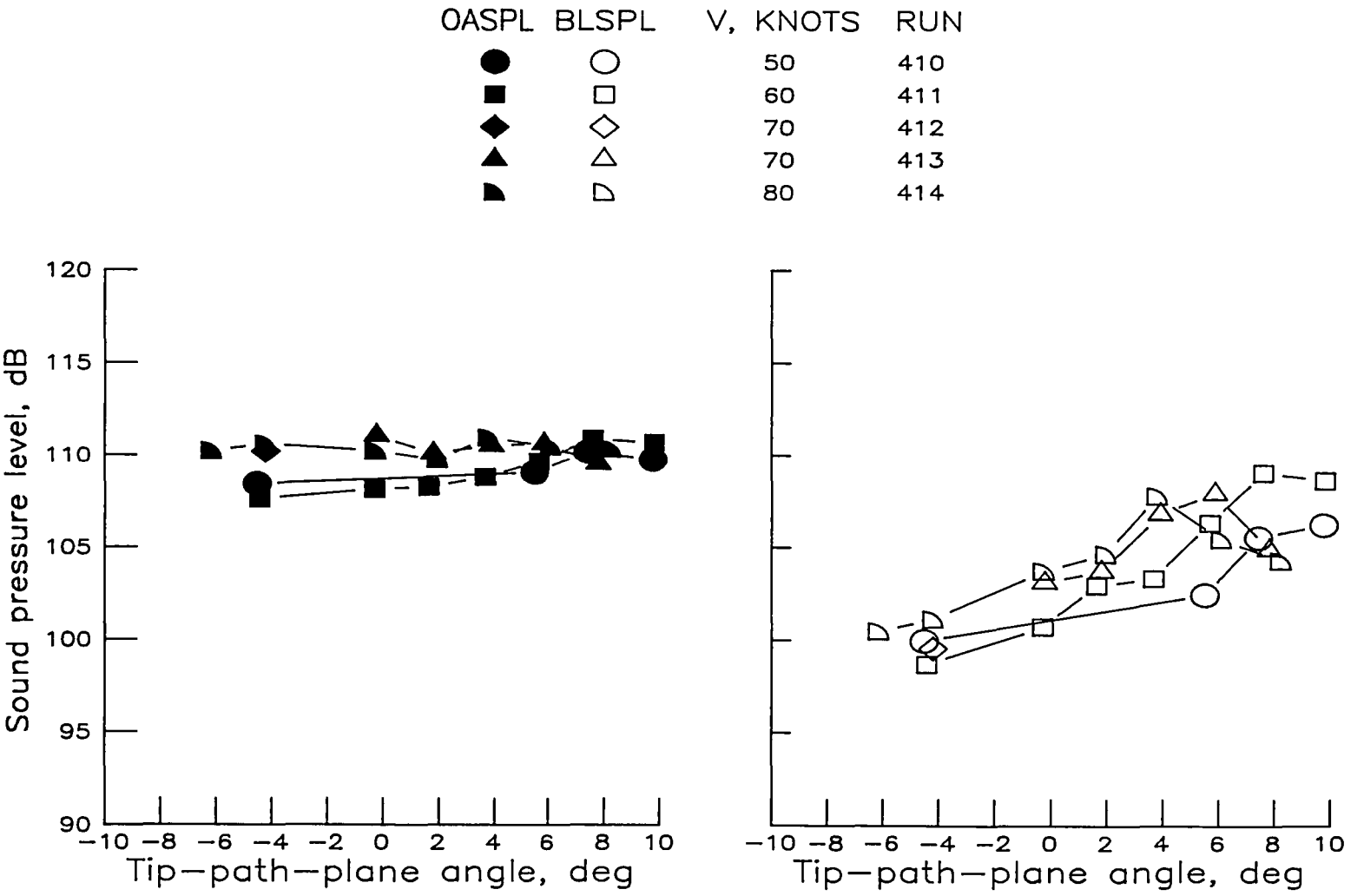

(b) High-twist swept tapered tip (SC1095 airfoil).

Figure A9.- Continued.

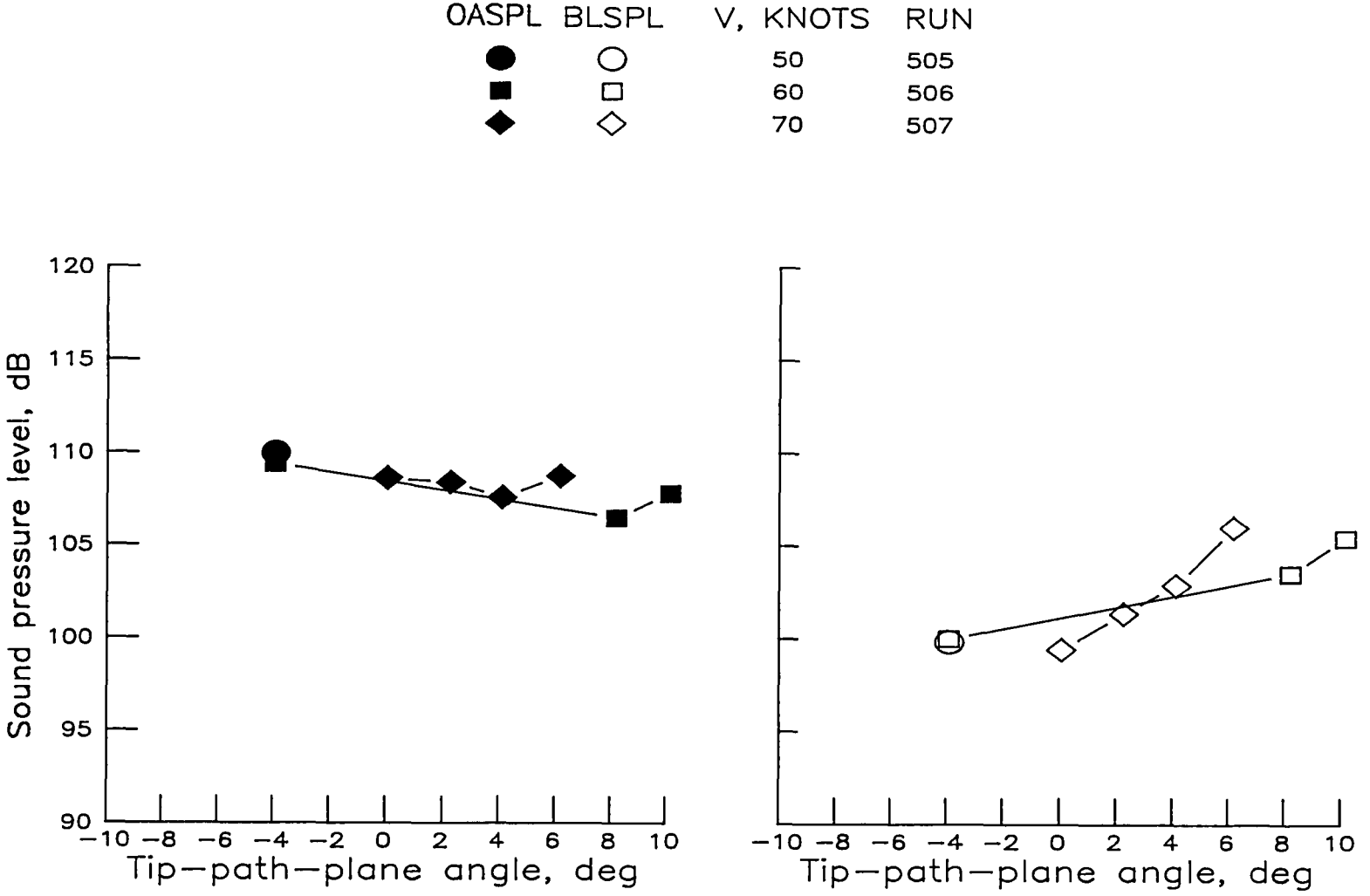

(c) High-twist swept tapered tip (SSC-A07 airfoil).

Figure A9.- Continued.

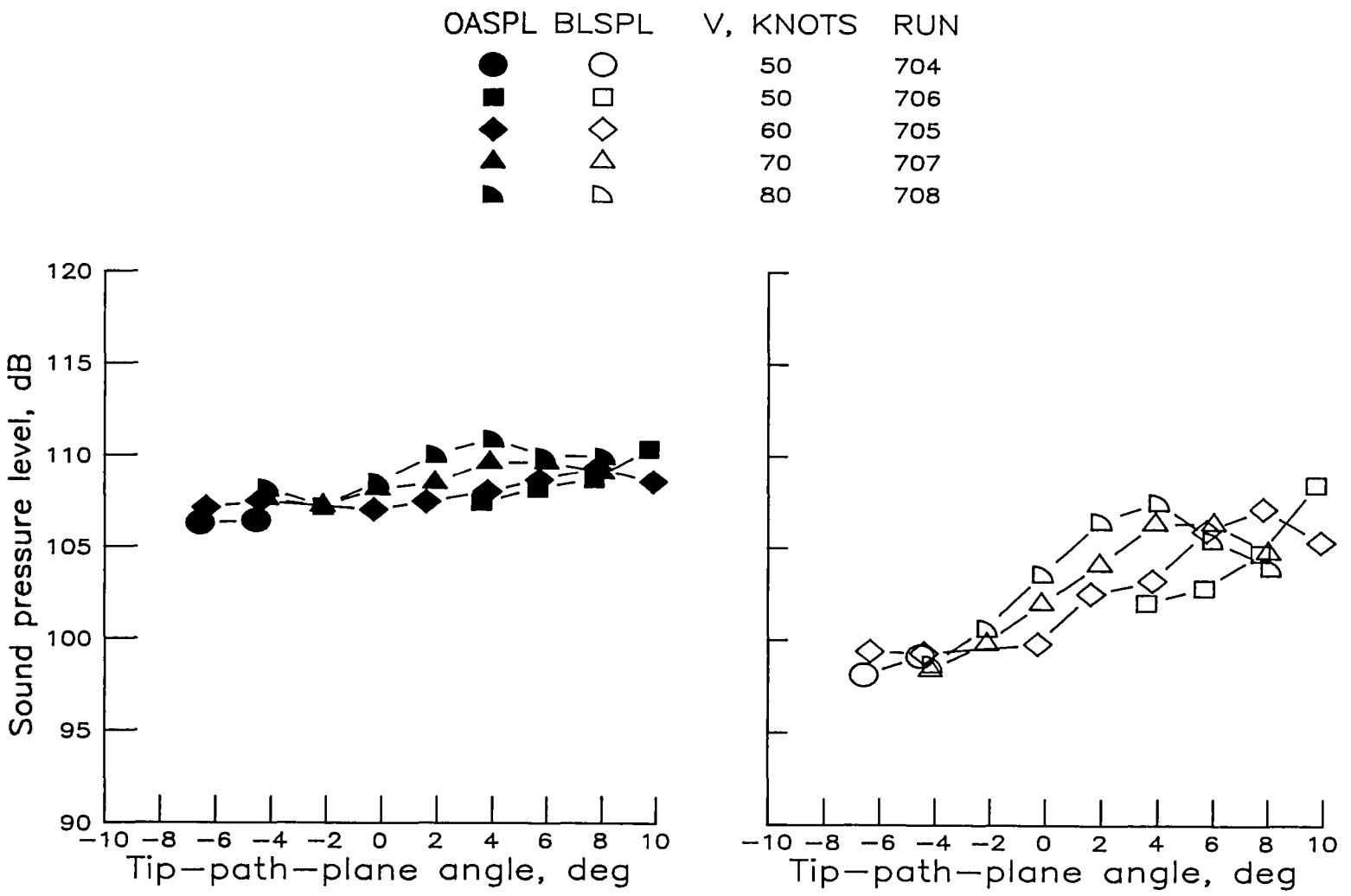

(d) High-twist parabolic tip.

Figure A9.- Continued.

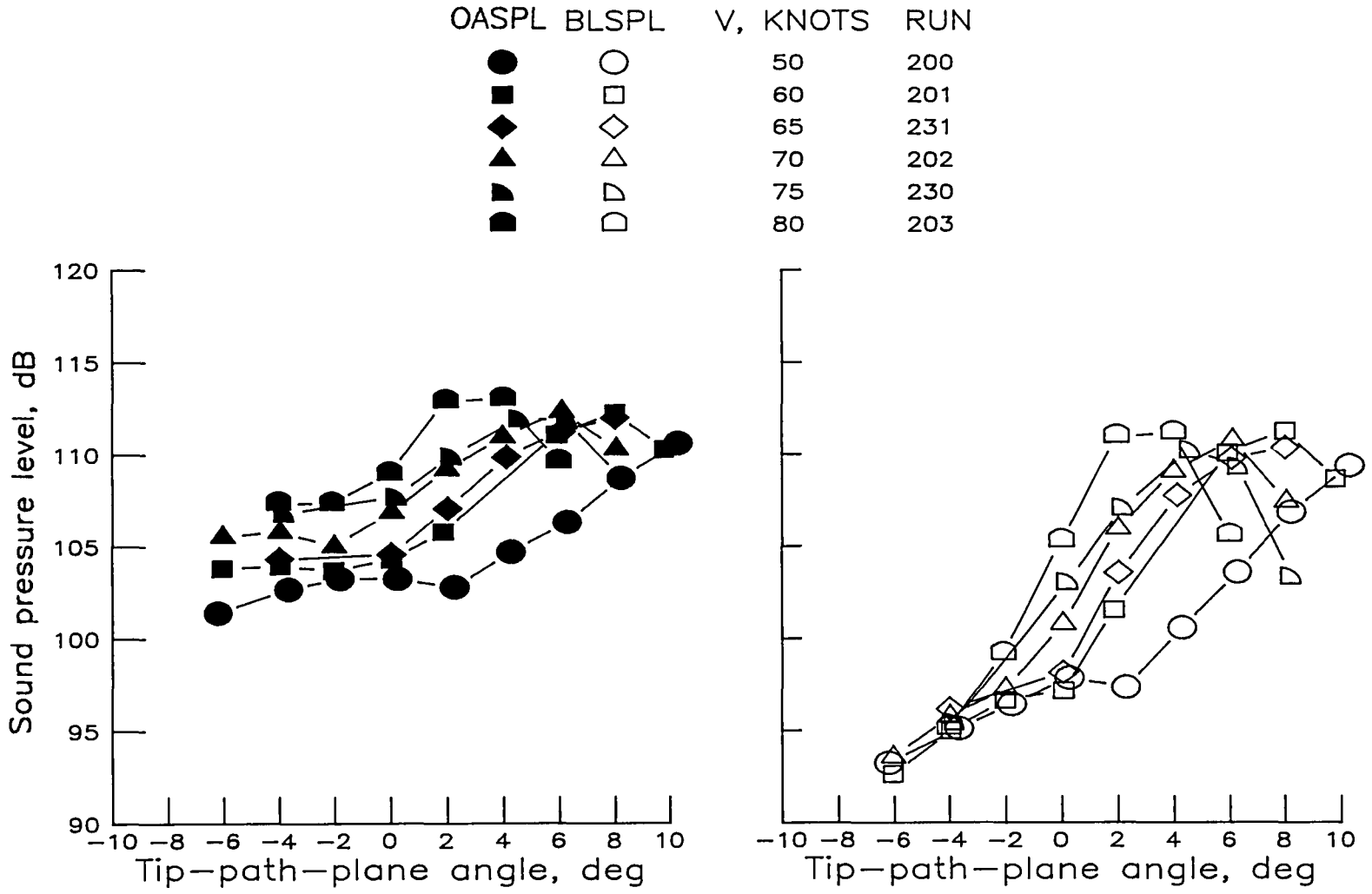

(e) Low-twist standard tip (fig. 25(b)).

Figure A9.- Continued.

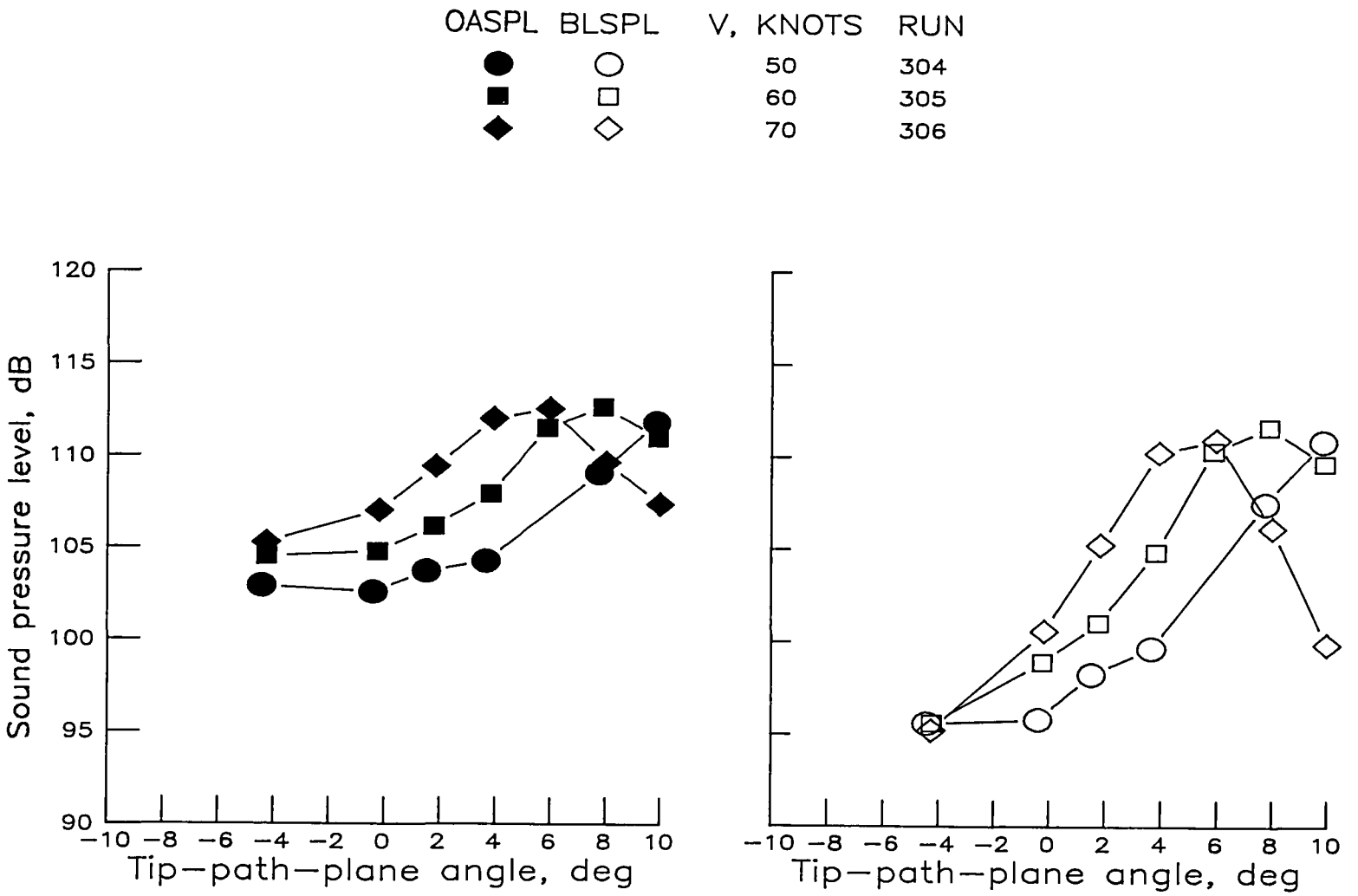

(f) Low-twist anhedral tip.

Figure A9.- Continued.

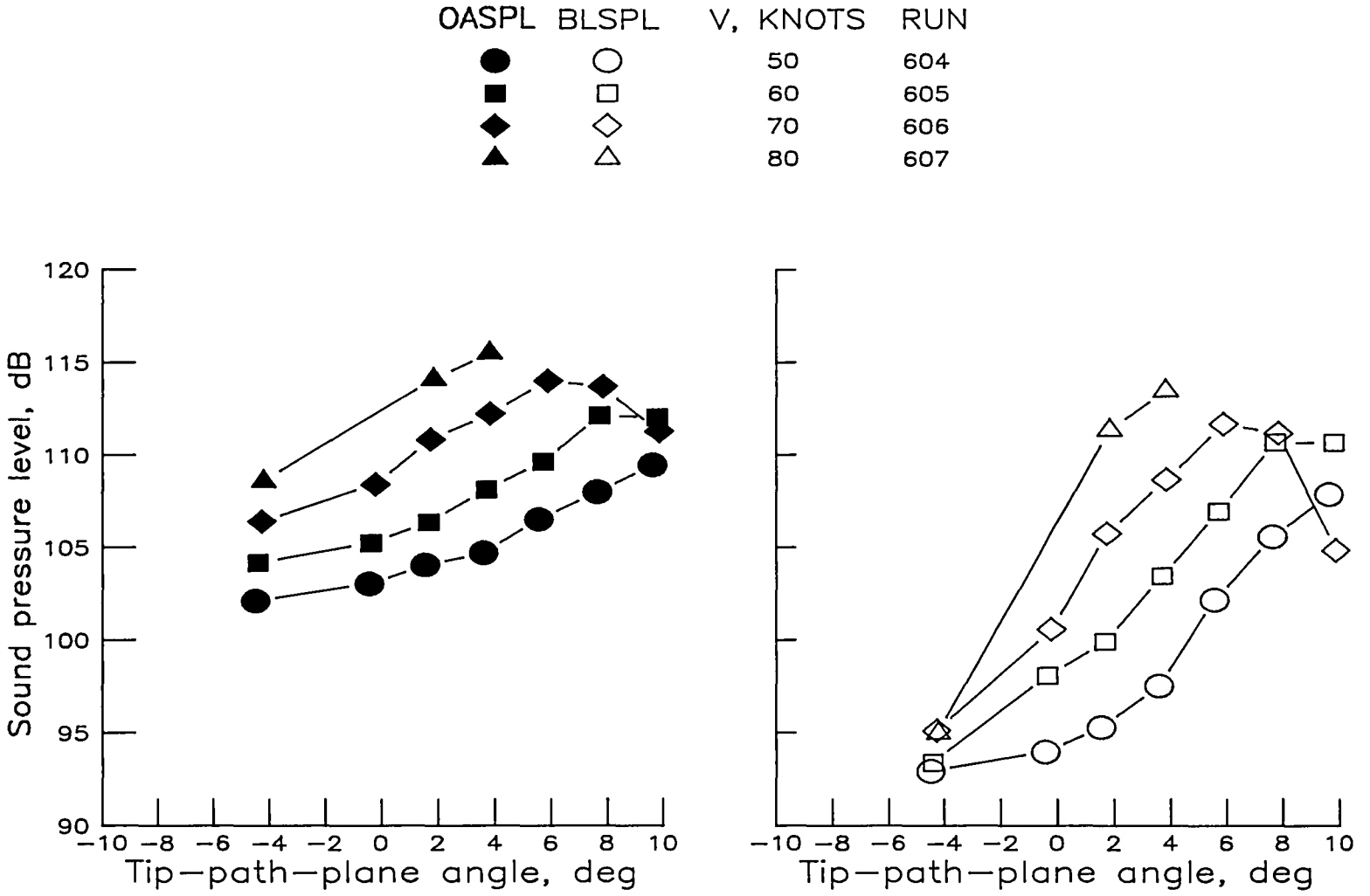

(g) Low-twist swept tip.

Figure A9.- Continued.

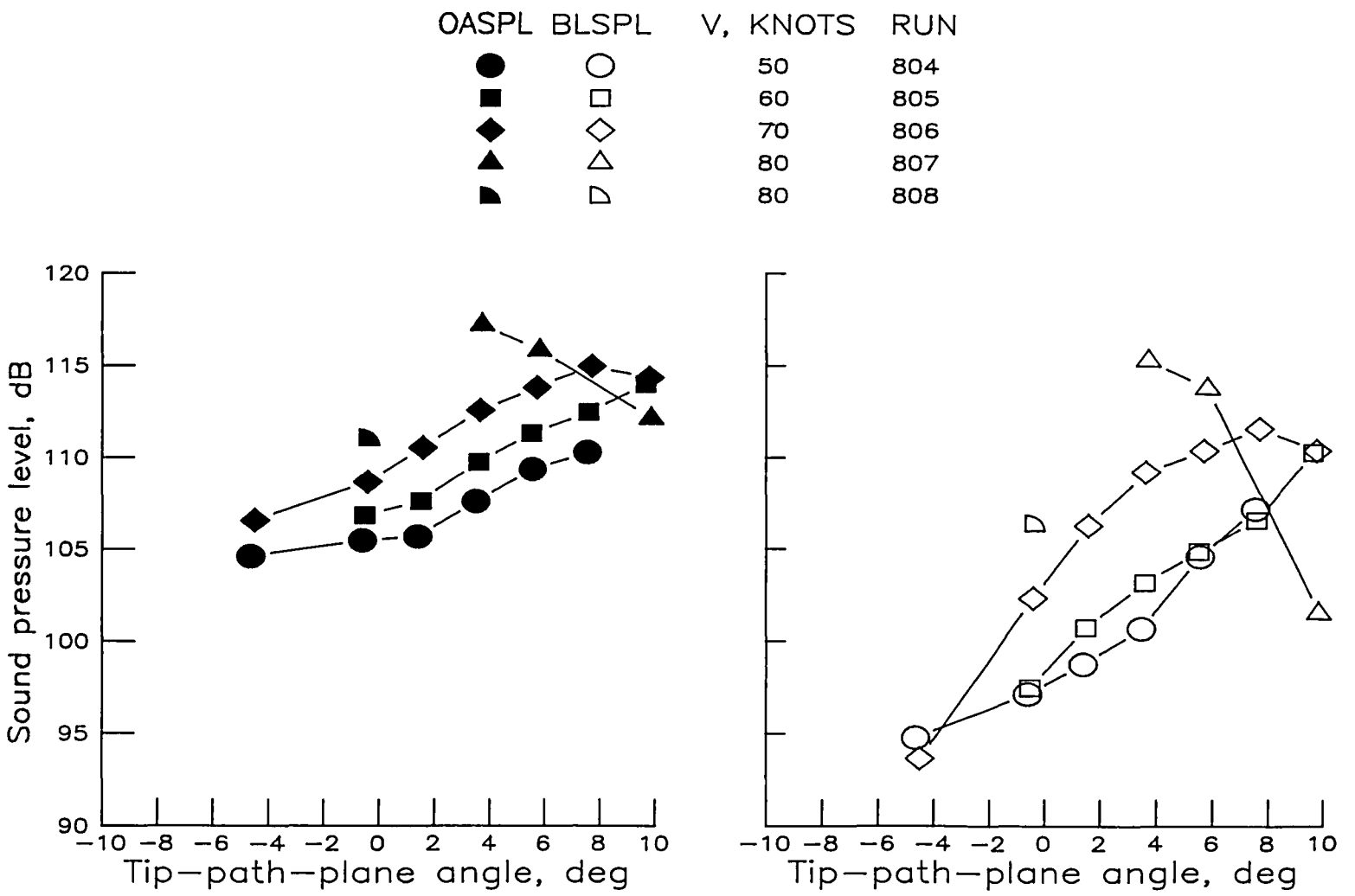

(h) Low-twist tapered tip.

Figure A9.- Continued.

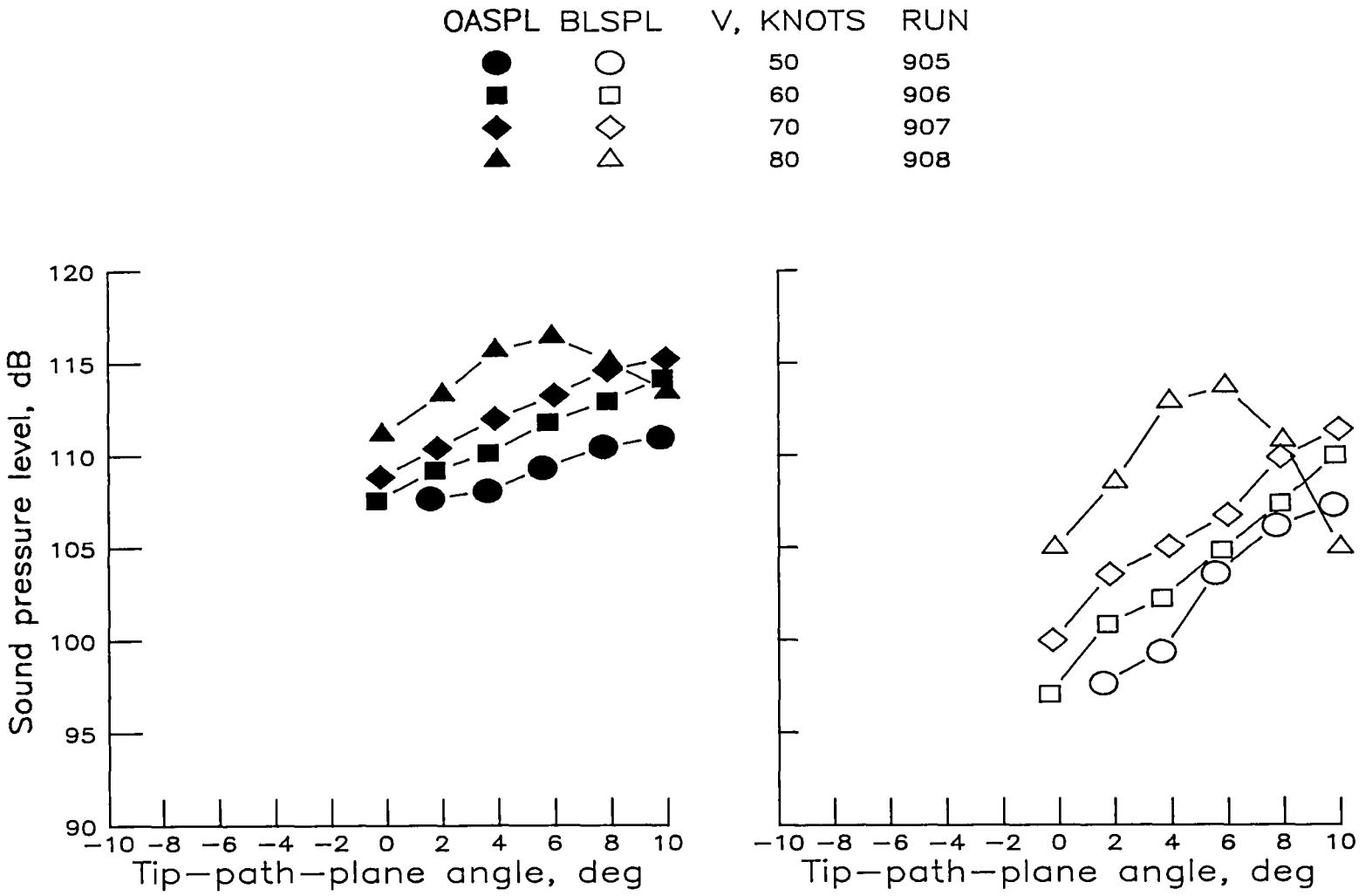

(1) Low-twist square tip.

Figure A9.- Concluded.

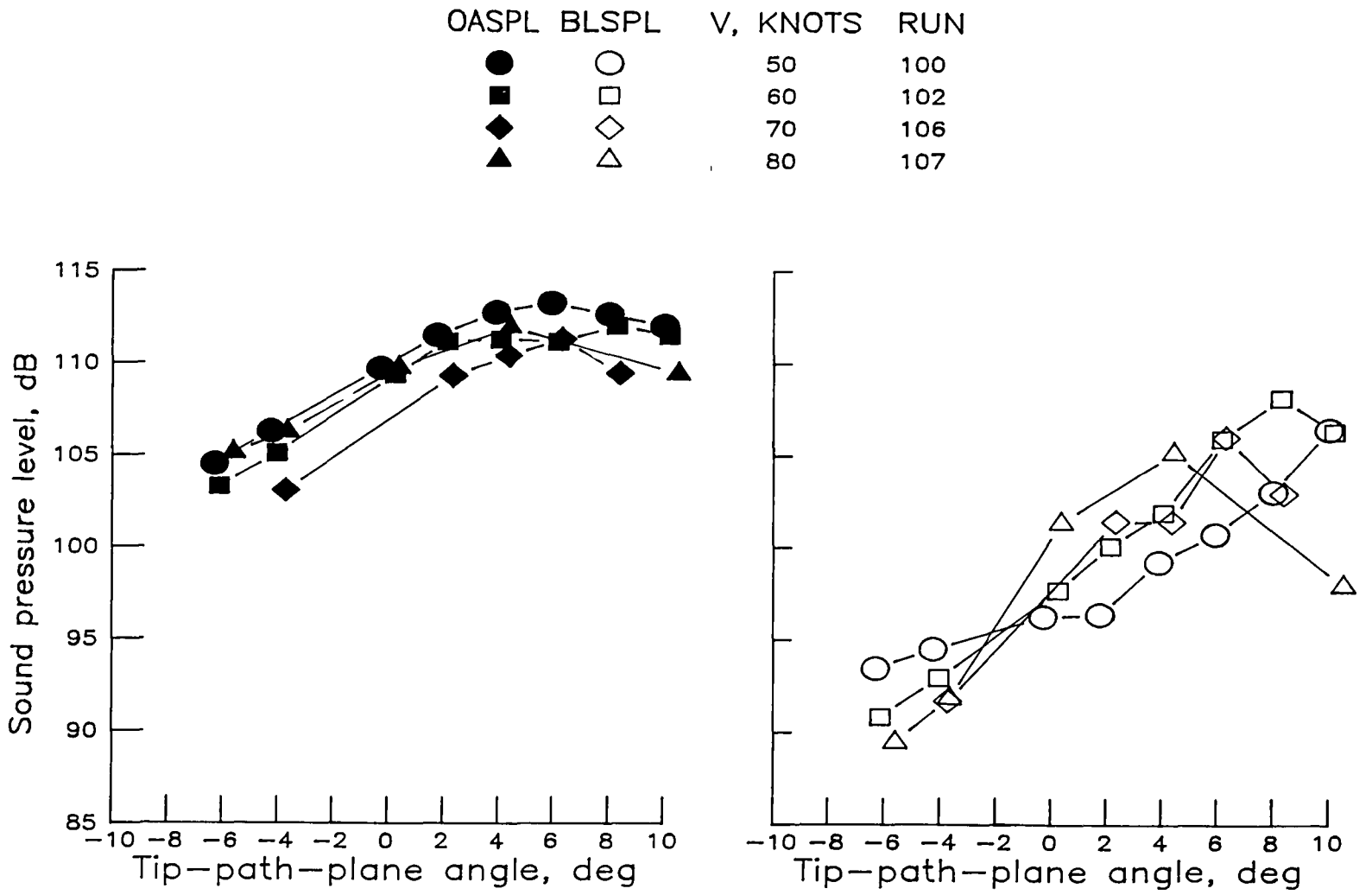

(a) High-twist standard tip (fig. 26(a)).

Figure A10.- Overall and band-limited sound pressure levels as a function of tip-path-plane angle over velocity range from 50 to 80 knots for microphone 17.

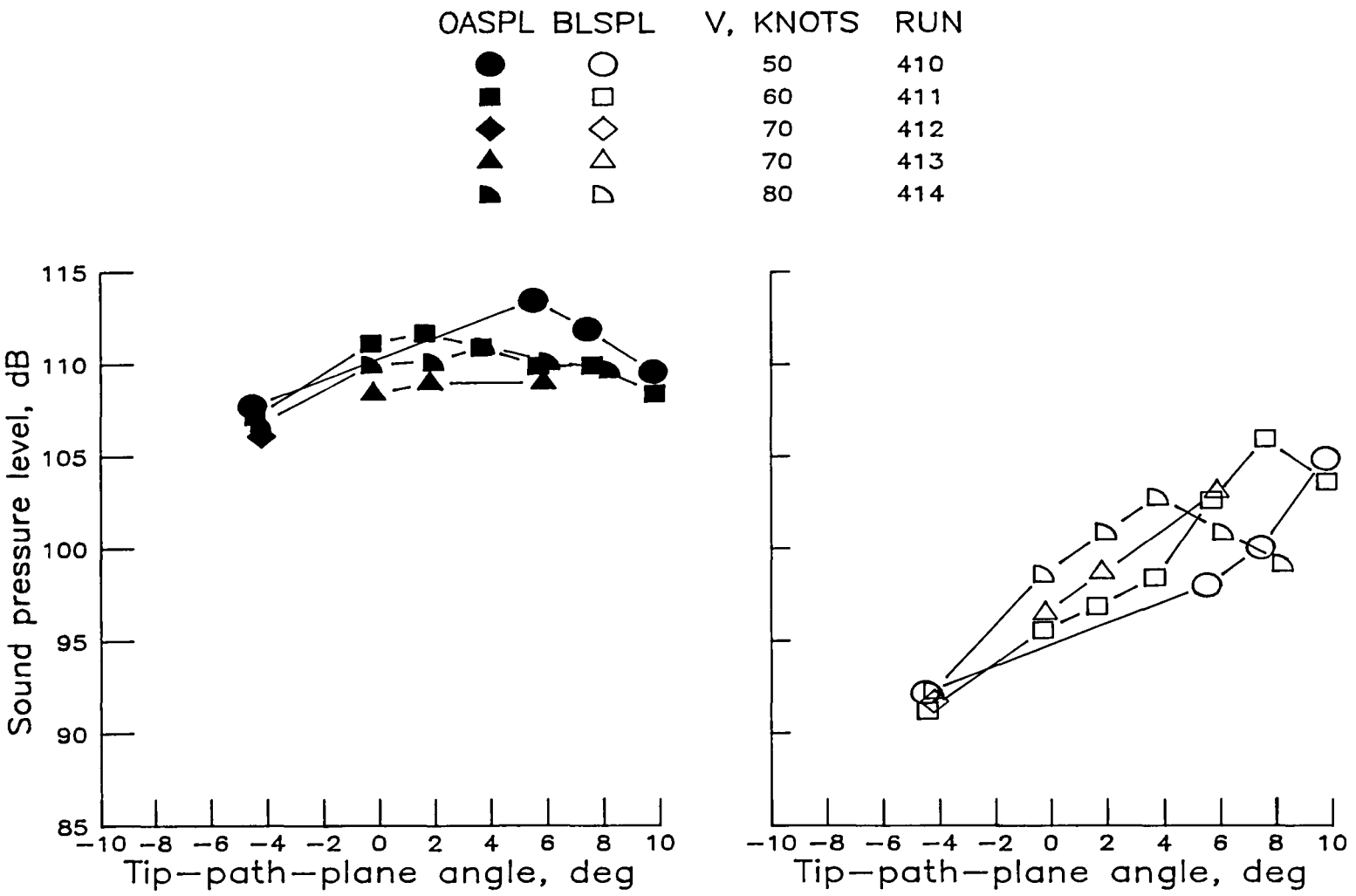

(b) High-twist swept tapered tip (SC1095 airfoil).

Figure A10.- Continued.

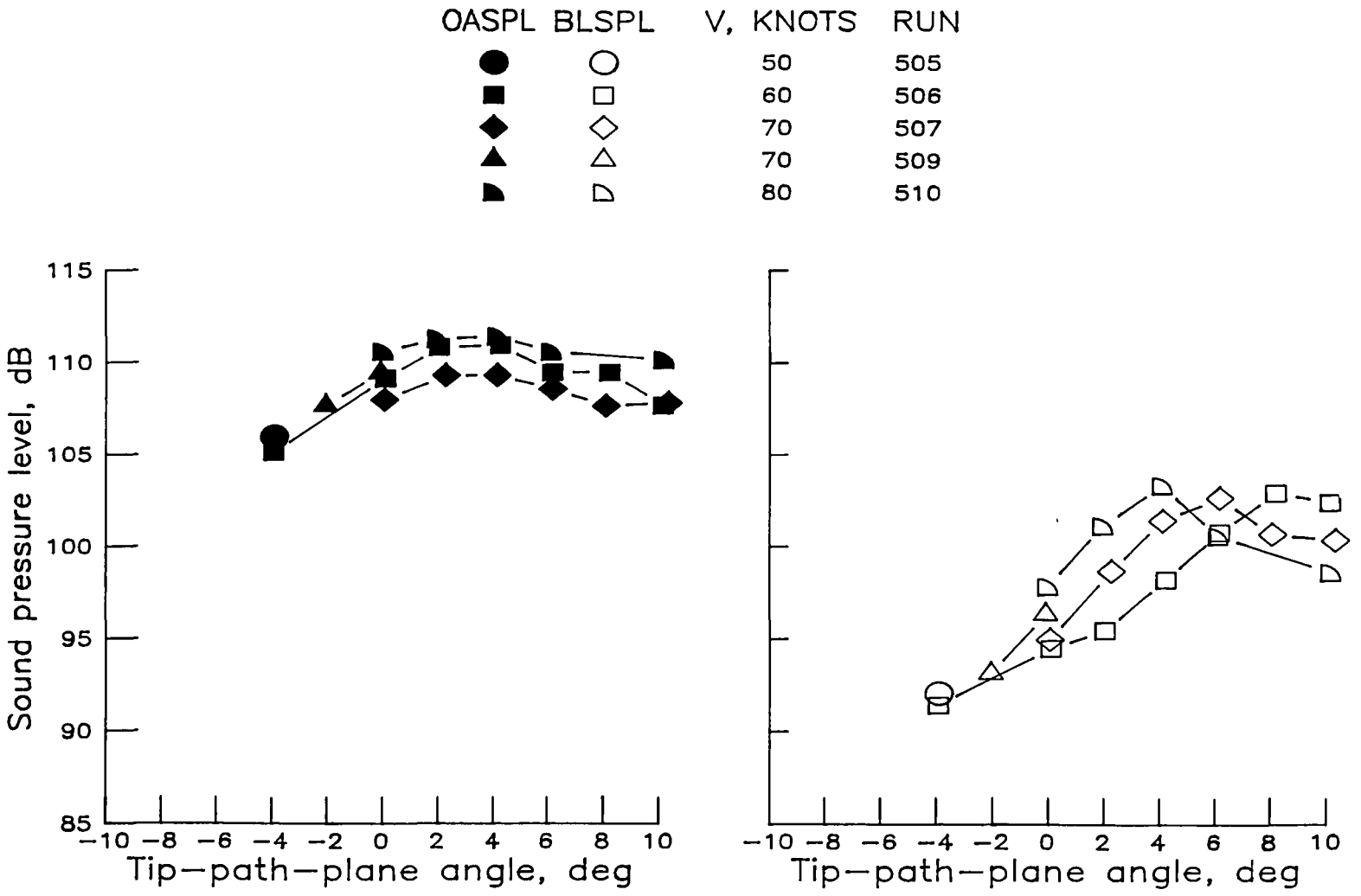

(c) High-twist swept tapered tip (SSC-A07 airfoil).

Figure A10.- Continued.

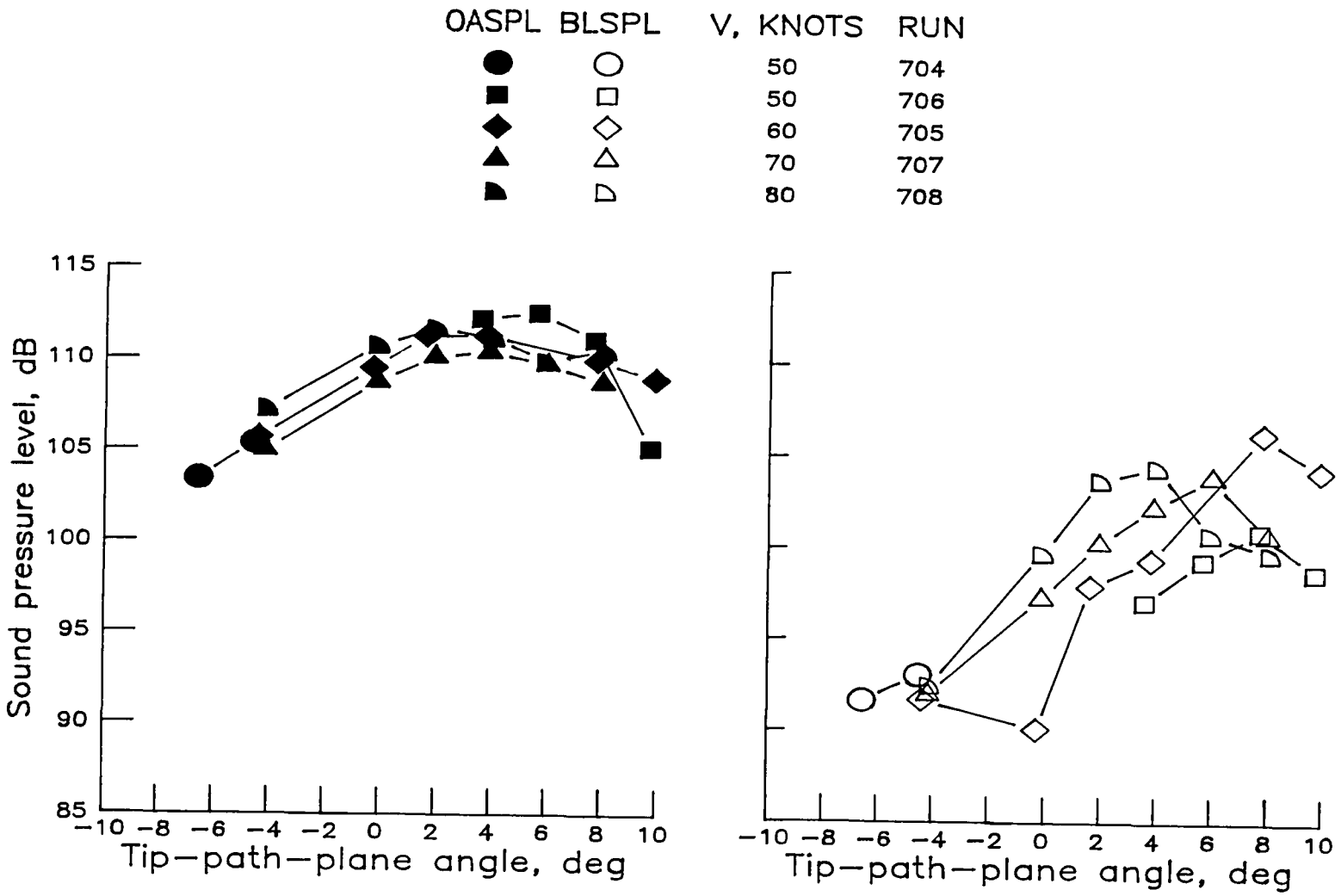

(d) High-twist parabolic tip.

Figure A10.- Continued.

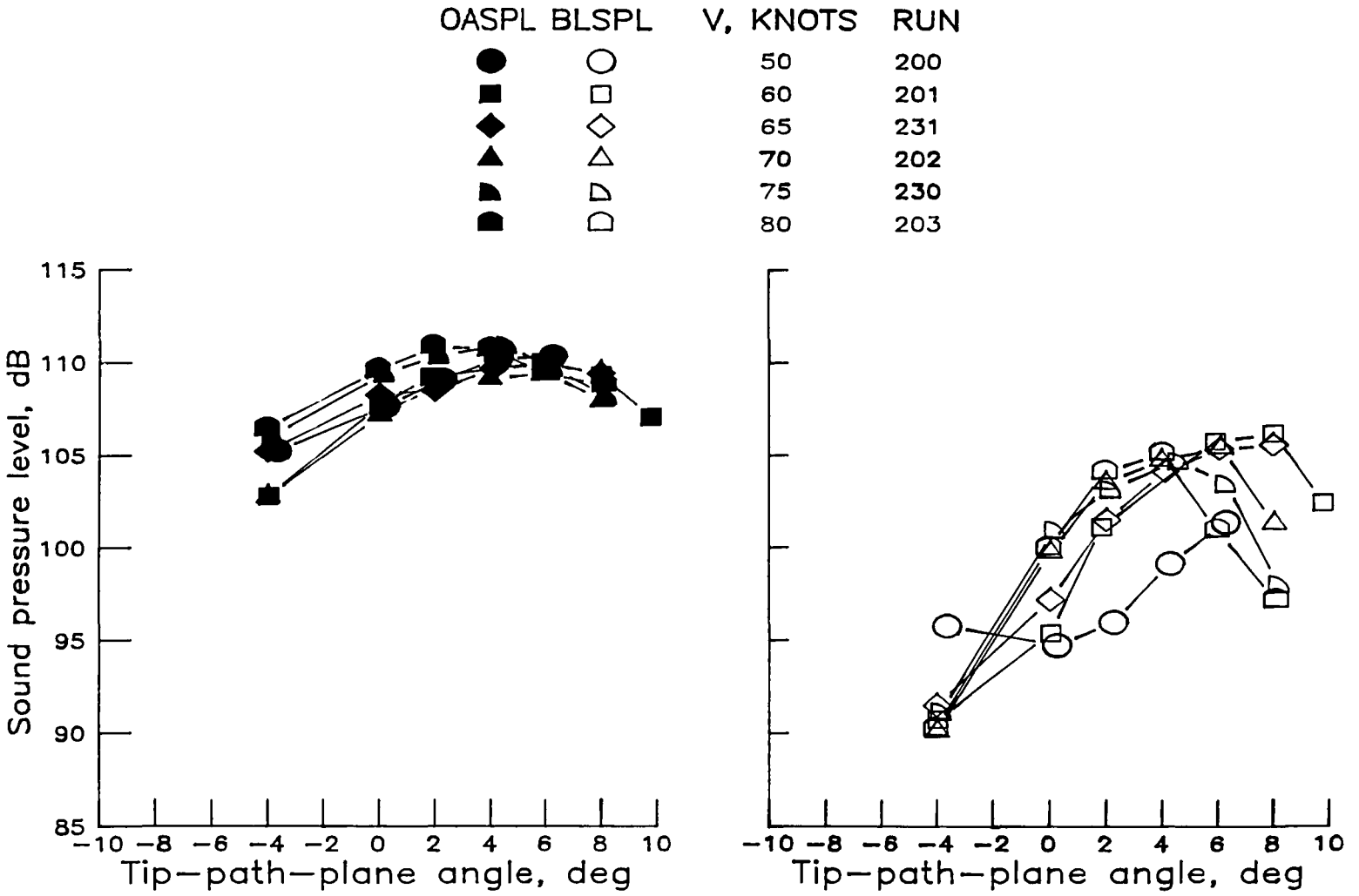

(e) Low-twist standard tip (fig. 26(b)).

Figure A10.- Continued.

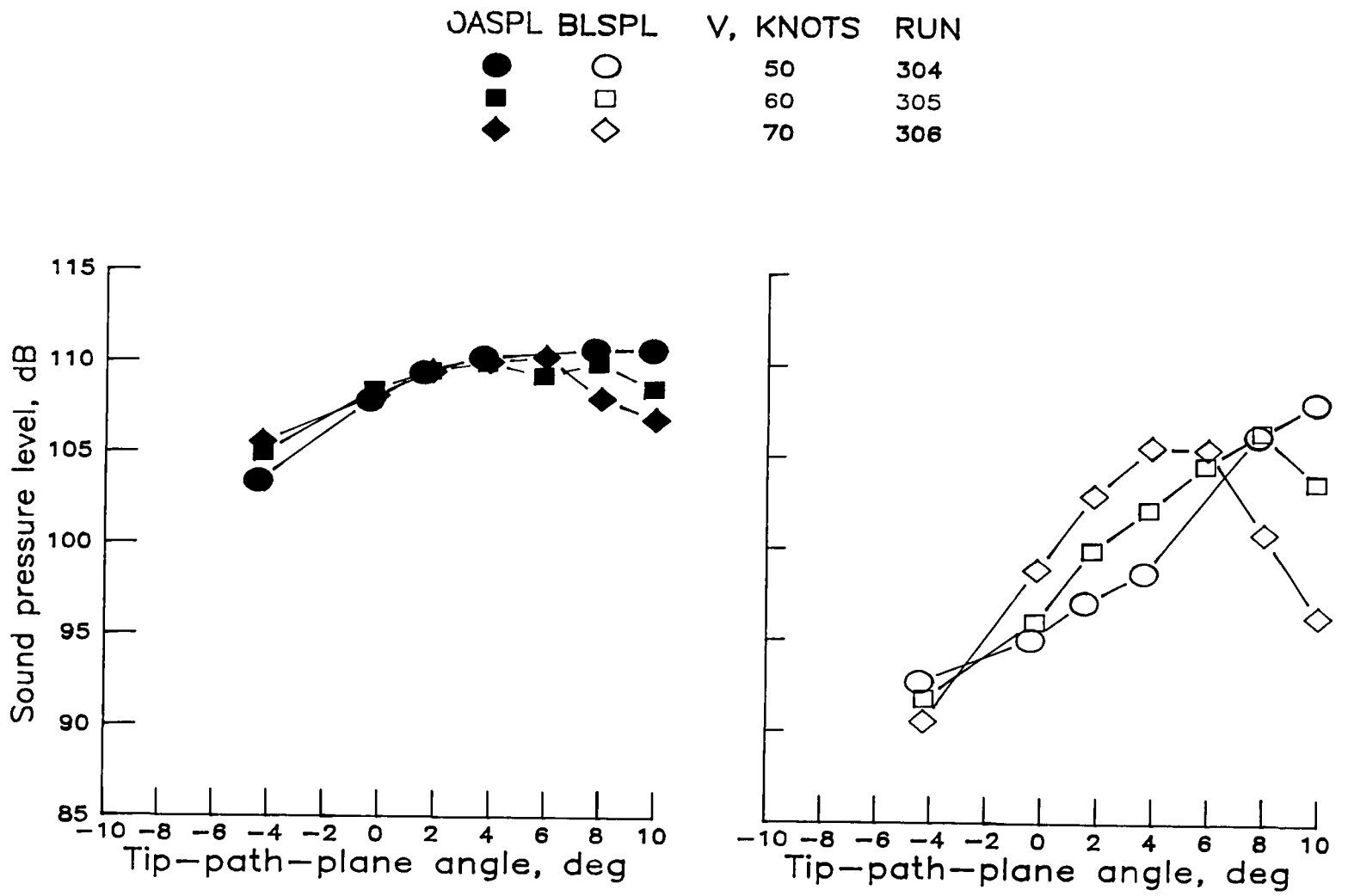

(f) Low-twist anhedral tip.

Figure A10.- Continued.

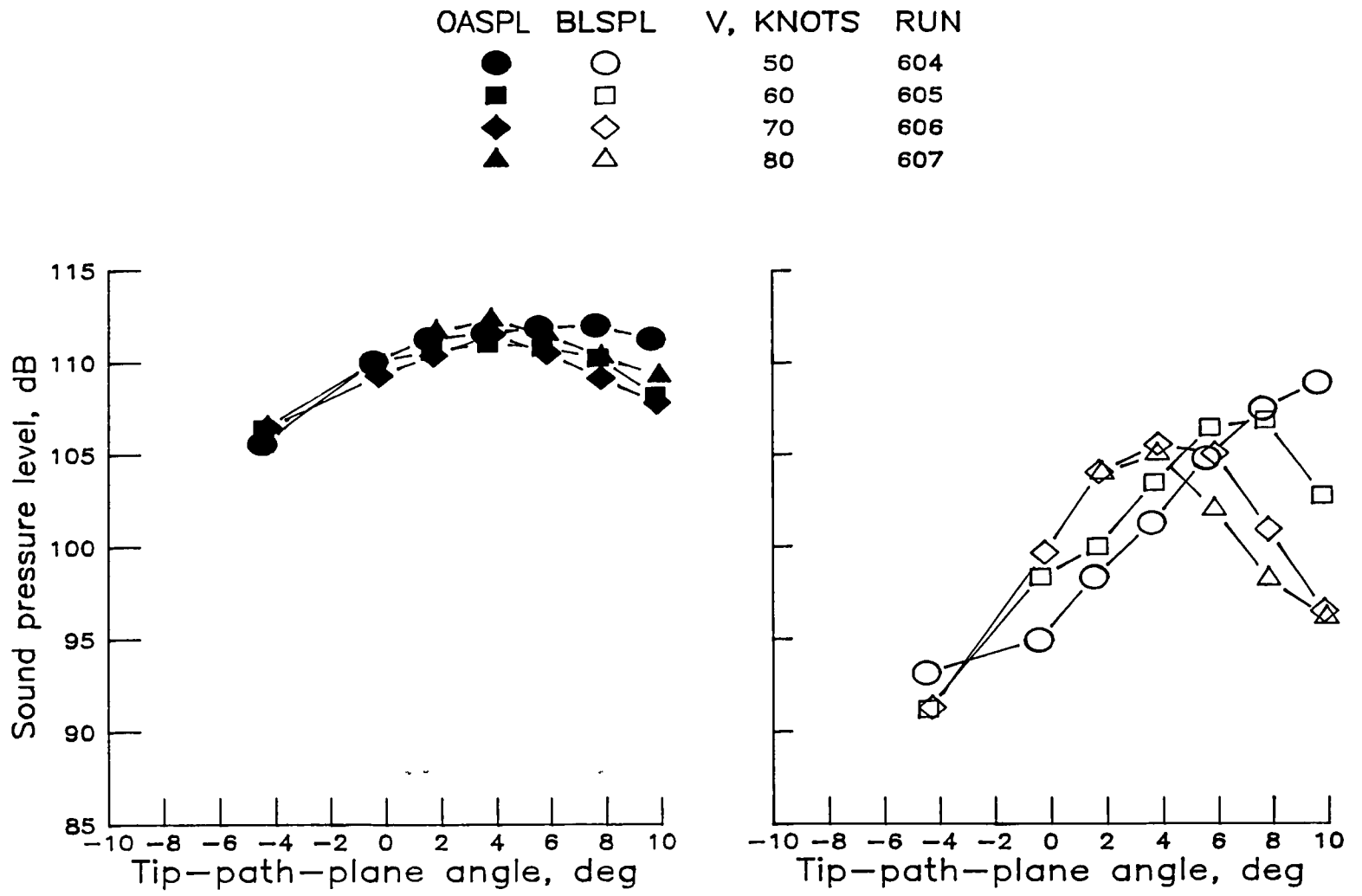

(g) Low-twist swept tip.

Figure A10.- Continued.

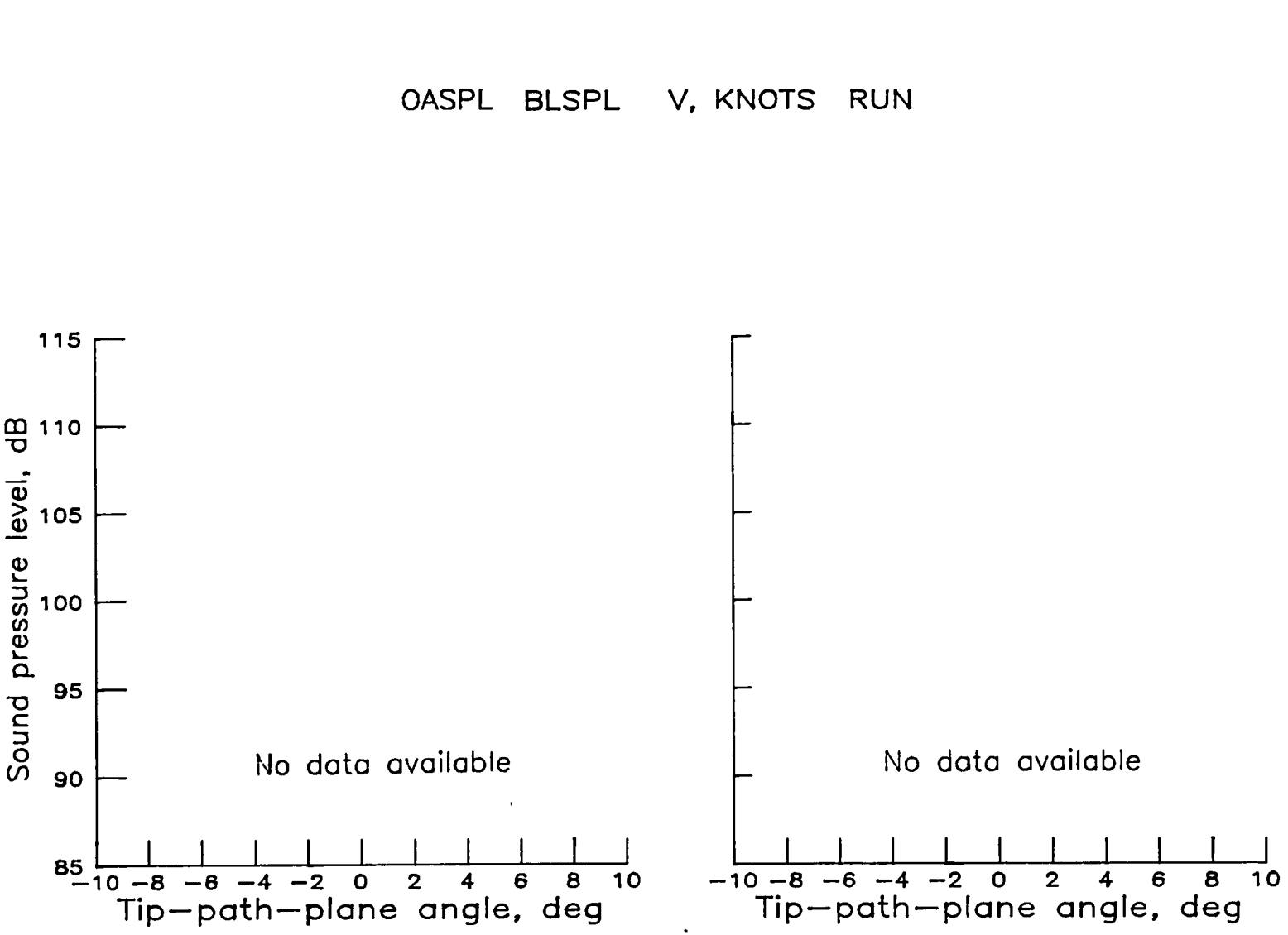

(h) Low-twist tapered tip.

Figure A10.- Continued.

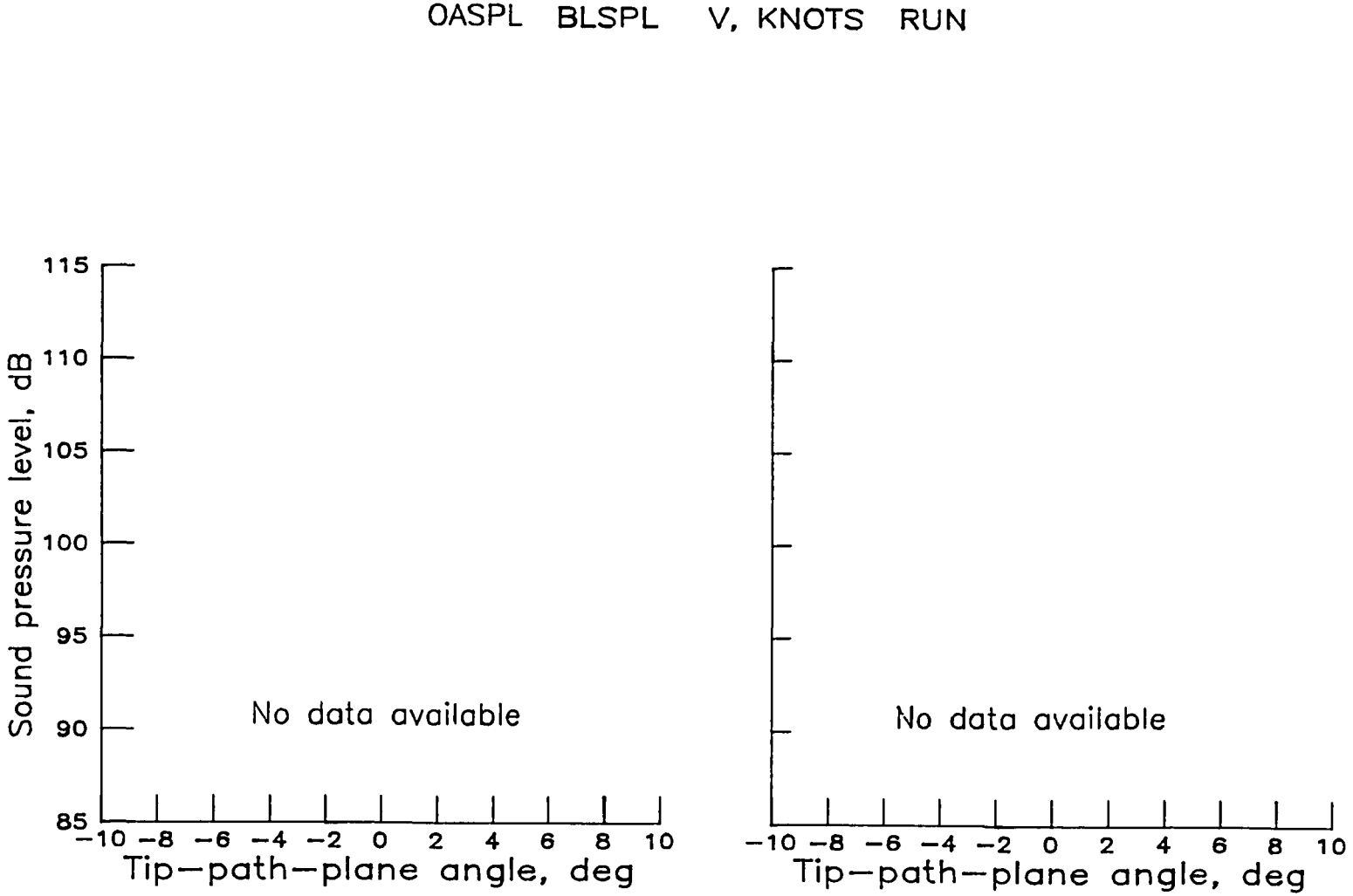

(i) Low-twist square tip.

Figure A10.- Concluded.

APPENDIX B

REPRESENTATIVE TIME HISTORIES AND NARROWBAND SPECTRA FOR SELECTED TEST POINTS IN APPENDIX A

This appendix contains plots of the instantaneous time histories and averaged narrowband spectra for three tip-path-plane angles at a tunnel speed of 70 knots for the baseline-tip high-twist rotor at all microphone locations. The test points selected were measured at tip-path-plane angles of -4°, 4°, and 8° to correspond, respectively, to three angles of interest (onset of BVI noise, maximum BVI noise, and decreasing BVI noise) at that speed. (See fig. 3.) The time history data have not been corrected, but the spectra have been corrected for background noise and acoustic reflections (ref. 15).

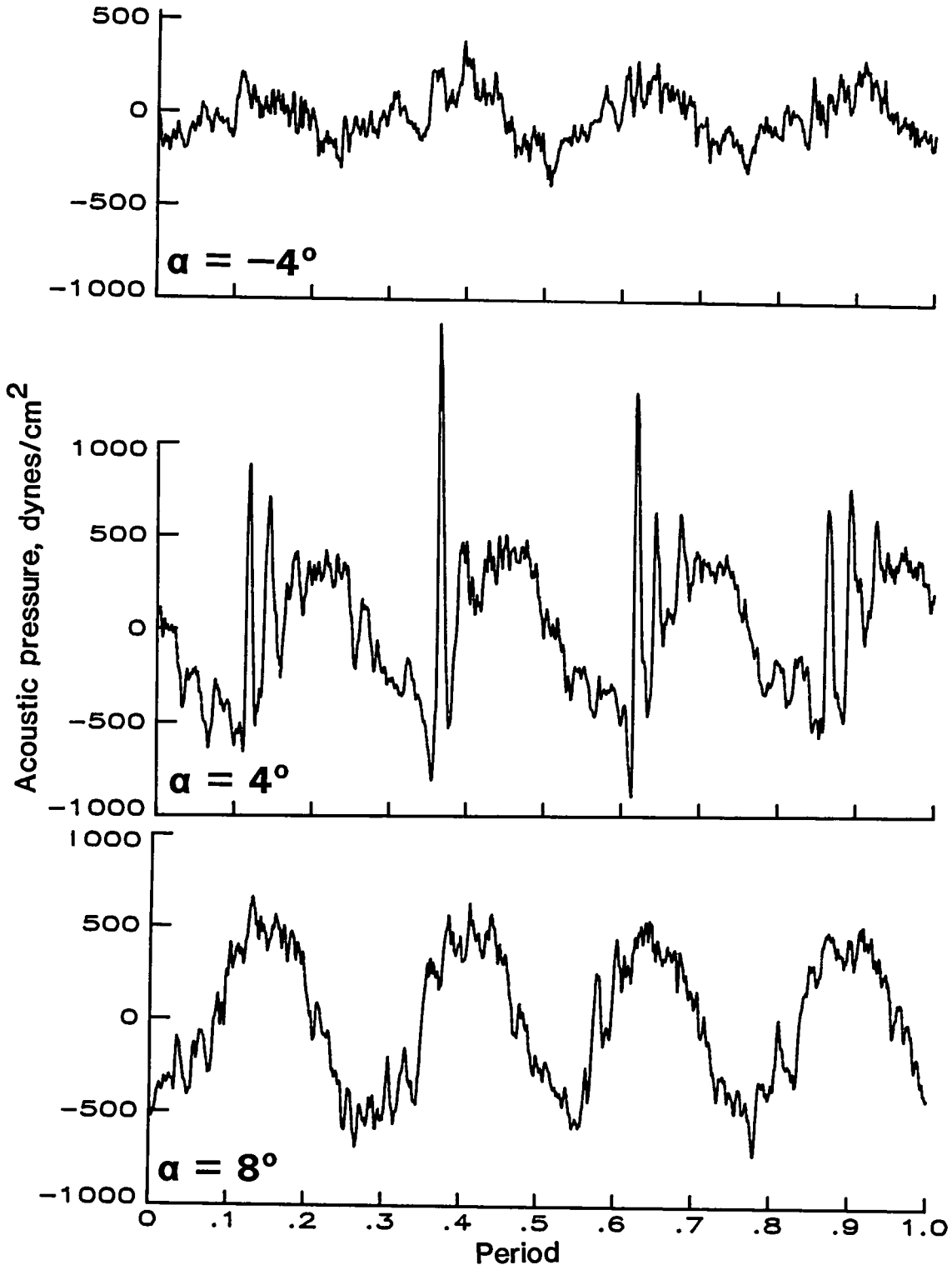

(a) Acoustic time history at α = -4°, 4°, and 8°.

Figure B1.- Data for baseline-tip high-twist rotor for microphone 1. V = 70 knots; run 106.

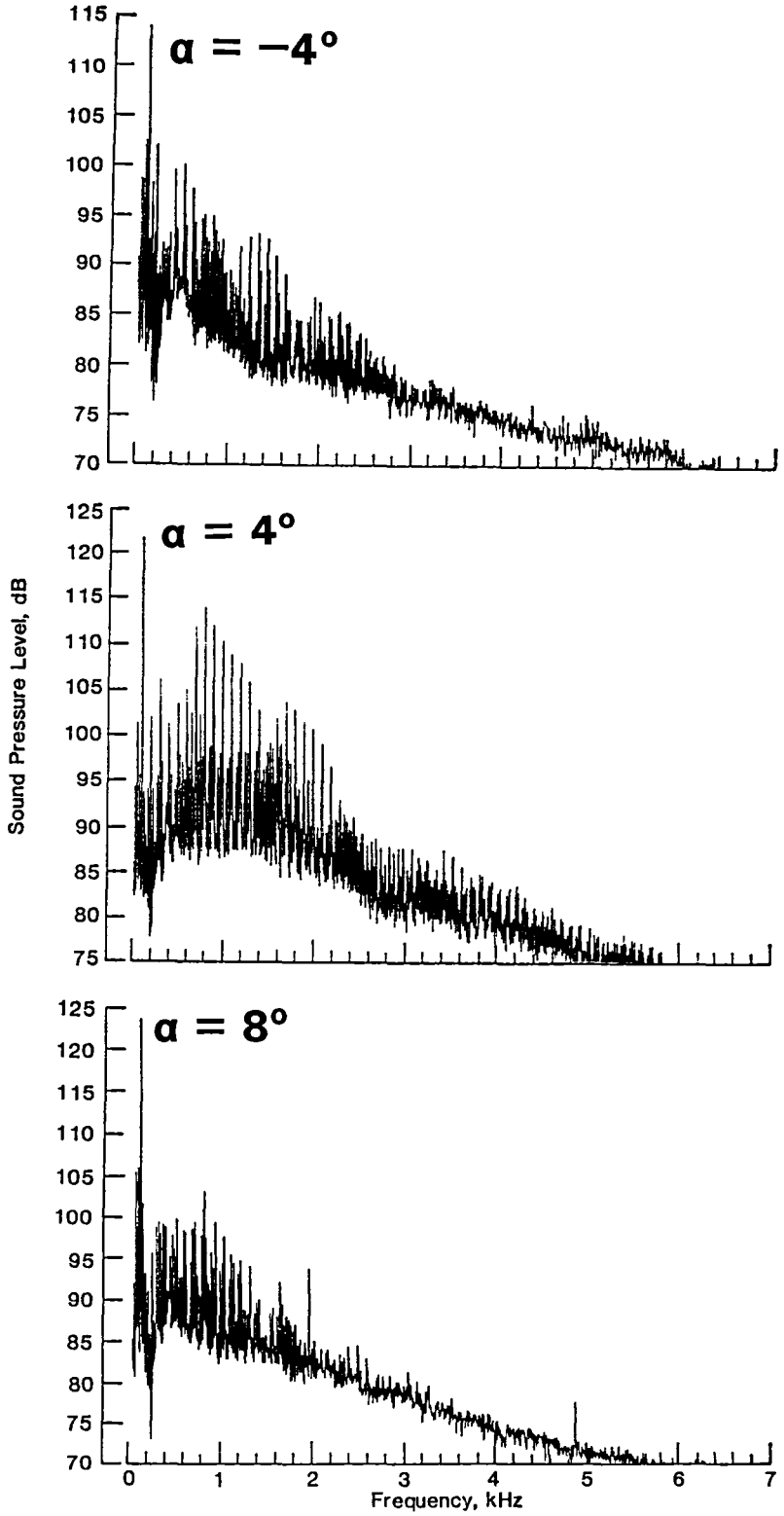

(b) Averaged spectrum at α = -4°, 4°, and 8°.

Figure B1.- Concluded.

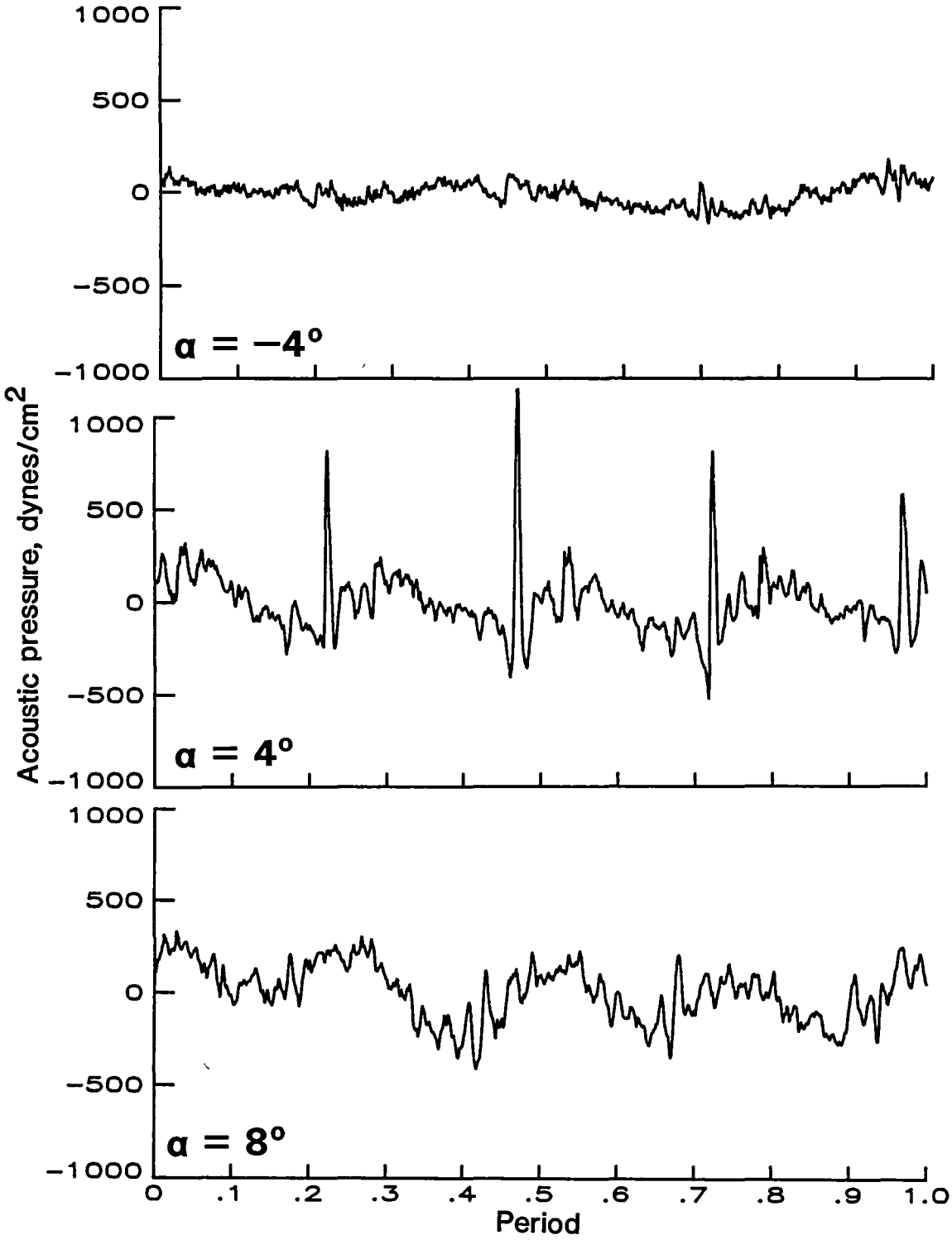

(a) Acoustic time history at α = -4°, 4°, and 8°.

Figure B2.- Data for baseline-tip high-twist rotor for microphone 2. V = 70 knots; run 106.

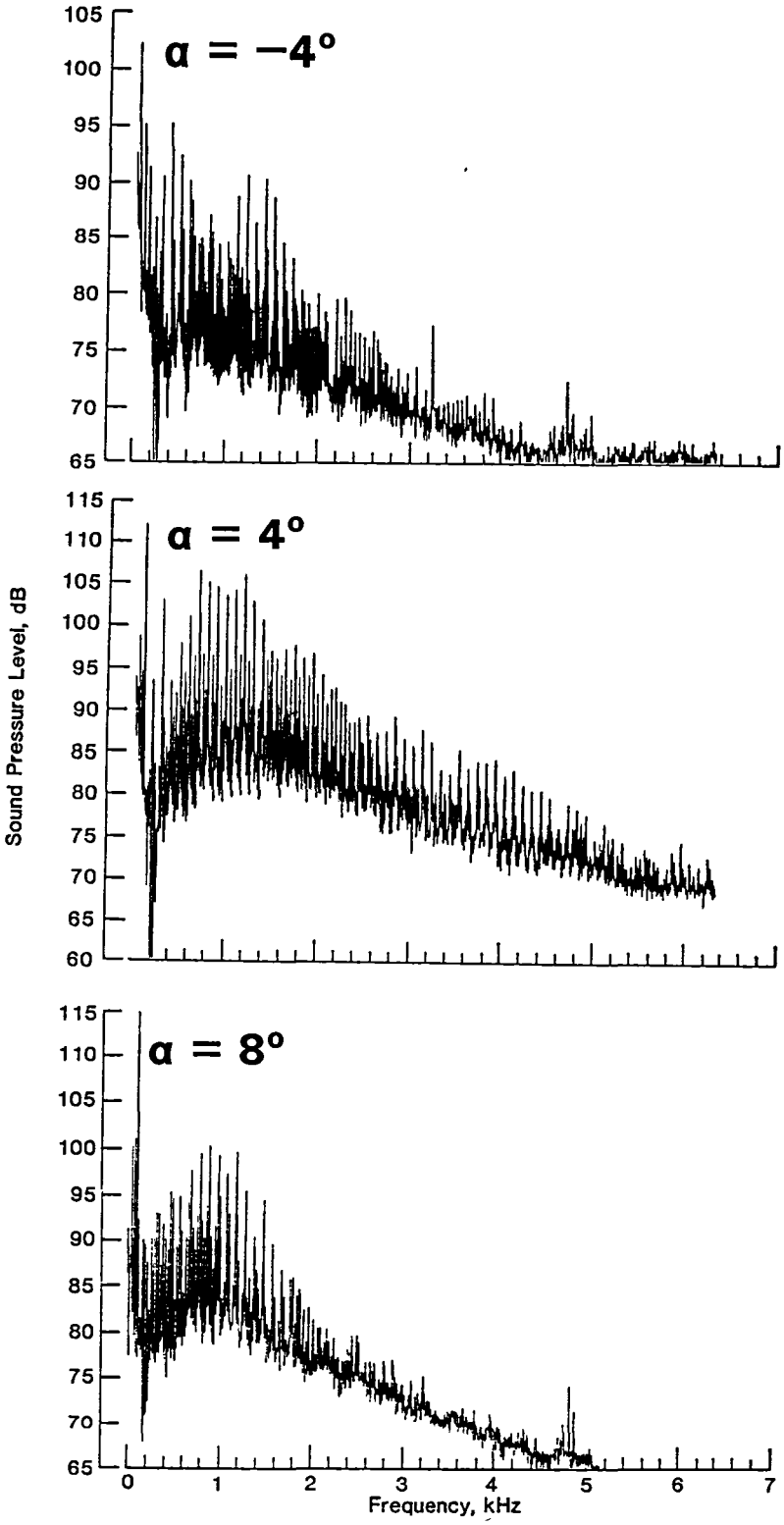

(b) Averaged spectrum at $\alpha = -4°$, 4°, and 8°.

Figure B2.- Concluded.

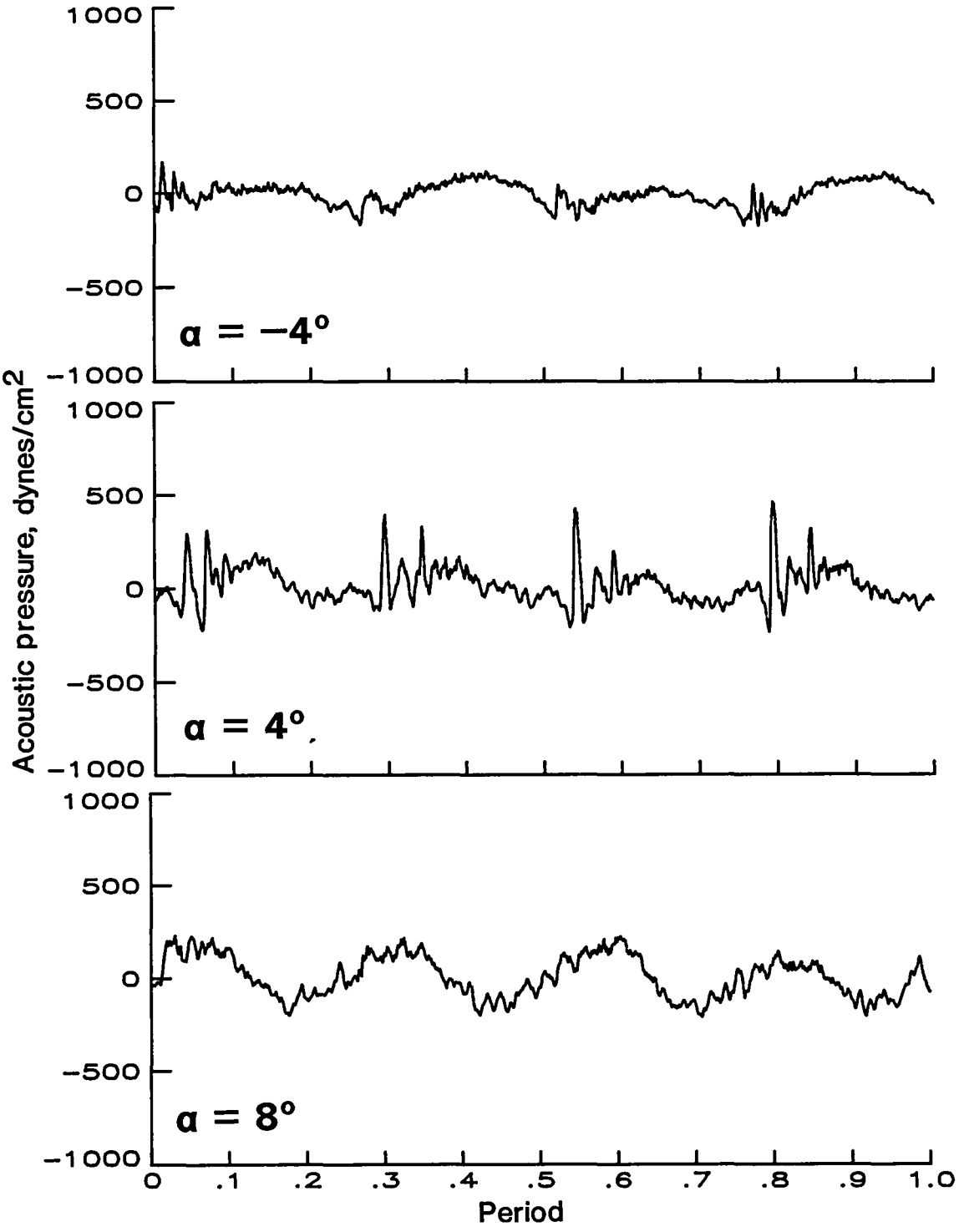

(a) Acoustic time history at α = -4°, 4°, and 8°.

Figure B3.- Data for baseline-tip high-twist rotor for microphone 3. V = 70 knots; run 106.

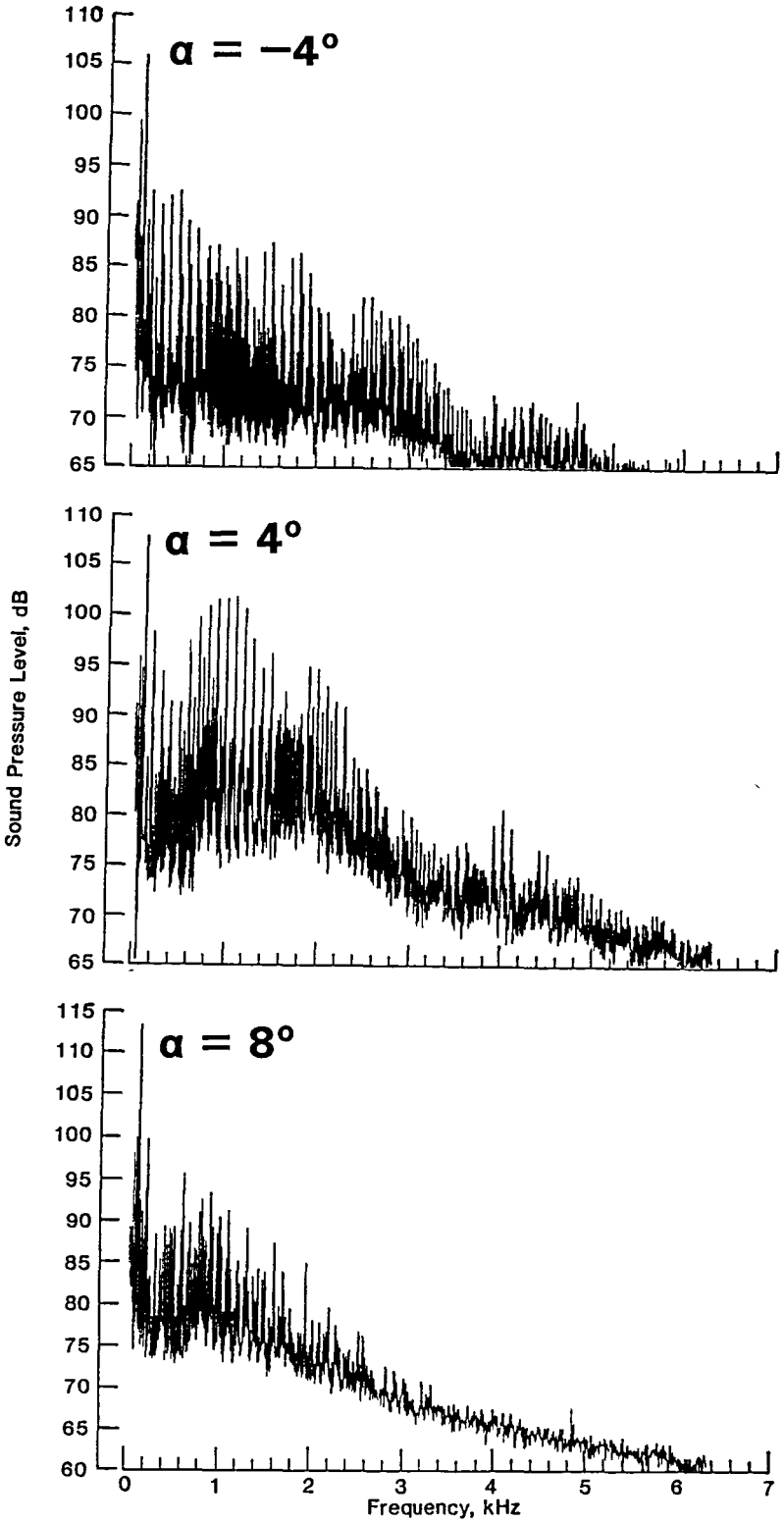

(b) Averaged spectrum at $\alpha = -4°$, 4°, and 8°.

Figure B3.- Concluded.

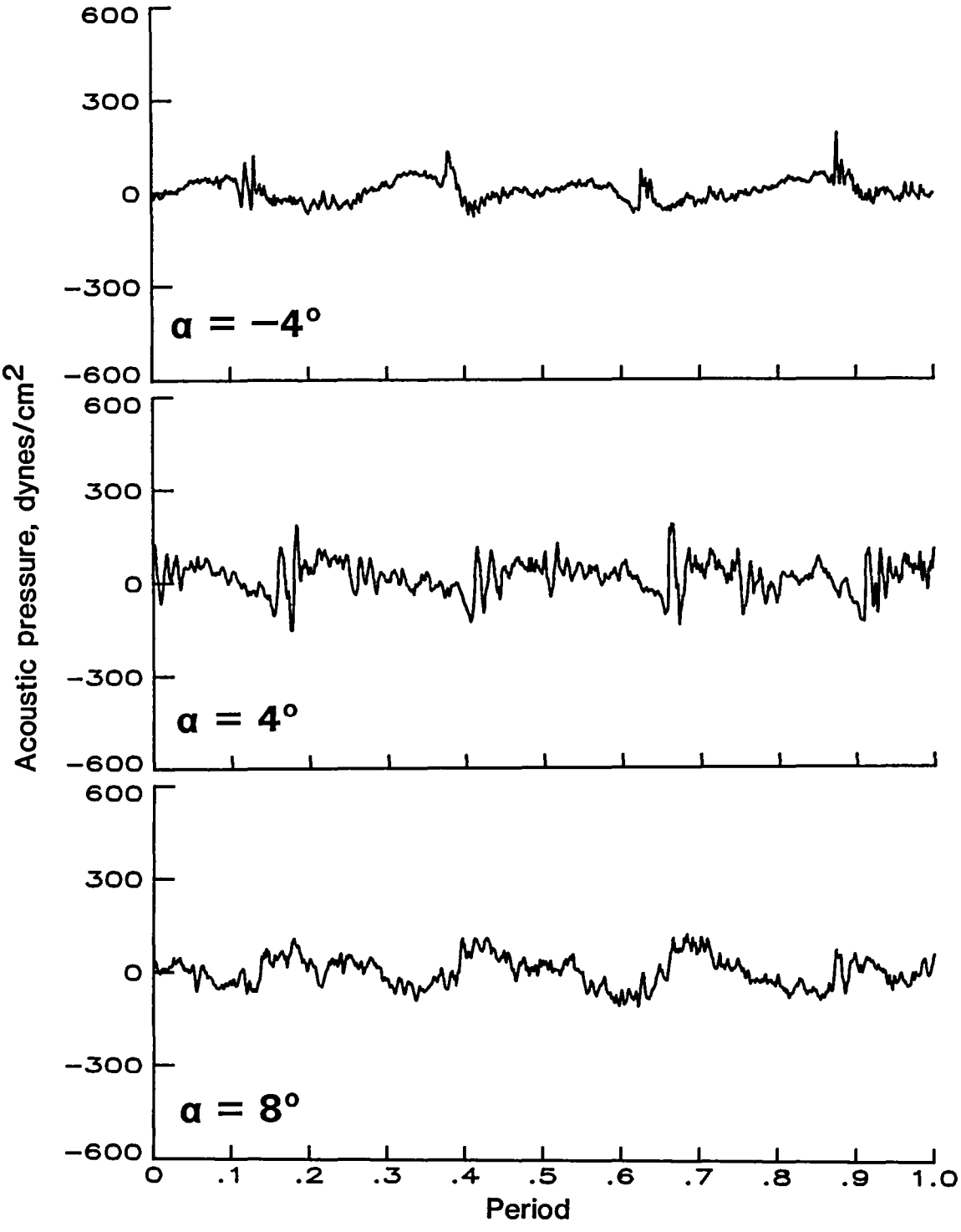

(a) Acoustic time history at α = -4°, 4°, and 8°.

Figure B4.- Data for baseline-tip high-twist rotor for microphone 4. V = 70 knots; run 106.

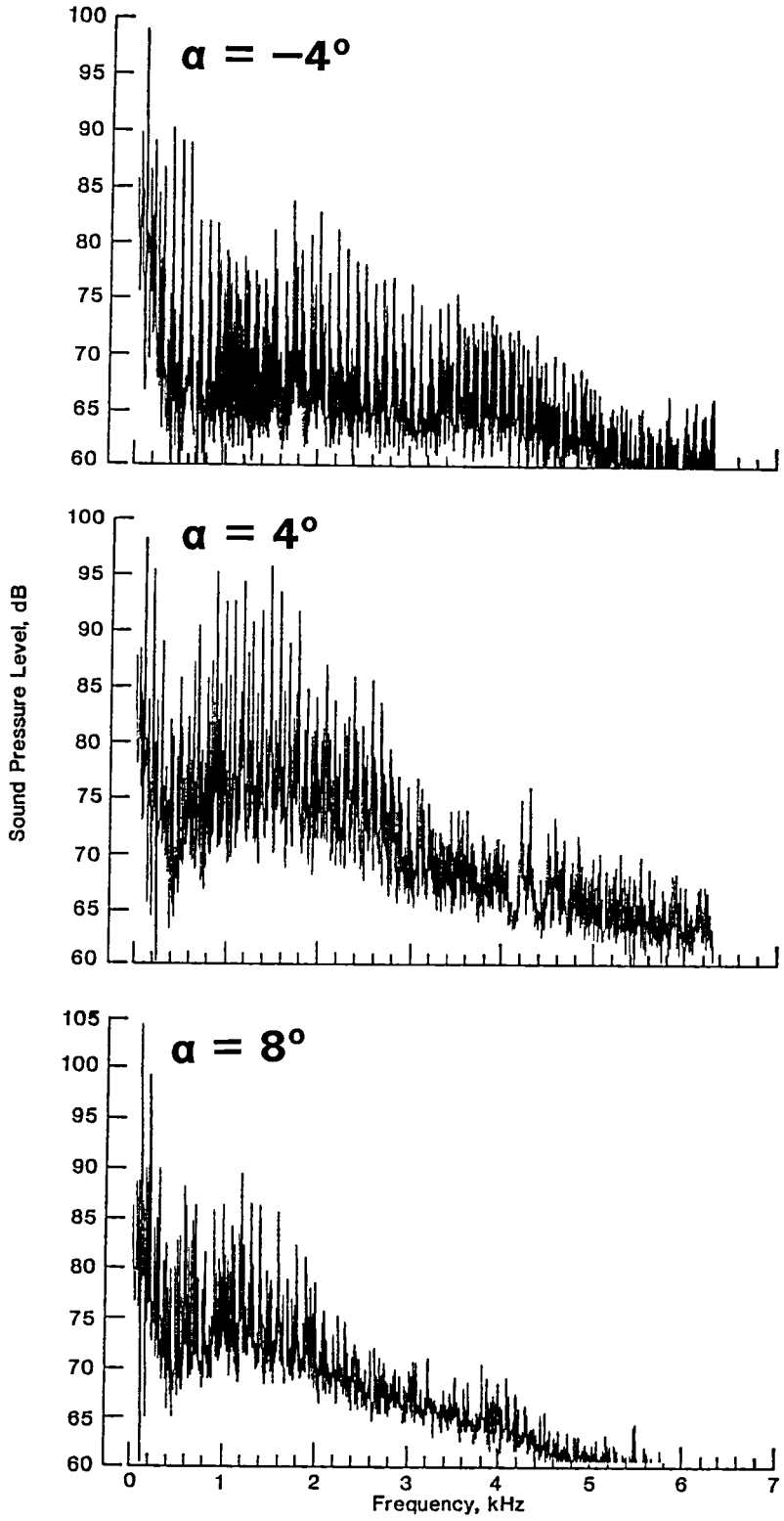

(b) Averaged spectrum at $\alpha = -4°$, 4°, and 8°.

Figure B4.- Concluded.

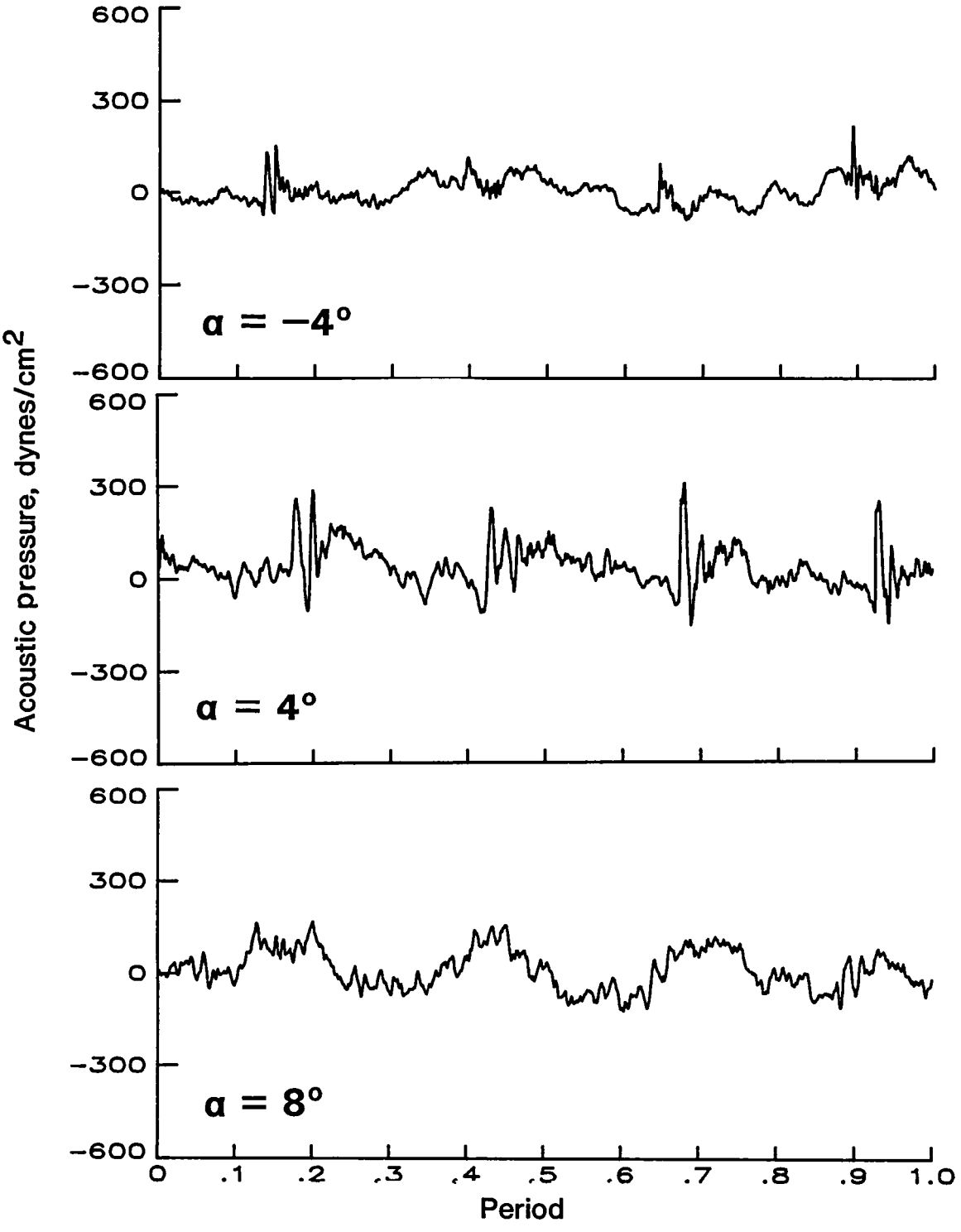

(a) Acoustic time history at α = -4°, 4°, and 8°.

Figure B5.- Data for baseline-tip high-twist rotor for microphone 5. V = 70 knots; run 106.

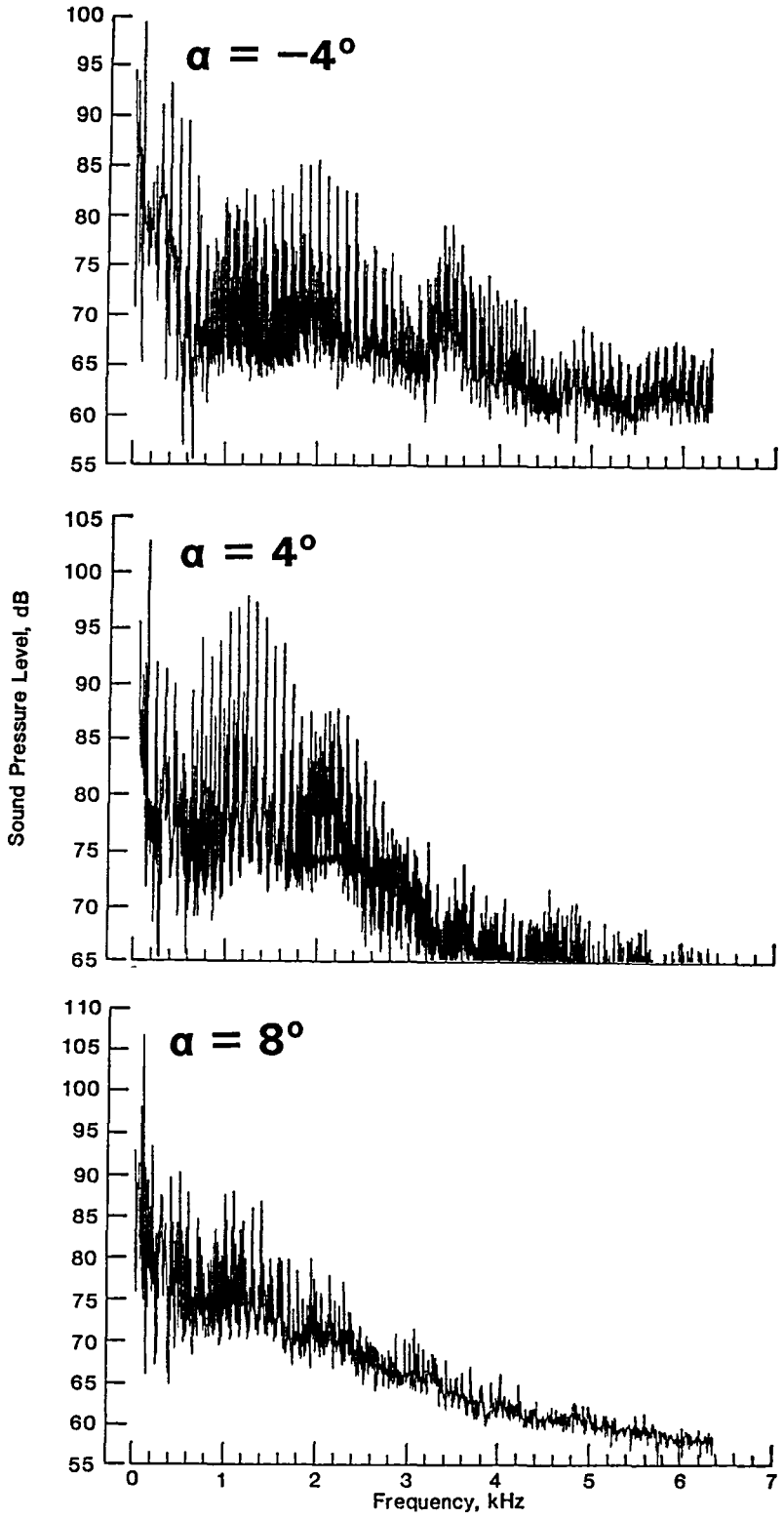

(b) Averaged spectrum at $\alpha = -4°$, 4°, and 8°.

Figure B5.- Concluded.

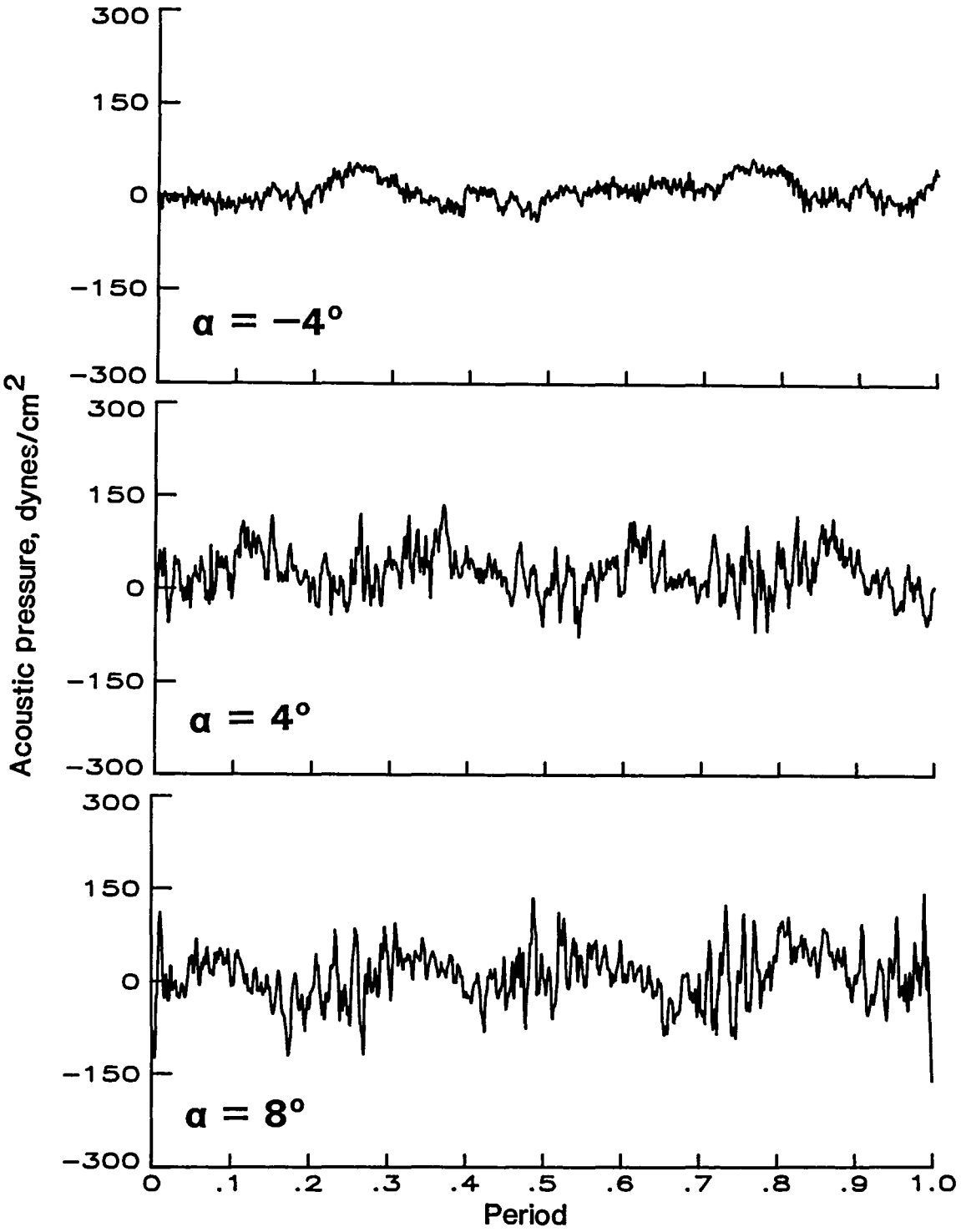

(a) Acoustic time history at α = -4°, 4°, and 8°.

Figure B6.- Data for baseline-tip high-twist rotor for microphone 7. V = 70 knots; run 106.

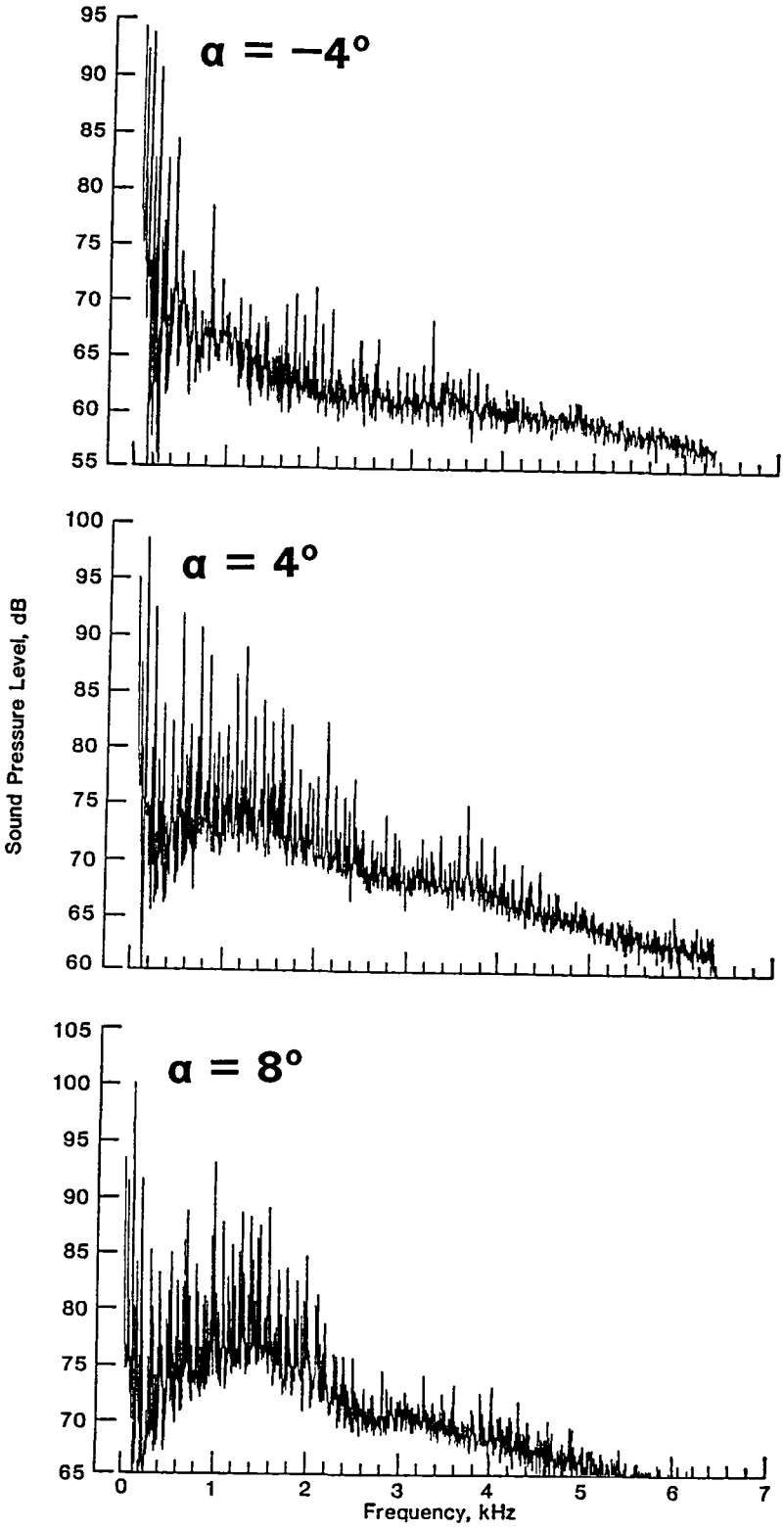

(b) Averaged spectrum at $\alpha = -4°$, 4°, and 8°.

Figure B6.- Concluded.

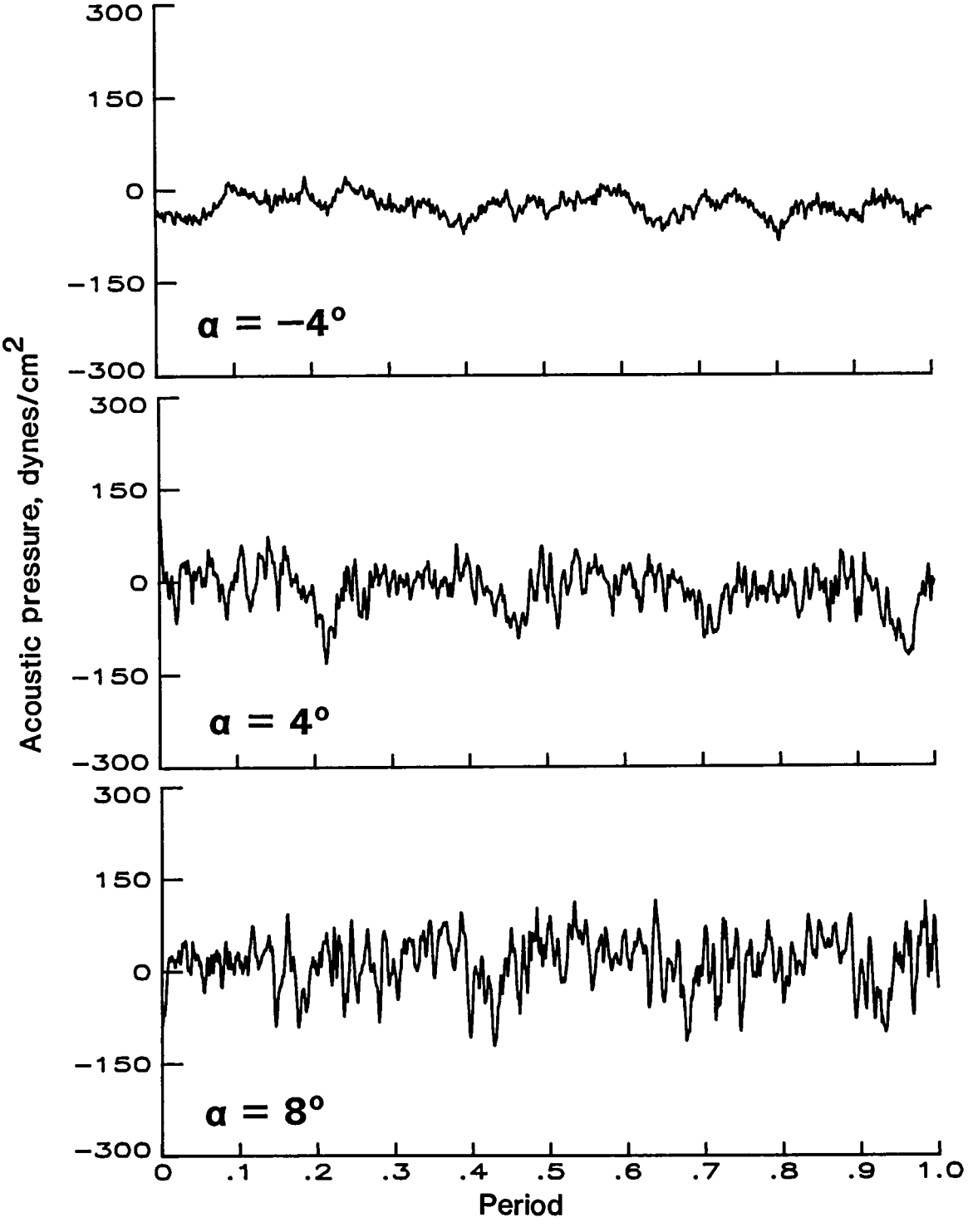

(a) Acoustic time history at α = -4°, 4°, and 8°.

Figure B7.- Data for baseline-tip high-twist rotor for microphone 8. V = 70 knots; run 106.

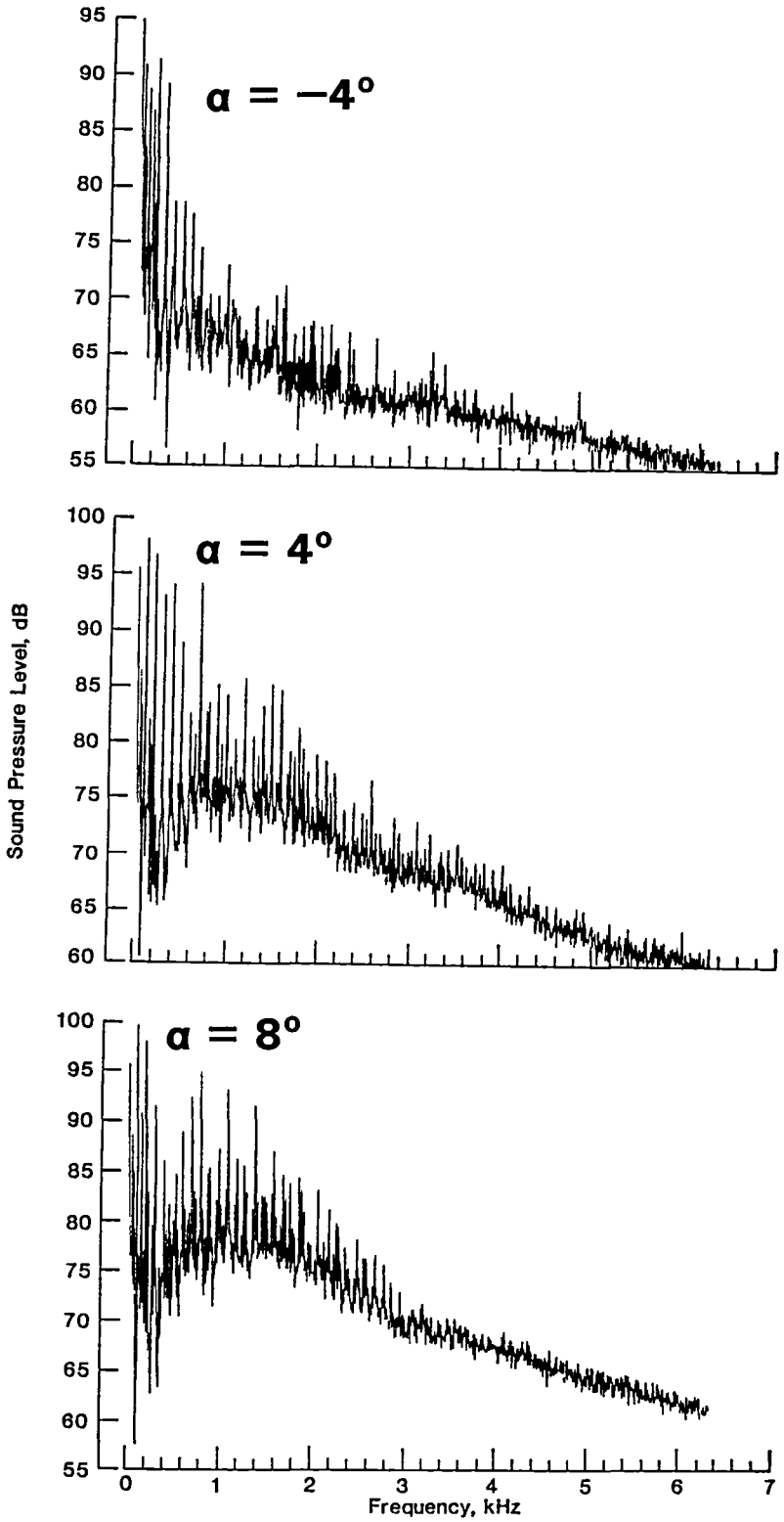

(b) Averaged spectrum at $\alpha = -4°$, 4°, and 8°.

Figure B7.- Concluded.

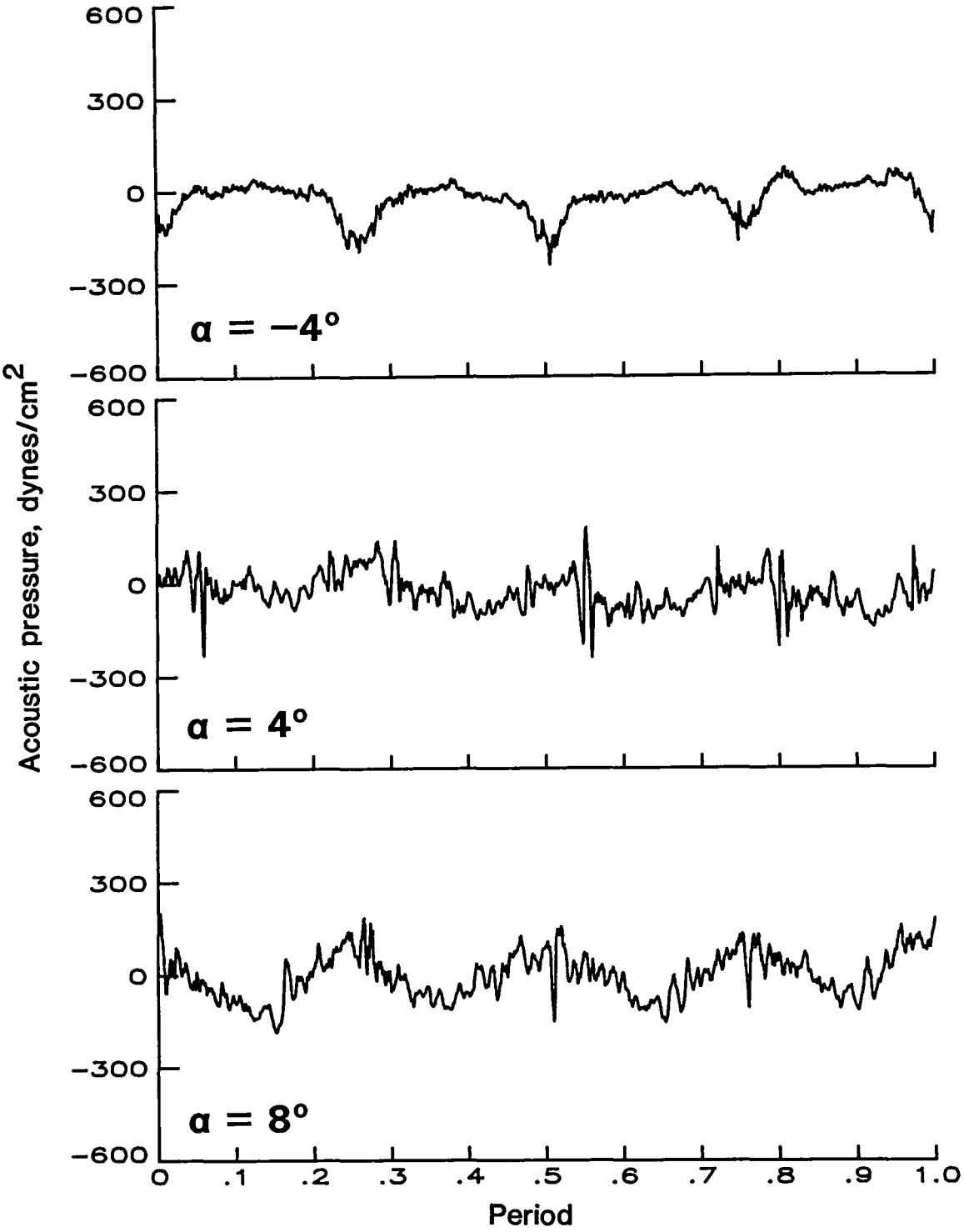

(a) Acoustic time history at α = -4°, 4°, and 8°.

Figure B8.- Data for baseline-tip high-twist rotor for microphone 9. V = 70 knots; run 106.

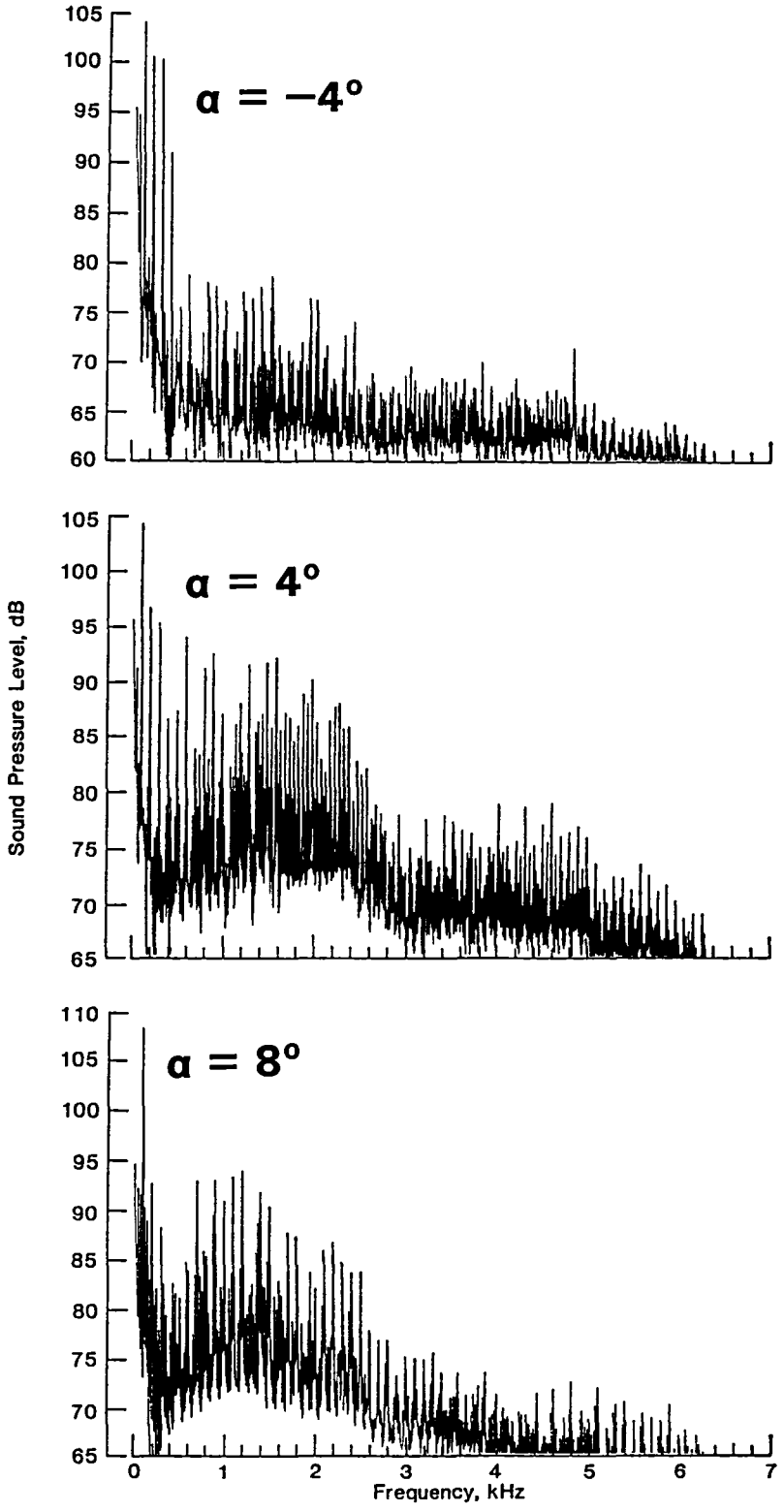

(b) Averaged spectrum at $\alpha = -4°$, 4°, and 8°.

Figure B8.- Concluded.

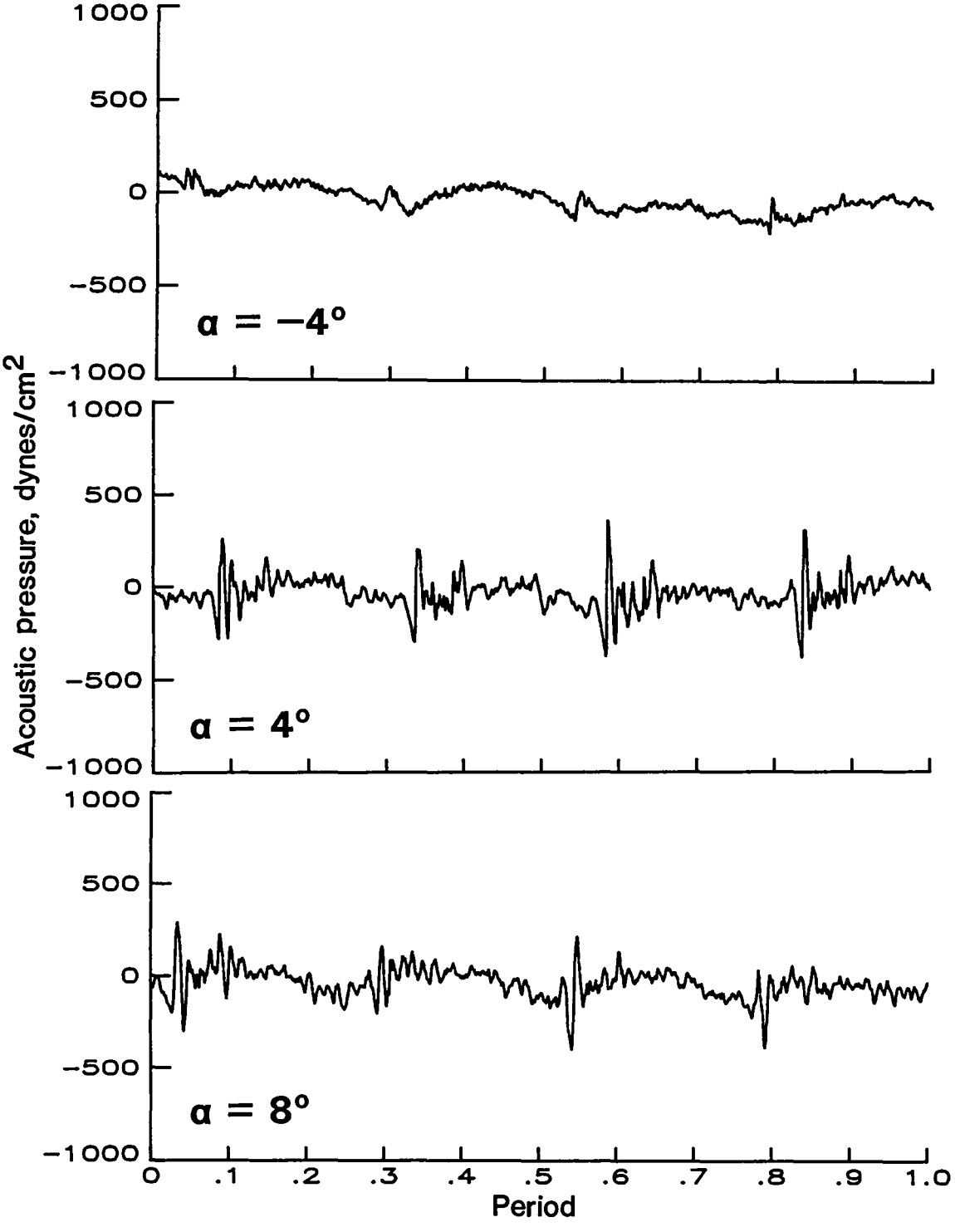

(a) Acoustic time history at α = -4°, 4°, and 8°.

Figure B9.- Data for baseline-tip high-twist rotor for microphone 12. V = 70 knots; run 106.

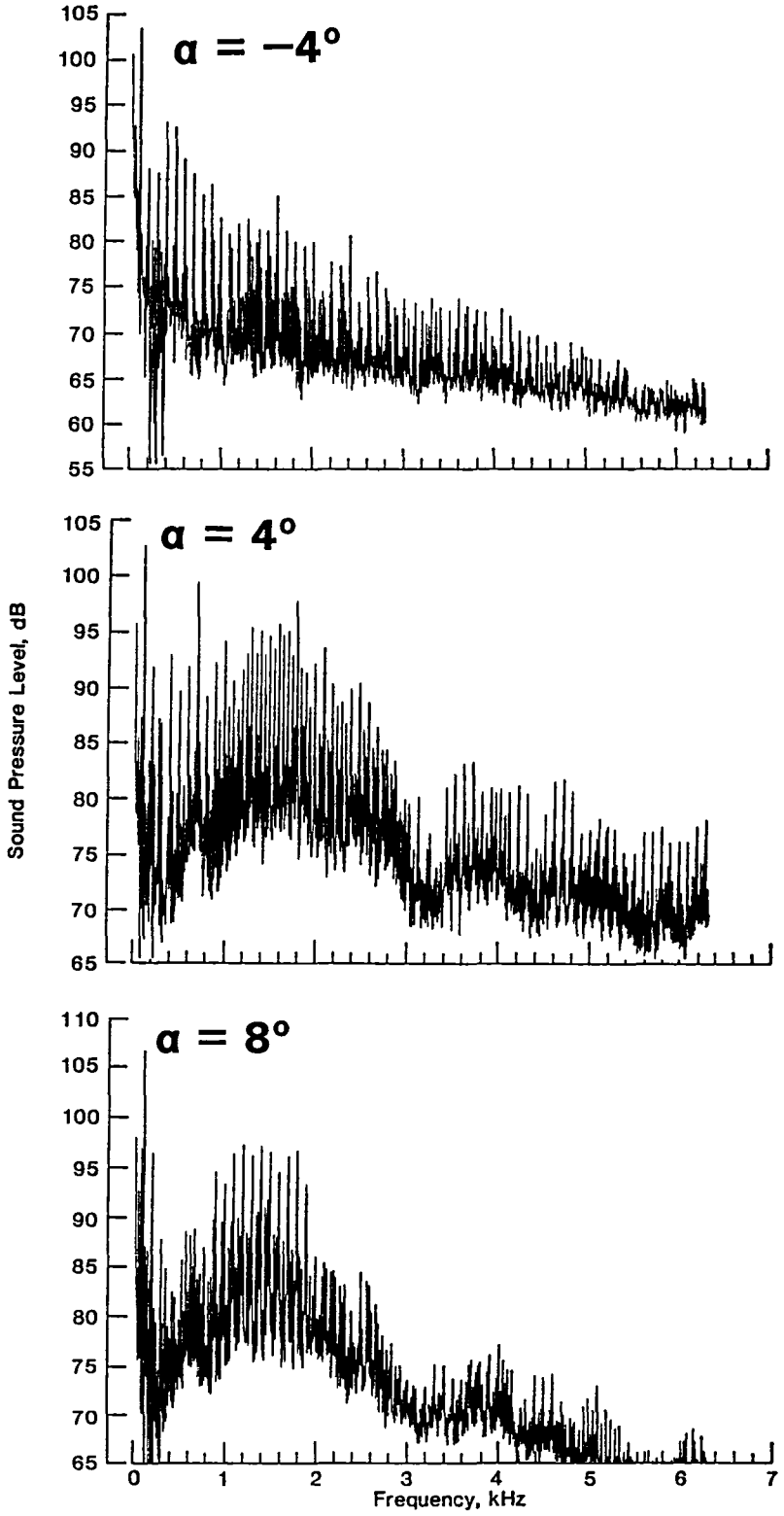

(b) Averaged spectrum at $\alpha = -4°$, 4°, and 8°.

Figure B9.- Concluded.

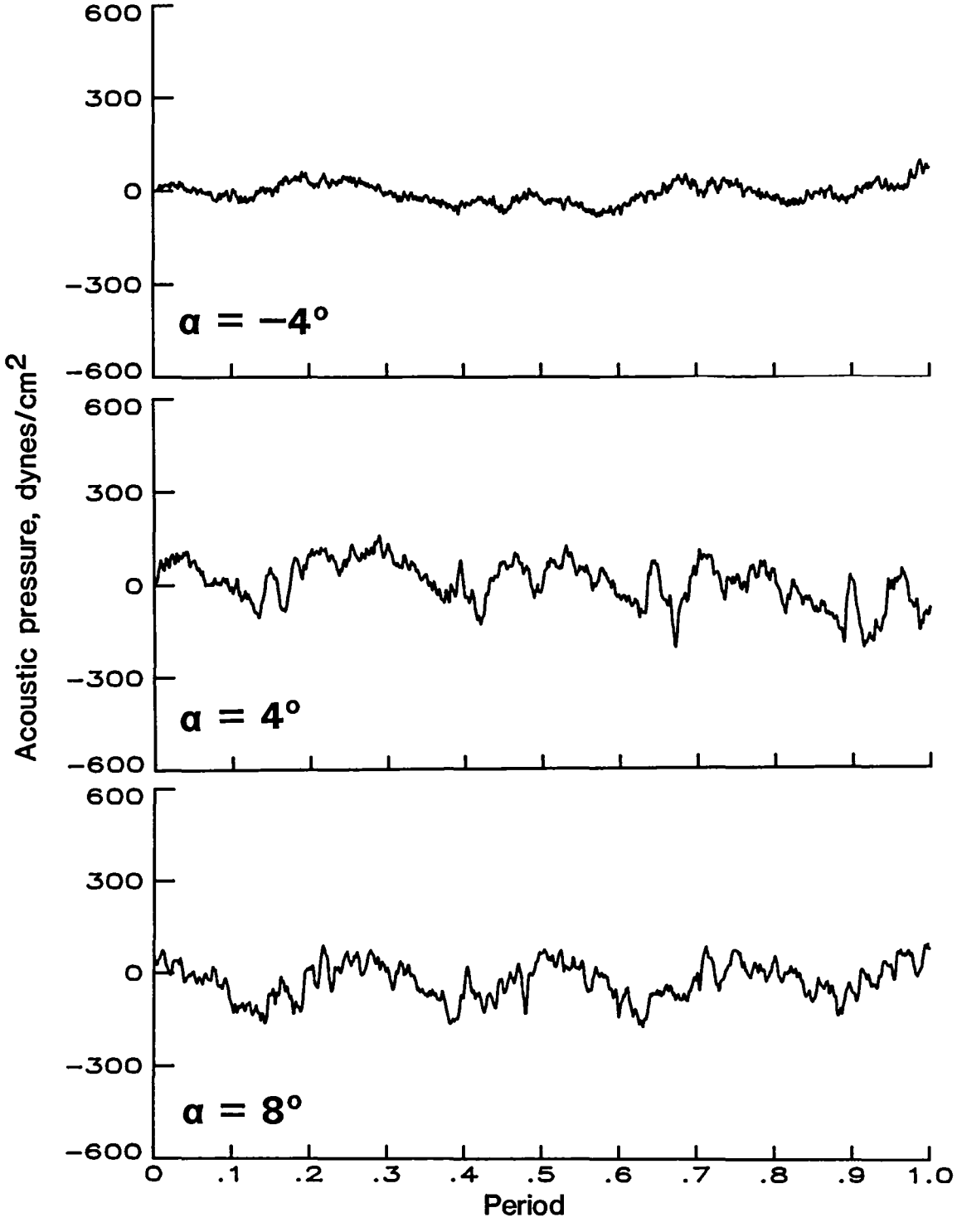

(a) Acoustic time history at α = -4°, 4°, and 8°.

Figure B10.- Data for baseline-tip high-twist rotor for microphone 17. V = 70 knots; run 106.

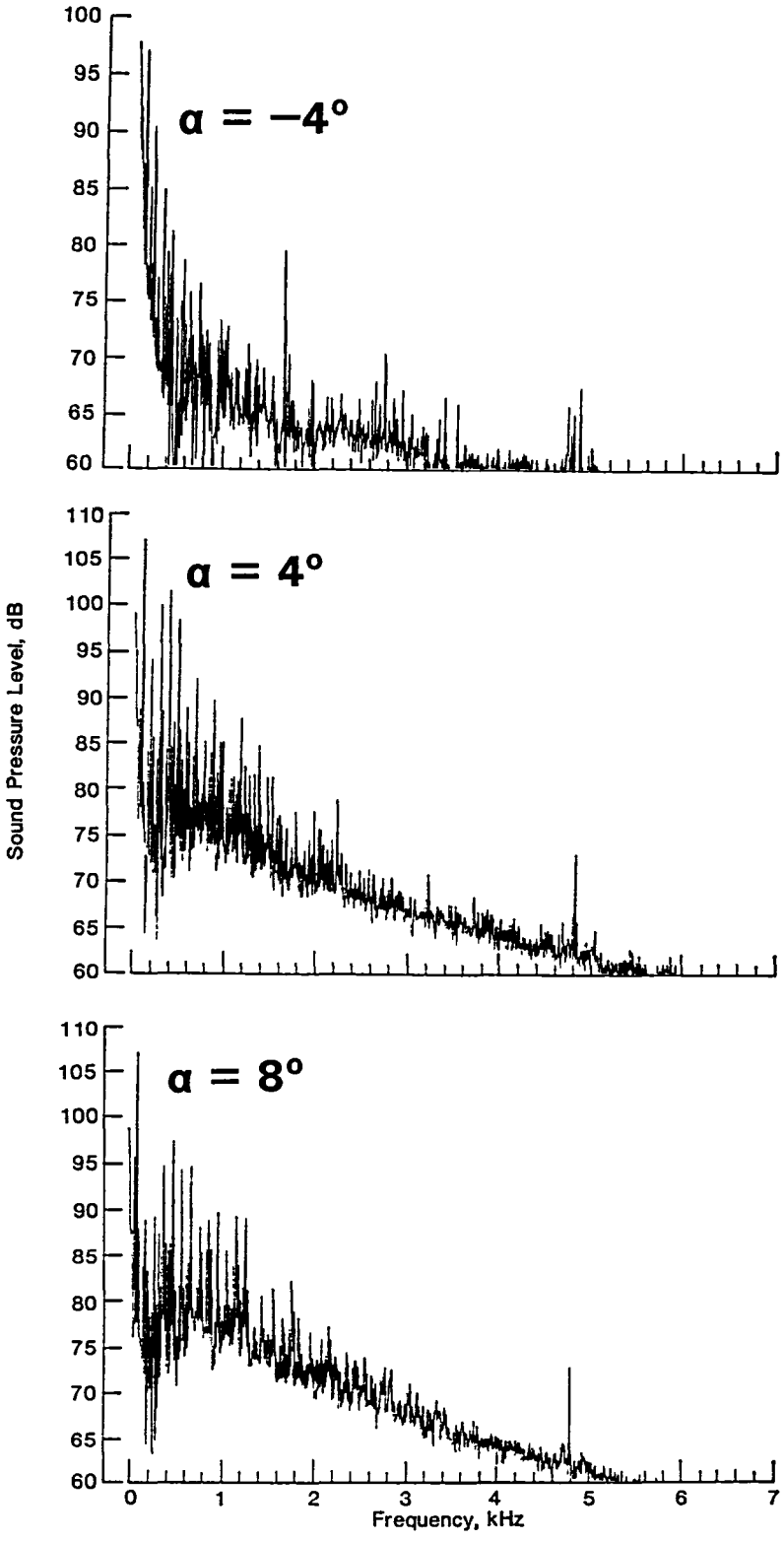

(b) Averaged spectrum at $\alpha = -4°$, 4°, and 8°.

Figure B10.- Concluded.

Standard Bibliographic Page

1 Report No	2 Government Accession No	3 Recipient's Catalog No
NASA TM-87698		

4 Title and Subtitle	5 Report Date
Wind-Tunnel Acoustic Results of Two Rotor Models With Several Tip Designs	July 1986
	6 Performing Organization Code: 532-06-13-06
7 Author(s): R. M. Martin and Andrew B. Connor	8 Performing Organization Report No: L-16081
9 Performing Organization Name and Address: NASA Langley Research Center, Hampton, VA 23665-5225	10 Work Unit No
	11 Contract or Grant No
12 Sponsoring Agency Name and Address: National Aeronautics and Space Administration, Washington, DC 20546-0001	13 Type of Report and Period Covered: Technical Memorandum
	14 Sponsoring Agency Code

15 Supplementary Notes

16 Abstract

A three-phase research program has been undertaken to study the acoustic signals due to the aerodynamic interaction of rotorcraft main rotors and tail rotors. During the first phase, two different rotor models with several interchangeable tips were tested in the Langley 4- by 7-Meter Tunnel on the U.S. Army rotor model system. An extensive acoustic data base was acquired, with special emphasis on blade-vortex interaction (BVI) noise. The details of the experimental procedure, acoustic data acquisition, and reduction are documented. The overall sound pressure level (OASPL) of the high-twist rotor systems is relatively insensitive to flight speed but generally increases with rotor tip-path-plane angle. The OASPL of the high-twist rotors is dominated by acoustic energy in the low-frequency harmonics. The OASPL of the low-twist rotor systems shows more dependence on flight speed than the high-twist rotors, in addition to being quite sensitive to tip-path-plane angle. An integrated band-limited sound pressure level, limited by 500 to 3000 Hz, is a useful metric to quantify the occurrence of BVI noise. The OASPL of the low-twist rotors is strongly influenced by the band-limited sound levels, indicating that the blade-vortex impulsive noise is a dominant noise source for this rotor design. The midfrequency acoustic levels for both rotors show a very strong dependence on rotor tip-path-plane angle. The tip-path-plane angle at which the maximum midfrequency sound level occurs consistently decreases with increasing flight speed. The maximum midfrequency sound level measured at a given location is constant regardless of the flight speed.

17 Key Words (Suggested by Authors(s))	18 Distribution Statement
Rotor acoustics Blade-vortex interaction noise Rotor noise Rotor tips	Unclassified - Unlimited Subject Category 71

19 Security Classif (of this report)	20 Security Classif (of this page)	21 No of Pages	22 Price
Unclassified	Unclassified	182	A09

For sale by the National Technical Information Service, Springfield, Virginia 22161

NASA-Langley, 1986

End of Document